CharitéCentrum für Innere Medizin und Dermatologie
Fächerverbund für Infektiologie, Pneumologie und Intensivmedizin
Klinik für Pneumologie, Beatmungsmedizin und Intensivmedizin
Klinik für Infektiologie und Intensivmedizin
Direktoren: Prof. Dr. Martin Witzenrath und Prof. Dr. Leif Erik Sander

# Habilitationsschrift

# Therapie und Immunabwehr respiratorischer Pathogene

zur Erlangung der Lehrbefähigung
für das Fach Experimentelle Medizin mit Schwerpunkt Infektionsimmunologie

vorgelegt dem Fakultätsrat der Medizinischen Fakultät
Charité - Universitätsmedizin Berlin

von

**Dr.-Ing. Geraldine Nouailles-Kursar**

**Eingereicht:** **Januar 2024**

**Dekan:** **Prof. Dr. med. Joachim Spranger**

# Inhaltsverzeichnis

# Abkürzungen

| | |
|---|---|
| APC | antigenpräsentierende Zellen |
| ARDS | akutes Atemnotsyndrom |
| Boost | Auffrischungsimpfung |
| C5a | Komplementkomponente C5a |
| CAP | Ambulant erworbene Pneumonie |
| CCR7 | C-C motif Chemokinrezeptor Typ 7 |
| COVID-19 | Coronavirus Erkrankung 2019 |
| CXCL5 | C-X-C motif Chemokin 5 |
| DC | dendritische Zellen |
| hACE2 | humanes Angiotensin-konvertierendes Enzym 2 |
| HIS | Humanes Immunsystem |
| HIV | Humanes Immundefizienz-Virus |
| IFNAR1 | Typ-I-IFN-Rezeptor |
| IFN-γ | Interferon-gamma |
| IgA | Immunglobulin A |
| IL | Interleukin |
| ILC | lymphoide Zellen des angeborenen Immunsystems |
| K18 | humaner Keratin 18 Promotor |
| LTBI | latente TB-Infektion |
| MHC | Haupthistokompatibilitätskomplex |
| miR | mikro-Ribonukleinsäure |
| mRNA | Boten-Ribonukleinsäuren |
| NK-Zellen | Natürliche Killerzellen |
| NSG | NOD scid gamma |
| PGE2 | Prostaglandin E2 |
| PRR | Mustererkennungsrezeptoren |
| RdRp | RNA-abhängige RNA Polymerase |
| RNA | Ribonukleinsäuren |
| RSV | respiratorisches Synzytial-Virus |
| SARS-CoV-2 | schweres akutes Atemwegssyndrom Coronavirus Typ 2 |
| TB | Tuberkulose |
| Tfh-Zellen | Follikuläre Helfer-T-Zellen |
| Th | Helfer-T-Zellen |
| WHO | Weltgesundheitsorganisation |

# 1 Einleitung

Weltweit zählen Erkrankungen des unteren Respirationstraktes zu den häufigsten Todesursachen durch Infektionskrankheiten[1]. Vor dem Ausbruch der *Coronavirus Disease 2019* (COVID-19) Pandemie im Jahr 2019, waren *Streptococcus pneumoniae* als häufigster Erreger der ambulant erworbenen Pneumonie (engl. *community-acquired pneumonia,* CAP) und *Mycobacterium tuberculosis* als häufigste infektionsbedingte Todesursache die wichtigsten Erreger von Atemwegsinfektionen[2-4]. Im Verlauf der Pandemie hat das schwere akute Atemwegssyndrom Coronavirus Typ 2 (SARS-CoV-2) *Mycobacterium tuberculosis* auf den zweiten Platz der häufigsten Todesursachen durch Infektionskrankheiten verdrängt[2].

In dieser Arbeit werden am Beispiel dieser drei prominenten Erreger von Lungeninfektionen, *Mycobacterium tuberculosis*, *Streptococcus pneumoniae* und SARS-CoV-2, allgemeine und spezifische Abwehrmechanismen der Lunge und des Immunsystems gegen respiratorische Erreger untersucht und geeignete Tiermodelle entwickelt und eingesetzt, um den Erfolg möglicher therapeutischer Maßnahmen zu evaluieren.

## 1.1 Tuberkulose

Tuberkulose (TB) ist eine Infektionskrankheit, die durch das Bakterium *Mycobacterium tuberculosis* verursacht wird. Infektions-begünstigende Faktoren sind Folgen von Armut, wie Unterernährung sowie Infektion mit dem Humanen Immundefizienz-Virus (HIV), da diese das Immunsystem schwächen. Die höchsten Prävalenzen finden sich in sogenannten Entwicklungsländern, insbesondere in Afrika, Asien und Lateinamerika[2,5].

Eine Infektion mit *Mycobacterium tuberculosis* manifestiert sich entweder als latente oder aktive Tuberkulose. Bei einer latenten TB-Infektion (LTBI) treten trotz Infektion keine Symptome auf. 90 % aller Erstinfektionen entwickeln sich zu einer LTBI, von der schätzungsweise ein Viertel der Weltbevölkerung betroffen ist. Bei einer LTBI ist das Immunsystem zwar in der Lage, die Mykobakterien zu kontrollieren und ihre Vermehrung zu hemmen, es kann sie aber nicht eliminieren. Daher sind LTBI-Patienten in der Regel nicht ansteckend und haben keine ausgeprägten infektionsbedingten Gesundheitsprobleme. Das Risiko, dass eine latente TB in eine aktive übergeht, bleibt jedoch bestehen und ist vor allem aus gesundheitspolitischer Sicht problematisch. Auslöser hierfür ist insbesondere eine Schwächung des Immunsystems durch Krankheit, Alter oder Immunsuppression. Dadurch wird die Wachstumshemmung der Mykobakterien aufgehoben. Diese Reaktivierung der Bakterien geht mit Symptomen wie Husten, Fieber, Nachtschweiß und Gewichtsverlust einher. Unbehandelt kann eine aktive Tuberkulose lebensbedrohlich sein, vor allem aber sind Patienten mit aktiver Tuberkulose auch ansteckend und können die Mykobakterien durch Aerosole wie Husten oder Niesen verbreiten[5-7].

*Mycobacterium tuberculosis* befällt hauptsächlich die Lunge, disseminierte Formen der Erkrankung sind eher selten. Charakteristisch für die TB ist die Bildung von Granulomen als Folge einer Immun- und Gewebsreaktion auf die Infektion mit Mykobakterien. Geordnete solide Granulome, wie sie bei LTBI vorkommen, dienen der Isolierung der Erreger. Der Kern des Granuloms besteht aus mit *Mycobacterium tuberculosis*-infizierten Makrophagen; T-Zellen und andere Immunzellen bilden ringförmige Strukturen, die die Erreger unter Kontrolle halten. Bei aktiver TB entwickeln die Granulome nekrotische Zentren, in denen eine ungehinderte Vermehrung der Bakterien stattfindet, was in Konsequenz zum Verlust der geordneten Granulomstruktur und zur Ausbreitung der Infektion führt[8,9].

Die Diagnose der TB erfolgt durch eine Kombination aus klinischer Untersuchung, molekularen Tests und bildgebenden Verfahren[10]. Die Behandlung einer latenten Infektion mit Antibiotika ist eher unüblich, kann aber durchgeführt werden, um die putative Entstehung einer aktiven TB zu verhindern. Aktive TB wird mit Antibiotikakombinationen behandelt, in der Regel über 6 Monate, um die langsam wachsenden Mykobakterien, die zum Teil in den Granulomen isoliert sind, vollständig zu eliminieren[5,11,12].

## 1.2 Ambulant erworbene Pneumonie (engl. *community-acquired pneumonia,* CAP)

Als CAP bezeichnet man Lungenentzündungen, deren auslösende Erreger außerhalb des Krankenhauses aufgenommen wurden. Die CAP ist eine der häufigsten Atemwegserkrankungen und tritt in allen Altersgruppen auf, mit einer höheren Prävalenz bei Säuglingen, älteren und immungeschwächten Personen[13-15].

Die häufigste Ursache der CAP sind Bakterien, wobei *Streptococcus pneumoniae* der häufigste Erreger ist. Andere CAP-Verursacher sind *Haemophilus influenzae*, *Legionella pneumophila* und *Mycoplasma pneumoniae*. Viren wie Influenza und das respiratorische Synzytial-Virus (RSV) können ebenfalls eine CAP verursachen, ebenso wie Pilze und andere Pathogene[16,17].

Zu den Symptomen der CAP zählen unter anderem Fieber, Husten, Brustschmerzen, Atemnot, Müdigkeit und Muskelschmerzen. Die Diagnose wird in der Regel durch eine Kombination aus körperlicher Untersuchung, Röntgenaufnahme des Thorax und Laboruntersuchungen wie Blut- und Sputumkulturen gestellt[18].

Präventive Maßnahmen umfassen die Impfung gefährdeter Personen gegen die häufigsten Erreger durch Pneumokokken- und jährliche Grippeimpfung. Hygienepraktiken wie Händewaschen und das Bedecken von Mund und Nase beim Husten oder Niesen minimieren die Ausbreitung von Infektionen[19]. Die Behandlung der CAP richtet sich nach dem zugrundeliegenden Erreger und dem Schweregrad der Erkrankung. Leichte Fälle von bakterieller CAP können mit oralen Antibiotika behandelt werden, während schwerere Fälle einen Krankenhausaufenthalt und intravenöse Antibiotika erfordern können. Virale CAP werden in schweren Fällen oder bei anfälligen Patienten mit antiviralen Medikamenten behandelt. Leichte unterstützende Maßnahmen wie Sauerstofftherapie und Flüssigkeitszufuhr und in schweren Fällen mechanische Beatmung können erforderlich sein. Eine rasche Diagnose und adäquate Behandlung der CAP sind wichtig, um Komplikationen wie Lungenabszesse, Sepsis und Lungenversagen zu vermeiden[20-22].

## 1.3 Coronavirus Erkrankung 2019 (COVID-19)

COVID-19 ist eine hochansteckende Atemwegserkrankung, die durch das neuartige Coronavirus SARS-CoV-2 hervorgerufen wird. SARS-CoV-2 wurde erstmals im Dezember 2019 in Wuhan, China entdeckt und hat sich seither weltweit verbreitet. Am 11. März 2020 erklärte die Weltgesundheitsorganisation (WHO) COVID-19 zur Pandemie. Erst mehr als drei Jahre später, am 5. Mai 2023 erklärte der Generaldirektor der WHO die gesundheitliche Notlage von internationaler Tragweite für beendet[23].

Die Übertragung von SARS-CoV-2 erfolgt in der Regel durch Tröpfcheninfektion über die Atemwege. Infizierte symptomatische, aber auch asymptomatische Personen können das Virus durch Husten, Niesen oder Sprechen übertragen[24]. Die Dauer der Inkubationszeit hängt von der infizierenden Virus-Variante ab und beträgt im Mittel etwa 3 – 5 Tage[25].

Zu den häufigsten Symptomen gehören Fieber, Husten, Kurzatmigkeit, Müdigkeit, Gliederschmerzen, Verlust des Geschmacks- und Geruchssinns und Halsschmerzen. In schweren Fällen kann COVID-19 einen Krankenhausaufenthalt erforderlich machen und zu Lungenentzündung, akutem Atemnotsyndrom (ARDS), Sepsis und sogar zum Tod führen[26]. Die WHO hat den Schweregrad von COVID-19 in vier Kategorien eingeteilt, die die Schwere der Symptome und die erforderliche medizinische Versorgung widerspiegeln. Nicht-schwerer Verlauf: Die Patienten zeigen leichte grippeähnliche Symptome wie Fieber, Husten und Müdigkeit. Die Patienten können zu Hause behandelt werden. Moderater Verlauf: Patienten zeigen Symptome wie Fieber, Husten und Atemnot, die Schwere der Symptome erfordert eine ärztliche Überwachung, ggf. benötigen die Patienten eine Sauerstofftherapie. Schwerer Verlauf: Patienten zeigen schwere Symptome wie Atemnot, beschleunigte Atmung, niedrige Sauerstoffsättigung und Lungenentzündung. Die Patienten müssen zur intensiven Überwachung und Behandlung stationär aufgenommen werden. Kritischer Verlauf: Patienten zeigen lebensbedrohliche Symptome wie Atemversagen, septischen Schock und Versagen mehrerer Organe. Die Patienten müssen stationär aufgenommen und intensivmedizinisch behandelt werden[27].

Die Maßnahmen zur Eindämmung der Pandemie konzentrierten sich in erster Linie auf öffentlich-gesundheitliche Maßnahmen wie zum Beispiel die soziale Distanzierung, das Tragen von Mund-Nasen-Schutz und Handhygiene. Zudem wurden Medikamente und Impfstoffe entwickelt, die einen wirksamen Schutz vor schweren COVID-19-Verläufe gewährleisten. Darüber hinaus werden gezielt antivirale Medikamente in gefährdeten Patientenpopulationen eingesetzt, um schwere COVID-19-Verläufe und damit Mortalität, Krankenhausaufenthalte und die Überlastung des Gesundheitssystems zu reduzieren[28].

COVID-19 hat erhebliche Auswirkungen auf die globale Gesundheit und Wirtschaft. Bis Oktober 2023 wurden weltweit über 770 Millionen Fälle und fast 7 Millionen Todesfälle gemeldet. Die Pandemie hat die Gesundheitssysteme weltweit überlastet, das tägliche Leben beeinträchtigt und erhebliche wirtschaftliche Verluste verursacht[3].

## 1.4 Immunabwehr in der Lunge

Die Lunge ist Teil des Atmungssystems, hat aber auch eine Schutzfunktion gegen Krankheitserreger und Fremdpartikel, die mit der Atemluft in den Körper gelangen. Zu den unmittelbar wirksamen Abwehrmechanismen der Lunge gehören mechanische und chemische Barrieren sowie die Besiedlung durch die normale Flora. Zu den mechanischen Barrieren gehören der Nies- und Hustenreflex, aber auch die aerodynamischen Filter in den Nasenmuscheln. Bei der Nasenatmung wird die Luft erwärmt, befeuchtet und gefiltert. Die aerodynamischen Filter verwirbeln den Luftstrom und erhöhen so den Kontakt mit der Nasenschleimhaut. Krankheitserreger und Fremdkörper werden von der Schleimhaut abgefangen[29,30]. Die mukoziliäre *Clearance* in den oberen Atemwegen stellt eine weitere mechanische Barriere dar. Durch koordiniertes Schlagen der Flimmerhärchen des Atemwegsepithels wird der produzierte Schleim einschließlich der eingeschlossenen Krankheitserreger und Fremdkörper aus der Lunge befördert[31,32]. Wie alle nach außen gerichteten Körperoberflächen ist auch die Lunge mit Epithelzellen ausgekleidet, die eindringende Krankheitserreger daran hindern, in tiefere Gewebeschichten einzudringen. Die Epithelzellen der Lunge erfüllen je nach Typ und Lokalisation sehr unterschiedliche Funktionen. Sie sind nicht nur Teil der mechanischen Abwehrmechanismen, sondern produzieren beispielsweise auch antimikrobielle Peptide, die der chemischen Immunabwehr zugeordnet werden[33,34]. Auch andere Immunzellen wie Neutrophile und Makrophagen produzieren

antimikrobielle und inflammatorische Mediatoren[35]. Die Schleimhäute werden zusätzlich durch einen bestimmten Antikörper-Isotyp, das sezernierte Immunglobulin A (IgA), geschützt. IgA kommt bevorzugt in Schleimhäuten vor, bildet Dimere und wirkt durch Neutralisation gegen eindringende Erreger[36].

Abwehrmechanismen, die auf der Erkennung von Erregern durch Rezeptoren des angeborenen Immunsystems beruhen, wirken innerhalb von Minuten, wie z. B. das Komplementsystem, bis hin zu Stunden bis Tagen, in denen z. B. die Rekrutierung von Neutrophilen und Monozyten über chemotaktische Moleküle erfolgt[37]. Die Pathogenklasse bestimmt über die Aktivierung von Mustererkennungsrezeptoren (engl. *pattern recognition receptors.* PRR) die Art der ausgelösten angeborenen Immunantwort[38]. Prominente Zellen des angeborenen Immunsystems, die bei Lungeninfektionen eine Rolle spielen, sind Alveolarmakrophagen, Neutrophile, geweberesidente inflammatorische Makrophagen, rekrutierte Makrophagen monozytären Ursprungs, lymphoide Zellen des angeborenen Immunsystems (ILC) und dendritische Zellen (DC). Alveolarmakrophagen, Neutrophile und inflammatorische Makrophagen sind Phagozyten, sie erkennen Krankheitserreger über spezielle Rezeptoren auf ihrer Oberfläche und können diese durch Phagozytose aufnehmen. Bei der Phagozytose fusioniert das Phagosom mit den eingeschlossenen Pathogenen mit dem Lysosom zum Phagolysosom. Durch Ansäuerung, antimikrobiell wirkende Enzyme, Proteine, Peptide sowie Sauerstoff- und Stickstoffradikale werden die Erreger abgetötet oder in ihrem Wachstum gehemmt. Die Aktivierung angeborener Immunzellen über PRR führt zur Sekretion von Effektormolekülen wie Lipidmediatoren, Zytokinen und Chemokinen[39]. ILC sind lokalisierte Lymphozyten, die keine antigenspezifischen Rezeptoren besitzen und über T-Helfer-ähnliche (ILC1-3) oder zytotoxische Effektorfunktionen (Natürliche Killerzellen, NK-Zellen) verfügen. Die Aktivierung der ILC-Effektorfunktionen erfordert keine Antigenpräsentation und erfolgt daher schnell[40]. Dendritische Zellen sind wie Makrophagen professionelle antigenpräsentierende Zellen (APC). Sie nehmen Krankheitserreger oder deren Bestandteile auf und wandern in die sekundären lymphatischen Organe und präsentieren sie dort den T-Zellen über Moleküle des Haupthistokompatibilitätskomplexes (MHC). Extrazelluläre Antigene werden durch Phagozytose aufgenommen, prozessiert und über MHCII CD4 T-Zellen präsentiert. Zytosolische Antigene werden durch MHCII CD8 T-Zellen präsentiert. Nach der Erkennung des Pathogens als fremd durch PRR werden die APC aktiviert, in der Folge kommt es zu einer verstärkten Antigenprozessierung und Präsentation auf dem MHC sowie zur Expression von kostimulatorischen Molekülen und des C-C motif Chemokinrezeptors Typ 7 (CCR7). CCR7 ermöglicht die Erkennung chemotaktischer Moleküle in den Lymphknoten und initiiert die Migration der aktivierten APC[41].

Die Aktivierung des adaptiven Immunsystems, T-Zellen und B-Zellen, in den sekundären lymphatischen Organen dauert am längsten und erfolgt je nach Antigenmenge innerhalb von Tagen bis Wochen. Für die T-Zell-Aktivierung müssen den Antigen-spezifischen T-Zellen drei Signale vermittelt werden. Signal 1 ist die Erkennung des Antigens im MHC-Komplex mittels spezifischer T-Zell-Rezeptoren, Signal 2 ist das kostimulatorische Signal, beides vermittelt über die aktivierte APC, und Signal 3 ist das Differenzierungssignal über das umgebende Zytokin-Milieu[42,43]. CD4 T-Zellen sind Helfer-T-Zellen (Th) und üben ihre Effektorfunktion indirekt aus, indem sie andere Immunzellen in ihrer Effektorfunktion unterstützen, z. B. aktivieren Th1-Zellen Makrophagen, Th17-Zellen aktivieren das Epithel und stimulieren es zur Rekrutierung von Neutrophilen, Follikuläre Helfer-T-(Tfh)-Zellen unterstützen die Aktivierung von B-Zellen[44]. Effektor CD8 T-Zellen sind zytotoxische T-Zellen, sie können infizierte Körperzellen gezielt abtöten. Die Aktivierung von B-Zellen zu Antikörper-sezernierenden Plasmazellen kann mit oder ohne Hilfe von T-Zellen erfolgen. B-Zellen werden aktiviert, indem sie Antigene über den

B-Zell-Rezeptor erkennen, das kostimulatorische Signal erhalten B-Zellen von aktivierten T-Helferzellen, denen sie ihr Antigen auf MHCII präsentieren. Das Zytokin-Milieu bestimmt den Antikörper-Isotyp, der durch Klassenwechsel in der Keimzellreaktion entsteht. In der Keimzellreaktion findet auch die Affinitätsreifung der B-Zellen und damit die Ausbildung hochspezifischer B-Zellrezeptoren und damit der sezernierten Antikörper statt[45].

Wenn der Erreger die ersten mechanischen und chemischen Barrieren überwunden hat und das angeborene Immunsystem als zweite Verteidigungslinie nicht in der Lage ist, den eindringenden Erreger zu eliminieren, bleibt die adaptive Immunantwort als dritte Verteidigungslinie. Versagt auch diese oder ist die durch die Immunreaktion verursachte Gewebeschädigung zu groß, kann es zu Organversagen und schließlich zum Tod des infizierten Organismus kommen.

# 2 Eigene Arbeiten

## 2.1 Tuberkulose: Angeborene Immunabwehr und Modelle zur Therapieevaluation

TB ist medikamentös behandelbar und kann bei Kindern durch eine Impfung im Neugeborenenalter teilweise verhindert werden. Wie bei vielen anderen bakteriellen Infektionskrankheiten treten jedoch auch bei Mykobakterien zunehmend Resistenzen gegen Antibiotika auf[10,46]. Die Entwicklung und Erprobung neuer Therapieformen und ein besseres Verständnis der Krankheitsmechanismen sind daher auch aus gesundheitspolitischer Sicht von hoher Relevanz.

Insbesondere die Immunmechanismen, die der Entwicklung einer LTBI zugrunde liegen, wie sie bei den angenommen 1,7 Milliarden asymptomatisch infizierten Menschen im Vergleich zu den geschätzten 10,6 Millionen Menschen, die jährlich eine aktive TB entwickeln, beobachtet wird, sind in Tiermodellen schwer darstellbar[5]. Klassische Aerosol-Infektionsmodelle mit niedrigen *Mycobacterium tuberculosis*-Infektionsdosen in resistenten Mausstämmen wie Balb/c und C57BL/6 zeigen ein sehr einheitliches Infektionsbild. Nach etwa 15 Tagen kommt es zur ersten Rekrutierung spezifischer adaptiver Immunzellen, deren Antwort um den 21. bis 28. Tag nach der Infektion ihren Höhepunkt erreicht. Die Mykobakterien werden zu diesem Zeitpunkt in ihrem Wachstum gehemmt, aber nicht vollständig eliminiert, so dass es zu einer chronischen Infektion kommt. Interferon-gamma (IFN-γ) ist hierfür unter anderem essentiell, wie Studien an IFN-γ-defizienten Mäusen zeigen konnten[47,48]. Der Einsatz alternativer Infektionsmodelle wie der hochdosierten *Mycobacterium tuberculosis*-Infektion oder von suszeptiblen Mausstämmen wie 129S2-Mäusen lieferte wichtige Hinweise darauf, dass auch die angeborene Immunantwort eine Rolle in der Pathogenese der TB spielt. Insbesondere Neutrophilenantworten waren in letalen TB-Modellen besonders ausgeprägt[49-51].

Auch die beim Menschen beobachtete Vielfalt der Granulome wird in Standard-Mausmodellen nicht abgebildet[52,53]. Granulome oder Tuberkuloseläsionen des Menschen reichen von Tuberkulosepneumonien bis hin zu typischen nekrotischen käsigen Granulomen, die durch einen inneren nekrotischen käsigen Kern, umgeben von einem inneren Makrophagenring und einem äußeren Lymphozytenring, gekennzeichnet sind. Es gibt aber auch nicht-nekrotische, fibrotische oder mineralisierte Granulomstrukturen[8,9,54]. Im Gegensatz dazu bilden sich in den gängigen Mausmodellen nur lockere Strukturen aus infiltrierenden Zellen und infizierten Makrophagen ohne die typischen nekrotischen Kerne[55,56]. Dies ist insofern von besonderer Bedeutung, als dass die Granulomstruktur maßgeblich für die notwendige lange chemotherapeutische Behandlung von TB-Patienten ist.

Unsere Forschung konzentrierte sich daher auf die Identifizierung und Charakterisierung pathologischer Krankheitsmechanismen sowie auf die Entwicklung neuer Tiermodelle mit komplexer Granulombildung, die für präklinische Medikamententests besser geeignet sind. Im Folgenden werden zwei ausgewählte eigene Studien vorgestellt, die zum einen die Bedeutung der epithelialen Immunantwort für die Rekrutierung pathologischer Neutrophile bei TB verdeutlichen[50] und zum anderen ein neues humanisiertes TB-Mausmodell beschreiben[57].

### 2.1.1 Epithelzellen vermitteln pathologische neutrophile Immunabwehr bei TB (Eigene Arbeit 1)

Veröffentlicht als: Forschungsartikel mit Erstautorschaft.
Der nachfolgende Text entspricht dem originalsprachlichen Abstrakt der Arbeit "*CXCL5-secreting pulmonary epithelial cells drive destructive neutrophilic inflammation in tuberculosis.*" (J Clin Invest. 2014 Mar;124(3):1268-82. doi: 10.1172/JCI72030)[50] der Autoren: **Geraldine Nouailles**, Anca Dorhoi, Markus Koch, Jens Zerrahn, January Weiner 3rd, Kellen C. Faé, Frida Arrey, Stefanie Kuhlmann, Silke Bandermann, Delia Loewe, Hans-Joachim Mollenkopf, Alexis Vogelzang, Catherine Meyer-Schwesinger, Hans-Willi Mittrücker, Gayle McEwen, und Stefan H.E. Kaufmann.

> „Successful host defense against numerous pulmonary infections depends on bacterial clearance by polymorphonuclear leukocytes (PMNs); however, excessive PMN accumulation can result in life-threatening lung injury. Local expression of CXC chemokines is critical for PMN recruitment. The impact of chemokine-dependent PMN recruitment during pulmonary *Mycobacterium tuberculosis* infection is not fully understood. Here, we analyzed expression of genes encoding CXC chemokines in *M. tuberculosis*–infected murine lung tissue and found that *M. tuberculosis* infection promotes upregulation of Cxcr2 and its ligand Cxcl5. To determine the contribution of CXCL5 in pulmonary PMN recruitment, we generated *Cxcl5*$^{-/-}$ mice and analyzed their immune response against *M. tuberculosis*. Both *Cxcr2*$^{-/-}$ mice and *Cxcl5*$^{-/-}$ mice, which are deficient for only one of numerous CXCR2 ligands, exhibited enhanced survival compared with that of WT mice following high-dose *M. tuberculosis* infection. The resistance of *Cxcl5*$^{-/-}$ mice to *M. tuberculosis* infection was not due to heightened *M. tuberculosis* clearance but was the result of impaired PMN recruitment, which reduced pulmonary inflammation. Lung epithelial cells were the main source of CXCL5 upon *M. tuberculosis* infection, and secretion of CXCL5 was reduced by blocking TLR2 signaling. Together, our data indicate that TLR2-induced epithelial-derived CXCL5 is critical for PMN-driven destructive inflammation in pulmonary tuberculosis."

**CXCL5-secreting pulmonary epithelial cells drive destructive neutrophilic inflammation in tuberculosis**

J Clin Invest. 2014 Mar;124(3):1268-82.

https://doi.org/10.1172/JCI72030

### 2.1.2 Pathologie der TB-Granulome in humanisierten Mäusen (Eigene Arbeit 2)

Veröffentlicht als: Forschungsartikel mit geteilter Letztautorschaft*.
Der nachfolgende Text entspricht dem originalsprachlichen Abstrakt der Arbeit "*Humanized mouse model mimicking pathology of human tuberculosis for in vivo evaluation of drug regimens.*" (Front Immunol. 2019 Jan 31;10:89. doi: 10.3389/fimmu.2019.00089)[57] der Autoren: Frida Arrey, Delia Löwe, Stefanie Kuhlmann, Peggy Kaiser, Pedro Moura-Alves, Gopinath Krishnamoorthy, Laura Lozza, Jeroen Maertzdorf, Tatsiana Skrahina, Alena Skrahina, Martin Gengenbacher, **Geraldine Nouailles***, und Stefan H E Kaufmann*.

> „Human immune system mice are highly valuable for *in vivo* dissection of human immune responses. Although they were employed for analyzing tuberculosis (TB) disease, there is little data on the spatial organization and cellular composition of human immune cells in TB granuloma pathology in this model. We demonstrate that human immune system mice, generated by transplanted human fetal liver derived hematopoietic stem cells develop a continuum of pulmonary lesions upon *Mycobacterium tuberculosis* aerosol infection. In particular, caseous necrotic granulomas, which contribute to prolonged TB treatment time, developed, and had cellular phenotypic spatial-organization similar to TB patients. By comparing two recommended drug regimens, we confirmed observations made in clinical settings: Adding Moxifloxacin to a classical chemotherapy regimen had no beneficial effects on bacterial eradication. We consider this model instrumental for deeper understanding of human specific features of TB pathogenesis and of particular value for the pre-clinical drug development pipeline."

frontiers in Immunology

ORIGINAL RESEARCH
published: 31 January 2019
doi: 10.3389/fimmu.2019.00089

# Humanized Mouse Model Mimicking Pathology of Human Tuberculosis for *in vivo* Evaluation of Drug Regimens

*Frida Arrey[1], Delia Löwe[2], Stefanie Kuhlmann[1‡], Peggy Kaiser[1], Pedro Moura-Alves[1], Gopinath Krishnamoorthy[1], Laura Lozza[1], Jeroen Maertzdorf[1], Tatsiana Skrahina[1‡], Alena Skrahina[3], Martin Gengenbacher[4], Geraldine Nouailles[5†] and Stefan H. E. Kaufmann[1*†]*

[1] Department of Immunology, Max Planck Institute for Infection Biology, Berlin, Germany, [2] Department of Molecular Pharmacology and Cell Biology, Leibniz Forschungsinstitut für Molekulare Pharmakologie, Berlin, Germany, [3] Republican Scientific and Practical Centre for Pulmonology and Tuberculosis, Minsk, Belarus, [4] Public Health Research Institute, New Jersey Medical School, Rutgers, The State University of New Jersey, Newark, NJ, United States, [5] Division of Pulmonary Inflammation, Charité-Universitätsmedizin Berlin, Berlin, Germany

Human immune system mice are highly valuable for *in vivo* dissection of human immune responses. Although they were employed for analyzing tuberculosis (TB) disease, there is little data on the spatial organization and cellular composition of human immune cells in TB granuloma pathology in this model. We demonstrate that human immune system mice, generated by transplanted human fetal liver derived hematopoietic stem cells develop a continuum of pulmonary lesions upon *Mycobacterium tuberculosis* aerosol infection. In particular, caseous necrotic granulomas, which contribute to prolonged TB treatment time, developed, and had cellular phenotypic spatial-organization similar to TB patients. By comparing two recommended drug regimens, we confirmed observations made in clinical settings: Adding Moxifloxacin to a classical chemotherapy regimen had no beneficial effects on bacterial eradication. We consider this model instrumental for deeper understanding of human specific features of TB pathogenesis and of particular value for the pre-clinical drug development pipeline.

**Keywords: *Mycobacterium tuberculosis*, humanized mouse models, lung, infection, granuloma, human immune system mice, antibiotics, pathology**

OPEN ACCESS

***Edited by:***
*Abhay Satoskar, The Ohio State University, United States*

***Reviewed by:***
*Shashank Gupta, Brown University, United States*
*Muazzam Jacobs, University of Cape Town, South Africa*

***Correspondence:**
*Stefan H. E. Kaufmann*
*kaufmann@mpiib-berlin.mpg.de*

*†These authors share co-last authorship*

***‡Present Address:***
*Stefanie Kuhlmann, Bayer Pharmaceuticals, Berlin, Germany*
*Tatsiana Skrahina, Immutep, Berlin, Germany*

***Specialty section:***
*This article was submitted to Microbial Immunology, a section of the journal Frontiers in Immunology*

***Received:*** *07 September 2018*
***Accepted:*** *14 January 2019*
***Published:*** *31 January 2019*

***Citation:***
*Arrey F, Löwe D, Kuhlmann S, Kaiser P, Moura-Alves P, Krishnamoorthy G, Lozza L, Maertzdorf J, Skrahina T, Skrahina A, Gengenbacher M, Nouailles G and Kaufmann SHE (2019) Humanized Mouse Model Mimicking Pathology of Human Tuberculosis for in vivo Evaluation of Drug Regimens. Front. Immunol. 10:89. doi: 10.3389/fimmu.2019.00089*

## INTRODUCTION

Tuberculosis (TB) is still the deadliest infectious disease, globally causing 5,000 deaths every day. In 2017, this added up to 1.6 million deaths and 10 million individuals fell ill from TB (1). TB is primarily transmitted through the aerosol route and manifests as a pulmonary disease in immunocompetent individuals with signs of dissemination in immunocompromised patients and children (2). The causative agent of TB, the intracellular pathogen *Mycobacterium tuberculosis* (Mtb), is phagocytosed by alveolar macrophages upon entry into the lungs and these macrophages congregate and act as a focus of infection together with other innate immune cells such as neutrophils (3). This focus is the first step in granuloma formation, a disease pathology which is the classical hallmark of pulmonary TB (4). The granuloma acts as a means to contain the infection (5) but also as a source of dissemination to other organs via the lymphatic system (6) and newly created blood vessels (7, 8). The granuloma also serves as a source of transmission upon cavitation and

rupture into the airways (9, 10). Lung TB lesions form a spectrum comprising solid non-necrotic granulomas, TB pneumonia, necrotic granulomas, and caseous necrotic granulomas with distinct microenvironments. Most mouse models of TB do not exhibit this granuloma heterogeneity (11) and murine models that do exhibit a broad granuloma range lack specific aspects of human TB (12–14). These limitations preclude studies on human immune cell trafficking, infiltration, and cellular interactions in the granuloma microenvironment.

Immuno-deficient NOD *scid* gamma (NSG) mice have emerged as one of the best-suited strains for human stem cell transplantations (15). Human immune system (HIS) NSG mice recapitulate key immuno-pathological features of major human diseases caused by viruses such as human immunodeficiency virus (HIV) (16), hepatitis C virus (17), Epstein-Barr virus (18) and bacteria such as *Salmonella typhi* (19), and *Borrelia hermsii* (20). Here, we describe the establishment of human fetal liver derived human stem cell NSG mice for analyzing pulmonary TB. We conducted immune-phenotyping, histopathology, and immunohistochemistry to determine the extent by which the developing granulomas in these mice resemble those of TB patients. Our results reveal that the HIS-NSG mice develop TB granuloma heterogeneity as seen in TB patients. More importantly, caseous necrotic granulomas expressed an immunophenotype and spatial-organization resembling what is observed in TB patients.

In recent years, there has been a push in shortening TB drug chemotherapy, as a means to improve compliance with TB treatment, reduce relapse, and restrict the emergence of drug resistant TB (21). Moxifloxacin (M), a fluoroquinolone antibiotic, has been proposed as an additive to canonical drug regimens to shorten treatment time of drug sensitive TB from six to four months (22). Taking into consideration that caseous necrotic granulomas account for reduced efficacy of anti-TB treatment, we compared the effects of M on combination therapy with isoniazid (H), rifampicin (R), and pyrazinamide (Z) (HRZ). Both regimens initially reduced lung bacterial loads within 2 weeks. However, prolonged treatment time of 4 weeks had no further beneficial effect on bacterial elimination, instead, lung bacterial loads gradually increased. This pattern could explain that Mtb is not eradicated during therapy because of impaired penetration of drugs into the granuloma caseum (23). In conclusion, HIS-NSG mice recapitulate key features of the human immune response and the corresponding pathology upon Mtb infection. Hence, it is tempting to propose HIS-NSG mice for preclinical model assessment of anti-TB drugs in an *in vivo* setting.

## MATERIALS AND METHODS

### Human Lungs Tissue

Human tissue samples were collected from materials removed during lung resection type surgery in patients who underwent elective surgery on the background of individualized (optimized) TB (MDR-TB) chemotherapy at the Republican Scientific and Practical Center for Pulmonology and Tuberculosis, Minsk, Belarus. For histopathological analysis, surgical lung cuts were sliced in small pieces and fixed in 4% paraformaldehyde overnight. According to the Helsinki Declaration 2008, ethical approval was obtained by the Ethical Committee of the Republican Research and Practical Center, appointed by Director Prof. Dr. Henadz Hurevich. Republican Research and Practical Center Dolginovski Trakt, 157, 220053, Minsk, Belarus.

### Mice

All animal studies have been ethically reviewed and approved by the State Office for Health and Social Services, Berlin, Germany. Experimental procedures were carried out in accordance with the European directive 2010/63/EU on Care, Welfare and Treatment of Animals. NOD.Cg-*Prkdc*$^{scid}$ *Il2rg*$^{tm1Wjl}$/SzJ (NSG) and C57BL/6 (BL/6) mice were obtained from The Jackson Laboratory and kept and bred under specific pathogen-free conditions. Infected mice were housed in a biosafety level 3 facility under specific pathogen–free conditions.

### Generation of HIS-NSG Mice

HIS-NSG mice (male and female) were generated using the human stem cell neonate NSG protocol as previously described (18, 19). In brief, human fetal liver was obtained from Advanced Bioscience Resources, California, USA. The tissue was mechanically cut into small pieces with surgical scissors and treated with 2 mg/mL collagenase D (Roche) in Hank's balanced salt solution with $CaCl_2$/$MgCl_2$ (Gibco) for 30 min in a 5% $CO_2$ at 37°C followed by filtering through 70-μm nylon cell strainers (BD Biosciences). $CD34^+$ human hematopoietic stem and progenitor cells (HSCs) were isolated using the direct CD34 MicroBead kit (Miltenyi Biotec). One- to three day-old NSG mice were irradiated with 100 cGy and injected intrahepatically with $1–2 \times 10^5$ $CD34^+$ HPCs 24 h after irradiation. Some NSG mice received 50 μl of PBS as a control. The mice were bled 10–12 weeks after engraftment and peripheral lymphocytes were stained with monoclonal antibodies purchased from BioLegend: anti-mouse CD45 (clone 30-F11), anti-human CD45 (clone HI30), anti-human CD3 (clone UCHT1), anti-human CD4 (clone OKT4), anti-human CD8 (clone SK-1), and anti-human CD19 (clone HIB19) for 30 min at 4°C. After red blood cell lysis, the samples were analyzed by flow cytometry using a BD LSR II to assess reconstitution of the human immune system and visualized using FlowJo software.

### Bacteria and Infection

Mtb strain H37Rv (ATCC#27294) was grown in Middlebrook 7H9 broth (BD Biosciences) supplemented with 0.2% glycerol, 0.05% Tween 80, and 10% ADC enrichment (BD Biosciences). Mid logarithmic cultures were harvested and stored at −80°C. Stocks were tested for virulence and titrated prior to use. Twelve-week-old animals were aerosol infected with Mtb, using a Glas-Col inhalation exposure system at a low dose of approximately 15–30 CFUs per mouse. At designated time points, serial dilutions of tissue homogenates were plated onto Middlebrook 7H11 agar supplemented with 10% OADC Enrichment (BD Biosciences) and ampicillin (25 μg/ml). CFUs were determined after 3 to 4 weeks of culture at 37°C.

## Histology and Immunohistochemistry

Mice were sacrificed at specific time points and tissues for histopathologic analyses were fixed in 4% (wt/vol) paraformaldehyde at 4°C for 24 h. Human and mouse tissues were processed as follows. Two- to three-μm thick formalin-fixed, paraffin-embedded tissue sections were deparaffinized and rehydrated and subsequently stained with either hematoxylin and eosin stain or a modified Ziehl-Neelsen stain for bacterial detection or immunohistochemistry stain, respectively (24). For immunohistochemistry, tissue sections underwent a steam pressure antigen retrieval step using Dako target retrieval solution, pH9. Slides were incubated with the following mouse primary antibodies: anti-human CD68 (clone KP1, Dako), anti-human CD15 (BD), anti-human CD4 (clone 4B12, Leica Biosystems), anti-human CD8 (clone 4B11, Leica Biosystems), and anti-human CD20 (clone L26, Leica Biosystems) for 1 h at room temperature in a humidified chamber. The tissue sections were developed with a biotin-free HRP- polymer system (MACH 4 Universal HRP-polymer kit, Biocare Medical) and DAB substrate (Dako). Tissue sections were imaged using a Leica DRMB microscope with a ProgResC12 (Jenoptik) Camera. Lung tissue sections were scanned using Aperio AT2 Leica slide scanner. Further analysis was carried out using ImageJ version 1.41.

## Cell Isolation From Tissues

A portion of the perfused right lung lobes was mechanically digested and incubated for 30 min at 37°C at 5% $CO_2$ in RPMI 1640 medium (Gibco) supplemented with glutamine, Na-pyruvate, 2-ME, penicillin, streptomycin, 10% heat-inactivated FCS, collagenase D (Roche), and collagenase type VIII (Sigma-Aldrich). Single-cell suspensions of lungs were then prepared by meshing the lungs through 40-μm nylon cell strainers and red blood cell lysis. Viable cells were counted by trypan blue exclusion. Cells were blocked with anti-mouse CD16/CD32 mAb (BioLegend) and human Fc receptor blocking solution (BioLegend), and then surface stained with monoclonal antibodies purchased from BioLegend: anti-mouse CD45 (clone 30-F11) anti-human CD45 (clone HI30), anti-human CD3 (clone UCHT1), anti-human CD4 (clone OKT4), anti-human CD8 (clone SK-1), anti-human CD19 (clone HIB19), anti-human CD20 (clone 2H7), anti-human CD33 (clone WM53), anti-human CD66a/c/e/b (clone ASL-32 and G10F5), anti-human CD14 (clone M5E2), and anti-human CD11c (clone Bu15) for 30 min at 4°C. The samples were analyzed by flow cytometry using a BD FACS CANTO II in the biosafety level 3 and visualized using FlowJo software.

## Human Biomolecule Characterization in Lung Tissues of HIS-NSG Mice

A portion of the perfused right lung lobes was homogenized in 700 μl of lysis buffer with protease inhibitor (Roche) at specific time points. Homogenized tissue was centrifuged at 6,708 × g and the supernatants were spun through 0.22 μm Spin-X filter tubes and stored in −80°C. Human cytokines, chemokines, growth factors, and antibody concentrations were analyzed in the supernatants by using Bio-Plex Pro Human Cytokine 27-plex Panel and Bio-Plex Pro Human Isotyping Panel (Bio-Rad). The data were acquired and analyzed on a Bio-Rad Bio-Plex 200 system.

## Drug Treatment and Bacterial Load Enumeration

Cord blood-engrafted HIS-NSG mice were purchased from Jackson Laboratory. Briefly, Jackson laboratory injected human $CD34^+$ stem cells i.v. into myeloablated NSG mice and 12 weeks later humanization was confirmed by presence of >25% huCD45+ in the peripheral blood. These HIS-NSG mice were Mtb infected at 12 weeks of age. Isoniazid (H: 30 mg/kg), rifampicin (R: 10 mg/kg) and pyrazinamide (Z: 125 mg/kg) (HRZ), and moxifloxacin (M: 100 mg/kg) were purchased from Sigma or ChemPacific. The regimens were formulated in 200 μl 0.4% methyl cellulose and administered 6 days per week by oral gavage starting at day 28 p.i. At 2 and 4 weeks after treatment start, serial dilutions of tissue homogenates were plated onto Middlebrook 7H11 agar supplemented with 10% OADC Enrichment (BD Biosciences). To reduce the effect of drug-carry over 0.4% w/v activated charcoal was added to Middlebrook 7H11 agar. CFUs were determined after 3–4 weeks of culture at 37°C.

## Statistical Analysis

PRISM GraphPad software was used for statistical analyses. Survival curves were analyzed using Kaplan-Meier method and log-rank (Mantel-Cox) test. Two groups were compared using Mann-Whitney *U* test for non-parametric data, more than two groups using Kruskal-Wallis/Dunn's multiple comparisons test (non-parametric) and grouped analyses were performed using 2-way ANOVA/Dunnett's multiple comparison test. *P*-values smaller than 0.05 were considered significant.

# RESULTS

## NOD Scid Gamma Mice Are Efficiently Human Immune Reconstituted by Human Stem Cells

To generate a HIS mouse model for TB, we implemented a NSG mouse breeding program where the resulting newborn (1–3 days old) pups received human fetal liver $CD34^+$ HSCs via intra-hepatic injection after 100 cGy sublethal irradiation. Depending on size and age of the fetal liver (16–24 weeks), cohorts of 10–50 HIS-NSG mice were generated per individual donor graft. Simultaneously, some of the NSG littermates underwent the same conditioning but received PBS (PBS-NSG). The mice were bled 10 weeks post engraftment and peripheral leukocytes were analyzed to assess human immune cell reconstitution (**Supplementary Figure 1A**). In HIS-NSG mice, we observed average frequencies of 55% human $CD45^+$ leukocytes in the blood by 3 months (**Supplementary Figure 1B**), although with variability between each mouse and donor graft. These cells included granulocytes, monocytes and lymphocytes, comprising $CD4^+$ helper T cells, $CD8^+$ cytotoxic T cells, and $CD19^+$ B cells (**Supplementary Figure 1B**) in line with previous findings (18, 25). To determine the extent of human immune cell reconstitution and penetrance in the lungs, HIS-NSG mice

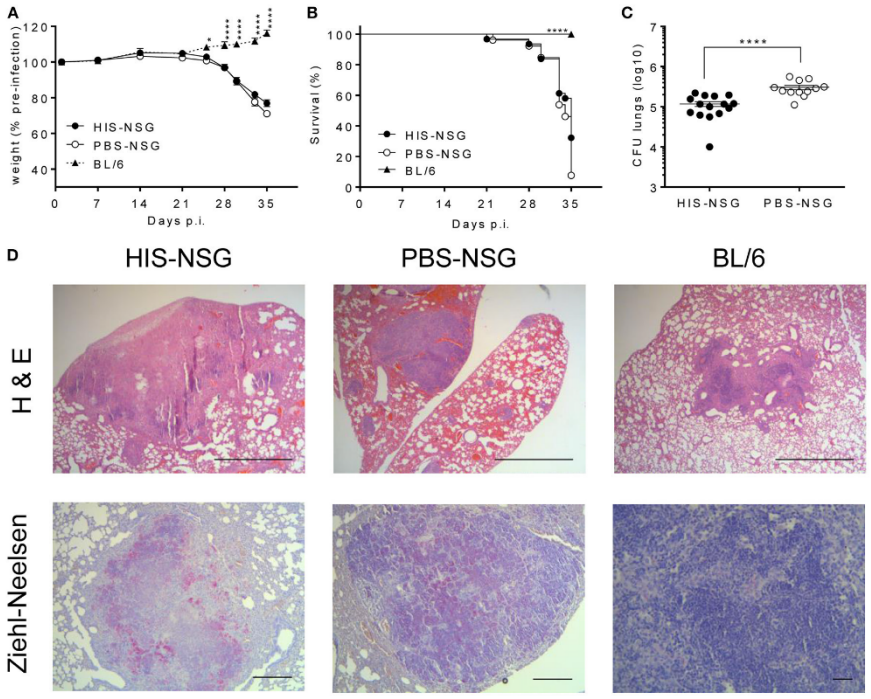


**FIGURE 1 |** HIS-NSG mice are susceptible to aerosolized Mtb and develop lung lesions upon Mtb infection. HIS-NSG mice, PBS-NSG mice and BL/6 mice were infected with low dose aerosol infection with Mtb (~20 CFUs). **(A)** Relative weight curves, 2-way ANOVA/Dunnett's multiple comparisons test, comparison to HIS-NSG mice, mean ± SEM. **(B)** Kaplan-Meier curves showing survival, log-rank test. **(C)** Bacterial burden in lungs of mice at day 35 p.i. Mann-Whitney *U* test, mean ± SEM. **(A–C)** Data were pooled from three independent experiments. ****$P < 0.0001$. **(D)** Microscopic analysis (Hematoxylin and Eosin; 25X, scale bar = 1,000 μm) of lesions in representative HIS-NSG, PBS-NSG, and BL/6 lungs were performed in addition to mycobacterial identification (Ziehl-Neelsen; 50X, scale bar = 500 μm, BL/6 lung at 200X, scale bar = 100 μm) at day 35 post Mtb infection. Data are representative of three independent experiments.

were sacrificed and lung tissue sections were immunostained using human specific antibodies. Naïve HIS-NSG lung tissue morphology showed a sponge like appearance with large alveolar spaces (**Supplementary Figure 1C**) and a spatial distribution of alveolar and parenchymal $CD68^+$ macrophages (**Supplementary Figure 1D**). $CD15^+$ neutrophils, $CD3^+$ T cells, and $CD20^+$ B cells were located in the lung parenchyma (**Supplementary Figure 1D**). Altogether, these data demonstrate that reconstitution of the human immune system endows HIS-NSG mice with human immune cells playing key roles in TB pathology.

## Mtb Infected HIS-NSG Mice Display Features of TB Pathology

To determine whether the HIS-NSG mice develop general characteristics of TB, we infected them with low dose aerosolized Mtb H37Rv (15–30 CFU) together with PBS-NSG and C57BL/6 (BL/6) mice as controls. HIS-NSG and PBS-NSG mice exhibited clinical TB symptoms such as lethargy and weight loss, starting from day 25 post infection (p.i.) (**Figure 1A**). In contrast to NSG groups and as previously reported, BL/6 mice maintained and even gained weight from day 25 p.i. (24, 26). Despite successful engraftment, HIS-NSG mice succumbed to infection by day 33 to day 35 p.i., comparable to PBS-NSG mice (**Figure 1B**). Disease susceptibility of HIS-NSG mice, due to their genetic immune-deficient background, fetal stem cell origin and inexperienced immune system likely resemble more to pediatric and immunocompromised individuals than healthy adults, indeed, inferior survival and TB outcome has been described for these individuals (27). Despite low dose aerosolized Mtb infection, HIS-NSG, and PBS-NSG mice displayed high bacterial numbers in lungs (**Figure 1C**) as well as mycobacterial dissemination into other organs including spleen, liver, kidney, and bone marrow (**Supplementary Figure 2A**). Notably, HIS-NSG mice harbored high, but significantly lower

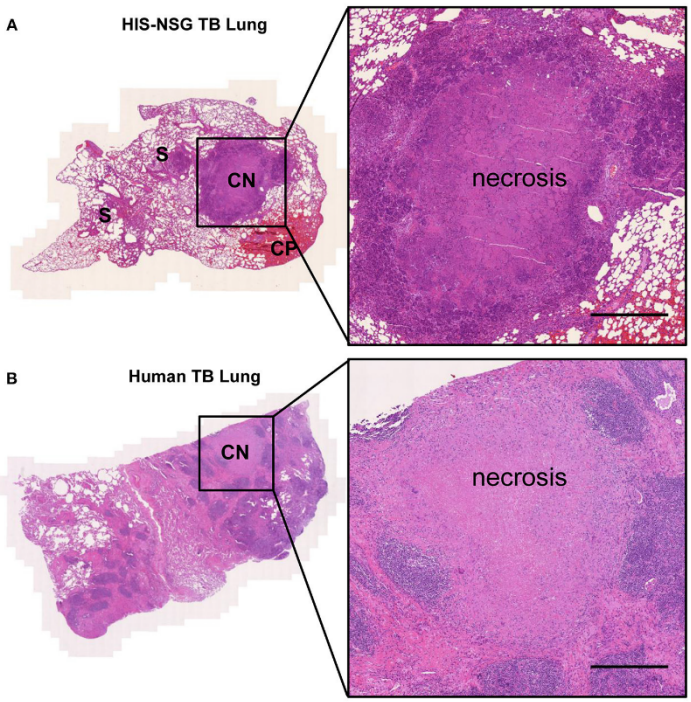


**FIGURE 2 |** HIS-NSG mice develop human like caseous necrotic granulomas. **(A)** Lesions in representative Mtb infected HIS-NSG lung sections at day 35 p.i., S, solid non-necrotic granulomas; CP, coalesced parenchyma; CN, caseous necrotic granuloma. **(B)** Representative tissue cuts from a TB patient's lungs. Tissue slide scan, Hematoxylin and Eosin 50X, scale bar = 500 μm.

bacterial loads in the lungs, as compared to PBS-NSG mice (**Figure 1C**), suggesting that the human immune cells in HIS-NSG mice participated in pulmonary immune defense against Mtb.

Next, we interrogated whether disease pathology in HIS-NSG mice following Mtb infection was similar to human TB. To this end, we performed *post-mortem* macroscopic and microscopic examination of organs around day 35 p.i. (animals reached experimental human endpoint criteria and were euthanized). All three groups had lung lesions evident at macroscopic examination (**Supplementary Figure 2B**). Microscopic examination of H&E staining, however, revealed differences: lung lesions in BL/6 and PBS-NSG mice comprised of non-necrotic cellular aggregates (**Figure 1D**). In contrast, HIS-NSG lungs contained caseous necrotic granulomas with a core consisting of necrotic debris and an outer cellular cuff (**Figures 1D**, **2A**). Ziehl-Neelsen staining identified Mtb in non-necrotic aggregates in BL/6 and PBS-NSG mice with fewer numbers in BL/6 compared to PBS-NSG mice. Caseous necrotic granulomas of HIS-NSG mice displayed extracellular bacteria in the necrotic core and apparent intracellular ones in the cuff (**Figure 1D**). Furthermore, in addition to caseous necrotic granulomas, HIS-NSG lungs presented small non-necrotic cellular aggregates and coalesced lung parenchyma (**Figure 2A**). Importantly, the pathology of caseous necrotic granulomas resembled what is being observed in active TB patients (**Figures 2A,B**).

Visual examination revealed white spots in Mtb-infected HIS-NSG and PBS-NSG spleens (**Supplementary Figure 3A**), while BL/6 spleens were unspotted. Microscopic examination unveiled centers of splenic caseous necrotic granulomas full of extracellular bacteria in HIS-NSG mice, whereas in PBS-NSG mice non-necrotic splenic aggregates consisted of innate leukocytes with bacteria (**Supplementary Figures 3B,C**). There were no splenic granulomas in the BL/6 mice, with a few bacteria interspersed throughout the spleen (**Supplementary Figures 3B,C**). Collectively, upon Mtb infection HIS-NSG mice developed granulomas resembling human-like pathology with dissemination most similar to pediatric and immunocompromised TB.

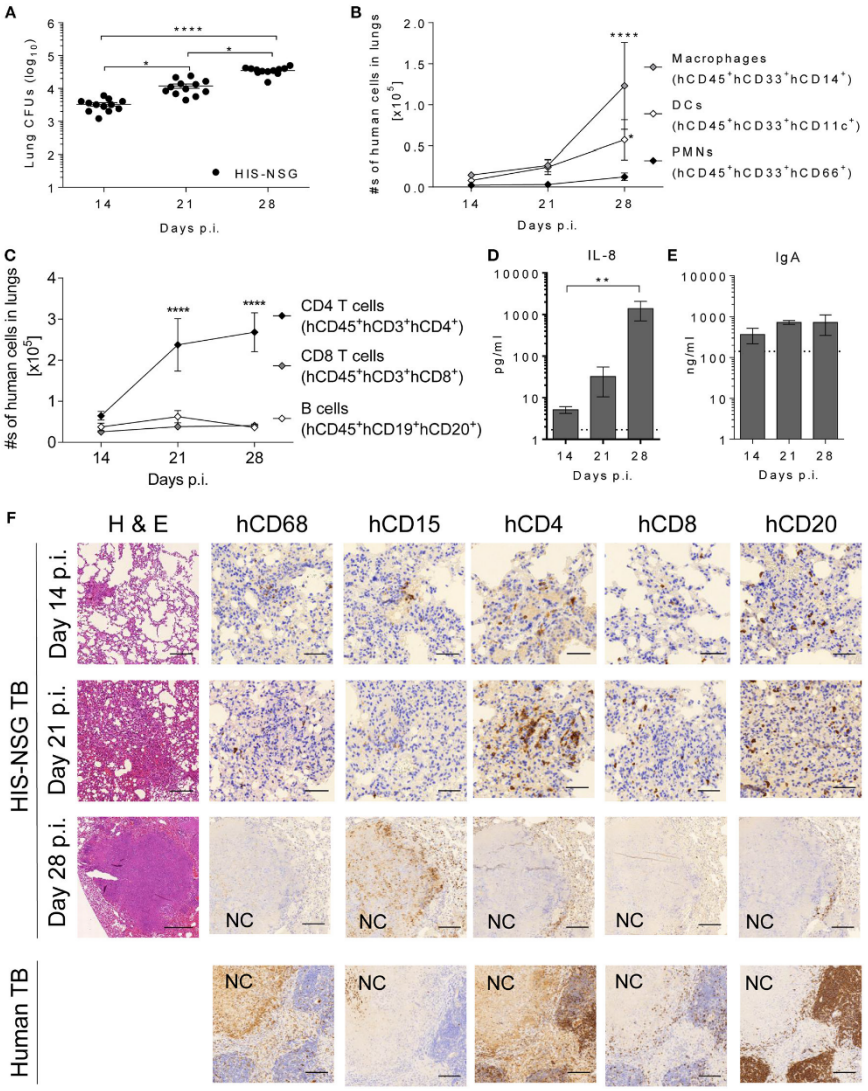


**FIGURE 3 |** Human immune cells are recruited and develop a human-like granuloma organization after Mtb infection. **(A)** Bacterial burden was determined at days 14, 21, and 28 p.i. in HIS-NSG lungs. Data were pooled from two independent experiments, $n_{pooled} = 12$ per time point, Kruskal Wallis/Dunn's multiple comparisons test. Line graphs showing the absolute numbers of **(B)** human innate immune cells and **(C)** human adaptive immune cells infiltrating HIS-NSG lungs at 14, 21, and 28 days p.i. Data pooled from one to three experiments, $n = 6$–12 mice per time point, 2-way ANOVA/Dunnett's Multiple comparisons test, effect within population compared to day 14 p.i. Bar graphs showing **(D)** IL-8, and **(E)** human IgA protein levels at 14, 21, and 28 days p.i. Dotted line: detection limit. $n = 4$–5 mice per time point, Kruskal-Wallis/Dunn's multiple comparisons test. **(A–E)** Mean ± SEM, $^{****}P < 0.0001$, $^{**}P < 0.01$, $^{*}P < 0.05$. **(F)** Microscopic analysis (Hematoxylin and Eosin 100X, scale bar = 200 μm) in representative HIS-NSG lungs at 14, 21, and 28 days p.i. was carried out. In addition, human immune-stains of macrophages (CD68), neutrophils (CD15), $CD4^+$ T cells (CD4), $CD8^+$ T cells (CD8), and B cells (CD20) were also performed in Mtb-infected HIS-NSG lungs and human TB lungs. NC, necrotic core (days 14 and 21 p.i., 400X, scale bar = 50 μm, day 28 p.i. and human TB lung, 100X, scale bar = 200 μm). Data are representative of three independent experiments, $n = 3$.

## Caseous Necrotic Granulomas in HIS-NSG Mice Display Neutrophil Rich Centers

To characterize local responses in the humanized lungs during Mtb infection, we assessed the spatial organization of human immune cells, expression of different biomolecules, and bacterial burden in HIS-NSG mice at 14, 21, and 28 days p.i. On day 14 p.i., infection was well-established in the lungs and bacterial loads further increased 4 fold by day 28 p.i. (**Figure 3A**). As measured by flow cytometry (**Supplementary Figure 4**), total numbers of human neutrophils ($CD45^+CD33^+CD66^+$), human DCs ($CD45^+CD33^+CD11c^+$), and human monocytes/macrophages ($CD45^+CD33^+CD14^+$) in the lungs markedly increased over this time frame (**Figure 3B**). Likewise, increasing numbers of pulmonary human helper T cells ($CD45^+CD3^+CD4^+$), human cytotoxic T cells ($CD45^+CD3^+CD8^+$), and human B cells ($CD45^+CD19^+CD20^+$) were detected (**Figure 3C**). Differences in the expression of immune/inflammatory biomolecules known to be involved in the recruitment and activation of immune cells crucial in human granuloma formation and development, were also observed. Expression of pro-inflammatory mediators (IL-1β, IL-6, MCP-1, MIP-1β, IP-10) in lung homogenates increased from day 14 to day 28 p.i. (**Supplementary Figure 5**). Notably, human-specific neutrophil chemoattractant IL-8 increased as TB disease progressed (**Figure 3D**). Finally, levels of human mucosal IgA antibodies were elevated in infected HIS-NSG lungs (**Figure 3E**). The predominantly pro-inflammatory response observed was consistent with previous studies in other animal models of TB and in lung samples from human TB patients (28). Hence, our results reveal a basic functional immune response to Mtb in the HIS-NSG lungs.

Biomolecules influence cellular spatial organization of leukocytes (28). To confirm human-like TB pathology and granuloma organization on a cellular level, lung sections were stained for innate and adaptive immune cells. At day 14 p.i. most HIS-NSG lungs contained small non-necrotic myeloid aggregates, surrounded by lymphocytes and normal healthy tissue (**Supplementary Figure 6**). At day 21 p.i., coalesced parenchyma known as TB pneumonia had developed, while at day 28 p.i., lesions consisted of large non-necrotizing and caseous necrotic granulomas with smaller adjacent caseous necrotic granulomas (**Supplementary Figure 6**). We conclude that the HIS-NSG mouse has the ability to model human-like lung granuloma initiation and formation. Sequential lung tissue sections were also stained for human leukocytes, including $CD68^+$ macrophages, $CD15^+$ neutrophils, $CD4^+$ T cells, $CD8^+$ T cells, and $CD20^+$ B cells to visually validate and localize the cellular infiltration observed by flow cytometry (**Figure 3F**). As pathology progressed, the lung infiltrates became increasingly organized with macrophages and neutrophils in the center, more macrophages and neutrophils generating an inner rim followed by T cells and B cells forming an outer cuff by day 28 p.i. In particular, at day 28 post Mtb infection, caseous necrotic granulomas in the HIS-NSG mice harbored cell populations that were organized in a pattern similar to that observed in patients with active pulmonary TB (**Figure 3F**). We conclude that the HIS-NSG mouse mimics human TB lung granuloma formation and development, intertwined with the associated human pulmonary immune response.

## Mtb Infected HIS-NSG Mice for Drug Testing: Moxifloxacin Confers No Added Advantage

We applied the humanized mouse model for drug testing. We used commercially available cord-blood engrafted HIS-NSG mice from Jackson Laboratory USA, which have similarities in their humanized immune response to human fetal liver engrafted mice (29, 30). We administered two different drug combinations to Mtb infected HIS-NSG mice from day 25 p.i., as depicted in **Figure 4A**, to assess the utility of the HIS-NSG mice for preclinical drug studies. The classical drug regimen HRZ comprising H, R, and Z was compared to the M supplemented experimental regimen HRZM. The drugs were administered 6 days per week by oral gavage. The total number of bacilli residing in lungs of HIS-NSG mice was $\sim 10^5$ CFU at treatment start (day 25 p.i.). After 2 weeks of treatment and independent of the regimen applied, the bacterial burden initially declined by 1–2 log ($\sim 10^3$ CFU). However, after a total of 4 weeks treatment time bacterial burden re-increased to $\sim 10^4$ CFU at both regimens (**Figure 4B**). There was no significant difference between the two treatment modalities at either time point. We also assessed treatment efficacy on bacterial burden in spleen, liver and kidney, as these organs are sites of infection in pediatric and immunocompromised TB patients. Mirroring the lungs, bacterial burdens decreased and then slightly increased during the treatment course in these organs (**Figure 4B**).

## DISCUSSION

Lung TB granuloma pathology is heterogeneous, not only amongst individuals, but also in each individual patient (11). Granuloma heterogeneity has been observed in Mtb infected non-human primates (NHPs) (31), guinea pigs (32), rabbits (33), $Nos2^{-/-}$ mice (24), and C3HeB/FeJ mice (34), however it is virtually missing in traditional inbred mouse strains. Additionally, several unique pathologic features of TB (35, 36) and HIV-TB comorbidity (37) in humans cannot be examined in these models. On the other hand, small rodents are of relatively low cost, immunologically well-characterized, and a remarkable analytical toolbox exists. To this end, we have established a murine model containing human immune cells that does develop human-like caseous necrotic granulomas as TB disease progresses. TB granulomas in these HIS-NSG mice comprised solid non-necrotic granulomas, tuberculoid pneumonia, and caseous necrotic granulomas. Furthermore, heterogeneous granuloma pathology in lungs of individual HIS-NSG mice and across various stem cell donors was observed. These human-like granulomas displayed an immunophenotype and spatial organization reminiscent of pathological samples from human TB patients and they were most similar to granulomas from pediatric or immunocompromised TB patients (35).

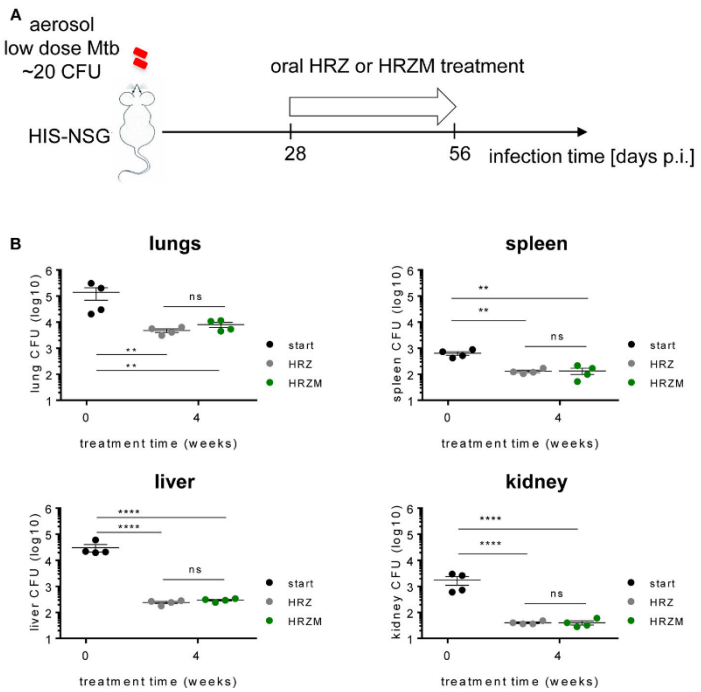


**FIGURE 4 |** Moxifloxacin confers no added advantage for treatment of Mtb infected HIS-NSG mice. **(A)** Treatment scheme of Mtb infected HIS-NSG mice. Treatment regimen of either HRZ or HRZM combinations was initiated at day 28 p.i. (treatment start) for a period of 4 weeks. **(B)** Bacterial burden in lungs, spleen, liver and kidney, $n = 4$, means ± SEM, one way ANOVA/Tukeys's multiple comparisons test on log transformed data; ns, non significant, $^{**}P < 0.01$, $^{****}P < 0.0001$.

Upon infection, HIS-NSG mice had significantly lower lung bacterial burdens in comparison to PBS-NSG mice, suggesting that the human immune system partially controlled bacterial replication. HIS-NSG mice lack HLA molecules for antigen presentation (38) and certain human cytokines (39). Thus, the human antigen presenting cells generated in this system may function sub-optimally in presenting Mtb antigens to human T cells, thereby compromising control of Mtb by adaptive immunity. As a corollary, despite successful engraftment of human immune cells in HIS-NSG mice, these animals succumbed to active TB disease around the same time post-Mtb infection as PBS-NSG mice. This period of 35 days did not allow for the formation of fibrotic granulomas (5, 35) which have been associated with latent TB infection.

The number of neutrophils in the lungs likely contributed to increased susceptibility to Mtb in HIS-NSG mice (40). To our knowledge, our HIS-NSG mouse model is the first to reveal increased levels of human-specific neutrophil attractant IL-8, which were correlated with recruitment of human neutrophils and were apparently associated with destructive tissue pathology during the course of infection. The presence of murine neutrophils of Mtb-infected HIS-NSG and PBS-NSG lungs is likely. Our earlier studies have shown that Mtb induces the secretion of neutrophil-chemoattractant CXCL5 by lung epithelial cells (26). Pulmonary epithelial cells remain of murine origin in the HIS-NSG mouse and likely remain functionally active. The murine neutrophils present in NSG mice, could thus follow the CXCL5 chemokine gradient into the lungs. Murine CXCR2 ligands, like CXCL5, can induce migration of human neutrophils *in vitro*. However, the increase in pulmonary human neutrophils strongly correlated with the presence of pulmonary human IL-8, arguing against a profound chemokine crosstalk between murine and human cells *in vivo*. Moreover, in various TB mouse studies (26, 41, 42) we showed that murine neutrophils are detrimental and cause lung pathology. Murine neutrophils could thus contribute to the observed susceptibility of HIS-NSG and PBS-NSG to low dose Mtb infection. Retrospectively, we would therefore recommend including markers for murine neutrophils in the analysis and possibly consider murine neutrophil depletion as a means to increase resistance of HIS-NSG mice in TB. A recent study with Mtb infected cynomolgus macaques (43) showed that granzyme-B expressing neutrophils correlated with

higher bacterial loads in lung granulomas suggesting that they promote Mtb replication. This feeds into the previously described dualistic role of neutrophils in TB (44). Thus, neutrophils and notably myeloid derived neutrophilic suppressor cells (45) that have been shown to exacerbate TB pathogenesis should be considered as targets for host directed therapy (HDT) in TB.

In parallel with elevated B and T cell numbers in the lymphocyte cuff, IgA, and IgM were detected in the lung microenvironment. In humans, the role of B cells and antibodies in TB remains controversial (46–48), and antibodies are likely protective or detrimental depending on the disease state. Even though significant numbers of human $CD4^+$ and $CD8^+$ T cells accumulated in the HIS-NSG Mtb infected lungs, the bacterial burden was high. This could be due to the impaired antigen specific responses by the granuloma associated $CD4^+$ (49) or $CD8^+$ T cells (50) and their putative failure to induce appreciable amounts of the TB-protective cytokine IFN-$\gamma$ (51). Likewise, the lack of human HLAs and poor human and murine cytokine cytokine-receptor crosstalk, particularly of IL-12 and IFN-$\gamma$ (52) contributed to poor adaptive immune activation. Moreover, the balance of pro- and anti-inflammatory cytokines in the HIS-NSG lung was skewed toward the Th1 like pole with a more pro-inflammatory signature linked to higher bacterial burden (28). Future studies with NSG strains that have endowed features (15) such as transgenic human cytokines and human HLA molecules will allow to more precisely assess the Mtb specific responses of the various human immune cells.

A caveat of the HIS-NSG mouse model is the presence of a residual innate immune system, endothelium, epithelium, and stroma of murine origin (53). Although the generated human mononuclear phagocytic network readily engulfs the vast majority of Mtb, certain residual murine cells can also engulf bacteria (54). In addition, inadequate antigen presentation by murine cells to the human T cells can cause anergy (15). This "hybrid species" phagocytosis and antigen presentation could influence the ensuing immune response thereby affecting the pathology analyzed in this study. Certain hallmarks of TB pathology, such as cavitary granulomas and fibrosis, were not detected in our model, which is consistent with other humanized mouse studies using Mtb or other mycobacteria (54–56). The lack of cavitary granulomas could be due to the short experimental observation window of 35 days or due to the single low dose infection with Mtb H37Rv employed in this study, compared to multiple reinfections with clinical strains in a high exposure environment, such as household contact (57). Other possible underlying factors include the lack of human HLAs, thus HIS-NSG mice do not develop a fully competent human adaptive immune system. Their immune system rather resembles those of pediatric and immunocompromised individuals. Indeed cases of cavitary TB are rare in children (58). Furthermore, distinct clinical strains of Mtb can induce slightly different immune responses, which could generate different granulomas (59). Each granuloma has a unique microenvironment with certain cellular and bacterial phenotypes, and this variability affects antibiotic efficacy.

Oral administration of HRZ and HRZM drug regimens reduced lung bacterial loads at similar rates, demonstrating that the HIS-NSG model is feasible for preclinical TB drug evaluation. Our model revealed that the HRZM regimen did not perform better than the HRZ regimen, in contrast to previous *in vitro* data (60) which indicated that addition of M could improve TB treatment. A large human trial revealed no additional benefit when either ethambutol or H were replaced by M in standard regimens (22, 36). That M becomes less effective in the presence of human-like lung pathology was also shown in C3HeB/FeJ (61) and $Nos2^{-/-}$ (62) mouse models of granuloma TB. However, HIS-NSG mice like the $Nos2^{-/-}$ mice (62) had homogenous bacterial loads and similar forms of granuloma heterogeneity post Mtb infection in contrast to the C3HeB/FeJ mice (34, 61), giving the HIS-NSG mice an advantage of consistent reproducibility. In order for drugs to be effective in the granuloma especially the caseous necrotic granuloma, they need to traverse different cell layers. Low penetrance and diffusion rates into the caseum of M has been shown (63). The observed increase in bacterial burden under therapy from 2 to 4 weeks generally suggests replication of bacteria in the caseous necrotic core of the granuloma along with poor penetrance of the applied drugs. Thus, we posit that caseous necrotic granulomas of HIS-NSG mice mimick human TB caseous necrotic granulomas during drug treatment. Provided that similarities between experimental TB drug treatment regimens in HIS-NSG mice and human trials can be validated, this mouse model will qualify as a late pre-clinical gating point for the decision whether to progress into clinical trial.

Another advantage of the HIS-NSG mouse model for preclinical drug studies is the known spatial location of human immune cells in the granuloma. As earlier stated, granulomas comprise various types, densities and locations of immune cells throughout the granuloma microenvironment similar to tumors (64). In tumors, larger numbers of $CD8^+$ cytotoxic T cells in the tumor margin and center correlated with better prognosis and provided a better target for enhancing antitumor responses by cancer immunotherapy (65). Therefore, future drug studies in HIS-NSG mice geared toward enhancing antibiotic effectiveness could incorporate HDTs, e.g., targeting $CD8^+$ T cells and their associated factors such as human programmed cell death protein 1 (PD1) and cytotoxic T lymphocyte associated protein 4 (CTLA4) (66).

In summary, our findings qualify the HIS-NSG mouse as a preclinical model for human TB and HIV-TB as well as for testing novel intervention strategies.

## DATA AVAILABILITY STATEMENT

The raw data supporting the conclusions of this manuscript will be made available by the authors, without undue reservation, to any qualified researcher.

## AUTHOR CONTRIBUTIONS

FA, GN, and SK contributed conception and design of the study. FA, LL, JM, and GN designed and performed flow cytometric analysis. FA, PM-A, MG, and GK designed and

performed drug study. FA, DL, SK, PK, and GN designed and performed experiments. FA and GN analyzed data. FA wrote the first draft of the manuscript. GN and SK wrote sections of the manuscript. PM-A, GK, LL, JM, MG, GN, SK, TS, and AS provided constructive input and editorial suggestions. All authors contributed to manuscript revision, read, and approved the submitted version.

## FUNDING

Provided by PreDiCT-TB (IMI JU Grant No. 115337), EU FP7 project ADITEC (HEALTH-F4-2011-280873) and EU Horizon 2020 TBVAC2020 (Grant No. 643381) to SK.

## ACKNOWLEDGMENTS

Dr. Gesa Rausch, Ines Neumann, and Jens Otto were involved in breeding and maintenance of NSG mouse strains in the bio safety three facilities at the Max Planck Institute of Infection Biology, Berlin, Germany. Prof. Dr. C. Loddenkemper and Provitro GmbH were instrumental in pathological analysis.

## SUPPLEMENTARY MATERIAL

The Supplementary Material for this article can be found online at: https://www.frontiersin.org/articles/10.3389/fimmu.2019.00089/full#supplementary-material

## REFERENCES

1. World Health Organization. *Global Tuberculosis Report* (2018). Available online at: www.who.int/tb/publications/global_report/en/ (Accessed November 25, 2017).
2. Gengenbacher M, Kaufmann SH. *Mycobacterium tuberculosis*: success through dormancy. *FEMS Microbiol Rev.* (2012) 36:514–32. doi: 10.1111/j.1574-6976.2012.00331.x
3. Dorhoi A, Kaufmann SH. Pathology and immune reactivity: understanding multidimensionality in pulmonary tuberculosis. In: Kaufmann SH, editor. *Semin Immunopathology*. Vol. 38. Berlin; Heidelberg: Springer (2016). p. 153–66. doi: 10.1007/s00281-015-0531-3
4. Lenaerts A, Barry III CE, Dartois V. Heterogeneity in tuberculosis pathology, microenvironments and therapeutic responses. *Immunol Rev.* (2015) 264:288–307. doi: 10.1111/imr.12252
5. Basaraba RJ, Hunter RL. Pathology of tuberculosis: how the pathology of human tuberculosis informs and directs animal models. *Microbiol Spectr.* (2017) 5. doi: 10.1128/microbiolspec.TBTB2-0029-2016
6. Basaraba RJ, Smith EE, Shanley CA, Orme IM. Pulmonary lymphatics are primary sites of *Mycobacterium tuberculosis* infection in guinea pigs infected by aerosol. *Infect Immun.* (2006) 74:5397–401. doi: 10.1128/IAI.00332-06
7. Polena H, Boudou F, Tilleul S, Dubois-Colas N, Lecointe C, Rakotosamimanana N, et al. *Mycobacterium tuberculosis* exploits the formation of new blood vessels for its dissemination. *Sci Rep.* (2016) 6:33162. doi: 10.1038/srep33162
8. Osherov N, Ben-Ami R. Modulation of host angiogenesis as a microbial survival strategy and therapeutic target. *PLoS Pathogens* (2016) 12:e1005479. doi: 10.1371/journal.ppat.1005479
9. Saeed W. Cavitating pulmonary tuberculosis: a global challenge. *Clin Med.* (2012) 12:40–1. doi: 10.7861/clinmedicine.12-1-40
10. Silva MT, Pestana NTS. The *in vivo* extracellular life of facultative intracellular bacterial parasites: role in pathogenesis. *Immunobiology* (2013) 218:325–37. doi: 10.1016/j.imbio.2012.05.011
11. Gupta U, Katoch V. Animal models of tuberculosis. *Tuberculosis* (2005) 85:277–93. doi: 10.1016/j.tube.2005.08.008
12. Heitmann L, Abad Dar M, Schreiber T, Erdmann H, Behrends J, Mckenzie AN, et al. The IL-13/IL-4R α axis is involved in tuberculosis-associated pathology. *J Pathol.* (2014) 234:338–50. doi: 10.1002/path.4399
13. Duque-Correa MA, Kühl AA, Rodriguez PC, Zedler U, Schommer-Leitner S, Rao M, et al. Macrophage arginase-1 controls bacterial growth and pathology in hypoxic tuberculosis granulomas. *Proc Natl Acad Sci USA.* (2014) 111:E4024–32. doi: 10.1073/pnas.1408839111
14. Kramnik I, Dietrich WF, Demant P, Bloom BR. Genetic control of resistance to experimental infection with virulent *Mycobacterium tuberculosis*. *Proc Natl Acad Sci USA.* (2000) 97:8560–5. doi: 10.1073/pnas.150227197
15. Rongvaux A, Takizawa H, Strowig T, Willinger T, Eynon EE, Flavell RA, et al. Human hemato-lymphoid system mice: current use and future potential for medicine. *Annu Rev Immunol.* (2013) 31:635–74. doi: 10.1146/annurev-immunol-032712-095921
16. Gorantla S, Makarov E, Finke-Dwyer J, Castanedo A, Holguin A, Gebhart CL, et al. Links between progressive HIV-1 infection of humanized mice and viral neuropathogenesis. *Am J Pathol.* (2010) 177:2938–49. doi: 10.2353/ajpath.2010.100536
17. Billerbeck E, Mommersteeg MC, Shlomai A, Xiao JW, Andrus L, Bhatta A, et al. Humanized mice efficiently engrafted with fetal hepatoblasts and syngeneic immune cells develop human monocytes and NK cells. *J Hepatol.* (2016) 65:334–43. doi: 10.1016/j.jhep.2016.04.022
18. Strowig T, Gurer C, Ploss A, Liu Y-F, Arrey F, Sashihara J, et al. Priming of protective T cell responses against virus-induced tumors in mice with human immune system components. *J Exp Med.* (2009) 206:1423–34. doi: 10.1084/jem.20081720
19. Libby SJ, Brehm MA, Greiner DL, Shultz LD, McClelland M, Smith KD, et al. Humanized nonobese diabetic-scid IL2rynull mice are susceptible to lethal *Salmonella* Typhi infection. *Proc Natl Acad Sci USA.* (2010) 107:15589–94. doi: 10.1073/pnas.1005566107
20. Vuyyuru R, Liu H, Manser T, Alugupalli KR. Characteristics of Borrelia hermsii infection in human hematopoietic stem cell-engrafted mice mirror those of human relapsing fever. *Proc Natl Acad Sci USA.* (2011) 108:20707–12. doi: 10.1073/pnas.1108776109
21. Pinho S, Rodrigues P, Andrade R, Serra H, Lopes J, Gomes M. Impact of tuberculosis treatment length and adherence under different transmission intensities. *Theor Popul Biol.* (2015) 104:68–77. doi: 10.1016/j.tpb.2015.06.004
22. Gillespie SH, Crook AM, McHugh TD, Mendel CM, Meredith SK, Murray SR, et al. Four-month moxifloxacin-based regimens for drug-sensitive tuberculosis. *N Engl J Med.* (2014) 371:1577–87. doi: 10.1056/NEJMoa1407426
23. Evangelopoulos D, da Fonseca JD, Waddell SJ. Understanding anti-tuberculosis drug efficacy: rethinking bacterial populations and how we model them. *Int J Infect Dis.* (2015) 32:76–80. doi: 10.1016/j.ijid.2014.11.028
24. Reece ST, Loddenkemper C, Askew DJ, Zedler U, Schommer-Leitner S, Stein M, et al. Serine protease activity contributes to control of *Mycobacterium tuberculosis* in hypoxic lung granulomas in mice. *J Clin Invest.* (2010) 120:3365–76. doi: 10.1172/JCI42796
25. Rongvaux A, Willinger T, Martinek J, Strowig T, Gearty SV, Teichmann LL, et al. Development and function of human innate immune cells in a humanized mouse model. *Nat Biotechnol.* (2014) 32:364. doi: 10.1038/nbt.2858
26. Nouailles G, Dorhoi A, Koch M, Zerrahn J, Weiner J, Faé KC, et al. CXCL5-secreting pulmonary epithelial cells drive destructive neutrophilic inflammation in tuberculosis. *J Clin Invest.* (2014) 124:1268–82. doi: 10.1172/JCI72030
27. Fox GJ, Orlova M, Schurr E. Tuberculosis in newborns: the lessons of the "Lübeck disaster"(1929–1933). *PLoS Pathogens* (2016) 12:e1005271. doi: 10.1371/journal.ppat.1005271
28. Gideon HP, Phuah J, Myers AJ, Bryson BD, Rodgers MA, Coleman MT, et al. Variability in tuberculosis granuloma T cell responses exists, but a balance of pro-and anti-inflammatory cytokines is associated with sterilization. *PLoS Pathogens* (2015) 11:e1004603. doi: 10.1371/journal.ppat.1004603

29. Patton J, Vuyyuru R, Siglin A, Root M, Manser T. Evaluation of the efficiency of human immune system reconstitution in NSG mice and NSG mice containing a human HLA. A2 transgene using hematopoietic stem cells purified from different sources. *J Immunol Methods* (2015) 422:13–21. doi: 10.1016/j.jim.2015.02.007
30. Lepus CM, Gibson TF, Gerber SA, Kawikova I, Szczepanik M, Hossain J, et al. Comparison of human fetal liver, umbilical cord blood, and adult blood hematopoietic stem cell engraftment in NOD-scid/$\gamma c^{-/-}$, Balb/c-Rag1$^{-/-}$ $\gamma c^{-/-}$, and C.B-17-scid/bg immunodeficient mice. *Hum Immunol.* (2009) 70:790–802. doi: 10.1016/j.humimm.2009.06.005
31. Via LE, Weiner DM, Schimel D, Lin PL, Dayao E, Tankersley SL, et al. Differential virulence and disease progression following *Mycobacterium tuberculosis* complex infection of the common marmoset (Callithrix jacchus). *Infect Iimmun.* (2013) 81:2909–19. doi: 10.1128/IAI.00632-13
32. Palanisamy GS, DuTeau N, Eisenach KD, Cave DM, Theus SA, Kreiswirth BN, et al. Clinical strains of *Mycobacterium tuberculosis* display a wide range of virulence in guinea pigs. *Tuberculosis* (2009) 89:203–9. doi: 10.1016/j.tube.2009.01.005
33. Manabe YC, Dannenberg AM, Tyagi SK, Hatem CL, Yoder M, Woolwine SC, et al. Different strains of *Mycobacterium tuberculosis* cause various spectrums of disease in the rabbit model of tuberculosis. *Infect Immun.* (2003) 71:6004–11. doi: 10.1128/IAI.71.10.6004-6011.2003
34. Irwin SM, Driver E, Lyon E, Schrupp C, Ryan G, Gonzalez-Juarrero M, et al. Multiple lesion types displaying vastly different microenvironments in C3HeB/FeJ mice following aerosol infection with *M. tuberculosis*. *Dis Model Mech.* (2015) 8:591–602. doi: 10.1242/dmm.019570
35. Hunter RL, Actor JK, Hwang S-A, Karev V, Jagannath C. Pathogenesis of post primary tuberculosis: immunity and hypersensitivity in the development of cavities. *Ann Clin Lab Sci.* (2014) 44:365–87. Available online at: http://www.annclinlabsci.org/
36. Jindani A, Harrison TS, Nunn AJ, Phillips PP, Churchyard GJ, Charalambous S, et al. High-dose rifapentine with moxifloxacin for pulmonary tuberculosis. *N Engl J Med.* (2014) 371:1599–608. doi: 10.1056/NEJMoa1314210
37. Silva AA, Mauad T, Saldiva PH, Pires-Neto RC, Coletta RD, Graner E, et al. Immunophenotype of lung granulomas in HIV and non-HIV associated tuberculosis. *MedicalExpress* (2014) 1:174–9. doi: 10.5935/MedicalExpress.2014.04.03
38. Billerbeck E, Horwitz JA, Labitt RN, Donovan BM, Vega K, Budell WC, et al. Characterization of human antiviral adaptive immune responses during hepatotropic virus infection in HLA-transgenic human immune system mice. *J Immunol.* (2013) 191:1753–64. doi: 10.4049/jimmunol.1201518
39. Jangalwe S, Shultz LD, Mathew A, Brehm MA. Improved B cell development in humanized NOD-scid IL2Rynull mice transgenically expressing human stem cell factor, granulocyte-macrophage colony-stimulating factor and interleukin-3. *Immun Inflamm Dis.* (2016) 4:427–40. doi: 10.1002/iid3.124
40. Niazi MK, Dhulekar N, Schmidt D, Major S, Cooper R, Abeijon C, et al. Lung necrosis and neutrophils reflect common pathways of susceptibility to *Mycobacterium tuberculosis* in genetically diverse, immune competent mice. *Dis Model Mech.* (2015) 8:1141–53. doi: 10.1242/dmm.020867
41. Dorhoi A, Yeremeev V, Nouailles G, Weiner 3rd J, Jörg S, Heinemann E, et al. Type I IFN signaling triggers immunopathology in tuberculosis-susceptible mice by modulating lung phagocyte dynamics. *Eur J Immunol.* (2014) 44:2380–93. doi: 10.1002/eji.201344219
42. Dorhoi A, Iannaccone M, Farinacci M, Faé KC, Schreiber J, Moura-Alves P, et al. MicroRNA-223 controls susceptibility to tuberculosis by regulating lung neutrophil recruitment. *J Clin Invest.* (2013) 123:4836–48. doi: 10.1172/JCI67604
43. Mattila JT, Maiello P, Sun T, Via LE, Flynn JL. Granzyme B-expressing neutrophils correlate with bacterial load in granulomas from *Mycobacterium tuberculosis*-infected cynomolgus macaques. *Cell Microbiol.* (2015) 17:1085–97. doi: 10.1111/cmi.12428
44. Lowe DM, Redford PS, Wilkinson RJ, O'Garra A, Martineau AR. Neutrophils in tuberculosis: friend or foe? *Trends Immunol.* (2012) 33:14–25. doi: 10.1016/j.it.2011.10.003
45. du Plessis N, Loebenberg L, Kriel M, von Groote-Bidlingmaier F, Ribechini E, Loxton AG, et al. Increased frequency of myeloid-derived suppressor cells during active tuberculosis and after recent *Mycobacterium tuberculosis* infection suppresses T-cell function. *Am J Respir Crit Care Med.* (2013) 188:724–32. doi: 10.1164/rccm.201302-0249OC
46. Lu LL, Chung AW, Rosebrock TR, Ghebremichael M, Yu WH, Grace PS, et al. A functional role for antibodies in tuberculosis. *Cell* (2016) 167:433–43.e14. doi: 10.1016/j.cell.2016.08.072
47. Zimmermann N, Thormann V, Hu B, Köhler AB, Imai-Matsushima A, Locht C, et al. Human isotype-dependent inhibitory antibody responses against *Mycobacterium tuberculosis*. *EMBO Mol Med.* (2016) 8:1325–39. doi: 10.15252/emmm.201606330
48. Li H, Wang X-X, Wang B, Fu L, Liu G, Lu Y, et al. Latently and uninfected healthcare workers exposed to TB make protective antibodies against *Mycobacterium tuberculosis*. *Proc Natl Acad Sci USA.* (2017) 114:5023–8. doi: 10.1073/pnas.1611776114
49. Fan L, Xiao H, Mai G, Su B, Ernst J, Hu Z. Impaired M. tuberculosis antigen-specific IFN-$\gamma$ response without IL-17 enhancement in patients with severe cavitary pulmonary tuberculosis. *PLoS ONE* (2015) 10:e0127087. doi: 10.1371/journal.pone.0127087
50. Andersson J, Samarina A, Fink J, Rahman S, Grundström S. Impaired expression of perforin and granulysin in CD8$^+$ T cells at the site of infection in human chronic pulmonary tuberculosis. *Infect Immun.* (2007) 75:5210–22. doi: 10.1128/IAI.00624-07
51. Flynn JL, Chan J, Triebold KJ, Dalton DK, Stewart TA, Bloom BR. An essential role for interferon gamma in resistance to *Mycobacterium tuberculosis* infection. *J Exp Med.* (1993) 178:2249–54. doi: 10.1084/jem.178.6.2249
52. Griffith JW, Sokol CL, Luster AD. Chemokines and chemokine receptors: positioning cells for host defense and immunity. *Annu Rev Immunol.* (2014) 32:659–702. doi: 10.1146/annurev-immunol-032713-120145
53. Leung C, Chijioke O, Gujer C, Chatterjee B, Antsiferova O, Landtwing V, et al. Infectious diseases in humanized mice. *Eur J Immunol.* (2013) 43:2246–54. doi: 10.1002/eji.201343815
54. Lee J, Brehm MA, Greiner D, Shultz LD, Kornfeld H. Engrafted human cells generate adaptive immune responses to *Mycobacterium bovis* BCG infection in humanized mice. *BMC Immunol.* (2013) 14:53. doi: 10.1186/1471-2172-14-53
55. Heuts F, Gavier-Widén D, Carow B, Juarez J, Wigzell H, Rottenberg ME. CD4$^+$ cell-dependent granuloma formation in humanized mice infected with mycobacteria. *Proc Natl Acad Sci USA.* (2013) 110:6482–7. doi: 10.1073/pnas.1219985110
56. Calderon VE, Valbuena G, Goez Y, Judy BM, Huante MB, Sutjita P, et al. A humanized mouse model of tuberculosis. *PLoS ONE* (2013) 8:e63331. doi: 10.1371/journal.pone.0063331
57. Jones-López EC, Kim S, Fregona G, Marques-Rodrigues P, Hadad DJ, Molina LPD, et al. Importance of cough and *M. tuberculosis* strain type as risks for increased transmission within households. *PLoS ONE* (2014) 9:e100984. doi: 10.1371/journal.pone.0100984
58. Griffith-Richards SB, Goussard P, Andronikou S, Gie RP, Przybojewski SJ, Strachan M, et al. Cavitating pulmonary tuberculosis in children: correlating radiology with pathogenesis. *Pediatr Radiol.* (2007) 37:798–804. doi: 10.1007/s00247-007-0496-z
59. Lerner TR, Borel S, Gutierrez MG. The innate immune response in human tuberculosis. *Cell Microbiol.* (2015) 17:1277–85. doi: 10.1111/cmi.12480
60. Tortoli E, Dionisio D, Fabbri C. Evaluation of moxifloxacin activity *in vitro* against *Mycobacterium tuberculosis*, including resistant and multidrug-resistant strains. *J Chemother.* (2004) 16:334–6. doi: 10.1179/joc.2004.16.4.334
61. Li S-Y, Irwin SM, Converse PJ, Mdluli KE, Lenaerts AJ, Nuermberger EL. Evaluation of moxifloxacin-containing regimens in pathologically distinct murine tuberculosis models. *Antimicrob Agents Chemother.* (2015) 59:4026–30. doi: 10.1128/AAC.00105-15

62. Gengenbacher M, Duque-Correa MA, Kaiser P, Schuerer S, Lazar D, Zedler U, et al. NOS2-deficient mice with hypoxic necrotizing lung lesions predict outcomes of tuberculosis chemotherapy in humans. *Sci Rep*. (2017) 7:8853. doi: 10.1038/s41598-017-09177-2
63. Prideaux B, Via LE, Zimmerman MD, Eum S, Sarathy J, O'brien P, et al. The association between sterilizing activity and drug distribution into tuberculosis lesions. *Nat Med*. (2015) 21:1223. doi: 10.1038/nm.3937
64. Galon J, Costes A, Sanchez-Cabo F, Kirilovsky A, Mlecnik B, Lagorce-Pagès C, et al. Type, density, and location of immune cells within human colorectal tumors predict clinical outcome. *Science* (2006) 313:1960–4. doi: 10.1126/science.1129139
65. Zhou P, Shaffer DR, Arias DAA, Nakazaki Y, Pos W, Torres AJ, et al. *In vivo* discovery of immunotherapy targets in the tumour microenvironment. *Nature* (2014) 506:52. doi: 10.1038/nature12988
66. Kaufmann SH, Dorhoi A, Hotchkiss RS, Bartenschlager R. Host-directed therapies for bacterial and viral infections. *Nat Rev Drug Discov*. (2018) 17:35. doi: 10.1038/nrd.2017.162

**Conflict of Interest Statement:** SK is currently employed by company Bayer Pharmaceuticals, Berlin, Germany. TS is currently employed by company Immunopep, Berlin, Germany.

The remaining authors declare that the research was conducted in the absence of any commercial or financial relationships that could be construed as a potential conflict of interest.

## 2.2 Streptokokken-Pneumonie: Modelle zur Therapieevaluation

Streptokokken-Pneumonien sind antibiotisch behandelbar und die Entwicklung antibiotikaresistenter Stämme ist begrenzt[58,59]. Dennoch liegt die Sterblichkeitsrate seit Einführung der Antibiotika in den 1940er Jahren bei ca. 10 – 15% geblieben[60-62]. Die Hauptursache hierfür liegt nicht in inadäquaten Therapien oder mangelndem Management von Komorbiditäten, sondern unter anderem in einer überschießenden Immunantwort, die Gewebeschäden verursacht, so dass die Lunge ihre physiologische Funktion, den Gasaustausch, nicht mehr vollständig ausüben kann[62-64]. Ein wichtiger Aspekt der präklinischen Forschung ist daher die Entwicklung adjuvanter Therapien, die in Kombination mit der Standardantibiotikatherapie die Lungenfunktion erhalten und die pathologische Immunantwort begrenzen.

Die Immunantwort gegen extrazelluläre Erreger wie Streptokokken ist eine Typ 3-Antwort. Das bedeutet, dass hauptsächlich Effektormechanismen initiiert werden, die die epitheliale Abwehr fördern und die Rekrutierung und Funktion von Neutrophilen verstärken. Die Initiierung einer typischen Th17-Antwort lässt sich in nasopharyngealen Besiedlungsmodellen mit *Streptococcus pneumoniae* untersuchen, in den Mausmodellen der akuten Pneumonie führt die Schwere des Infektionsverlaufs bereits vor der Einwanderung spezifischer Th17-T-Zellen zum Erreichen humaner Endpunktkriterien[65]. Die akuten Pneumonie Modelle sind jedoch sehr gut geeignet, die Lungenpathologie der Pneumonie abzubilden, die Funktion der alveolo-kapillären Lungenbarriere sowie angeborene Immunantworten zu untersuchen. Nach transnasaler Infektion mit *Streptococcus pneumoniae* zeigen die Versuchstiere Symptome einer schweren Pneumonie, wie Dyspnoe, Hypothermie und Gewichtsverlust. Bereits nach 6 Stunden ist eine deutliche Rekrutierung von Neutrophilen zu beobachten. Diese Immunzellen sind von besonderem Interesse, da sie bei einer zu starken oder unkontrollierten Reaktion schwere Gewebeschäden verursachen können. Sie sind aber auch essentiell für die Elimination von Streptokokken, wie in Mausmodellen gezeigt werden konnte[66-68].

Im Patienten übernehmen Antibiotika die Abtötung der Streptokokken, so dass dieser positive Effekt der initiierten Neutrophilenantwort durch ihre gewebeschädigende Wirkung überdeckt wird. In unseren TB-Studien konnten wir zeigen, dass der pathologische Aspekt der Neutrophilen bei einer chronischen Infektion überwiegt[50,69].

Der Schwerpunkt unserer Streptokokken-Forschung lag einerseits auf der Entwicklung eines Tiermodells, das die präklinische Evaluierung von putativen adjuvanten Therapien erlaubt[70], und andererseits auf der Untersuchung der Regulation und pathologischen Mechanismen der Neutrophilenantwort[71] und Rekrutierung in einem akuten Infektionsmodell. Im Folgenden wird eine ausgewählte eigene Studie vorgestellt, die ein neuartiges Mausmodell mit zeitlich gestaffelter Antibiotikagabe beschreibt, welches es erlaubt, milde bis letale Krankheitsverläufe unter Antibiotikatherapie abzubilden[70].

### 2.2.1 Mausmodelle der schweren CAP unter Antibiotikatherapie (Eigene Arbeit 3)

Veröffentlicht als: Forschungsartikel mit geteilter Letztautorschaft*.

Der nachfolgende Text entspricht dem originalsprachlichen Abstrakt der Arbeit "*Delay in antibiotic therapy results in fatal disease outcome in murine pneumococcal pneumonia.*" (Crit Care. 2018 Nov 1;22(1):287. doi: 10.1186/s13054-018-2224-5)[70] der Autoren Sarah Berger, Cengiz Goekeri, Shishir K Gupta, Julio Vera, Kristina Dietert, Ulrike Behrendt, Jasmin Lienau, Sandra-Maria Wienhold, Achim D Gruber, Norbert Suttorp, Martin Witzenrath*, und **Geraldine Nouailles***.

„Background: Community-acquired pneumonia (CAP) remains a major cause of death worldwide. Mechanisms underlying the detrimental outcome despite adequate antibiotic therapy and comorbidity management are still not fully understood.

Methods: To model timely versus delayed antibiotic therapy in patients, mice with pneumococcal pneumonia received ampicillin twice a day starting early (24 h) or late (48 h) after infection. Clinical readouts and local and systemic inflammatory mediators after early and late antibiotic intervention were examined.

Results: Early antibiotic intervention rescued mice, limited clinical symptoms and restored fitness, whereas delayed therapy resulted in high mortality rates. Recruitment of innate immune cells remained unaffected by antibiotic therapy. However, both early and late antibiotic intervention dampened local levels of inflammatory mediators in the alveolar spaces. Early treatment protected from barrier breakdown, and reduced levels of vascular endothelial growth factor (VEGF) and perivascular and alveolar edema formation. In contrast, at 48 h post infection, increased pulmonary leakage was apparent and not reversed by late antibiotic treatment. Concurrently, levels of VEGF remained high and no beneficial effect on edema formation was evident despite therapy. Moreover, early but not late treatment protected mice from a vast systemic inflammatory response.

Conclusions: Our data show that only early antibiotic therapy, administered prior to breakdown of the alveolar-capillary barrier and systemic inflammation, led to restored fitness and rescued mice from fatal streptococcal pneumonia. The findings highlight the importance of identifying CAP patients prior to lung barrier failure and systemic inflammation and of handling CAP as a medical emergency."

Berger et al. Critical Care (2018) 22:287
https://doi.org/10.1186/s13054-018-2224-5

Critical Care

RESEARCH Open Access

# Delay in antibiotic therapy results in fatal disease outcome in murine pneumococcal pneumonia

Sarah Berger[1], Cengiz Goekeri[1], Shishir K. Gupta[2], Julio Vera[2], Kristina Dietert[3], Ulrike Behrendt[1], Jasmin Lienau[1], Sandra-Maria Wienhold[1], Achim D. Gruber[3], Norbert Suttorp[4], Martin Witzenrath[1,4*†] and Geraldine Nouailles[1*†]

## Abstract

**Background:** Community-acquired pneumonia (CAP) remains a major cause of death worldwide. Mechanisms underlying the detrimental outcome despite adequate antibiotic therapy and comorbidity management are still not fully understood.

**Methods:** To model timely versus delayed antibiotic therapy in patients, mice with pneumococcal pneumonia received ampicillin twice a day starting early (24 h) or late (48 h) after infection. Clinical readouts and local and systemic inflammatory mediators after early and late antibiotic intervention were examined.

**Results:** Early antibiotic intervention rescued mice, limited clinical symptoms and restored fitness, whereas delayed therapy resulted in high mortality rates. Recruitment of innate immune cells remained unaffected by antibiotic therapy. However, both early and late antibiotic intervention dampened local levels of inflammatory mediators in the alveolar spaces. Early treatment protected from barrier breakdown, and reduced levels of vascular endothelial growth factor (VEGF) and perivascular and alveolar edema formation. In contrast, at 48 h post infection, increased pulmonary leakage was apparent and not reversed by late antibiotic treatment. Concurrently, levels of VEGF remained high and no beneficial effect on edema formation was evident despite therapy. Moreover, early but not late treatment protected mice from a vast systemic inflammatory response.

**Conclusions:** Our data show that only early antibiotic therapy, administered prior to breakdown of the alveolar–capillary barrier and systemic inflammation, led to restored fitness and rescued mice from fatal streptococcal pneumonia. The findings highlight the importance of identifying CAP patients prior to lung barrier failure and systemic inflammation and of handling CAP as a medical emergency.

**Keywords:** *Streptococcus pneumoniae*, Blood–air barrier, Bacterial pneumonia, Acute lung injury, Ampicillin, Innate immunity

## Background

Community-acquired pneumonia (CAP) is a significant cause of morbidity and mortality worldwide, with *Streptococcus pneumoniae* being the most prevalent causative pathogen [1, 2]. Since the 1950s, the in-hospital mortality rate of CAP has remained about 12–13% in most high-income countries [3]. Severe forms of CAP necessitate admission to the intensive care unit (ICU) and result in mortality rates ranging from 18 to 38% [4–6]. Antibiotic intervention within 4 h of hospital arrival is associated with reduced mortality compared to a delayed start of treatment in CAP [7, 8]. To improve survival in severe pneumonia, CAP is nowadays described as a medical emergency and early and aggressive treatment is therefore proposed on an empiric basis [9–14]. However, the pathophysiological differences in the course of pneumonia resulting from early as opposed to late treatment are unknown.

* Correspondence: martin.witzenrath@charite.de; geraldine.nouailles@charite.de
†Martin Witzenrath and Geraldine Nouailles contributed equally to this work.
[1]Division of Pulmonary Inflammation, Charité — Universitätsmedizin Berlin, corporate member of Freie Universität Berlin, Humboldt-Universität zu Berlin, and Berlin Institute of Health, Charitéplatz 1, 10117 Berlin, Germany
Full list of author information is available at the end of the article

Differences in survival of CAP patients receiving antibiotic therapy result from a wide range of contributors, which can be pathogen, drug or host related. The host's immune response may aggravate detrimental pulmonary barrier failure and lung edema development [15–19]. Particularly, activation of lung resident cells (e.g., alveolar macrophages and epithelial cells) by pathogen-associated molecular patterns (PAMPs) results in local inflammation, which in turn promotes attraction of inflammatory cells like polymorphonuclear leukocytes (PMNs) into the lungs [20–22]. As professional phagocytes, PMNs are crucial for antimicrobial defense; however, PMNs also cause host tissue injury, leading to increased permeability of the alveolar–capillary barrier [23, 24]. As a further consequence of pulmonary barrier failure, CAP can progress to life-threatening sepsis and multiorgan dysfunction [25]. However, specific reasons for host-related differences in survival that depend on timely versus delayed antibiotic treatment remain unclear to date. Analysis of processes contributing to host-related therapy failure and high mortality rates due to delayed treatment are needed to foster the development of new adjunctive therapies. We hypothesized that antibiotic treatment decelerates exaggerated immune responses, but does not relevantly reduce established lung barrier dysfunction and lung edema. In the current study, we performed in-depth examination of mice with severe pneumococcal pneumonia receiving early versus late antibiotic treatment.

## Methods

A detailed methodology and materials are presented in Additional file 1: Materials and methods.

### Study approval

Female C57BL/6 N mice (8–10 weeks old; Charles River, Germany) were housed under specific-pathogen-free conditions. All animal studies have been ethically reviewed and approved by the State Office for Health and Social Services, Berlin, Germany.

### Murine bacterial pneumonia

Mice were transnasally inoculated as previously described in detail [26] with $5 \times 10^6$ colony-forming units (CFUs) of *S. pneumoniae* serotype 3 in 20 µl PBS. Control mice received sham infection (PBS). Starting at 24 h or 48 h p.i., ampicillin (0.4 mg/mouse) or 0.9% NaCl (solvent control) was injected intraperitoneally every 12 h (Additional file 1: Figure S1). Body weight, temperature and murine pneumonia symptoms (scaling from 0 (absent) to 1 (present) and 2 (severe)) were assessed twice daily. Detailed information about the scoring system for murine pneumonia symptoms is presented in Additional file 1: Materials and methods, and Table S3. The summary of scored symptoms provides individual clinical scores. Mice meeting the inclusion criteria at 24 h p.i. (body weight loss more than 10% and/or body temperature < 37.0 °C) were analyzed. Numbers of analyzed mice per group per time point are summarized in Additional file 1: Tables S1 and S2. At defined endpoints, mice were anesthetized and exsanguinated prior to analysis. EDTA-blood was used for hemogram (measured with Scil Vet abc; scil animal care company GmbH) and bacterial load determination. The remaining blood was collected in serum separator tubes (BD) and sera were stored at − 80 °C.

### Bronchoalveolar lavage

Mice were sacrificed prior to lavage. Airways were washed twice with 800 µl PBS. Bronchoalveolar lavage (BAL) suspensions were used to determine the bacterial burden. Supernatant (BAL fluid (BALF)) was frozen at − 80 °C. BAL cells were used for leukocyte differentiation.

### Bacterial loads

Serial dilutions of EDTA-blood and BAL suspensions were plated onto Columbia agar with 5% sheep blood (BD) and incubated for 24 h at 37 °C under 5% $CO_2$ prior to CFU counting.

### Histological analysis

Mice were sacrificed prior to histological analysis. Lungs were immersion-fixed in 4% buffered formalin, embedded in paraffin, cut into 2-µm sections and stained with hematoxylin and eosin (H&E) as described previously [27, 28]. Lung inflammation was scored based on consideration of specific parameters graded on a scale of 0 (absent) to 4 (severe), including the degree of inflammation, infiltration of neutrophils, pleuritis and steatitis. A lung edema score was assessed as a sum of distribution and degree of interstitial (perivascular) and alveolar edema graded on a scale of 0 (absent) to 5 (massive).

### Blood clinical analytes

AST and urea levels were measured using Cobas-800 0-C701 (Roche) by LABOKLIN (Bad Kissingen, Germany).

### Leukocyte differentiation

BAL cells were preincubated with blocking antibody and stained with anti-CD11c, anti-CD11b, anti-F4/80, anti-Ly6G, anti-Ly6C and anti-MHCII antibodies. Cells were measured and analyzed with FACS Canto II (BD) and FACSDiva software. Cell numbers were calculated using CountBright Absolute Counting Beads (ThermoFisher Scientific).

### Pulmonary vascular leakage

Mouse serum albumin (MSA) levels in BALF and serum were measured by ELISA (BETHYL). The alveolar–

capillary barrier permeability index was calculated as the ratio of BALF/serum MSA.

#### Multiplex assay and ELISA

Mouse cytokine/chemokine levels were measured in BALF and serum with the ProcartaPlex Custom Mix & Match according to the manufacturer's instructions (AffymetrixBioscience). BALF levels of CXCL2 and CXCL5 were measured by ELISA (RD).

#### Cytokine-immune cell network

Details for construction of the network are described in Additional file 1: Materials and methods.

#### Data analyses

GraphPad Prism 6 software was used for statistical analyses. Survival curves were analyzed using the Kaplan–Meier method and log-rank (Mantel–Cox) test. The Kruskal–Wallis test/Dunn's multiple comparisons test and one-way ANOVA/Dunnett's multiple comparisons test were used for comparison to *S. pneumoniae*-infected mice at the start of therapy. Grouped analyses were performed using two-way ANOVA/Sidak's multiple comparison test. $p < 0.05$ was considered significant.

## Results

#### Late yet efficient antibiotic treatment did not rescue *S. pneumoniae*-infected mice

To improve understanding of clinical deterioration of individuals with bacterial pneumonia despite adequate antibiotic therapy, *S. pneumoniae*-infected mice were treated with ampicillin starting at different times p.i. Mice receiving ampicillin therapy starting 24 h p.i. showed a significantly higher survival rate (97.1%) than animals with late (48 h p.i.) therapy (20.4%) (Fig. 1a). Clinical signs of murine pneumonia like disheveled fur or an accelerated breathing rate and behavioral or somatic changes (Fig. 1b), weight loss (Fig. 1c), decrease in body temperature (Additional file 2: Figure S2), as well as lung infiltrates, assessed by histology (Additional file 2: Figure S2B), were already apparent at 24 h p.i. In line with superior survival rates, early antibiotic therapy led to normalization of body temperature and murine clinical scores within 12 h and increased body weight within 24 h. Mice receiving ampicillin from 48 h p.i. onward failed to restore their body weight and to reverse their murine clinical score within the following 48 h (Fig. 1b, c). Hence, for accurate interpretation of results at 72 h p.i. and beyond, the poor survival rates of untreated and late-treated groups (below 25%, Additional file 1: Tables S1 and S2) need consideration.

Notably, antibiotic therapy failure was not responsible for different outcomes in survival. At 24 h and 48 h p.i., before initiation of an antibiotic regimen, all mice analyzed at these time points had developed bacteremia. Within 12 h both regimens reduced the mean bacterial load in the blood by over 99% and in the alveolar spaces by over 85% (Fig. 1d, Additional file 2: Figure S3A).

#### Antibiotic treatment had no major impact on innate leukocyte kinetics in BAL and blood

Resident and recruited innate immune cells participate in defense against pulmonary pathogens [29] and may be influenced by antibiotic treatment. Consequently, we analyzed kinetics of PMNs, alveolar macrophages and Ly6C$^{hi}$ inflammatory macrophages during infection and therapy (gating strategy; Additional file 2: Figure S4). After an initial recruitment wave, the number and frequency of BAL PMNs steadily declined from 24 h p.i. onward in treated and control groups (Fig. 2a, b, Additional file 2: Figure S3B). In the blood, however, frequencies but not total numbers of neutrophils (Fig. 2c, Additional file 2: Figure S3B) were significantly lower after early antibiotic intervention compared to the solvent-treated control group, whereas no difference was detected after late treatment. Likewise, antibiotic treatment did not affect the population size of alveolar macrophages, which remained unaffected throughout the infection course. Recruitment of Ly6C$^{hi}$ inflammatory macrophages into alveolar spaces significantly increased following infection and remained unaltered by antibiotic therapy (Additional file 2: Figure S5A, B). Kinetics of blood monocyte number and frequency remained unaffected by antibiotic treatment. Similar results were obtained for eosinophils and platelets (Additional file 2: Figure S5C).

#### Antibiotic treatment suppressed lung inflammation

Alveolar concentrations of chemokines and growth factors were measured in BALF (Fig. 3a, Additional file 2: Figures S3C and S6A). Levels of monocyte-recruiting chemokines CCL3 and CCL2 decreased within 24 h after antibiotic therapy compared to the concentration at treatment start. Notably, only after an early therapy start were significant differences between ampicillin-treated and solvent-treated mice with pneumonia observed for CCL2. Kinetics of neutrophil growth factor G-CSF levels resembled the kinetics of CCL2. After an initial increase in GM-CSF levels following an early therapy start, concentrations in BALF decreased with antibiotic therapy. CXCL1/KC, CXCL2/MIP-2 and CXCL5/LIX, homologs of human IL-8, are responsible for alveolar neutrophil recruitment [30]. Infected, solvent-treated mice showed an infection-time-dependent increase in CXCL1, CXCL2 and CXCL5. Notably, antibiotic intervention solely inhibited the increase of CXCL1 and CXCL2, but not CXCL5.

Both early and late antibiotic therapy led to a reduction in the local inflammatory cytokines IL-6, IL-1β,

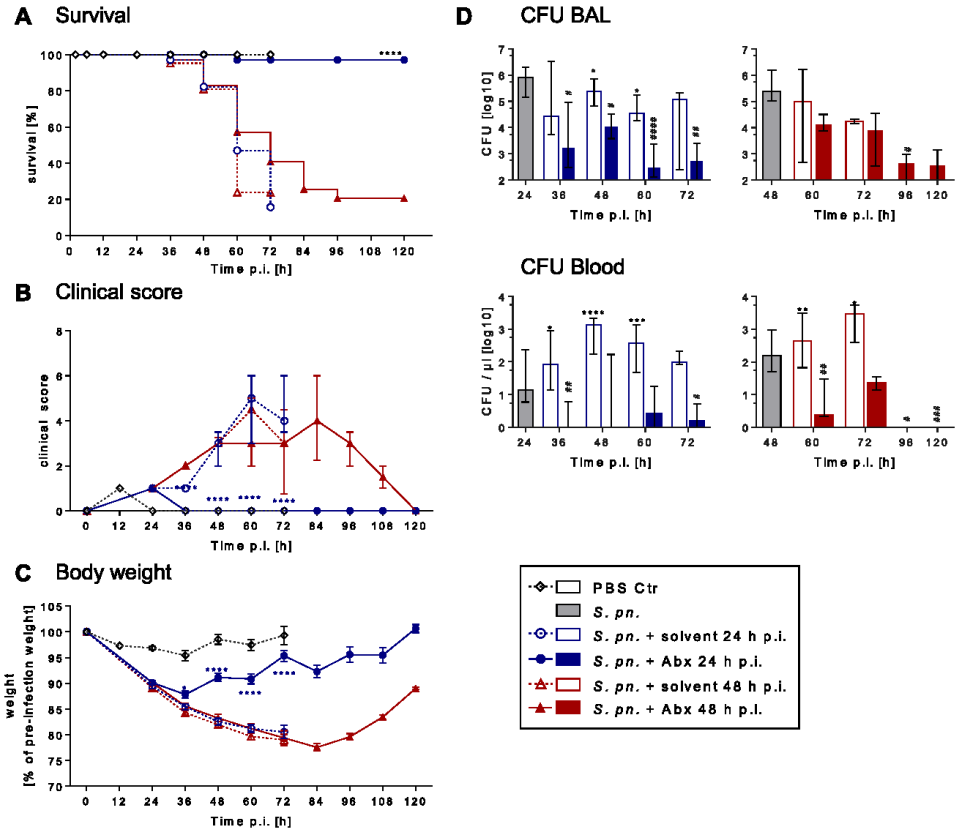


**Fig. 1** Late antibiotic therapy failed to rescue *S. pneumoniae*-infected mice. Mice were infected with *S. pneumoniae* and assigned equally to groups and analysis time points ($n_{total} = 9$ per time point). Starting 24 h or 48 h p.i., intervention groups were treated with ampicillin. As controls, mice were sham infected (PBS; $n_{total} = 7$ per time point) or treated with solvent (0.9% NaCl). Survival, murine clinical score and weight assessed for all mice until designated analysis time point. Mice surviving until designated analysis time point were sacrificed for BAL and blood sampling (number analyzed per time point presented in Additional file 1: Table S1). **a** Kaplan–Meier curves showing survival of experimental groups, log-rank test. **b** Murine clinical disease score. Median and 25–75% interquartile range (IQR). **c** Relative weight curves. Mean ± SEM. **d** Bacterial burden in BAL and blood of respective mice analyzed at indicated time points. Median and 25–75% IQR. **a**–**d** Results pooled from three independent experiments per time point. **b**–**d** Two-way ANOVA/Sidak's multiple comparisons test for comparison of ampicillin versus solvent treatment. Kruskal–Wallis test/Dunn's multiple comparisons test for comparison to *S. pneumoniae*-infected mice at therapy start. *Significant difference between groups at time point, #significant difference from therapy start: $^{*/\#}p < 0.05$, $^{**/\#\#}p < 0.01$, $^{***/\#\#\#}p < 0.001$ and $^{****/\#\#\#\#}p < 0.0001$. Abx antibiotics, BAL bronchoalveolar lavage, CFU colony forming unit, Ctr control, PBS phosphate buffered saline, p.i. post infection, *S. pn. Streptococcus pneumoniae*

TNF-α and IFN-γ in the BALF. Likewise, the anti-inflammatory cytokine IL-10 decreased after early and late antibiotic therapy. On the contrary, IL-12p40 levels increased within 12 h after early therapy start and decreased after late antibiotic intervention (Fig. 3b, Additional file 2: Figures S3C and S6B). In line with these observations, the lung inflammation score, composed of specified histopathological inflammation parameters, was significantly decreased after early antibiotic therapy but remained unchanged after late antibiotic therapy (Fig. 3c, Additional file 2: Figures S3D and S7). Particularly, early but not late antibiotic intervention prevented development of pleuritis and steatitis of the adjacent mediastinal adipose tissue but did not show any impact on the innate cell recruitment into the lungs.

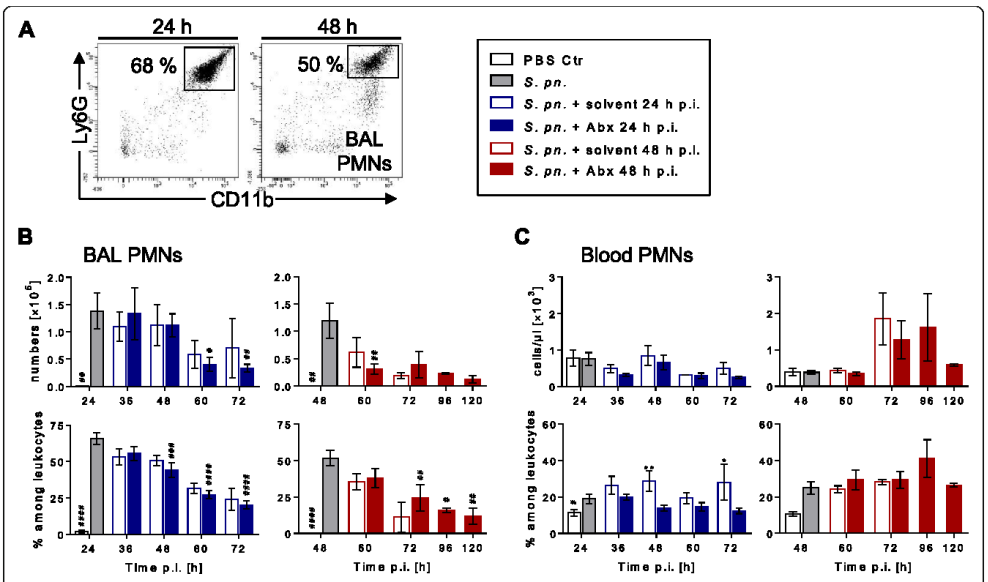


**Fig. 2** Antibiotic therapy has no impact on alveolar neutrophil recruitment. Mice were infected with *S. pneumoniae* and assigned equally to groups and analysis time points ($n_{total} = 9$ per time point). Starting 24 h or 48 h p.i., intervention groups were treated with ampicillin. As controls, mice were sham infected (PBS; $n_{total} = 7$ per time point) or treated with solvent (0.9% NaCl). Mice surviving until designated analysis time point were sacrificed for BAL and blood sampling (number analyzed per time point presented in Additional file 1: Table S1). **a** Representative dot blots illustrating gating of innate BAL PMN populations at 24 h and 48 h p.i. **b** Numbers and frequencies of PMNs in BAL of mice analyzed at indicated time points p.i., quantified by flow cytometry. **c** Numbers and frequencies of PMNs measured in EDTA-blood by Scil Vet abc hematology analysis of respective mice. **b, c** Results pooled from three independent experiments per time point. Mean ± SEM. Two-way ANOVA/Sidak's multiple comparisons test for comparison of ampicillin versus solvent treatment. One-way ANOVA/Dunnett's multiple comparisons test for comparison to *S. pneumoniae*-infected mice at therapy start. *Significant difference between groups at time point, #significant difference from therapy start: $^{*/\#}p < 0.05$, $^{**/\#\#}p < 0.01$, $^{\#\#\#}p < 0.001$ and $^{\#\#\#\#}p < 0.0001$. Abx antibiotics, BAL bronchoalveolar lavage, Ctr control, PBS phosphate buffered saline, p.i. post infection, PMN polymorphonuclear leukocyte, *S. pn. Streptococcus pneumoniae*

### Network analysis of alveolar immune cells and local effector molecules illustrated pronounced downregulation of cytokines by antibiotic treatment

The aim of the network analysis was to visualize and summarize consequences of early versus late antibiotic therapy on local cellular and cytokine/chemokine responses (Additional file 2: Figure S8). Hereby, we illustrate that recruitment of innate cells (Additional file 2: Figure S8, left) was independent of antibiotic treatment and treatment commencement. Cellular effector mechanisms such as cytokine secretion of IFN-γ, IL-1β, IL-6 and TNF-α were also strongly reduced by antibiotic treatment, while secretions of neutrophil-attracting chemokines (e.g., CXCL1, CXCL2, CXCL5 and G-CSF) were only modestly affected (Additional file 2: Figure S8, right).

### Early antibiotic treatment prevented systemic inflammatory responses

Following local pulmonary inflammation and bacteremia, the development of a systemic inflammatory response in untreated yet infected mice was observed. At 24 h p.i., prior to early antibiotic treatment, systemic cytokines were close to basal levels, although bacteremia was established. Notably, treatment with antibiotics starting 24 h p.i. prevented upsurge of inflammatory mediators such as IL-6, TNF-α and IFN-γ in serum compared to untreated yet infected mice. Late antibiotic therapy only led to a significant reduction in serum levels of IFN-γ, but basal levels were not reached. Systemic IL-10 concentrations were rarely detectable (Fig. 4a, Additional file 2: Figures S3E and S9A).

Generally, kinetics of systemic proinflammatory chemokines and growth factors highly resembled kinetics of systemic proinflammatory cytokines (Fig. 4a, b, Additional file 2: Figures S3E and S9A, B). Similar to systemic cytokine concentrations, systemic levels of chemokines and G-CSF increased later than in alveolar spaces.

At 24 h p.i., systemic chemokine levels were five times (CXCL1) to 90 times (CCL3) lower than prior late antibiotic therapy at 48 h p.i. Early antibiotic intervention prevented dramatic increases of G-CSF, CCL2 and CXCL1 in

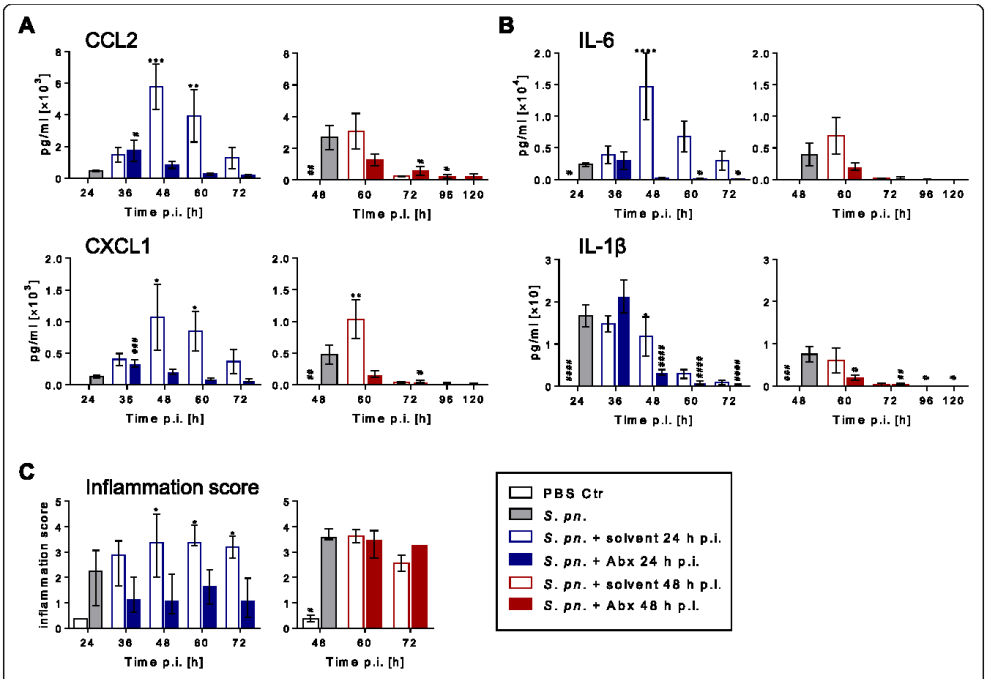


**Fig. 3** Antibiotic therapy reduced levels of alveolar inflammatory mediators. Mice were infected with *S. pneumoniae* and assigned equally to groups and analysis time points (**a**, **b** $n_{total} = 9$, **c** $n_{total} = 4$ per time point). Starting 24 h or 48 h p.i., intervention groups were treated with ampicillin. As controls, mice were sham infected (PBS; **a**, **b** $n_{total} = 7$, **c** $n_{total} = 4$ per time point) or treated with solvent (0.9% NaCl). Mice surviving until designated analysis time point were sacrificed for BAL sampling (number analyzed per time point presented in Additional file 1: Table S1) or histopathological analysis (number analyzed per time point presented in Additional file 1: Table S2). **a** Chemokine and **b** cytokine protein levels in BAL fluid measured by multiplex analysis or ELISA. **a**, **b** Results pooled from three independent experiments per time point. Mean ± SEM. **c** Lung inflammation score calculated from specified histopathological parameters displaying distribution, severity and main character of lung lesions. Results pooled from two independent experiments per time point. Median and 25–75% interquartile range. **a**–**c** Two-way ANOVA/Sidak's multiple comparisons test for comparison of ampicillin versus solvent treatment. **a**, **b** One-way ANOVA/Dunnett's multiple comparisons test and **c** Kruskal–Wallis test/Dunn's multiple comparisons test for comparison to *S. pneumoniae*-infected mice at therapy start. *Significant difference between groups at time point, #significant difference from therapy start: $^{*/\#}$ $p < 0.05$, $^{**/\#\#}$ $p < 0.01$, $^{***/\#\#\#}$ $p < 0.001$ and $^{****/\#\#\#\#}$ $p < 0.0001$. Abx antibiotics, Ctr control, IL interleukin, PBS phosphate buffered saline, p.i. post infection, *S. pn. Streptococcus pneumoniae*

serum, with significant differences from the respective solvent-treated control groups. Early therapy did not lead to a significant change in CCL3 levels. After late antibiotic therapy, systemic CXCL1, G-CSF and CCL2 concentrations decreased, but no significant differences from the respective control groups were observed (Fig. 4b, Additional file 2: Figures S3E and 9B). Systemic levels of GM-CSF were below the detection limit (data not shown). To determine the functional integrity of the liver and kidneys, aspartate aminotransferase (AST) and urea were measured in serum. Increased concentrations of AST were found at 48 h but not at 24 h p.i. Early antibiotic therapy prevented increase of AST levels in infected mice. Late antibiotic treatment had no beneficial effect on AST concentrations (Fig. 4c, Additional file 2: Figure S3F). The urea concentration increased following early antibiotic therapy whereas no differences were detected following late intervention (Additional file 2: Figure S9C).

### Early antibiotic intervention protected alveolar–epithelial barrier integrity and reduced VEGF levels

Measurements of the alveolar–capillary barrier permeability index allow estimation of the degree of vascular leakage into alveolar spaces. Prior to treatment of infected mice, vascular leakage was evident at 48 h but not at 24 h p.i. Early antibiotic treatment successfully prevented development of vascular leakage observed in *S. pneumoniae*-infected solvent-treated control mice (Fig. 5a, Additional file 2: Figure S3G). In contrast, late antibiotic therapy failed to significantly reverse established lung permeability. In line

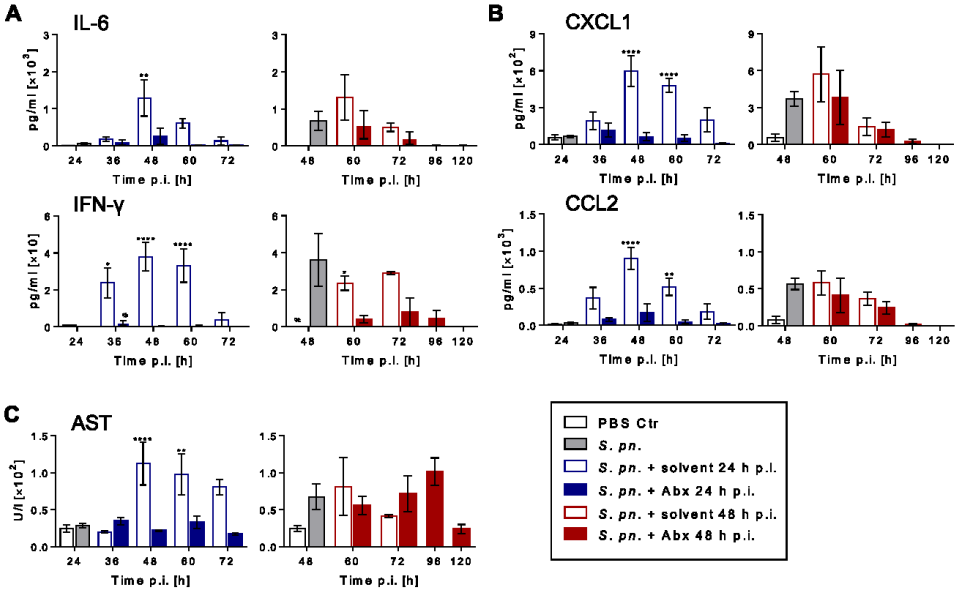


**Fig. 4** Early antibiotic treatment prevented systemic inflammation. Mice were infected with *S. pneumoniae* and assigned equally to groups and analysis time points ($n_{total} = 9$ per time point). Starting 24 h or 48 h p.i., intervention groups were treated with ampicillin. As controls, mice were sham infected (PBS; $n_{total} = 7$ per time point) or treated with solvent (0.9% NaCl). Mice surviving until designated analysis time point were sacrificed for blood sampling (number analyzed per time point presented in Additional file 1: Table S1). **a** Cytokine and **b** chemokine protein levels in serum measured by multiplex analysis. **c** Serum AST levels measured by Cobas 8000 C701. **a–c** Results pooled from three independent experiments per time point. Mean ± SEM. Two-way ANOVA/Sidak's multiple comparisons test for comparison of ampicillin versus solvent treatment. One-way ANOVA/Dunnett's multiple comparisons test for comparison to *S. pneumoniae*-infected mice at therapy start. *Significant difference between groups at time point, #significant difference from therapy start: $^{*/\#}p < 0.05$, $^{**}p < 0.01$ and $^{****}p < 0.0001$. Abx antibiotics, AST aspartate aminotransferase, Ctr control, IFN interferon, IL interleukin, PBS phosphate buffered saline, p.i. post infection, *S. pn. Streptococcus pneumoniae*

with this finding, histopathological analysis of lung tissue integrity revealed significantly reduced interstitial and alveolar edema formation in early antibiotic-treated animals compared to solvent-treated controls. However, late antibiotic therapy did not reduce edema formation (Fig. 5b, c, Additional file 2: Figures S3H and S10A, B). Vascular endothelial growth factor (VEGF) and binding leukocytes trigger destabilization of endothelial cell–cell contacts [31]. VEGF levels in BALF of *S. pneumoniae*-infected mice were modestly elevated compared to PBS-infected control groups at the time points 24 h and 48 h p.i. Only after early ampicillin therapy did alveolar VEGF concentrations significantly decrease compared to the late treatment start and solvent-treated control groups (Fig. 5d, Additional file 2: Figure S3G).

## Discussion

Upon CAP diagnosis, commencement of immediate treatment is considered critical since a delay increases the likelihood of lethality [7, 9]. However, some patients present themselves in a phase of advanced disease or diagnosis is belated. In these cases, antibiotic treatment can become insufficient to avoid development of acute lung injury; thus, adjuvant therapeutic options are needed. Understanding the pathophysiology of acute lung injury in pneumonia with delayed treatment is a prerequisite to successful therapy development. Therefore, we established a mouse model of CAP comprising early and late antibiotic treatment of bacterial pneumonia mirroring different treatment commencements in CAP patients. Validity of the model was achieved as: severe pneumonia was established before early and late treatment start; treatment success rates in terms of survival outcome depended on timely treatment; and antibiotic treatment efficacy in terms of bacterial elimination was independent of timely treatment. Our model settings are thus in line with observations made in immunocompetent ICU patients with CAP who received an adequate antibiotic regimen and management of comorbidities, but nonetheless showed high mortality rates [32, 33].

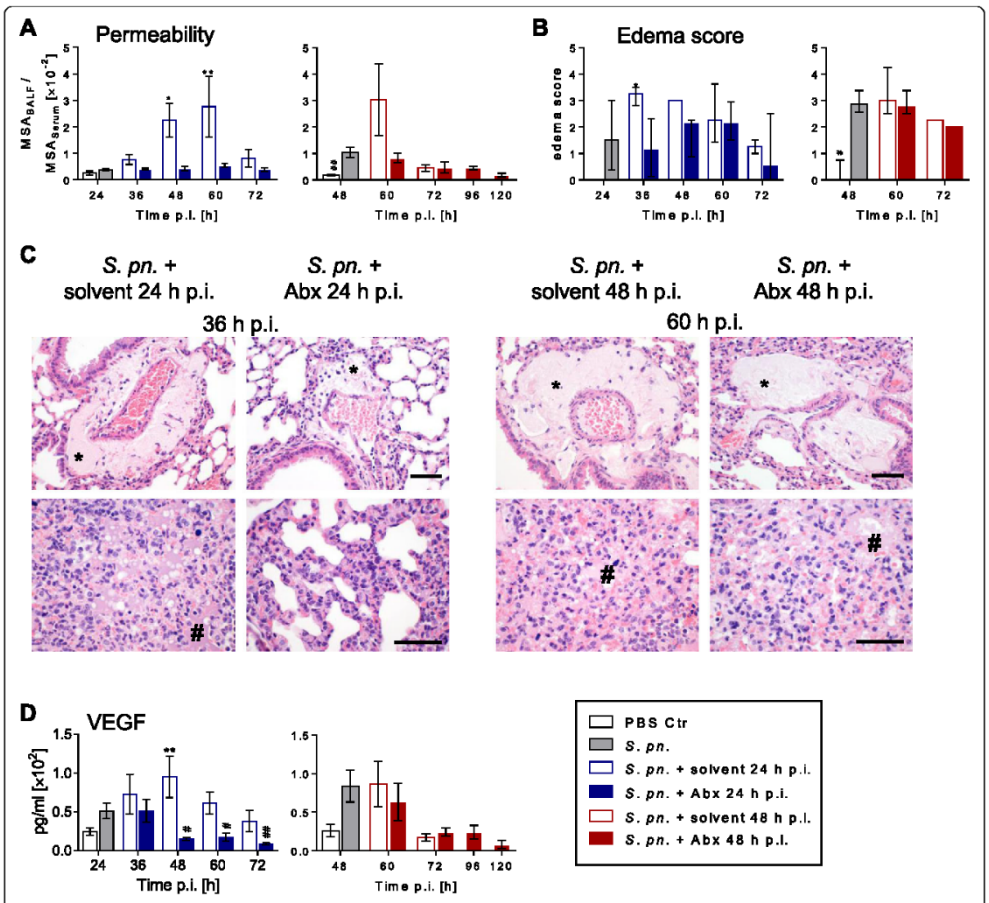


**Fig. 5** Early antibiotic treatment reduced lung barrier failure and VEGF levels. Mice were infected with *S. pneumoniae* and assigned equally to groups and analysis time points (**a**, **d** $n_{total} = 9$, **b**, **c** $n_{total} = 4$ per time point). Starting 24 h or 48 h p.i., intervention groups were treated with ampicillin. As controls, mice were sham infected (PBS; **a**, **d** $n_{total} = 7$, **b**, **c** $n_{total} = 4$ per time point) or treated with solvent (0.9% NaCl). Mice surviving until designated analysis time point were sacrificed for BAL and blood sampling (number analyzed per time point presented in Additional file 1: Table S1) or histopathological analysis (number analyzed per time point presented in Additional file 1: Table S2). **a** Ratios of mouse serum albumin (MSA) BALF/serum reflecting lung barrier integrity, calculated from ELISA readouts. **b** Lung edema score, calculated from specified histopathological parameters displaying perivascular and alveolar edema formation. Results pooled from two independent experiments per time point. Median and 25–75% interquartile range. **c** Representative H&E staining. *Perivascular edema, #alveolar edema. Scale bars: 100 μm. **d** VEGF levels measured in BAL fluid by multiplex analysis. **a**, **d** Results pooled from three independent experiments per time point. Mean ± SEM. Two-way ANOVA/Sidak's multiple comparisons test for comparison of ampicillin versus solvent treatment. **a**, **b** Kruskal–Wallis test/Dunn's multiple comparisons test and **d** one-way ANOVA/Dunnett's multiple comparisons test for comparison to *S. pneumoniae*-infected mice at therapy start. *Significant difference between groups at time point, #significant difference from therapy start: **a**, **b**, **d** $^{*/\#}p < 0.05$, $^{**/\#\#}p < 0.01$. Abx antibiotics, BALF bronchoalveolar lavage fluid, Ctr control, PBS phosphate buffered saline, p.i. post infection, *S. pn. Streptococcus pneumoniae*

Aiming to identify host-related factors responsible for detrimental disease outcome, we suspected an inadequate immune response, as described and reviewed by Mizgerd [34], as the underlying mechanism following late therapy. Indeed, histopathological analyses revealed that only late antibiotic treatment failed to reduce neutrophilic infiltration into the pleura and adjacent mediastinal adipose tissue. In contrast, recruitment of inflammatory cells into lung tissue and air spaces appeared unaffected by early and late antibiotic interventions but, nevertheless, alveolar

levels of inflammatory mediators were found to be repressed.

In order to assist interpreting these confounding observations, we implemented our data in a cytokine–cell network model. The network analysis illustrated that antibiotic treatment suppressed proinflammatory cytokines more efficiently than inflammatory chemokines (such as CXCL1, CXCL5 and GM-CSF). This indicates that recruiting mechanisms like chemokine gradients were less affected by antibiotic treatment. However, pronounced antibiotic-dependent reduction in inflammatory mediators suggests that, contrary to cellular numbers, the activation state and effector functions of alveolar immune cells were dampened by antibiotic-governed bacterial eradication.

An intact blood–air barrier is crucial for gas exchange, and fatal barrier breakdown during streptococcal pneumonia, leading to acute respiratory distress syndrome (ARDS), is well described (reviewed in [35–37]). Accordingly, we observed that an intact lung barrier was associated with favorable therapy outcome in antibiotic-treated mice exhibiting severe pneumococcal pneumonia. Furthermore, differences in survival correlated with extended exposure time to pneumococci, resulting in a prolonged local and systemic contact with infection-induced inflammatory mediators. In line, early as opposed to late treatment prevented systemic inflammation.

The evident local and systemic inflammation might as well have occurred due to release of proinflammatory cytosolic components upon cell death processes. Necroptosis, a form of programmed necrosis, can be initiated by *S. pneumoniae* in pulmonary immune cells like macrophages and epithelial cells [38, 39]. In our pneumonia model, alveolar macrophage numbers remained stable upon infection, whereas numbers of inflammatory macrophages significantly increased with infection time, without showing significant differences between treatment and control groups. Due to their slow replenishment rates [40], stable numbers of alveolar macrophages rather speak against necroptosis. Monocyte-derived macrophages that were actively recruited to infected lung tissue could potentially have undergone necroptosis and been replaced by newly recruited cells. To date, it remains likely but unproven that higher rates of monocyte-derived macrophage and epithelial cell necroptosis, following a late antibiotic regimen, are one of the underlying mechanisms for elevated inflammation and vascular leakage. Correspondingly, the presence of PAMPs as well as necroptosis-independent DAMPS could have likely regulated the activation status of local and systemic immune cells, thereby altering levels of inflammatory mediators following antibiotic intervention.

In severe pneumonia, only early antibiotic therapy, administered prior to barrier breakdown, prevented systemic inflammation, development of pleuritis, steatitis and elevated AST levels, which was followed up by restoration of fitness and rescue of mice from fatal outcome. Gracia et al. [41] have shown in *S. pneumoniae*-infected rats that early and late antibiotic regimens similarly eliminated bacterial burdens whereas only early therapy helped to prevent lung damage. However, the authors started early therapy just 1 h p.i., an important difference to our protocol whereby infected mice already developed pneumonia prior to antibiotic treatment. We therefore conclude that our model represents the patients' situation in a more compatible fashion.

Nonetheless, our mouse model remains a species-different approach to a highly complex human disease. It does not include therapeutic measures conducted in the ICU such as additional intake of fluids, (high flow) oxygen or macrolide therapy. Furthermore, laboratory mice which did not experience pathogen contact before generally show a modified immune response as humans do, for example, since they are missing mucosal memory cells [42]. Nevertheless, mice exhibited many parallels to the patients' course of infection; from a contained local infection, pneumonia developed into life-threatening systemic inflammation as often seen in CAP patients. Further studies from our laboratory likewise described processes in murine pneumonia which resembled the human course of pneumonia [43–45].

As a consequence, we stress the importance of defining CAP as an emergency and to identify and treat CAP patients at risk prior to lung barrier failure and systemic inflammation [13, 14, 46]. Besides many promising studies [47–52], specific adjunctive therapies for CAP are still missing. Such therapies should be coadministered with antibiotics in order to reduce lung barrier failure, thereby alleviating the disease course and finally reducing mortality and the length of hospital stay.

Our mouse model of antibiotic-treated CAP will aid in investigating how barrier-stabilizing interventions can prevent fatal disease progression in mice. Conclusively, proof-of-concept analyses indicating to which extent this mouse model adequately mirrors a significant range of patients must follow.

## Conclusions

By combining a mouse model of severe pneumococcal pneumonia with antibiotic treatment, we identified host factors of high relevance for successful therapy outcome. We were able to show that antibiotic treatment effectively reduces local pulmonary inflammation independent of treatment start and without beneficial effect on survival rates. However, despite being unable to reverse lung barrier dysfunction, lung edema and systemic inflammation once established, timely antibiotic intervention effectively prevented their development, significantly increasing survival. Handling CAP as an emergency along with new lung

barrier stabilizing therapies might thus aid in finally lowering mortality rates.

## Additional files

**Additional file 1:** Supplementary Materials and methods. **Table S1.** Total numbers of mice analyzed per group per analysis time point. **Table S2.** Total numbers of mice analyzed per group per histopathological analysis time point. **Table S3.** Murine pneumonia scoring system. **Figure S1.** Infection, antibiotic regimen and analysis time points (PDF 272 kb)

**Additional file 2: Figure S2.** Body temperature and histopathological analysis. **Figure S3.** Early versus late antibiotic regimen at 60 h and 72 h p.i. **Figure S4.** Innate immune cell gating strategy. **Figure S5.** Innate immune cell analysis in BAL and blood. **Figure S6.** Chemokine and cytokine levels in BAL fluid. **Figure S7.** Histopathological analysis of lung inflammation. **Figure S8.** Cytokine–cell network. **Figure S9.** Cytokine, chemokine and urea levels in serum. **Figure S10.** Histopathological analysis of edema development (PDF 1638 kb)

### Abbreviations

ARDS: Acute respiratory distress syndrome; AST: Aspartate aminotransferase; BAL: Bronchoalveolar lavage; BALF: Bronchoalveolar lavage fluid; CAP: Community-acquired pneumonia; CFU: Colony forming unit; ELISA: Enzyme-linked immunosorbent assay; G-CSF: Granulocyte colony-stimulating factor; GM-CSF: Granulocyte–macrophage colony-stimulating factor; H&E: Hematoxylin and eosin; ICU: Intensive care unit; IFN: Interferon; IL: Interleukin; MSA: Mouse serum albumin; p.i.: Post infection; PAMP: Pathogen-associated molecular pattern; PBS: Phosphate buffered saline; PMN: Polymorphonuclear leukocyte; TNF: Tumor necrosis factor; VEGF: Vascular endothelial growth factor

### Acknowledgements

*S. pneumoniae* PN36 was kindly provided by S. Hammerschmidt, University of Greifswald, Germany. Furthermore, the authors thank Angela Linke for excellent technical assistance with histological lung processing and Dres. Birgitt Gutbier and Katrin Reppe for managing the in-laboratory animal facilities.

### Funding

This work was supported by the German Federal Ministry of Education and Research (BMBF) within the framework of the e:Med research and funding concept (grant numbers 01ZX1304B to NS and MW, and 01ZX1304F to JV). The authors further acknowledge support from the German Research Foundation (DFG) (SFB-TR84 project B1 to NS, C3/C6/C9 to MW and Z1b to ADG). The funders had no role in the study design, data collection and analysis, decision to publish or preparation of the manuscript.

### Availability of data and materials

The datasets generated and analyzed during the current study are available from the corresponding author on reasonable request.

### Authors' contributions

SB and GN planned and performed experiments, supervised the study, analyzed the data and drafted the manuscript. MW and JL planned and supervised the study and drafted the manuscript. CG, S-MW and UB performed experiments and critically revised the manuscript for important intellectual content. SKG and JV performed network analysis and contributed to writing the manuscript. KD and ADG performed histological examination and contributed to writing the manuscript. NS was involved in the study design and participated in drafting the manuscript. All authors read and approved the final version of the manuscript.

### Ethics approval and consent to participate

All animal procedures were approved by local institutional (Charité — Universitätsmedizin Berlin) and governmental (Landesamt für Gesundheit und Soziales (LaGeSo) Berlin) authorities.

### Consent for publication

Not applicable.

### Competing interests

The authors declare that they have no competing interests.

## Publisher's Note



### Author details

[1]Division of Pulmonary Inflammation, Charité — Universitätsmedizin Berlin, corporate member of Freie Universität Berlin, Humboldt-Universität zu Berlin, and Berlin Institute of Health, Charitéplatz 1, 10117 Berlin, Germany. [2]Department of Dermatology, Laboratory of Systems Tumor Immunology, Friedrich-Alexander-Universität Erlangen-Nürnberg, Erlangen, Germany. [3]Department of Veterinary Pathology, Freie Universität Berlin, Berlin, Germany. [4]Department of Infectious Diseases and Respiratory Medicine, Charité — Universitätsmedizin Berlin, corporate member of Freie Universität Berlin, Humboldt-Universität zu Berlin, and Berlin Institute of Health, Berlin, Germany.

Received: 8 June 2018 Accepted: 9 October 2018
Published online: 01 November 2018

### References

1. Welte T, Torres A, Nathwani D. Clinical and economic burden of community-acquired pneumonia among adults in Europe. Thorax. 2012;67:71–9.
2. Woodhead M, Blasi F, Ewig S, Garau J, Huchon G, Ieven M, Ortqvist A, Schaberg T, Torres A, van der Heijden G, Read R, Verheij TJ. Guidelines for the management of adult lower respiratory tract infections—full version. Clin Microbiol Infect. 2011;17(Suppl 6):E1–E59.
3. Ludwig E, Bonanni P, Rohde G, Sayiner A, Torres A. The remaining challenges of pneumococcal disease in adults. Eur Respir Rev. 2012;21:57–65.
4. Angus DC, Marrie TJ, Obrosky DS, Clermont G, Dremsizov TT, Coley C, Fine MJ, Singer DE, Kapoor WN. Severe community-acquired pneumonia: use of intensive care services and evaluation of American and British Thoracic Society Diagnostic criteria. Am J Respir Crit Care Med. 2002;166:717–23.
5. Kellum JA, Kong L, Fink MP, Weissfeld LA, Yealy DM, Pinsky MR, Fine J, Krichevsky A, Delude RL, Angus DC. Understanding the inflammatory cytokine response in pneumonia and sepsis: results of the Genetic and Inflammatory Markers of Sepsis (GenIMS) Study. Arch Intern Med. 2007;167:1655–63.
6. Woodhead M, Welch CA, Harrison DA, Bellingan G, Ayres JG. Community-acquired pneumonia on the intensive care unit: secondary analysis of 17,869 cases in the ICNARC Case Mix Programme Database. Crit Care. 2006; 10(Suppl 2):S1.
7. Houck PM, Bratzler DW, Nsa W, Ma A, Bartlett JG. Timing of antibiotic administration and outcomes for Medicare patients hospitalized with community-acquired pneumonia. Arch Intern Med. 2004;164:637–44.
8. Daniel P, Rodrigo C, McKeever TM, Woodhead M, Welham S, Lim WS, British Thoracic Society. Time to first antibiotic and mortality in adults hospitalised with community-acquired pneumonia: a matched-propensity analysis. Thorax. 2016;71:568–70.
9. Phua J, Dean NC, Guo Q, Kuan WS, Lim HF, Lim TK. Severe community-acquired pneumonia: timely management measures in the first 24 hours. Crit Care. 2016;20:237.
10. Renaud B, Santin A, Coma E, Camus N, Van Pelt D, Hayon J, Gurgui M, Roupie E, Herve J, Fine MJ, Brun-Buisson C, Labarere J. Association between timing of intensive care unit admission and outcomes for emergency department patients with community-acquired pneumonia. Crit Care Med. 2009;37:2867–74.
11. Lim HF, Phua J, Mukhopadhyay A, Ngerng WJ, Chew MY, Sim TB, Kuan WS, Mahadevan M, Lim TK. IDSA/ATS minor criteria aid pre-intensive care unit resuscitation in severe community-acquired pneumonia. Eur Respir J. 2014; 43:852–62.
12. Gattarello S, Borgatta B, Solé-Violán J, Vallés J, Vidaur L, Zaragoza R, Torres A, Rello J. Decrease in mortality in severe community-acquired pneumococcal pneumonia: impact of improving antibiotic strategies (2000-2013). Chest. 2014;146:22–31.
13. Ewig S, Torres A. Community-acquired pneumonia as an emergency: time for an aggressive intervention to lower mortality. Eur Respir J. 2011;38:253–60.
14. Kolditz M, Ewig S, Klapdor B, Schutte H, Winning J, Rupp J, Suttorp N, Welte T, Rohde G. Community-acquired pneumonia as medical emergency: predictors of early deterioration. Thorax. 2015;70:551–8.

15. Witzenrath M, Gutbier B, Hocke AC, Schmeck B, Hippenstiel S, Berger K, Mitchell TJ, de los Toyos JR, Rosseau S, Suttorp N, Schutte H. Role of pneumolysin for the development of acute lung injury in pneumococcal pneumonia. Crit Care Med. 2006;34:1947–54.
16. Rigor RR, Shen Q, Pivetti CD, Wu MH, Yuan SY. Myosin light chain kinase signaling in endothelial barrier dysfunction. Med Res Rev. 2013;33:911–33.
17. Tauseef M, Knezevic N, Chava KR, Smith M, Sukriti S, Gianaris N, Obukhov AG, Vogel SM, Schraufnagel DE, Dietrich A, Birnbaumer L, Malik AB, Mehta D. TLR4 activation of TRPC6-dependent calcium signaling mediates endotoxin-induced lung vascular permeability and inflammation. J Exp Med. 2012;209:1953–68.
18. Gavard J, Gutkind JS. VEGF controls endothelial-cell permeability by promoting the beta-arrestin-dependent endocytosis of VE-cadherin. Nat Cell Biol. 2006;8:1223–34.
19. Bachofen M, Weibel ER. Alterations of the gas exchange apparatus in adult respiratory insufficiency associated with septicemia. Am Rev Respir Dis. 1977;116:589–615.
20. Nouailles G, Dorhoi A, Koch M, Zerrahn J, Weiner J 3rd, Fae KC, Arrey F, Kuhlmann S, Bandermann S, Loewe D, et al. CXCL5-secreting pulmonary epithelial cells drive destructive neutrophilic inflammation in tuberculosis. J Clin Invest. 2014;124:1268–82.
21. Bhowmick R, Tin Maung NH, Hurley BP, Ghanem EB, Gronert K, McCormick BA, Leong JM. Systemic disease during Streptococcus pneumoniae acute lung infection requires 12-lipoxygenase-dependent inflammation. J Immunol. 2013;191:5115–23.
22. Moreland JG, Bailey G, Nauseef WM, Weiss JP. Organism-specific neutrophil-endothelial cell interactions in response to Escherichia coli, Streptococcus pneumoniae, and Staphylococcus aureus. J Immunol. 2004;172:426–32.
23. Kevil CG, Oshima T, Alexander B, Coe LL, Alexander JS. H(2)O(2)-mediated permeability: role of MAPK and occludin. Am J Physiol Cell Physiol. 2000; 279:C21–30.
24. van Wetering S, van Buul JD, Quik S, Mul FP, Anthony EC, ten Klooster JP, Collard JG, Hordijk PL. Reactive oxygen species mediate Rac-induced loss of cell-cell adhesion in primary human endothelial cells. J Cell Sci. 2002;115: 1837–46.
25. Laterre PF, Garber G, Levy H, Wunderink R, Kinasewitz GT, Sollet JP, Maki DG, Bates B, Yan SC, Dhainaut JF. Severe community-acquired pneumonia as a cause of severe sepsis: data from the PROWESS study. Crit Care Med. 2005; 33:952–61.
26. Saleh M, Abdullah MR, Schulz C, Kohler T, Pribyl T, Jensch I, Hammerschmidt S. Following in real time the impact of pneumococcal virulence factors in an acute mouse pneumonia model using bioluminescent bacteria. J Vis Exp. 2014;84:e51174.
27. Dames C, Akyuz L, Reppe K, Tabeling C, Dietert K, Kershaw O, Gruber AD, Meisel C, Meisel A, Witzenrath M, Engel O. Miniaturized bronchoscopy enables unilateral investigation, application, and sampling in mice. Am J Respir Cell Mol Biol. 2014;51:730–7.
28. Reppe K, Radunzel P, Dietert K, Tschernig T, Wolff T, Hammerschmidt S, Gruber AD, Suttorp N, Witzenrath M. Pulmonary immunostimulation with MALP-2 in influenza virus-infected mice increases survival after pneumococcal superinfection. Infect Immun. 2015;83:4617–29.
29. Quinton LJ, Mizgerd JP. Dynamics of lung defense in pneumonia: resistance, resilience, and remodeling. Annu Rev Physiol. 2015;77:407–30.
30. Mei J, Liu Y, Dai N, Favara M, Greene T, Jeyaseelan S, Poncz M, Lee JS, Worthen GS. CXCL5 regulates chemokine scavenging and pulmonary host defense to bacterial infection. Immunity. 2010;33:106–17.
31. Broermann A, Winderlich M, Block H, Frye M, Rossaint J, Zarbock A, Cagna G, Linnepe R, Schulte D, Nottebaum AF, Vestweber D. Dissociation of VE-PTP from VE-cadherin is required for leukocyte extravasation and for VEGF-induced vascular permeability in vivo. J Exp Med. 2011;208:2393–401.
32. Rodríguez A, Lisboa T, Blot S, Martin-Loeches I, Sole-Violan J, De Mendoza D, Rello J. Mortality in ICU patients with bacterial community-acquired pneumonia: when antibiotics are not enough. Intensive Care Med. 2009;35:430–8.
33. File TM Jr. Optimal treatment strategies for community-acquired pneumonia: non-responders to conventional regimens. Chemotherapy. 2001;47(Suppl 4):11–8.
34. Mizgerd JP. Acute lower respiratory tract infection. N Engl J Med. 2008;358: 716–27.
35. Matthay MA, Zemans RL. The acute respiratory distress syndrome: pathogenesis and treatment. Annu Rev Pathol. 2011;6:147–63.
36. Muller-Redetzky HC, Suttorp N, Witzenrath M. Dynamics of pulmonary endothelial barrier function in acute inflammation: mechanisms and therapeutic perspectives. Cell Tissue Res. 2014;355:657–73.
37. Ware LB, Matthay MA. The acute respiratory distress syndrome. N Engl J Med. 2000;342:1334–49.
38. Coleman FT, Blahna MT, Kamata H, Yamamoto K, Zabinski MC, Kramnik I, Wilson AA, Kotton DN, Quinton LJ, Jones MR, et al. Capacity of pneumococci to activate macrophage nuclear factor κB: influence on necroptosis and pneumonia severity. J Infect Dis. 2017;216:425–35.
39. González-Juarbe N, Bradley KM, Shenoy AT, Gilley RP, Reyes LF, Hinojosa CA, Restrepo MI, Dube PH, Bergman MA, Orihuela CJ. Pore-forming toxin-mediated ion dysregulation leads to death receptor-independent necroptosis of lung epithelial cells during bacterial pneumonia. Cell Death Differ. 2017;24:917–28.
40. Maus UA, Janzen S, Wall G, Srivastava M, Blackwell TS, Christman JW, Seeger W, Welte T, Lohmeyer J. Resident alveolar macrophages are replaced by recruited monocytes in response to endotoxin-induced lung inflammation. Am J Respir Cell Mol Biol. 2006;35:227–35.
41. Gracia M, Martinez-Marin C, Huelves L, Gimenez MJ, Aguilar L, Carcas A, Ponte C, Soriano F. Pulmonary damage and bacterial load in assessment of the efficacy of simulated human treatment-like amoxicillin (2,000 milligrams) therapy of experimental pneumococcal pneumonia caused by strains for which amoxicillin MICs differ. Antimicrob Agents Chemother. 2005;49(3): 996–1001.
42. Beura LK, Hamilton SE, Bi K, Schenkel JM, Odumade OA, Casey KA, Thompson EA, Fraser KA, Rosato PC, Filali-Mouhim A, et al. Normalizing the environment recapitulates adult human immune traits in laboratory mice. Nature. 2016;532(7600):512–6.
43. Muller-Redetzky HC, Will D, Hellwig K, Kummer W, Tschernig T, Pfeil U, Paddenberg R, Menger MD, Kershaw O, Gruber AD, et al. Mechanical ventilation drives pneumococcal pneumonia into lung injury and sepsis in mice: protection by adrenomedullin. Crit Care. 2014;18:R73.
44. Gutbier B, Neuhauss AK, Reppe K, Ehrler C, Santel A, Kaufmann J, Scholz M, Weisssmann N, Morawietz L, Mitchell TJ, et al. Prognostic and pathogenic role of angiopoietin-1 and -2 in pneumonia. Am J Respir Crit Care Med. 2018. https://doi.org/10.1164/rccm.201708-1733OC.
45. Witzenrath M, Schmeck B, Doehn JM, Tschernig T, Zahlten J, Loeffler JM, Zemlin M, Muller H, Gutbier B, Schutte H, et al. Systemic use of the endolysin Cpl-1 rescues mice with fatal pneumococcal pneumonia. Crit Care Med. 2009;37:642–9.
46. Kolditz M, Tesch F, Mocke L, Hoffken G, Ewig S, Schmitt J. Burden and risk factors of ambulatory or hospitalized CAP: a population based cohort study. Respir Med. 2016;121:32–8.
47. Fan H, Goodwin AJ, Chang E, Zingarelli B, Borg K, Guan S, Halushka PV, Cook JA. Endothelial progenitor cells and a stromal cell-derived factor-1alpha analogue synergistically improve survival in sepsis. Am J Respir Crit Care Med. 2014;189:1509–19.
48. Gutbier B, Jiang X, Dietert K, Ehrler C, Lienau J, Van Slyke P, Kim H, Hoang VC, Maynes JT, Dumont DJ, et al. Vasculotide reduces pulmonary hyperpermeability in experimental pneumococcal pneumonia. Crit Care. 2017;21:274.
49. Nie W, Zhang Y, Cheng J, Xiu Q. Corticosteroids in the treatment of community-acquired pneumonia in adults: a meta-analysis. PLoS One. 2012; 7:e47926.
50. Anderson R, Steel HC, Cockeran R, Smith AM, von Gottberg A, de Gouveia L, Brink A, Klugman KP, Mitchell TJ, Feldman C. Clarithromycin alone and in combination with ceftriaxone inhibits the production of pneumolysin by both macrolide-susceptible and macrolide-resistant strains of Streptococcus pneumoniae. J Antimicrob Chemother. 2007;59:224–9.
51. Torres A, Sibila O, Ferrer M, Polverino E, Menendez R, Mensa J, Gabarrus A, Sellares J, Restrepo MI, Anzueto A, et al. Effect of corticosteroids on treatment failure among hospitalized patients with severe community-acquired pneumonia and high inflammatory response: a randomized clinical trial. JAMA. 2015;313:677–86.
52. Bergeron Y, Ouellet N, Simard M, Olivier M, Bergeron MG. Immunomodulation of pneumococcal pulmonary infection with N(G)-monomethyl-L-arginine. Antimicrob Agents Chemother. 1999;43:2283–90.

## 2.3 COVID-19: Immunabwehr und Therapieevaluation in Syrischen Hamstern

COVID-19 stellte nicht nur die Gesellschaft, sondern auch die Forschung vor besondere Herausforderungen. Die dringende Notwendigkeit, Behandlungsmethoden und Impfstoffe gegen COVID-19 zu entwickeln, verlangte in bisher nicht gekannter Geschwindigkeit Erkenntnisse zu erzielen. Erschwerend kam hinzu, dass die gängigste experimentelle Tierspezies *Mus musculus* gegen SARS-CoV-2 resistent ist. Die genetische Expression von humanem Angiotensin-konvertierendem Enzym 2 (hACE2) unter dem humanen Keratin 18 Promotor (K18) machte die K18-hACE2 transgenen Mäuse sehr anfällig, aber sie zeigten keine typischen COVID-19-Pneumonien[72,73]. Nicht-resistente Tiermodelle, die die menschlichen COVID-19 Verläufe gut reproduzieren, sind Rhesusaffen, Frettchen und syrische Hamster[74].

Anhand von Patienten- und Bevölkerungsstudien zeigte sich bald, dass schwere COVID-19-Verläufe in bestimmten Bevölkerungsgruppen gehäuft auftreten, z. B. bei älteren Erwachsenen und Personen mit Grunderkrankungen[75]. Bestimmte genetische Faktoren der Immunantwort auf das Virus spielen ebenfalls eine Rolle und insbesondere schwere und kritische COVID-19 Verläufe sind durch eine Immunpathologie gekennzeichnet[76,77]. Diese überschießende Immunantwort wird durch Entzündungszellen wie Neutrophile und Monozyten ausgelöst. Als Folge der Entzündungsreaktion kommt es zu Gewebe- und Organschäden sowie zum akuten Lungenversagen wie beim ARDS, einer schweren Lungenschädigung, die letal verlaufen kann. Immunmodulatoren wie Dexamethason können die Schwere der Erkrankung mildern[78-81].

Das Verständnis von vorteilhaften und pathologischen Immunantworten ist für die Entwicklung und Prüfung wirksamer Therapien und Impfstoffe von entscheidender Bedeutung. Dies erfordert einerseits gut charakterisierte Tiermodelle und andererseits die Validierung anhand menschlicher Immunantworten[82].

Der Syrische Hamster (*Mesocricetus auratus*) ist ein geeignetes Modell zur Abbildung moderater COVID-19 Verläufe, war aber zu Beginn der Pandemie immunologisch kaum charakterisiert[83-85]. Hierfür fehlten auch die klassischen immunologischen Werkzeuge, Hamster-spezifische Antikörper, die zur Identifizierung von Immunzellen mittels Durchflusszytometrie oder Immunhistopathologie verwendet werden. Unser Beitrag zur COVID-19-Forschung konzentrierte sich daher zunächst auf die Charakterisierung der Immunantwort im Syrischen Hamster mittels Einzelzell-Transkriptomanalysen[86]. Anschließend haben wir die hier gewonnenen Erkenntnisse auf andere Hamstermodelle mit schweren Verläufen übertragen und den Erfolg von Therapiestrategien und Impfstoffen evaluiert[87,88].

Im Folgenden werden zwei ausgewählte eigene Studien vorgestellt, die zum einen die hocheffektive moderate angeborene und adaptive Immunantwort des Syrischen Hamsters[86] und zum anderen die Reaktivierung der lokalen Gedächtnisimmunantwort gegen SARS-CoV-2 nach nasaler Impfung mit einem neuartigen Lebendimpfstoff im Syrischen Hamster[87] auf der Basis von Einzelzell-Transkriptomanalysen beschreiben.

### 2.3.1 Immunantwort gegen SARS-CoV-2 beim Syrischen Hamster (Eigene Arbeit 4)

Veröffentlicht als: Forschungsartikel mit geteilter Erstautorschaft*.

Der nachfolgende Text entspricht dem originalsprachlichen Abstrakt der Arbeit "*Temporal omics analysis in Syrian hamsters unravel cellular effector responses to moderate COVID-19.*" (Nat Commun. 2021 Aug 11;12(1):4869. doi: 10.1038/s41467-021-25030-7)[86] der Autoren **Geraldine Nouailles***, Emanuel Wyler*, Peter Pennitz, Dylan Postmus, Daria Vladimirova, Julia Kazmierski, Fabian Pott, Kristina Dietert, Michael Muelleder, Vadim Farztdinov, Benedikt Obermayer, Sandra-Maria Wienhold, Sandro Andreotti, Thomas Hoefler, Birgit Sawitzki, Christian Drosten, Leif E Sander, Norbert Suttorp, Markus Ralser, Dieter Beule, Achim D Gruber, Christine Goffinet, Markus Landthaler, Jakob Trimpert, und Martin Witzenrath.

> "In COVID-19, immune responses are key in determining disease severity. However, cellular mechanisms at the onset of inflammatory lung injury in SARS-CoV-2 infection, particularly involving endothelial cells, remain ill-defined. Using Syrian hamsters as a model for moderate COVID-19, we conduct a detailed longitudinal analysis of systemic and pulmonary cellular responses, and corroborate it with datasets from COVID-19 patients. Monocyte-derived macrophages in lungs exert the earliest and strongest transcriptional response to infection, including induction of pro-inflammatory genes, while epithelial cells show weak alterations. Without evidence for productive infection, endothelial cells react, depending on cell subtypes, by strong and early expression of anti-viral, pro-inflammatory, and T cell recruiting genes. Recruitment of cytotoxic T cells as well as emergence of IgM antibodies precede viral clearance at day 5 post infection. Investigating SARS-CoV-2 infected Syrian hamsters thus identifies cell type-specific effector functions, providing detailed insights into pathomechanisms of COVID-19 and informing therapeutic strategies."

nature COMMUNICATIONS

ARTICLE

https://doi.org/10.1038/s41467-021-25030-7 OPEN

# Temporal omics analysis in Syrian hamsters unravel cellular effector responses to moderate COVID-19

Geraldine Nouailles[1,2,17✉], Emanuel Wyler[3,17✉], Peter Pennitz[1], Dylan Postmus[2,4], Daria Vladimirova[5], Julia Kazmierski[2,4], Fabian Pott[2,4], Kristina Dietert[6,7], Michael Muelleder[8], Vadim Farztdinov[8], Benedikt Obermayer[9], Sandra-Maria Wienhold[1], Sandro Andreotti[10], Thomas Hoefler[5], Birgit Sawitzki[11], Christian Drosten[4], Leif E. Sander[12], Norbert Suttorp[12], Markus Ralser[13,14], Dieter Beule[9], Achim D. Gruber[6], Christine Goffinet[2,4], Markus Landthaler[3,15], Jakob Trimpert[5,18✉] & Martin Witzenrath[1,12,16,18✉]

In COVID-19, immune responses are key in determining disease severity. However, cellular mechanisms at the onset of inflammatory lung injury in SARS-CoV-2 infection, particularly involving endothelial cells, remain ill-defined. Using Syrian hamsters as a model for moderate COVID-19, we conduct a detailed longitudinal analysis of systemic and pulmonary cellular responses, and corroborate it with datasets from COVID-19 patients. Monocyte-derived macrophages in lungs exert the earliest and strongest transcriptional response to infection, including induction of pro-inflammatory genes, while epithelial cells show weak alterations. Without evidence for productive infection, endothelial cells react, depending on cell subtypes, by strong and early expression of anti-viral, pro-inflammatory, and T cell recruiting genes. Recruitment of cytotoxic T cells as well as emergence of IgM antibodies precede viral clearance at day 5 post infection. Investigating SARS-CoV-2 infected Syrian hamsters thus identifies cell type-specific effector functions, providing detailed insights into patho-mechanisms of COVID-19 and informing therapeutic strategies.

[1] Charité – Universitätsmedizin Berlin, Corporate Member of Freie Universität Berlin and Humboldt-Universität zu Berlin, Division of Pulmonary Inflammation, Berlin, Germany. [2] Berlin Institute of Health (BIH), Berlin, Germany. [3] Berlin Institute for Medical Systems Biology (BIMSB), Max Delbrück Center for Molecular Medicine in the Helmholtz Association (MDC), Berlin, Germany. [4] Charité – Universitätsmedizin Berlin, Corporate Member of Freie Universität Berlin and Humboldt-Universität zu Berlin, Institute of Virology, Berlin, Germany. [5] Institute of Virology, Freie Universität Berlin, Berlin, Germany. [6] Institute of Veterinary Pathology, Freie Universität Berlin, Berlin, Germany. [7] Veterinary Centre for Resistance Research, Freie Universität Berlin, Berlin, Germany. [8] Charité – Universitätsmedizin Berlin, Corporate Member of Freie Universität Berlin and Humboldt-Universität zu Berlin, Core Facility – High-Throughput Mass Spectrometry, Berlin, Germany. [9] Berlin Institute of Health at Charité – Universitätsmedizin Berlin, Core Unit Bioinformatics, Berlin, Germany. [10] Bioinformatics Solution Center, Freie Universität Berlin, Berlin, Germany. [11] Charité – Universitätsmedizin Berlin, Corporate Member of Freie Universität Berlin and Humboldt-Universität zu Berlin, Institute of Medical Immunology, Berlin, Germany. [12] Charité – Universitätsmedizin Berlin, Corporate Member of Freie Universität Berlin and Humboldt-Universität zu Berlin, Department of Infectious Diseases and Respiratory Medicine, Berlin, Germany. [13] The Francis Crick Institute, Molecular Biology of Metabolism Laboratory, London, UK. [14] Charité – Universitätsmedizin Berlin, Corporate Member of Freie Universität Berlin and Humboldt-Universität zu Berlin, Department of Biochemistry, Berlin, Germany. [15] IRI Life Sciences, Institute for Biology, Humboldt-Universität zu Berlin, Berlin, Germany. [16] German Center for Lung Research (DZL), Berlin, Germany. [17] These authors contributed equally: Geraldine Nouailles, Emanuel Wyler. [18] These authors jointly supervised this work: Jakob Trimpert, Martin Witzenrath. ✉email: geraldine.nouailles@charite.de; emanuel.wyler@mdc-berlin.de; jakob.trimpert@fu-berlin.de; martin.witzenrath@charite.de

The enduring severe acute respiratory syndrome coronavirus 2 (SARS-CoV-2) pandemic has emphasized the urgent need for experimental models to rapidly identify pathomechanisms and therapeutic targets of corona virus disease 2019 (COVID-19).

COVID-19 causes a wide range of disease manifestations, spanning from asymptomatic infections to acute respiratory distress syndrome (ARDS) and fatal multi-organ dysfunction[1]. Disease severity is influenced by age, sex, and specific comorbidities, making it evident that host-specific factors influence the course of the disease and require further investigation. While blood of COVID-19 patients is accessible to detailed longitudinal investigation irrespective of disease severity, and bronchoalveolar lavage (BAL) can be safely performed in intubated patients, pulmonary tissue responses remain inaccessible in mild and moderate COVID-19 courses, since lung tissue is only available upon autopsy from patients with fatal disease. Hence, experimental models of COVID-19 are needed, which reflect the complexity of human responses to SARS-CoV-2 infections, including the spatiotemporal dynamics of airway and alveolar infection, local pulmonary immune responses, the activation of systemic inflammatory, complement and coagulation cascades, the impairment of endothelial barrier function, and also mechanisms of resilience, resolution, and repair.

The hamster family (Cricetinae) is of particular interest for experimental modeling of COVID-19, as we and others have observed that animals without genetic modifications can be infected with SARS-CoV-2 and develop phenotypes ranging from mild to lethal COVID-19, depending on age and species[2–6]. Notably, immune cell influx into the lungs, bronchointerstitial pneumonia and diffuse alveolar damage in hamsters bear resemblance to COVID-19 in human patients[7–9].

Since its initial description as animal model for SARS-CoV[10], the Syrian hamster has been used to study different aspects of SARS-CoV and Middle East respiratory syndrome (MERS) coronavirus infection[11–13]. Consequently, it now serves as a versatile non-transgenic rodent model to study SARS-CoV-2 infection and therapeutic interventions such as antiviral treatments, immunomodulatory therapies, and vaccines[3,7,14]. The disease observed in hamster species primarily affects the lower respiratory tract, which more closely resembles the common courses of human disease as opposed to clinically severely affected transgenic mice, in many of which infection of the central nervous system (CNS) is the predominant manifestation of the disease[15,16].

Despite the advantages of hamster models for investigating COVID-19 pathogenesis, unavailability of molecular tools and reagents for hamsters limits investigations of immuno-pathomechanisms, leaving unanswered how closely SARS-CoV-2 evoked disease in hamsters models human COVID-19. We therefore in-depth evaluated SARS-CoV-2-infected Syrian hamsters (*Mesocricetus auratus*), elucidating the innate and adaptive steps of immunity and pathogenesis by pairing single-cell RNA sequencing (scRNA-Seq) data from lung cells and white blood cells (WBC), histopathology and quantitative proteomics analysis of lungs and blood following nasal SARS-CoV-2-infection of *Mesocricetus auratus*. We compared our findings with own data from scRNA-Seq and proteomics analyses from human biosamples of COVID-19 patients. This enabled in-depth investigations on central COVID-19 pathomechanisms in compartments inaccessible in humans, particularly in moderate disease.

In this work, we show that (i) monocyte-derived macrophages in lungs are exerting the earliest and strongest transcriptional response to infection, (ii) epithelial cells show weak alterations, (iii) early in the infection, endothelial cells strongly express antiviral, pro-inflammatory, and T cell recruiting genes without evidence for productive infection, and (iv) recruitment of cytotoxic T cells, as well as emergence of IgM antibodies, precedes viral clearance at day 5 post infection.

## Results

**SARS-CoV-2 induces self-resolving moderate pneumonia and robust pulmonary immune cell recruitment in Syrian hamsters**. After infection with SARS-CoV-2 (Supplementary Fig. 1), clinical disease manifested in Syrian hamsters with moderate transient weight loss analogous to previous reports (refs. [2,3,6], Supplementary Fig. 2a). High viral loads were detected in respiratory tracts at 2, 3, and 5 days post infection (dpi). At 14 dpi, only minimal viral RNA load remained, and no replication-competent virus was detected in the respiratory tract (Supplementary Fig. 2b–d).

Similar to previous observations[2,9], histopathology identified necrosuppurative bronchitis and bronchointerstitial pneumonia at 2 and 3 dpi, characterized by intrabronchial and intraalveolar infiltration by neutrophils and macrophages as well as severe, diffuse alveolar damage. Numbers and density of infiltrating immune cells, hyperplasia of bronchial and alveolar epithelial cells as well as alveolar and interstitial edema and endothelialitis peaked at 5 dpi. By 14 dpi, cellular influx into alveolar spaces was largely resolved, with fewer neutrophils, macrophages, and lymphocytes observed within the interalveolar septa, while marked hyperplasia of alveolar epithelial cells remained (Supplementary Fig. 2e–n). Again, consistent with previous reports[2,9] no evidence of thrombotic events were observed.

To obtain higher resolution of pulmonary responses, we performed scRNA-Seq. Cell type clusters detected in lungs corresponding to leukocyte-subset-signatures included alveolar, interstitial, and monocytic macrophages, *Treml4*$^{+}$-monocytes, neutrophils, dendritic cells, B, T, and natural killer (NK) cells. We further identified resident cell types, including alveolar epithelial cells type 1 (AT1) and 2 (AT2), ciliated epithelial, endothelial, and smooth muscle cells, and fibroblasts (Figs. 1a, S3a). By integrating scRNA-Seq-derived cell frequencies with manually counted cell numbers over time, we mapped dynamics of infection-induced pulmonary leukocyte recruitment compared to uninfected animals (Fig. 1b, c). The influx of monocyte-derived macrophages peaked at 5 dpi. NK and T lymphocyte recruitment to lungs was first detected at 5 dpi and peaked at day 14 (Fig. 1c). Peak of lung inflammation on 5 dpi (Supplementary Fig. 2l) coincided with the highest proportion of inflammatory macrophages (monocytic macrophage cluster) and proliferating cytotoxic cells (T/NK cell cluster) among lung cells (Supplementary Fig. 3b).

Notably, despite pronounced neutrophilic bronchitis (Supplementary Fig. 2g), overall neutrophil frequencies remained low and changes were non-significant. In line with histopathology, the peak of neutrophil recruitment was at 2 dpi, when neutrophil proportions presented ~3% of lung cells (Fig. 1e). In contrast, monocytic macrophages population at day 5 peaked at ~25% of lung cells (Figs. 1d, e, S3b). Relative numbers of pulmonary tissue cell subsets fluctuated mildly, declining proportionally as inflammatory cell influx rose (Supplementary Fig. 3c, d). At 14 dpi, increased numbers of AT2 matched histopathology observations of epithelial hyperplasia, indicating tissue repair (Supplementary Figs. 2i, k, 3c).

Analogously, we analyzed scRNA-Seq data from WBC populations to study systemic responses evoked by pulmonary SARS-CoV-2 infection. Detected cell populations included neutrophils, monocytes, dendritic, NK, B, and T cells and various subpopulations thereof (Figs. 1f, S3e). Infected hamsters displayed significant leukopenia at 3 and 5 dpi. By 14 dpi this trend

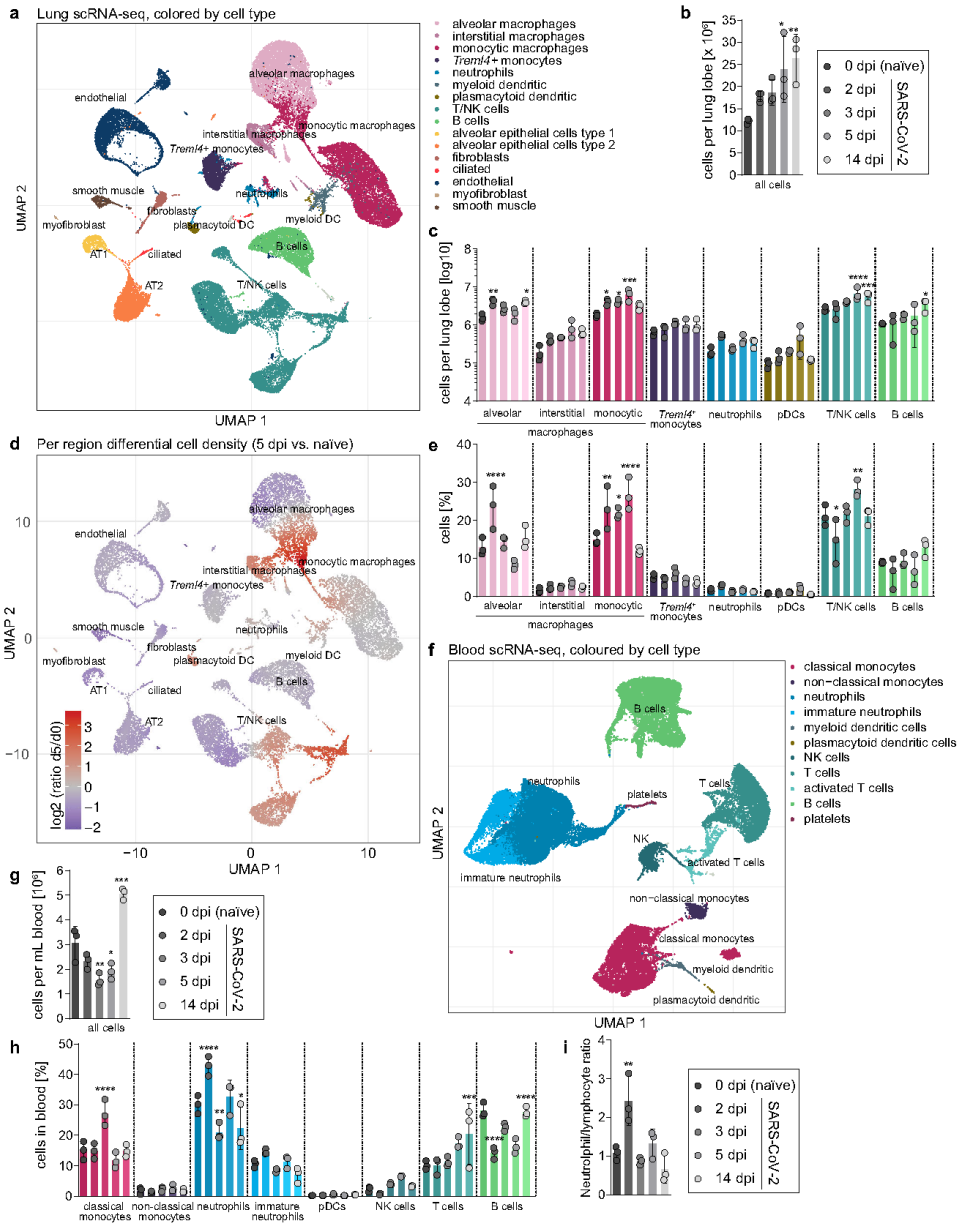


was inverted and peripheral blood leukocyte numbers were significantly higher than in naive animals (Figs. 1g, S3f). Increased proportions of neutrophils were found at 2 dpi and increasing proportions of T cells at 14 dpi (Figs. 1h, S3b). Notably, calculated neutrophil–lymphocyte ratios only transiently increased at 2 dpi to a minor extent, matching observations in humans with non-severe as opposed to severe COVID-19[17,18] (Fig. 1i). Overall, scRNA-Seq cell profiling defined kinetics of immune cell trafficking in greater detail.

**Bulk transcriptomics, proteomics, and single-cell RNA sequencing reveal activation of anti-SARS-CoV-2 pro-inflammatory immunity in hamsters**. After evaluating immune cell dynamics, we performed bulk RNA-sequencing of lungs and

**Fig. 1 Single-cell dynamics in lungs and blood of SARS-CoV-2 infected Syrian hamsters.** **a** Uniform manifold approximation and projection (UMAP) plot of identified cell populations in Syrian hamster lungs. Colors representing individual cell types are depicted in legend. **b** Cell count of isolated cells per lung lobe over time (2, 3, 5, and 14 days post infection (dpi)) and control group (naive, "d0"). **c** Count of hematopoietic cells per lung lobe in naive hamsters and over time pi. **d** Changes in cellular density of lung cells in UMAP projection. Coloration indicates log2 fold change between control group and 5 dpi. **e** Percentage of hematopoietic cells per lung lobe in naive hamsters and over time pi. **f** UMAP plot of identified cell populations in blood samples. **g** Cell count of isolated cells per mL blood in naive hamsters and over time pi. **h** Percentage of identified cell populations in blood samples over time pi and naive animals. **i** Neutrophil-lymphocyte ratio in blood samples over time pi and naive animals. **a**, **d** and **f** Clusters defined by Louvain clustering, $n = 3$ per time point. **b**, **c**, **e**, **g**, **h** and **i** Bar plots are plotted per cell type in the order: naive, 2 dpi, 3 dpi, 5 dpi, and 14 dpi (colors fade from dark to light). Data display means ± SD. $n = 3$ per time point. Ordinary one-way ANOVA, Dunnett's (**b**, **g**, **i**) and Šídák's multiple comparisons (**c**, **e**, **h**) test versus corresponding 0 dpi (naive). $^{*}p < 0.05$, $^{**}p < 0.01$, $^{***}p < 0.001$, $^{****}p < 0.0001$. AT1 and AT2: alveolar epithelial cell type 1 and 2, DC: dendritic cells, NK, natural killer cells. Exact $p$-values in order of appearance: **b** $^{*}p = 0.0255$; $^{**}p = 0.0078$ **c** alveolar: $^{**}p = 0.0041$; $^{*}p = 0.0102$, monocytic: $^{*}p = 0.0213$; $^{*}p = 0.0226$; $^{****}p < 0.0001$; T/NK: $^{****}p < 0.0001$; $^{***}p = 0.0002$; B cells: $^{*}p = 0.0106$ **e** alveolar: $^{****}p < 0.0001$; monocytic: $^{**}p = 0.0010$; $^{*}p = 0.0138$; $^{****}p < 0.0001$; T/NK: $^{*}p = 0.0225$; $^{**}p = 0.0099$ **g** $^{**}p = 0.0033$; $^{*}p = 0.0174$; $^{***}p = 0.0004$ **h** classical monocytes: $^{****}p < 0.0001$; neutrophils: $^{****}p < 0.0001$; $^{**}p = 0.0040$; $^{*}p = 0.0257$; T cells: $^{***}p = 0.0004$; B cells: $^{****}p < 0.0001$; $^{****}p < 0.0001$ **i** $^{**}p = 0.0024$.

blood and matched proteomics of lungs and serum to gain insights into alterations of SARS-CoV-2-induced immune responses.

Gene ontology (GO) enrichment analysis of the infection-triggered most differentially expressed genes in lungs and blood provided expected GO terms such as defense response to virus, innate immune response, and cell activation (Supplementary Fig. 4a, b). Pulmonary gene sets related to type 1 interferon (IFN) signaling correlated with the presence of viral RNA, thus vanished by 14 dpi. Similarly, pulmonary gene sets related to response to interferon-gamma (Ifng) were highest at 5 dpi (Supplementary Fig. 4c). In blood, type 1 IFN signaling and response to IFN-γ gene sets were highest at 2 and 3 dpi (Supplementary Fig. 4d), perhaps reflecting recruitment of specific cells from blood to lungs. Overall, bulk RNA-seq identified an anti-viral immune response that was effectively resolved when the virus was cleared.

The proteome host response was in line with the sequencing data, with differentially expressed serum proteins peaking at 3 dpi and lung proteins at 5 dpi (Supplementary Fig. 4e). Agreement between bulk RNA sequencing and proteomics was consistent in lungs at 5 dpi ($r = 0.9$) (Supplementary Fig. 4f). The principal component analysis (PCA) is detailed in the supplementary note, showing that the maximal response was observed at 5 dpi (supplementary note PCA on bulk transcriptomic data and PCA on bulk proteomics data). Functional terms connected with immune response, such as innate and adaptive immunity, activation of complement system, humoral immune response, and regulation of immune system processes were most enriched (Figs. 2a, S4g). In lungs, response to interferon-beta peaked at 3 dpi and stayed high until 5 dpi (Fig. 2a). Most processes were resolved by 14 dpi.

We next aimed at comparing our data to published datasets from COVID-19 patients. In hamster serum, 37 differentially expressed proteins were identified ($\alpha = 0.01$, providing FDR below 6%), 17 compared to control and 31 proteins compared to 14 dpi when most effects are resolved. Of 31 proteins, 20 have been reported in human COVID-19 studies, 7 (Actg1, Apoa1, Apoc1, Gsn, Hp, Itih3, Lbp) of which correlate with disease severity[19], all showing the same direction (Supplementary Fig. 4h).

In hamster lungs, at peak response (5 dpi) we identified 150 differentially expressed proteins. 13 differentially expressed proteins have been reported to be regulated in human plasma[20] with 9 showing the same trend (Supplementary Table 2). Of these, 6 proteins (C4b, Hp, Hpx, Ighm, Igkv7-33, Itih3) are also changed in hamster serum (Fig. 2b). Although a comparison to moderate disease in human lung tissue is not possible, 22 proteins are reported to be regulated in human BAL fluid of critically ill patients[21]. The few proteins showing opposite regulation to COVID-19 patients were confirmed by bulk sequencing. Five out of 7 conflicting responses, namely C4b, Hpx, Rbp4, Cfd, and Agt in hamster serum compared to human plasma as well as 8 out of 12 for hamster lung tissue compared to human BAL were confirmed.

Next, we refined transcriptome analyses with scRNA-Seq and related identified bulk GO terms to cell types, concentrating on inflammatory mediators (Fig. 3). Indeed, various pro-inflammatory chemokines were expressed by lung cells and showed distinct cellular and temporal expression patterns. Classical pro-inflammatory cytokines, e.g., *Il1a* and *Il1b* transcripts were elevated only early at 2 and 3 dpi in alveolar and monocytic macrophages, and alveolar macrophages and *Treml4*$^{+}$ monocytes, respectively. By 5 dpi, AT2 cells showed a unique range of upregulated inflammatory mediators such as *Cxcl17*, *Lipopolysaccharide Binding Protein (Lbp)*, *fibrinogen gamma gene (Fgg)*, and *clusterin (Clu)*. At the same time point, we found, among others, downregulation of the *Il6 receptor* (also known as CD126) and *S100a4*. Transiently decreased expression of these two inflammatory mediators might be part of the efficient yet self-regulating inflammatory response in this disease model. *Galectin 3-binding protein* (*Lgals3bp*) gene stood out as being upregulated in many cell types from 2 dpi to 5 dpi (Fig. 3). Notably, we likewise measured increased levels of Lgals3bp protein in lungs (Fig. 2c), which was shown to be regulated also in plasma of COVID-19 patients and correlated with severity[19].

Taken together, we identified clear changes in transcriptome, proteome and pro-inflammatory signatures on single-cell level in response to SARS-CoV-2 infection, displaying highly active immune responses that to large extents were also described in COVID-19 patients.

**Migratory myeloid cells dominate pulmonary transcriptional response to SARS-CoV-2 infection in Syrian hamsters and COVID-19 patients**. To pinpoint individual roles of identified cells in anti-SARS-CoV-2 immunity, we analyzed the 15–20 most differently expressed genes in each cell subset. In early stages of infection at 2 dpi, robust, local transcriptome changes were observed primarily in lung monocytic and interstitial macrophages, neutrophils, and endothelial cells, whereas AT1 and AT2 epithelial cells and alveolar macrophages showed comparably little change in mRNA expression (Fig. 4a). A common set of anti-viral effector genes was found upregulated in many cell types[22]. These include e.g., *interferon-stimulated gene 15* (*Isg15*), *MX dynamin like GTPase (Mx)1, Mx2, Interferon-induced protein with tetratricopeptide repeats 3* (*Ifit3*), and *Sp100*, as well as transcription factors, such as *Interferon regulatory factor* (*Irf*) *7* and *Irf9* (Fig. 4a, Supplementary Fig. 5a). Blood transcriptome

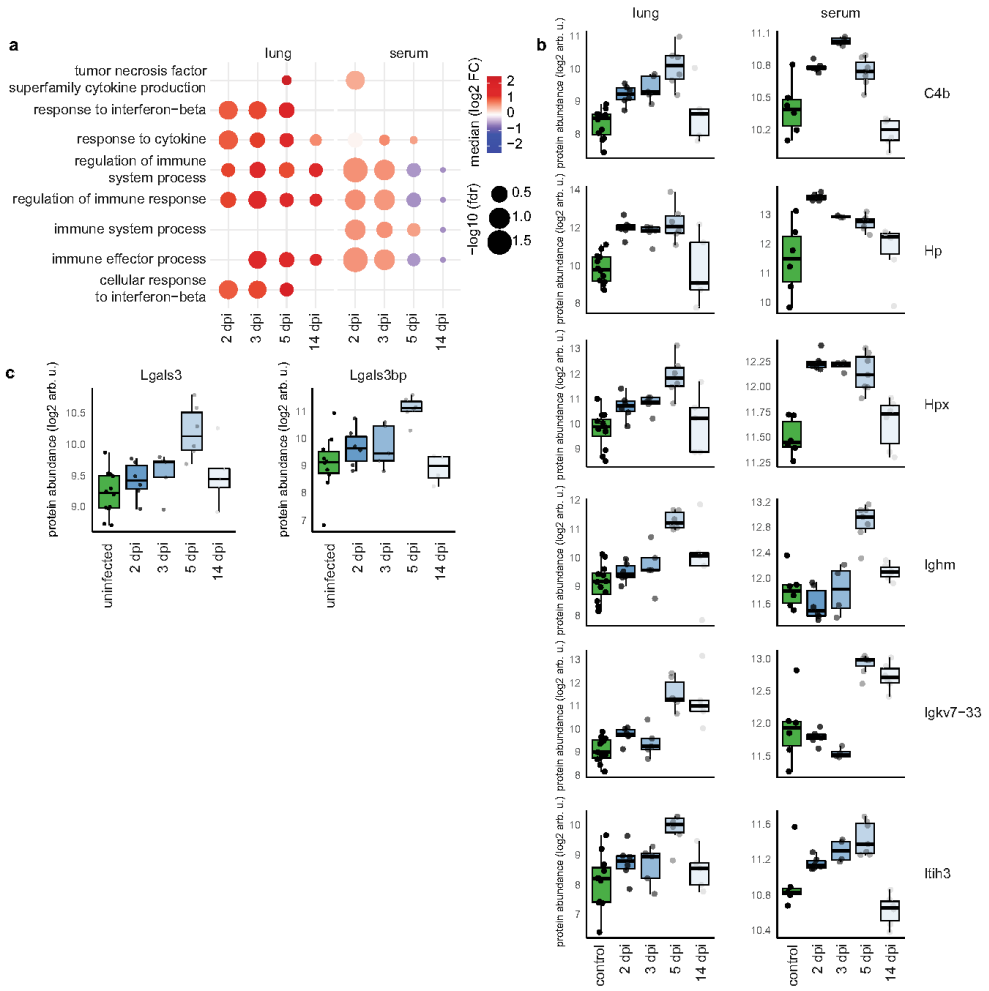


**Fig. 2 Proteomics analysis recapitulates transcriptomics and human COVID-19 patient data. a** Temporal evolution of gene ontology/biological process terms connected with immune system response in lung tissue (left part) and in serum (right part), for the indicated time points compared to samples from uninfected control animals. Enriched terms were filtered for terms mentioning immune, interferon, neutrophil, T cell and B cell and attained false discovery rates (fdr) below 0.2 at least at one-day post infection (dpi) in lungs or serum. The redundancy of terms was then reduced using REVIGO. Size of dots correspond to the inverse of the false discovery rate, color corresponds to median log2(fold change (FC)) of proteins, contributing to the term. **b** Expression values for differentially regulated proteins in hamster serum (control versus infected at 3 dpi, $p < 0.01$) and lung (control vs. infected at 5 dpi, $p < 0.01$) that correlate with disease severity in human plasma. Controls from different days are plotted together. Lung sample group sizes: control: $n = 12$, 2 dpi: $n = 6$, 3 dpi: $n = 5$, 5 dpi: $n = 6$, 14 dpi: $n = 5$. Serum sample group sizes: control: $n = 6$, 2 dpi: $n = 6$, 3 dpi: $n = 4$, 5 dpi: $n = 7$, 14 dpi: $n = 6$. All non-missing values are shown. **c** Expression values for the differentially expressed (control vs. infected at 5 dpi, $p < 0.01$) proteins Lgals3 and Lgals3bp (only detected in lung samples). Individual data points are shown in shades of gray. Lung sample group sizes: control: $n = 12$, 2 dpi: $n = 6$, 3 dpi: $n = 5$, 5 dpi: $n = 6$, 14 dpi: $n = 5$. **b**, **c** Box plots, the middle line in the boxplot displays the median, the box indicates the first and third quartile, whiskers the 1.5 interquartile range (IQR). arb.u.: arbitrary units.

analysis recapitulated this early transcriptional activity at 2 dpi (Fig. 4b, Supplementary Fig. 5b), but declined by 5 dpi, whereas the signature persisted in the lungs until 14 dpi (Supplementary Fig. 5a, b).

Genes that differed most between classical blood monocytes and their counterparts in lungs encoded chemokines and activation markers, including *CXC chemokine ligand 10* (*Cxcl10*), *Slamf9*, *Il18bp*, *Ifitm2*, *Ccl8*, *Ccl4*, and *Ccl5* (Fig. 4c, Supplementary Fig. 5c), indicating that activation and acquisition of effector function occurred in lungs. Although AT2 cells are a main target of SARS-CoV-2 in lungs[23], they displayed weaker and later transcriptional changes upon infection compared to monocytic

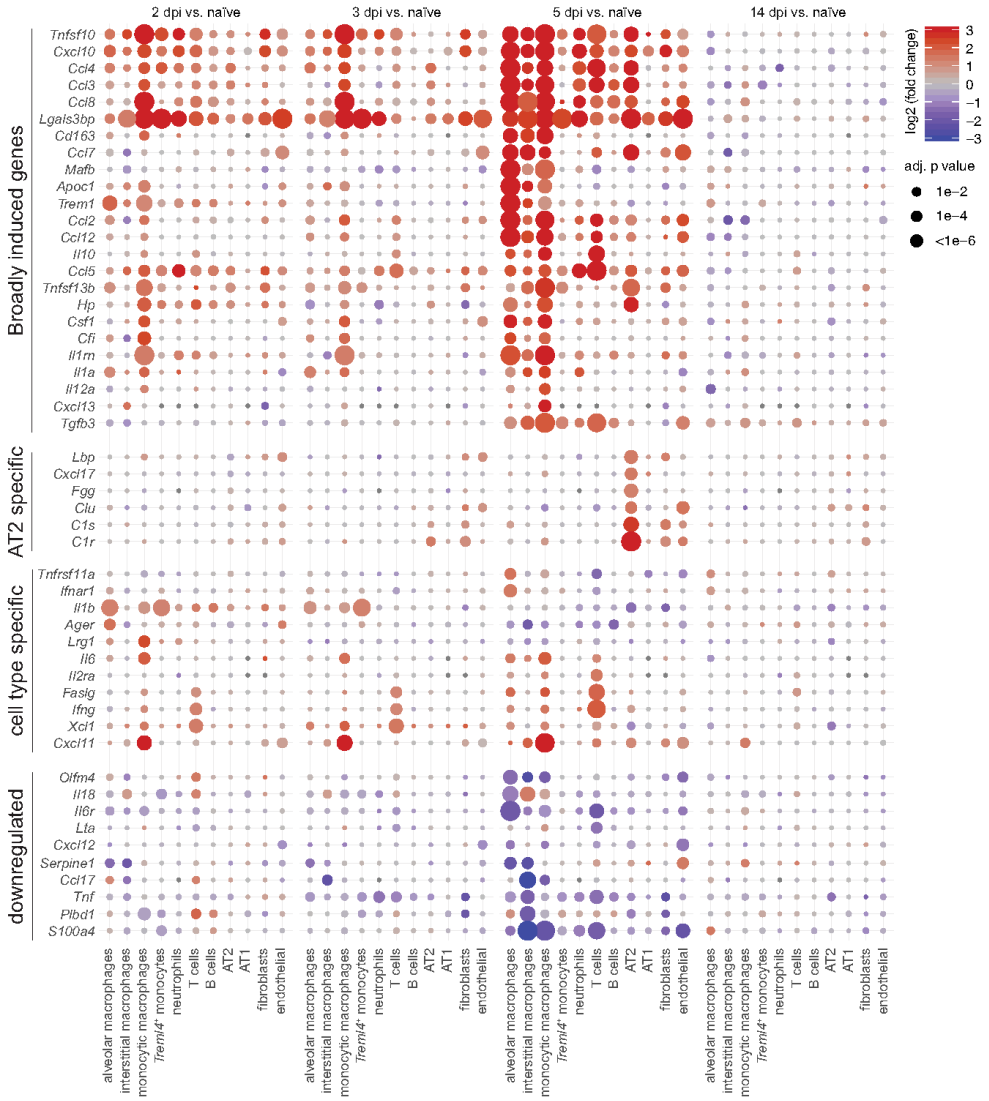


**Fig. 3 Induction of inflammatory mediators are strongest and earliest in myeloid cells.** Dotplots of differentially expressed cytokines and inflammatory mediators in lungs. Shown are genes that display a significant absolute log2-transformed fold change of at least one in at least one comparison, and are grouped into four categories indicated on the left. Coloration and point size indicate log2-transformed fold changes (FC) and *p*-values, respectively, of genes at 2 days post infection (dpi) relative to control groups (naive). Adjusted (adj) *p*-values were calculated by DEseq2 using Benjamini–Hochberg corrections of two-sided Wald test *p*-values. Genes are ordered by unsupervised clustering, cell type as in Fig. 1.

macrophages (Figs. 4a, d, S5a, d). Notably, at 14 dpi differential transcriptional responses related to defense resolved in blood and lung cells. Instead, we observed upregulation of cell cycle proliferation genes in AT2 cells including *Marker of Proliferation Ki-67* (*Mki67*), *Ubiquitin-conjugating enzyme E2 C* (*Ube2c*), *Aurora B kinase* (*Aurkb*), and *Stathmin* (*Stmn1*) (Supplementary Fig. 5a). This transcriptome profile indicated initiation of a repair program by AT2 cells, proliferating to replace damaged AT1 cells[24]. Finally, we put our hamster lung scRNA-Seq data in context with BAL scRNA-Seq data from patients with moderate-to-severe COVID-19[25] and healthy controls[26]. As in hamster data, we observed stronger transcriptional responses in macrophages compared to epithelial cells (Supplementary Fig. 5e). Furthermore, the upregulated gene program containing e.g.,

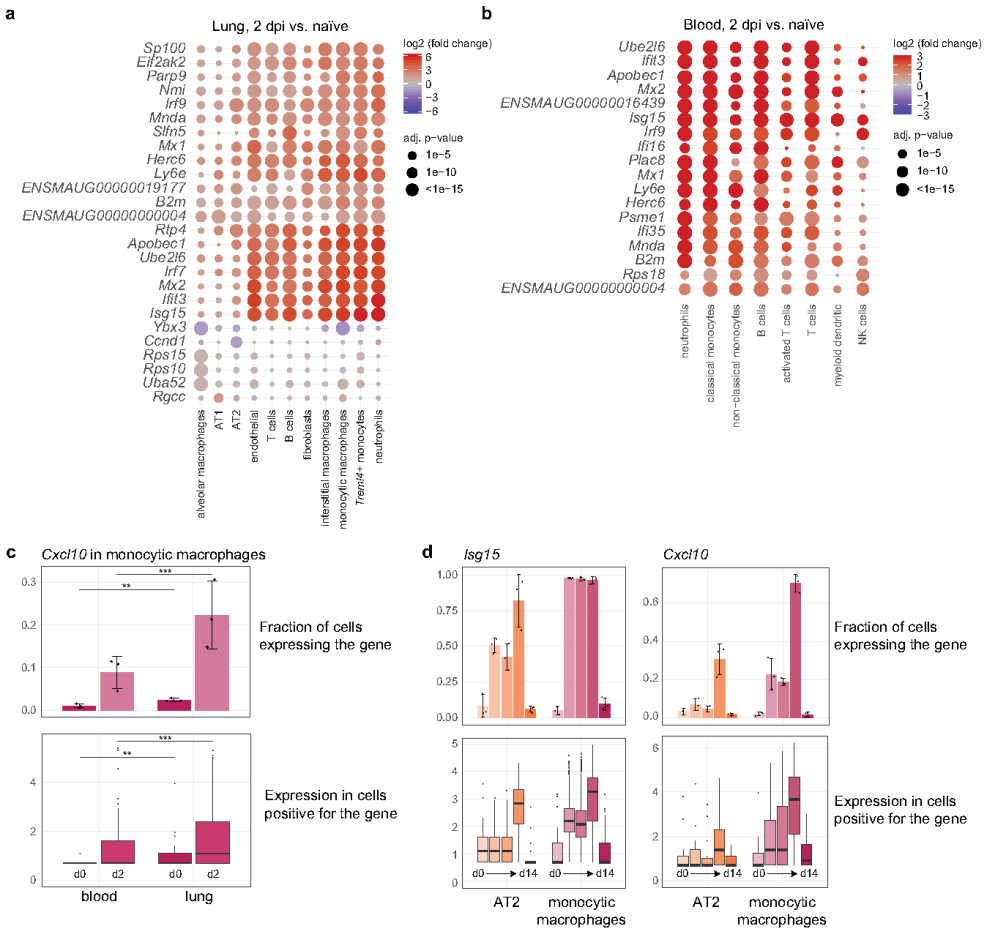


**Fig. 4 Transcriptional response to SARS-CoV-2 infection is strong in myeloid and moderate in epithelial cells. a**, **b** Dotplot of differentially expressed genes in lungs (**a**) and blood (**b**). Shown are genes that are in at least one cell type among the top four most changing genes as ranked by adjusted *p*-value. Example: top 4 most changing genes in alveolar macrophages are *Ybx3*, *Rps15*, *Rps10*, and *Uba52*. Coloration and point size indicate log2-transformed fold changes (FC) and *p*-values, respectively, of genes at 2 days post infection (dpi) relative to control groups (naive). Adjusted (adj.) *p*-values were calculated by DEseq2 using Benjamini–Hochberg corrections of two-sided Wald test *p*-values. Cell types and genes are ordered by unsupervised clustering. **c** Top, fraction of monocytic macrophages expressing *Cxcl10* in blood and lungs from naive animals and 2 dpi. Bottom, boxplots of *Cxcl10* gene expression values of cells positive for *Cxcl10* expression. Significance levels were calculated using two-sided generalized linear mixed-effects models for bar plots and a two-sided Wilcoxon rank-sum test on all cells (i.e., not only the ones expressing the gene) for boxplots. $*p < 0.05$; $**p < 0.01$; $***p < 0.0001$. See "Methods" for details. **d** As in (**c**), but only in lungs, all time points and both alveolar epithelial cells type 2 (AT2) and monocytic macrophages. Displayed are values for *Isg15* (left) and *Cxcl10* (right). For all bar plots, data display means ± SD, $n = 3$ per time point. For all boxplots, cell gene expression data derived from $n = 3$ animals per time point. The middle line in the boxplot displays the median, the box indicates the first and third quartile, whiskers the 1.5 interquartile range (IQR). Outliers beyond are marked by single dots. AT1 and AT2: alveolar epithelial cell type 1 and 2, DC: dendritic cells, NK, natural killer cells; d0: day 0 = naive, d14: 14 dpi. Exact *p*-values in (**c**): upper panel: $**p = 0.0022$; $***p < 0.0001$; lower panel: $**p = 0.0015$; $***p < 0.0001$.

*CXCL10*, *CCL2*, or *CCL8* was substantially overlapping (Supplementary Fig. 5f).

To test whether hamster tissue responses are representative of infected human epithelial cells, we next referred to our scRNA-Seq dataset derived from nasopharyngeal swabs of 19 COVID-19 patients and 5 healthy controls[27]. Here again, human and hamster epithelial cells derived from infected individuals and animals, respectively, showed a similar, moderate induction of most inflammatory mediators (Supplementary Fig. 6a, b). As notable difference, strong induction of neutrophil-recruiting chemokines targeting CXC chemokine receptor (CXCR) 2, such as *CXCL1*, *CXCL3*, *CXCL6*, and *CXCL8*, were found only in human basal and secretory cells with severe COVID-19 but were absent in moderately-ill Syrian hamsters (Supplementary Fig. 6a,

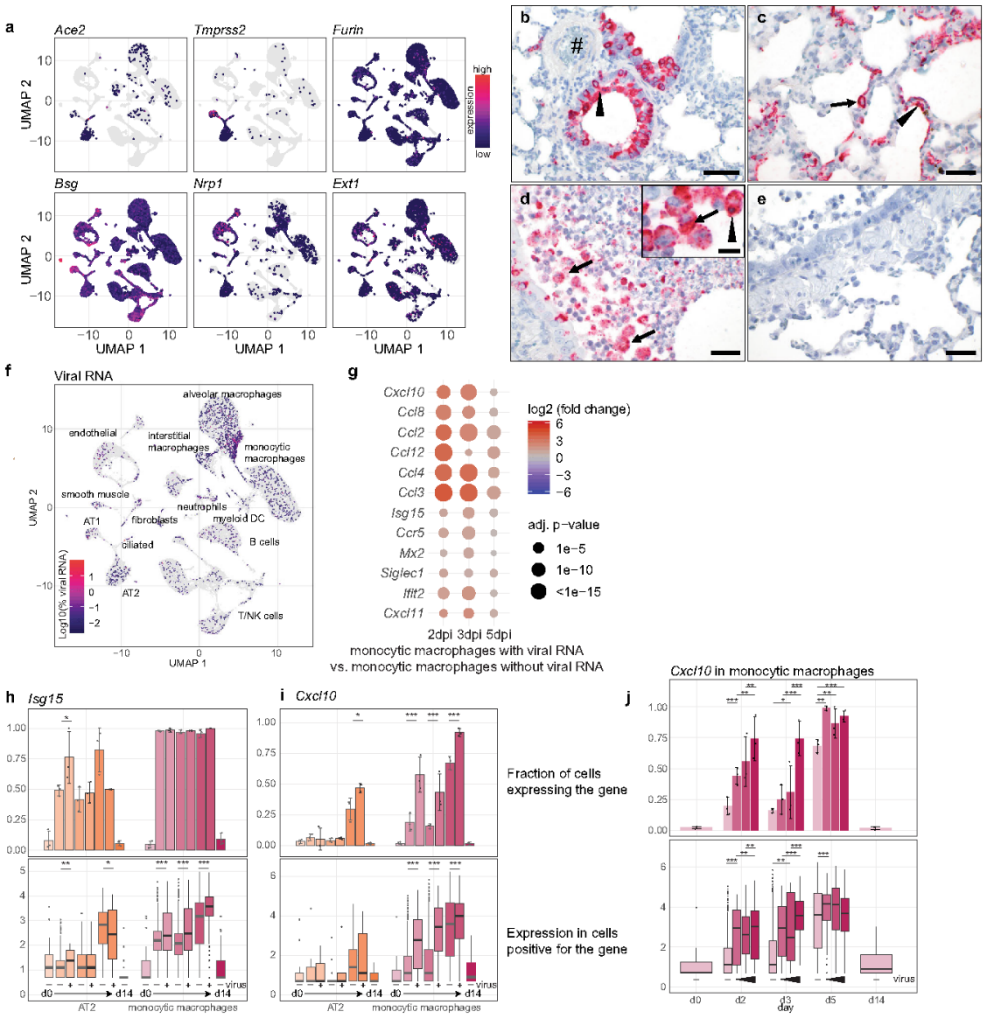


Fig. 3). Aside from the epithelial inductions of neutrophil-attractant transcripts unique to severe COVID-19, SARS-CoV-2 infected hamsters and patients displayed strikingly similar pro-inflammatory immune profiles specifically in migratory myeloid cells.

**Early activation of TLR/NF-kB-dependent transcription of pro-inflammatory cytokines in monocytic macrophages by SARS-CoV-2 infection**. Next, we asked whether observed cellular transcriptional responses to SARS-CoV-2 infection were influenced by the presence of virus in individual cell types. First, we determined fractions of cells expressing SARS-CoV-2 entry receptors, *Angiotensin-converting enzyme 2* (*Ace2*) *and transmembrane serine protease 2* (*Tmprss2*), putative alternative receptors, *Basigin (Bsg)* and *Furin*, and cofactors, such as neuropilins (*Nrp1*), and heparan sulfate (*exostosin-1, Ext1*))[28–30] in hamster lungs (Fig. 5a, Supplementary Table 3). Ciliated epithelial cells most frequently expressed *Ace2* (~4–22%), as did a smaller proportion of AT2 cells (~3–5%) (Supplementary Table 3). By in situ-hybridization, we visualized SARS-CoV-2 RNA in bronchial epithelial cells (Fig. 5b), and AT1 (Fig. 5c, arrowhead) and AT2 (Fig. 5c, arrow) cells, whereas endothelial cells were consistently devoid of virus (Fig. 5b, hash). Importantly, viral RNA was detected in high numbers of intrabronchial and intraalveolar macrophages (Fig. 5d, arrows) at early time points. A fraction of macrophages contained high loads of virus without cell debris, pointing toward uptake of cell-free virus (Fig. 5d, inset). For comparison, a control staining section of alveoli is shown (Fig. 5e).

ScRNA-Seq data suggested that most viral RNA content was found in monocytic macrophages, and not in epithelial cells (Fig. 5f, Supplementary Table 3). For epithelial and endothelial cells, frequencies of virus-positive cells were highest at 3 dpi, declining by 5 dpi to become absent at 14 dpi, indicating removal

**Fig. 5 Virus RNA in monocytic macrophages leads to dose-dependent activation of pro-inflammatory cytokines by TLR signaling. a** Feature plots of entry factor expression in Uniform manifold approximation and projection (UMAP) projection. Coloration indicates expression values of indicated genes. **b**–**e** Detection of viral RNA by in situ-hybridization. Labeled are supposed endothelium (**b**, hash), bronchial epithelial cells (**b**, arrowhead), AT1 (**c**, arrowhead) and AT2 (**c**, arrow). (**d**, inset), macrophages containing viral RNA and cell debris (arrowhead), and an example of high levels of viral RNA without cell debris in the inset (arrow). For **b**–**e** red signals viral RNA and blue hemalaun counterstain. Time points: **b, c** from 2 dpi, **d** from 3 dpi, **e** staining control. Bars: **b**, **d**, **e** = 50 µm, **c** = 100 µm, Inset in **d** = 20 µm. Micrographs representative of $n = 6$ per time point pi. **f** Cells in the UMAP projection are colored by amount of viral RNA (log10 transformed percentage of viral RNA per cell), along with overview of identified cell types in lungs. **g** Dotplot of cytokine expression in monocytic macrophages containing viral RNA compared to those without viral RNA. Coloration and point size indicate log2 fold change and adjusted (adj.) *p*-value for each time point 2, 3, and 5 dpi. Adjusted (adj.) *p*-values were calculated by DEseq2 using Benjamini–Hochberg corrections of two-sided Wald test *p*-values. **h, i** Bar- and boxplots of *Isg15* (h) and *Cxcl10* (i) gene expression in AT2 and monocytic macrophages along, comparing cells containing viral RNA to those without for 2, 3, and 5 dpi. Barplot shows percentage of cells positive for respective gene. Boxplots show gene expression levels in cells positive for respective gene, **j** Bar- and boxplots of *Cxcl10* in monocytic macrophages and fraction of *Cxcl10* positive cells for each time point pi and naive animals, with cells grouped by increasing virus levels for 2, 3, and 5 dpi. **h**–**j** Barplots, data display means ± SD, $n = 3$ animals per time point. Significance levels calculated using two-sided generalized linear mixed-effects models. For box plots, the middle line in the boxplot displays the median, the box indicates the first and third quartile, whiskers the 1.5 interquartile range (IQR), cell gene expression data derived from $n = 3$ animals per time point two-sided Wilcoxon rank-sum test on all cells (i.e., not only the ones expressing the gene) for boxplots. $^{*}p < 0.05$; $^{**}p < 0.01$; $^{***}p < 0.0001$. See "Methods" for details. AT1 and AT2: alveolar epithelial cell type 1 and 2, DC: dendritic cells, NK, natural killer cells; d0: day 0 = naive, d14: 14 dpi. Exact *p*-values in order of appearance in (**h**) upper panel: $^{*}p = 0.0338$; lower panel: $^{**}p = 0.0093$; $^{*}p = 0.014$; $^{***}p < 0.0001$; $^{***}p < 0.0001$; $^{***}p < 0.0001$; **i** upper panel: $^{*}p = 0.0270$; $^{***}p < 0.0001$; $^{***}p < 0.0001$; $^{***}p < 0.0001$; lower panel: $^{***}p < 0.0001$; $^{***}p < 0.0001$; $^{***}p < 0.0001$; **j** upper panel: $^{***}p < 0.0001$; $^{**}p = 0.0004$; $^{**}p = 0.0022$; $^{*}p = 0.0131$; $^{***}p < 0.0001$; $^{***}p < 0.0001$; $^{**}p = 0.0003$; $^{**}p = 0.0033$; $^{***}p < 0.0001$; lower panel: $^{***}p < 0.0001$; $^{**}p = 0.0015$; $^{**}p = 0.0064$; $^{**}p = 0.0034$; $^{***}p < 0.0001$; $^{***}p < 0.0001$; $^{***p} < 0.0001$.

of virus-containing cells (Supplementary Table 3). In contrast, alveolar macrophages showed highest viral loads at 5 dpi (~25%), paralleling decline of virus-positive tissue cells, thus pointing toward potential increase in phagocytic activities (Supplementary Table 3). We attempted to identify viral replication from our scRNA-Seq data without obtaining significant results (analysis details and results depicted in supplementary note assessing viral replication from sequencing data).

To further investigate how cell-specific gene expression is modulated by cell-associated viral RNA, we tested the correlation between gene expression and viral load in monocytic macrophages. We first compared gene expression levels in monocytic macrophages that did (vRNA$^+$), or did not (vRNA$^-$) contain viral RNA (Figs. 5g, S7a). This revealed a set of genes that only at early disease stages (2 dpi, 3 dpi), were present at higher levels in vRNA$^+$ monocytic macrophages (Supplementary Fig. 7a). Gene ontology and KEGG pathway analysis showed that this gene set was enriched for Toll-like receptor (TLR) signaling (Supplementary Fig. 7b). Specifically, this gene set contained a range of pro-inflammatory cytokines such as *Cxcl10* or *Ccl2* (Fig. 5g), which are activated by the NF-kB pathway downstream of TLRs[31]. On the other side, expression levels of NF-kB independent ISGs such as *Isg15* or *Mx2*, induced by interferons or cytosolic RNA sensors[32], were only slightly more elevated in vRNA$^+$ compared to vRNA$^-$ monocytic macrophages (Fig. 5g). Therefore, we investigated representative genes, *Isg15* and *Cxcl10*, in more detail (Fig. 5h, i). *Isg15* expression was found in about 2/3 of AT2 and all monocytic macrophages at 2 dpi. *Isg15* levels in gene-positive cells were higher at 2 dpi in vRNA$^+$ AT2 cells and at 2, 3, and 5 dpi vRNA$^+$ monocytic macrophages compared to corresponding vRNA$^-$ cells (Fig. 5h). In comparison, *Cxcl10* was nearly absent in AT2 cells at 2 dpi and 3 dpi. *Cxcl10*-positive cell fractions and gene expression levels were significantly higher in vRNA$^+$ monocytic macrophages compared to vRNA$^-$ cells at 2, 3, and 5 dpi (Fig. 5i). We further analyzed dose-dependency of this transcriptional response to virus in monocytic macrophages. Cells were binned in three groups of equal size with increasing content of viral RNA. We found that at earlier time points (2 and 3 dpi), but not at 5 dpi, cells with higher amounts of viral RNA-signal, also expressed more *Cxcl10* (Fig. 5j).

Overall, this indicated that sensing of viral RNA activated monocytic macrophages in a dose-dependent manner, leading to increase of NF-kB-regulated pro-inflammatory chemokines. At 5 dpi, broad inflammation likely masked direct viral RNA-triggered responses by activating expression of pro-inflammatory genes in vRNA$^+$ and vRNA$^-$ cells equally. In contrast, AT2 cells showed less activation of both NF-kB-dependent and -independent transcriptional responses as compared to monocytic macrophages.

**Endothelial cells participate in anti-viral and pro-inflammatory responses.** Having observed vast similarities of human and Syrian hamster immune responses in moderate SARS-CoV-2 infection on transcriptomic and proteomic levels, we next turned our attention to dissection of molecular mechanisms in lung tissue compartments that have so far not been assessed longitudinally in moderate COVID-19 patients, since invasive tissue sampling is hardly possible.

Endothelial cells likely participate in COVID-19 pathogenesis[33,34], but little is known about dynamics of their responses to inflammation in vivo. Subclustering of cells of endothelial origin identified endothelial cells of lymphatic and bronchial vasculature, pulmonary arteries, capillaries, and veins with unique features (Fig. 6a, Supplementary Fig. 8a, b). Interestingly, bronchial endothelial cells, pulmonary artery, and capillary endothelial cells all displayed strong and early anti-viral gene expression profiles at 2 dpi (Fig. 6b). Pulmonary arterial endothelial cells responded most rapidly to infection, with high expression of *Cxcl10*, *Tnfsf10*, and *Ccl7* by 2 dpi (Fig. 6c). Responses of bronchial vasculature, pulmonary capillary and pulmonary vein endothelial cells were similar but delayed, peaking at 5 dpi. In addition to distinct temporal dynamics of endothelial activation in different tissues, we observed a spatial regulation of expression of monocyte and effector T cells attractants. Pulmonary artery and vein endothelial cells preferentially transcribed *Ccl7*, a chemoattractant binding multiple CC receptors, including CCR1-3, CCR5, and CCR10[35]. Pulmonary capillary endothelial cells, however, preferentially expressed the pleiotropic *Ccl8*, binding at least CCR2, CCR3 and CCR5[36], while bronchial vasculature endothelial cells were characterized by *Ccl2* (Fig. 6c). ICAM-1 and VCAM-1 upregulation, occurs following inflammatory stimuli to allow for leukocyte transmigration[37], and was highest in bronchial endothelial cells and pulmonary artery cells at 5 dpi, corresponding to influx of T cells (Fig. 6c). Overall lung endothelial cells shared an anti-viral gene profile but revealed distinct patterns of chemokines targeting

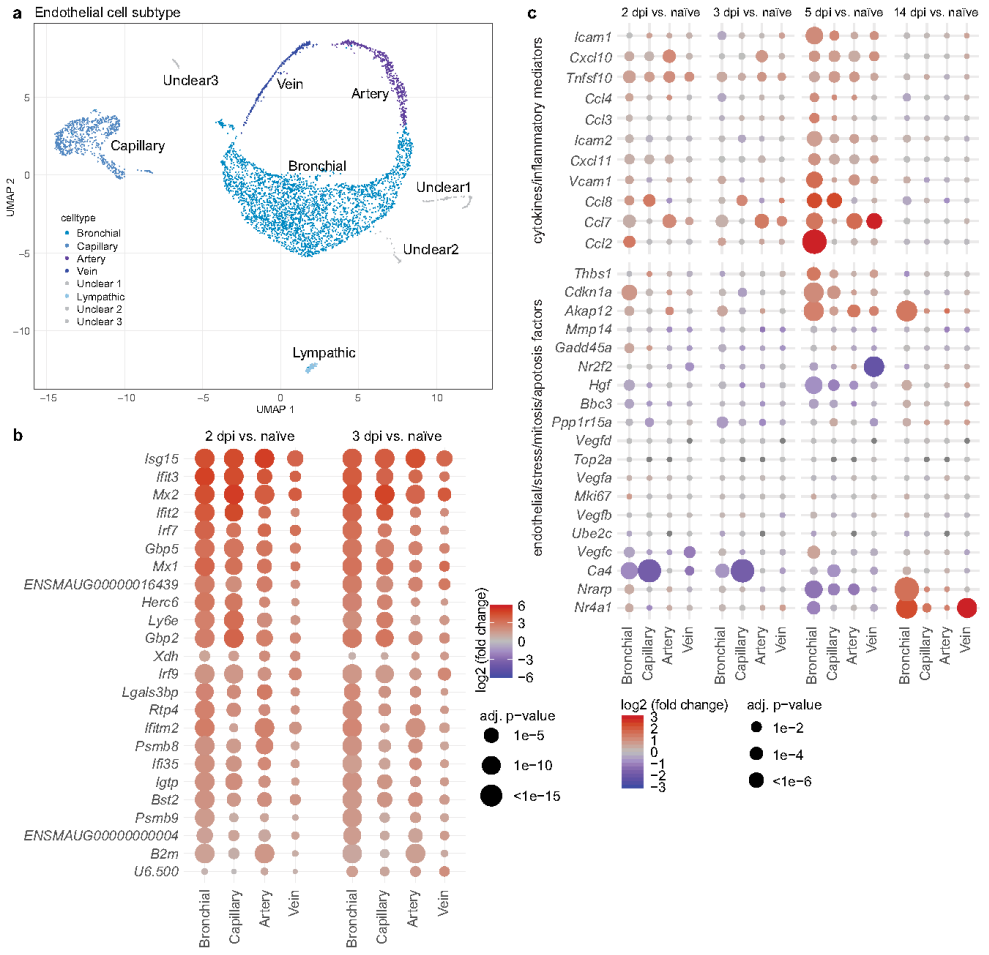


**Fig. 6 Endothelial cells show subtype and time specific activation of cytokines. a** Uniform manifold approximation and projection (UMAP) plot of lung endothelial cell subpopulations. Clusters defined by Louvain clustering, $n = 3$ per time point. Colors representing individual cell types are depicted in legend. **b** Dotplot of differentially expressed genes in lung endothelial cell subpopulations over time. Shown are genes that are in at least one cell type among the top 10 most changing genes as ranked by adjusted (adj.) *p*-value. Adjusted (adj.) *p*-values were calculated by DEseq2 using Benjamini–Hochberg corrections of two-sided Wald test *p*-values. **c** Dotplot of differentially expressed genes from two sets (upper set: cytokine/inflammatory mediators; lower set: endothelial/stress/mitosis/apoptosis factors) as indicated in lung endothelial cell subpopulations over time pi. For both **b**, **c** coloration and point size indicate log2-transformed fold changes and *p*-values, respectively, of genes at 2 days post infection (dpi) relative to control groups (naive). Adjusted (adj.) *p*-values were calculated by DEseq2 using Benjamini–Hochberg corrections of two-sided Wald test *p*-values.

primarily monocytes and Th1 cells. Unlike cells of epithelial origin, endothelial cells failed to show evidence of proliferation and cell cycle activity that could have indicated their participation in tissue repair processes during the study period (*DNA topoisomerase 2-alpha* (*Top2a*), *Mki67*, *Ube2c*) (Fig. 6c).

**Type 1 effector T cells are efficiently recruited to lungs in SARS-CoV2 infection**. Our initial cellular analysis of scRNA-Seq data from lung samples had grouped T and NK cells in one set of connected clusters, and we had observed their significant increase in lungs at 5 and 14 dpi (Fig. 1). We hypothesized that cytotoxic immunity might be linked to viral clearance observed at 5 dpi, and elimination by 14 dpi (Supplementary Fig. 2). Therefore, we subclustered NK and T cells to identify 4 subpopulations based on *Cd3e*, *Cd4*, *Cd8a*, and *Natural Killer Cell Granule Protein 7* (*Nkg7*) gene expression (Fig. 7a, Supplementary Fig. 9a), $CD4^+$ T cells ($Cd3e^+Cd4^+$), $CD8^+$ T cells ($Cd3e^+Cd8a^+$), NK cells ($Cd3e^-Nkg7^+$) and innate lymphoid-(ILC) like cells ($Cd3e^-Cd4^-Cd8a^-Nkg7^-$). $CD4^+$ T, $CD8^+$ T and NK cell numbers increased with infection time and peaked at 5 dpi (Fig. 7b). SARS-CoV-2 infection initiated type 1 immunity and cytotoxic effector

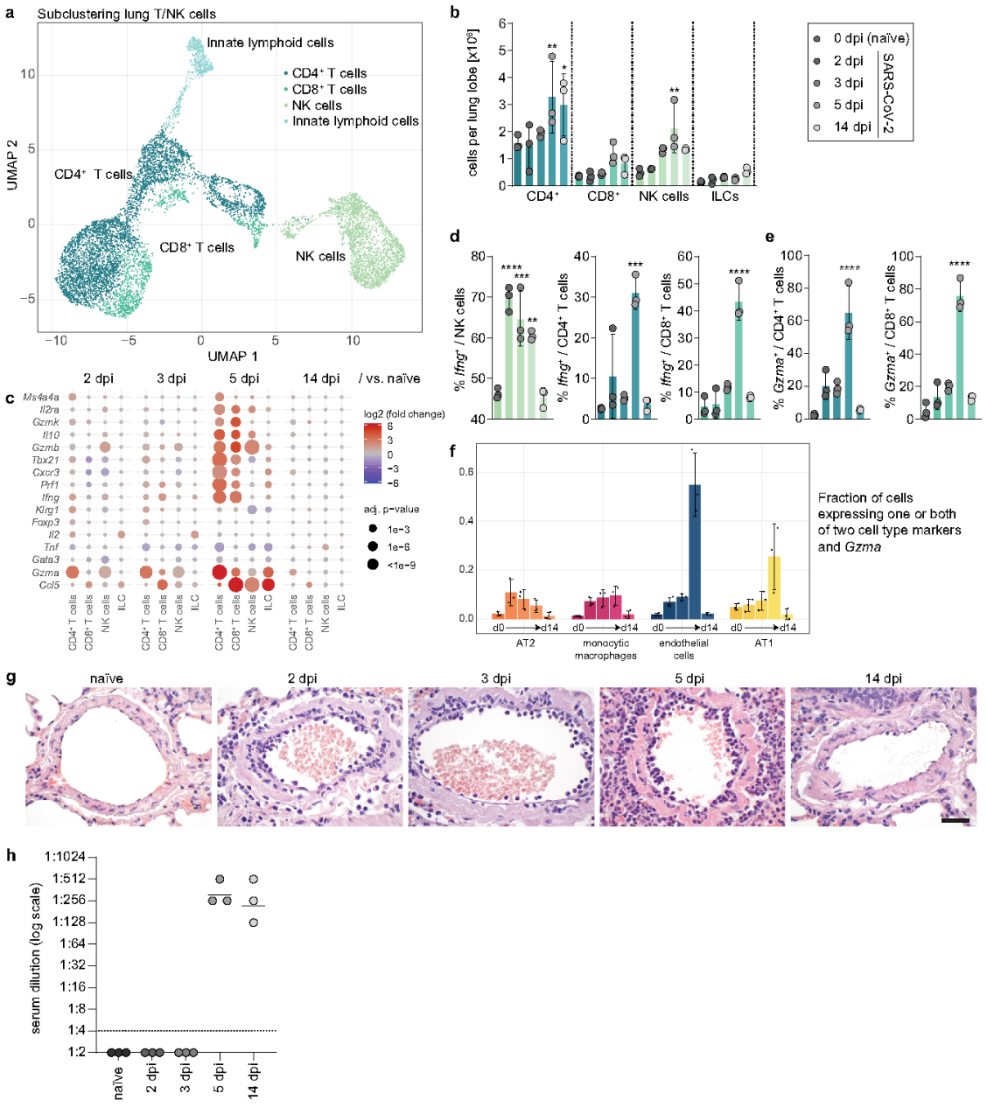


mechanisms in lungs (Fig. 7c, Supplementary Fig. 9b). The fraction of NK cells expressing interferon gamma (*Ifng*) increased significantly at 2 dpi and peaked at 3 dpi (Fig. 7d, left). In contrast, *Ifng*$^+$ effector T cells (*Ifng*$^+$ CD4$^+$, and CD8$^+$ T cells) peaked at 5 dpi (Fig. 7d, right). By 14 dpi, both *Ifng*$^+$ NK and T cell responses had declined to naive levels (Fig. 7d).

NK cells and CD8$^+$ T cells expressed high levels of cytotoxic genes, but upregulation of *Gzma* was highest in CD4$^+$ T cells (Fig. 7c, Supplementary Fig. 9b). Cytotoxic effector function of T cells was evident, 60% of all CD4$^+$ T and 70% of all CD8$^+$ T cells expressed *Gzma* at 5 dpi (Fig. 7e). Furthermore, we detected cells carrying both a specific cell type marker (for AT1/AT2/endothelial cells, or monocytic macrophages), and simultaneously the cytotoxic cell marker *Gzma*. These possible doublets were absent in naive animals and appeared particularly and reproducibly for endothelial and AT1 cells at the peak of effector T cell recruitment 5 dpi (Fig. 7f), indicating possibly either killer-target interaction or T cell transmigration. The latter notion was supported by the strong immigration of lymphocytes in the endothelium observed in histopathology (Fig. 7g).

Induction of high-affinity neutralizing antibodies is the primary aim of most vaccination strategies against viruses. In the here described primary infection with SARS-CoV-2, neutralizing antibodies were evident by 5 dpi and declined mildly until 14 dpi (Fig. 7h). Matching course of μ heavy chain protein levels measured by proteomics (Ighm, Fig. 2b). Peak of T cells and

**Fig. 7 Syrian hamsters exhibit a strong cytotoxic T/NK cell response at day 5 post infection. a** Uniform manifold approximation and projection (UMAP) plot of lung T/NK cell subclustering indicating cell subpopulations. Clusters defined by Louvain clustering, $n = 3$ per time point. Colors representing individual cell types are depicted in legend. **b** Count of lung T cell subpopulations and NK cells per lung lobe. **c** Dotplot of master regulators of T cell differentiation and effector genes. Coloration and point size indicate log2 fold change and adjusted (adj.) *p*-value, respectively. Adjusted (adj.) *p*-values were calculated by DEseq2 using Benjamini–Hochberg corrections of two-sided Wald test *p*-values. Data from $n = 3$ animals per time point. **d** Fraction of *Ifng*$^+$ cells in CD4$^+$ T, CD8$^+$ T and NK cells at 2, 3, 5, and 14 days post infection (dpi) and naive. **e** Fraction of *Gzma*$^+$ cells in CD8$^+$ T cells at 2, 3, 5, and 14 dpi and naive. **f** Fraction of AT2 cells, monocytic macrophages, endothelial cells, and AT1 cells containing both at least one cell type marker gene (AT2: *Sftpa1*, *Sftpc*—monocytic macrophages: *Fcn1*, *Saa3*—endothelial cells: *Cldn5*, *Plvap*—AT1: *Ager*, *Aqp5*) together with *Gzma*. Data display means ± SD, $n = 3$ animals per time point. **g** Histopathology of blood vessels at different time points, scale bar for all time points: 50 µm. Micrographs represent $n = 6$ animals per time point pi. **h** Serum neutralization titers of SARS-CoV-2 infected hamsters at 5 and 14 dpi. Serum titers of naive, 2 and 3 dpi did not neutralize up to detection limit 1:4 (dotted line). Data display $n = 3$ animals with mean per time point. **b**, **d**, **e** Bar plots are plotted per cell type in the order: naive, 2 dpi, 3 dpi, 5 dpi, and 14 dpi. (colors fade from dark to light). Data display means ± SD. $n = 3$ animals per time point. Ordinary one-way ANOVA, Šídák's multiple comparisons test versus corresponding 0 dpi (naive). *P*-values: $^*p < 0.05$, $^{**}p < 0.01$, $^{***}p < 0.001$, $^{****}p < 0.0001$. AT1 and AT2: alveolar epithelial cell type 1 and 2, NK: natural killer cells, ILC: Innate lymphoid cells. d0: day 0 = naive, d14: 14 dpi. Exact *p*-values in order of appearance: **b** CD4: $^{**}p = 0.0036$; $^*p = 0.0261$; NK: $^{**}p = 0.0046$ **c** IfnγNK: $^{****}p < 0.0001$; $^{***}p = 0.0003$; $^{**}p = 0.0024$; IfnγCD4: $^{***}p = 0.0002$; IfnγCD8: $^{****}p < 0.0001$; GzmaCD4: $^{****}p < 0.0001$; GzmaCD8: $^{****}p < 0.0001$.

neutralizing IgM antibodies corresponded with vanishing virus, indicating successful adaptive effector programs.

## Discussion

Detailed understanding of COVID-19 pathophysiology is imperative for the development of therapies to reduce numbers of patients developing lung injury. Notably, recent patient-centered research on COVID-19 was compromised by three blind spots: (i) biomaterial is usually sampled after hospital admission, therefore the early phase of infection and host response has rarely been investigated. (ii) the BAL procedure to access the alveolar compartment is too dangerous for non-intubated patients with COVID-19 pneumonia, so that alveolar host responses can hardly be investigated in mild and moderate COVID-19. (iii) Lung tissue can exclusively be harvested after death in COVID-19 patients, precluding from investigations of non-myeloid alveolar or endothelial host responses in early disease, and enabling for analysis of later disease stadium only in case of fatal outcome. Thus, we performed in-depth analysis of the full course of moderate, self-limited disease that develops in SARS-CoV-2 infected Syrian hamsters. In this model, lungs are fully accessible, providing for detailed analysis of myeloid and non-myeloid compartments including vascular endothelium. Yet, while the immune response is qualitatively similar between human and hamsters in central aspects, the viral dose applied in experimental infections is likely to be higher than in natural aerosol infection. Consequently, infection kinetics, viral decay rate, and immune responses are accelerated[38,39]. In line, we observed the pulmonary peak of viral load, inflammation, and cellular response between 3 and 5 dpi, whereas at 14 dpi the infection was resolved and mechanisms of tissue regeneration were induced. This course of disease confirms observations in other animal models including non-human primates.

Syrian hamsters developed rapid, but moderate, neutrophil recruitment predominantly to bronchi and lung parenchyma, which resolved by 3 dpi. We also observed little of the typical neutrophil-dependent alveolar damage. Although single-cell RNA-sequencing analysis likely underestimates the numbers of this fragile cell type[40], these findings suggest a minor role for neutrophils. Nonetheless, the neutrophil response is noteworthy, as many other respiratory viruses, e.g., Influenza A Virus and MERS Virus, initiate little or no neutrophil trafficking in rodents[41]. In fact, blood N/L ratios in COVID-19 patients were reported as markers for disease severity, and neutrophil extracellular traps, as well as reactive oxygen species, are suspected to contribute to adverse vascular events[42,43]. Confirming our classification of hamsters as a moderate disease model, N/L ratios were only mildly elevated at 2 dpi, and gene signatures of dysfunctional immunosuppressive neutrophils were observed in severe COVID-19 patients[44], but not in Syrian hamsters.

In line with COVID-19 patient reports, alveolar macrophage numbers did not decrease in moderate disease settings[25], and monocytic macrophages were the largest cell population recruited to the lungs, with notable recruitment from 2 dpi on, and peak presence at 5 dpi[27,44]. Monocyte trafficking to lungs was initiated by local expression of CCR2 ligands, and endogenous chemokine expression served as a feedforward loop. Consequently, macrophages were the predominant inflammatory cell type in alveolar spaces as identified by histopathology. Moreover, macrophages presented the earliest and strongest transcriptional response to the infection, primarily responding to intracellular viral RNA with pro-inflammatory cytokines such as CXCL10, CCL2, and others. Notably, the monocytic macrophage pro-inflammatory expression profile was rather productive than dysregulated as it tended more toward effector T cell recruiting chemokines targeting CXCR3 and CCR5, and less toward pro-inflammatory cytokine expression. This matches observations on moderate versus severe courses of COVID-19 in patients and stands in contrast to findings in animal models with severe disease progression such as K18-hACE2 mice[16,25]. It seems unlikely that intracellular viral RNA found in macrophages is the result of active infection of these cells, as they have been demonstrated to be largely resistant to infection ex vivo[45]. scRNA-Seq data obtained from African green monkeys infected with SARS-CoV-2 likewise did not support virus replication in macrophages[46]. Instead, virus uptake may derive from complement receptor and Fc receptor-mediated phagocytosis of complement and antibody-labeled virus, as suggested by neutralizing antibody titers at 5 dpi[47]. Further, we observed early increase in complement factors and IgM µ chain by proteomics analysis in lung tissue. Taken together, the Syrian hamster model endorses the hypothesis that monocyte-derived macrophages are a primary source of the strong pro-inflammatory response observed in COVID-19, yet highlights that their presence not necessarily results in fatal outcome[48].

Presumably, in the lungs SARS-CoV-2 primarily infects AT2 cells[23]. Of note, only few of them were infected and they reacted with only marginal transcriptional responses, which is probably explained by the recent observation in human lungs that less than 10% of AT2 cells express the crucial entry receptor ACE2[45]. Moreover, coronaviruses are endowed with a multitude of mechanisms that block immunological cascades downstream of interferon signaling and cytoplasmic RNA sensing[49]. Only a small subset of in vitro highly infected cells express pro-inflammatory

genes[50,51]. Thus, despite being the primary target for viral replication, epithelial cells were not accountable for early systemic propagation of anti-viral or pro-inflammatory signatures.

Endothelial barrier dysfunction, resulting from endothelial cell stress or death, evokes lung edema and thus contributes to lung failure in severe COVID-19[34,52–54]. However, mechanisms driving endothelial barrier failure in COVID-19 are not well understood, as the endothelial compartment is not accessible in living humans suffering from COVID-19. Autopsy studies reported presence of viral particles in human endothelial cells[34], but infection of endothelial cells by SARS-CoV has been questioned[55]. In SARS-CoV-2 infected non-human primates viral infection of endothelial cells was not observed[46]. Here, we found that endothelial cells showed a rapid and strong induction of anti-viral response genes, but considering the absence of histopathological evidence for intraendothelial virus, we speculate that virus-positive endothelial cells found by scRNA-Seq were not infected, but were rather an artifact originating from contact with ambient virus or its RNA[2,9]. Concomitant cellular and molecular inflammatory responses in blood suggested that systemic responses were additive to direct, local endothelial cell activation. Notably, this observation is in line with our recent findings that virus-free plasma of COVID-19 patients induced significant endothelial gap formation and loss of junctional VE-cadherin in human endothelial monolayers and lung tissue[33]. Endotheliallitis, as observed in autopsies of deceased COVID-19 patients, was also found in infected hamsters[2,9] and corresponded to their transcriptional pro-inflammatory chemokine responses[34]. Histopathological evidence of pronounced lymphocyte trafficking via capillary endothelial cells also correlated with endothelial *Ccl8* expression.

Lymphocyte recruitment in response to CXCR3 and CCR5 targeting chemokines resulted in the presence of $CD4^+$ and $CD8^+$ T cells with cytotoxic expression pattern in lungs starting at 3 dpi. Most importantly, viral clearance coincided with appearance of effector T and NK cells stressing their relevance for resolution of SARS-CoV-2 infection and highlighting their importance in vaccination strategies. Studies from other coronaviruses suggest that type 1 immunity is the primary mechanism controlling the infection[56,57]. In severe COVID-19, blood $CD4^+$ T, $CD8^+$ T, and NK cells expressed markers of exhaustion[58], a finding not mirrored in moderately sick Syrian hamsters. In contrast, T and NK responses were effective and self-resolving. This matches observations of broad T cell antigen-specificity in the majority of resolved cases independent of mild or severe infection[59]. In our study, we found SARS-CoV-2 neutralizing antibodies at 5 dpi, likely of IgM type, as early appearance and corresponding elevated Ighm protein levels suggested. Seroconversion in COVID-19 patients occurred 7–14 days post diagnosis with IgG titers appearing at later time points[60,61].

At 14 dpi, infectious virus was no longer detected in hamster lungs, and most transcriptional activity had returned to basal levels. Upregulation of mitotic markers in AT2 cells may reflect regeneration mechanisms after clearing the infection.

The pulmonary capillary microvascular niche in lungs supports alveolar epithelial repair mechanisms following injury, e.g., by secretion of MMP14, VEGF, thrombospondin-1 (THBS1)[62]. Analysis of pulmonary endothelial cell subclusters revealed that bronchial, pulmonary capillary and pulmonary vein endothelial cells showed increased expression of *Thbs1* at 5, but not 14 dpi. Similarly, no increase in *Mmp14* or *Vegf* expression was detected at 14 dpi. In murine influenza characterized by lung injury and pronounced alveolar damage, a pulmonary population of proliferating endothelial cells is present at 14 dpi[63] that was absent in SARS-CoV-2 infected Syrian hamsters, indicating that the alveolar endothelial and epithelial damage remained moderate in our model. Most notably, lung endothelial cells showed an anti-fibrotic gene signature at 14 dpi (*Nr4a1*[64], *Akap12*[65], *Nrarp* (downstream of Notch-signaling))[66], indicating regeneration rather than repair of lung tissue, thereby matching histopathology findings.

Taken together, we provide evidence that Syrian hamsters recapitulate the course of moderate human SARS-CoV-2 infection. Hamsters displayed nearly prototypic antiviral immune responses starting with rapid, yet self-restricted neutrophilic response, along with a fast and strong monocytic innate immune response following activation after virus uptake, augmenting local anti-viral responses and pro-inflammatory CC chemokine production recruiting a potent type 1 T cell response that probably contributed to elimination of pulmonary residing virus via cytotoxic effector mechanisms. Neutralizing antibodies of IgM type aided in preventing viral spread and fostered cellular virus uptake. Viral infection and inflammatory response in and by lung epithelium is not predominant. Upon successful elimination of virus, alveolar epithelial repair mechanisms started, along with endothelial suppression of fibrotic programs, thus enabling pulmonary regeneration in convalesced hamsters.

Hence, Syrian hamsters represent a highly suitable model to study the pathophysiology of moderate COVID-19, virus-directed and immunomodulatory therapies, and potentially vaccines. SARS-CoV-2 infected Syrian hamsters mount immune responses consistent with COVID-19 patients and enable for detailed investigations on the kinetics and role of specific cell populations, highlighting the dominant contribution of monocytic macrophages, endothelial cells, and T cells to inflammatory responses and resolution of SARS-CoV-2 infection.

Although we present several lines of evidence suggesting a comparable course of disease in Syrian hamsters and moderate COVID-19 in humans, the extent to which results from this animal model can be translated to human patients is limited. This limitation particularly arises from the unavailability of human samples from time points post infection, yet pre symptom onset, as well as lung tissue samples from living human subjects. Due to the lack of an available cell atlas for our model system, we used a combination of marker expression and label transfer from available *Mus musculus* and human datasets for manual curation of lung and blood cell atlases for Syrian hamster. Owing to the limited amount of molecular tools and reagents available for hamsters, such as antibodies, it is not possible to confirm key findings from our transcriptomic analysis e.g., by immunostaining of tissue sections or by ELISAs for cytokines in the blood.

## Methods

**Ethics statement and animal husbandry**. All experiments involving animals were approved by institutional and governmental authorities (Freie Universität Berlin and LaGeSo Landesamt für Gesundheit und Soziales Berlin, Germany, permit number G 0086/20). Female and male Syrian hamsters (*Mesocricetus auratus*; breed RjHan:AURA, Janvier Labs, France) were housed in biosafety level 3 (BSL-3) conditions in individually ventilated cages with enrichment. Food and water was provided *ad libidum*. Daily cage temperature and relative humidity measurements ranged from 22–24 °C and 40–55%, respectively. Animals were acclimatized for a minimum of 7 days prior to infection.

**Virus stocks**. SARS-CoV-2 isolate (BetaCoV/Germany/BavPat1/2020)[67] was kindly provided by Daniela Niemeyer and Christian Drosten, Charité Berlin, Germany. Virus stocks were propagated under BSL-3 conditions in Vero E6 cells (ATCC CRL-1586). All hamsters described here received virus from the same batch.

**Animal infection**. At 10–12 weeks of age hamsters were intranasally infected with $1 \times 10^5$ pfu SARS-CoV-2 under anesthesia (0.15 mg/kg medetomidine, 2 mg/kg midazolam and 2.5 mg/kg butorphanol) by applying 60 µL MEM with $1 \times 10^5$ pfu SARS-CoV-2 or plain cell culture medium for mock-infected animals. Anesthesia was antagonized with 0.15 mg/kg atipamezole immediately following intranasal application[2]. Clinical signs and weight were monitored daily. Animals with >15% body weight loss over 48 h were euthanized in accordance with animal-use

protocols. Euthanasia was performed by cervical dislocation under the anesthesia described above[2]. 1 mL peripheral blood was collected in EDTA-coated syringes. The left lung lobe was collected for histopathology, the right caudal lobe for single-cell analysis, the right cranial lobe for virological assessments and the right medial for bulk RNA as well as proteomics analysis. Experimental design and analysis are summarized in the Supplementary material (Supplementary Fig. 1a). Numbers of animals ($n$) analyzed per read-out and sample type are depicted in Supplementary Fig. 1b. Data for clinical, virological, and transcriptome analysis were derived from two independent experiments (E1 and E2), per experiment $n = 12$ hamsters were infected as described above, per experiment 3 animals from these groups were sacrificed at 2, 3, 5, and 14 dpi to collect samples. For transcriptome analysis ($n = 3$ per time-point) as well as $n = 3$ naive hamsters were used. For the presentation of clinical and virological data, subjects from E1 and E2 were combined ($n = 6$ per time point). For proteome analysis, samples from the same hamsters that were used for transcriptome analysis were employed, additionally, samples from 1 to 4 hamsters and time-point controls (mock-infected, $n = 3$–6 per time point) from an independent third experiment (E3) where animals underwent the exact same infection and treatment were used for proteome analysis to achieve a larger sample size.

**Viral burden assessment**. Virus titers were determined by serial dilutions of lung homogenates (50 mg) plated on Vero E6 cells, cells were fixed in 10% formalin, stained with crystal violet (0.75% aqueous solution) and plaques were counted by eye in appropriate dilutions[2].

For RNA extractions and quantitative RT-PCR, RNA from oropharyngeal swabs, lung tissue, and whole blood was isolated with the innuPREP Virus DNA/RNA Kit (Analytic Jena) according to the manufacturer's instructions. One-step RT-qPCR reaction with the NEB Luna Universal Probe One-Step RT-qPCR (New England Biolabs) and the 2019-nCoV RT-qPCR primers and probe E_Sarbeco[68] quantified viral RNA on an Applied Biosystems OneStepPlus qPCR cycler (Thermo Fisher).[2]. Viral RNA copies were calculated per $1 \times 10^5$ hamster *Rpl18* transcripts. Primers and probes are listed in the Supplementary Information (Supplementary Table 1).

**Measurement of neutralizing antibodies titer**. Serum neutralization tests were performed by two fold serial dilutions (1:4 to 1:512) of complement inactivated (56 °C, 2 h) hamster serum plated on sub-confluent monolayers of Vero E6 cells. 50 pfu SARS-CoV-2 were added per well and incubated for 72 h at 37 °C, fixed with 10% formalin for 24 h and stained with crystal violet (0.75% aqueous solution). Serum neutralization was considered effective in wells that did not show any cytopathic effect, the highest effective dilution was counted.

**Histopathology and in situ-hybridization of SARS-CoV-2 RNA**. For histopathology and in situ-hybridization (ISH), lungs were processed as described[2]. Left lung lobes were immersion-fixed in 10% formalin, pH 7.0, for 48 h, embedded in paraffin, and cut into 2 µm sections. Hematoxylin and eosin (HE) staining and in situ-hybridizations were performed as described[7] using the ViewRNA™ ISH Tissue Assay Kit (Invitrogen) following the manufacturer's instructions with minor adjustments. SARS-CoV-2 RNA was localized with probes detecting N gene sequences (NCBI database NC_045512.2, nucleotides 28,274–9533, assay ID: VPNKRHM). An irrelevant probe for detection of pneumolysin was used to control for sequence-specific binding[4]. Amplifier and label probe hybridizations were performed following the manufacturer's instructions using fast red as chromogen with hemalaun counterstain. Tissues were histopathologically evaluated by board-certified veterinary pathologists (KD, ADG) in a blinded fashion following standardized recommendations[9], including pneumonia-specific scoring parameters[41] as described for SARS-CoV-2 infection in hamsters[2].

**Single cell isolation from whole blood and hamster lungs**. Protocols were adapted for BSL-3 facility regulations. For isolation of cells from whole blood, 250 µL blood were lysed in red blood cell lysis buffer (BioLegend), washed and centrifuged according to the manufacturer's instructions. Resulting RBC-free pellets were resuspended in low-BSA buffer (1× PBS, 0.04% BSA), filtered with 40 µm FloMi filters (Merck) and counted by hemocytometer in trypan blue.

For isolation of single cells caudal lung lobe was removed and placed in storage medium (1× PBS, 0.5% BSA) until further processing. Storage and isolation media contained 2 µg/mL ActinomycinD. Tissues and cells were centrifuged at 350 × *g* for 6 min at 4 °C. Lung lobes were mechanically disassociated with tweezers for 2 min in enzymatic digestion medium containing 3.4 mg/mL Collagenase Cls II (Merck) and 1 mg/mL DNase I (PanReac AppliChem) in 2 mL Dispase medium (Corning) per lung lobe followed by 30 min incubation at 37 °C and 5% $CO_2$. After dissociation of digested lung tissue, cell suspensions were pressed through 70 µm cell strainers with plungers. Red blood cells were lysed (BioLegend), washed with an excess of PBS/BSA and resuspended in low-BSA buffer (1× PBS, 0.04% BSA), and filtered with 40 µm low-volume FloMi filters (Merck). Cells were counted in trypan blue.

**Single cell RNA sequencing**. Barcoding, cDNA Library generation, and sequencing; filtered cells were adjusted to a final concentration of ~1000 cells/µL in 1× PBS with 0.04% BSA and subjected to partitioning into Gel-Beads-in-Emulsions (GEMs) aiming to recover 6000 single cells per hamster and organ by following the instructions for the Chromium Next GEM Single Cell 3′ GEM, Library & Gel Bead Kit v3.1 (10× Genomics). Resulting single-cell libraries were quantified using Qubit (ThermoFisher) and quality-controlled using the Bioanalyzer system (Agilent). Sequencing was performed on a Novaseq 6000 device (Illumina), with SP or S1 flow cells (read1: 28 nucleotides, read2: 64 nucleotides).

**Bulk RNA sequencing**. For lung RNA Bulk Sequencing the medial lung lobe was removed and stored in RNA Later Solution for a maximum of 24 h at 4 °C (ThermoFisher). Lung tissue was homogenized using the TissueLyser II system (Qiagen) and homogenates stored in Trizol reagent (Zymo research). For WBC RNA Bulk Sequencing, white blood cells were isolated as described for scSeq followed by lysis in Trizol reagent. RNA extractions were performed according to the Direct-zol RNA Miniprep protocol (Zymoresearch). Bulk RNA sequencing libraries constructed using the Nebnext Ultra II Directional RNA Library Prep Kit (New England Biolabs), and sequenced on a Nextseq 500 device with read length 76.

**Proteomics sample preprocessing**. Lung tissue and serum were added to lysis and inactivation buffer (RIPA) and boiled for 10 min at 95 °C before storage at −80 °C. Samples were thawed on ice, volume was adjusted to 50 µl with water and 25 µl of 50 U benzonase, 50 mM ABC, 2 mM $MgCl_2$ added before incubation for 30 min at 37 °C. Lysates were processed on a Biomek i7 workstation using the SP3 protocol as previously described with single-step reduction and alkylation[69]. Samples were used for LC-MS/MS analysis without additional conditioning or clean-up.

**Liquid chromatography−mass spectrometry analysis (LC−MS)**. High-throughput analysis of serum and lung tissue; Peptide separation has been accomplished in a 5-min water to acetonitrile gradient on an Agilent Infinity II HPLC coupled to a Sciex Triple TOP 6600 mass spectrometer (IonDrive TurboV Source) operating in ScanningSWATH mode with minor changes in the liquid chromatography method[70]. As follows: 5 µg of peptides were loaded and resolved in a linear gradient from 1 to 35% buffer B in 4.5 min before increasing to 40% B in 0.5 min and washing for 0.2 min with 80% buffer B before equilibration for 2.2 min with initial conditions (buffer A: 0.1% formic acid, buffer B: 100% ACN, 0.1% formic acid). For library generation by gas phase fractionation (GPF), 6 single 1 µg injections of pooled serum samples were analyzed by online nanoflow liquid chromatography tandem mass spectrometry on an Ultimate3000 Thermo Scientific Q Exactive Plus Orbitrap, LC-MS instrument (Thermo Fisher Scientific, Waltham, USA). The peptides were concentrated for 3 min on a trap column (PepMap C18, 5 mm × 300 µm × 5 µm, 100 Å, Thermo Fisher Scientific) with a buffer containing 2:98 (v/v) acetonitrile/water containing 0.1% (v/v) trifluoroacetic acid at a flow rate of 20 µl/min. They were separated by a 250 mm LC column (Acclaim PepMap C18, 2 µm; 100 Å; 75 µm, Thermo Fisher Scientific). The mobile phase (A) was 0.1% (v/v) formic acid in water, and (B) 80% acetonitrile in 0.1% (v/v) formic acid. In 155 min total acquisition time gradient B increased in 90 min to 25%, and in 30 min to 40% with a flow rate of 300 nl/min. The MS instrument was operated in the data independent mode as followed: the Orbitrap worked in centroid mode with 4 *m/z* DIA spectra (4 *m/z* precursor isolation windows at 17,500 resolution, AGC target 1e6, maximum inject time 60 ms, 27 NCE). An overlapping window pattern from narrow mass ranges using window placements (i.e., 395–505, 495–605, 595–705, 695–805, 795–805, 895–905 *m/z*) was set. Two precursor spectra, a wide spectrum (395–505 *m/z* at 35,000 resolution) and a narrow spectrum matching the range using an AGC target of 1e6 and a maximum inject time of 60 ms were interspersed every 25 MS/MS spectra at resolution of 17,500. Typical mass spectrometric conditions were as follows: spray voltage, 2.1 kV; no sheath and auxiliary gas flow; heated capillary temperature: 275 °C; normalized HCD collision energy 27%. As lock mass acted the background ion *m/z* 445.1200.

**Computational proteomics**. For *Mesocricetus auratus* serum samples, a project specific library was generated by gas-phase fractionation, whereas the lung tissue library was constructed using standard settings in library free mode with DIA-NN (version 1.7.12)[71]. Proteins were annotated either using a protein database generated by translation of the Ensembl 99 annotation of the *M. auratus* genome sequence, or the Uniprot reference proteome (UP000189706). The latter was not used for statistical or functional analysis but is available through PRIDE (PXD025164). The libraries were automatically refined based on the project dataset at 0.01 global *q*-value (using the Generate spectral library option in DIA-NN) as previously described[19]. The output was filtered at 0.01 false discovery rate (FDR) at the peptide level.

**Materials proteomics**. Hydrophobic Sera-Mag magnetic carboxylate modified particles (44152105050250 Fisher Scientific), hydrophilic Sera-Mag magnetic carboxylate modified particles (24152105050250 Fisher Scientific), Twintec skirted low bind plates (0030129512 Eppendorf), TCEP (646547 Sigma Aldrich), SDS (A7249.1000 Applichem), CAA (22788 Merck/Millipore), ammonium bicarbonat (/871.2 Roth), 100% ACN (955-212 Fisher Scientific), 80% ethanol (1.00983.2500

Millipore), 230 µl Biomek Tips (B85903 Beckmann Coulter), Eppendorf 500 µl deep well plates (30501101 Eppendorf), Waters Acquity UPLC 700 µl plates (186005837 Waters GmbH) Sequencing grade modified Trypsin (V5117 Promega), Pierce Quantitative Fluorometric Peptide Assay (number 23290), formic acid (85178 Thermo Scientific), water (1.15333.2500 Merck), protease inhibitor cocktail complete mini (Roche 04693124001), benzonase nuclease (Sigma Aldrich E1014-25KU).

**Proteomics data pre-processing**. Four serum samples showed low quality and were removed. Peptides with excessive missing values (>30% per group) were excluded from analysis. Batch correction was applied. The peptide matrix was filtered using factor Proteotypic keeping only peptides belonging to one protein group. To obtain a quantitative protein data matrix, the log2-intensities of peptides belonging to one protein group were summarised by maxLFQ method[72] into protein log intensity.

**Proteomics statistical analysis**. Statistical analysis of proteomics data was carried out using internally developed R scripts. Linear modeling was based on the R package LIMMA[73]. Following model was applied to the sets of lung/serum samples (log(p) is log2 transformed expression of a protein): log(p) ~ 0 + Class(Day) + Gender

Here, categorical factor Class(Day) has 8 levels:
Infected(D02), Infected(D03), Infected(D05), Infected(D14),
Control(D02), Control(D03), Control(D05), Control(D14)
Categorical factor Gender has two levels: male, female.

The following contrasts were evaluated to trace time dependence of response to viral infection (Note that Contrast5 addresses the average difference between infected and recovered animals and Contrast6 addresses the difference between infected and control animals on average):

Contrast1: Infected(D02) – Control(D02)
Contrast2: Infected(D03) – Control(D03)
Contrast3: Infected(D05) – Control(D05)
Contrast4: Infected(D14) – Control(D14)
Contrast5: [Infected(D02) + Infected(D03) + Infected(D05)]/3 [Control(D02) + Control(D03) + Control(D05)]/3 − [Infected(D14) − Control(D14)]
Contrast6: [Infected(D02) + Infected(D03) + Infected(D05)]/3 − [Control (D02) + Control(D03) + Control(D05)]/3

In serum set of samples there was only one control group at 3 dpi and it was used to build contrasts replacing control groups at other dpi's.

For finding regulated features following criteria were applied:

Significance level alpha was set to guarantee false discovery rate below 10% at the response maximum (5 dpi) in both sample types. We found that alpha = 0.01 was delivering regulated proteins with Benjamini–Hochberg FDR below 8% in lung tissue and below 6% in serum and used it for feature selection.

The log fold change criterion was applied to guarantee that the measured signal is above the average noise level. As such we have taken mean residual standard deviation of linear model: log2(T) = mean residual SD of linear modeling (T = 1.45 in lung and T = 1.37 in serum).

**Functional analysis of proteomics data**. Functional analysis was carried out using gprofiler2 R package[74]. For selecting the most (de)regulated GO terms we applied filter: 2≤ term size ≤200. Redundancy of terms was then reduced using REVIGO[75]. Default REVIGO settings were applied. Analyses for each Contrast 1–6 and then all in parallel were carried out with Benjamini–Hochberg FDR threshold 0.2. Organism for search was specified as mauratus—*Mesocricetus auratus* (Syrian hamster). Statistical domain scope was set to custom, list of all identified proteins was provided as background.

**Statistical analyses of clinical hamster data**. GraphPad Prism 9.1.2 software was used for statistical analysis of clinical data. The statistical details of all analyzed experiments are given in the respective figure legends.

**Annotation of the *M. auratus* genome**. The *M. auratus* genome (MesAur1.0) sequence and annotation (gtf file, version 99) was downloaded from Ensembl. We noticed that 3′-UTRs in this annotation were frequently too short to capture all transcriptome reads and particularly the 3′ end reads in single-cell RNA-sequencing, so we extended all 3′-UTRs for coding genes by 1000 bp. The *Ifit2* gene was extended by 2000 bp. For key genes analyzed in this manuscript, we verified that this extension did not lead to overlaps with downstream genes. The details of this approach are depicted in the supplementary note under Elongation of 3′-UTRs in the Ensembl 99 MesAur 1.0 annotation.

The Ensemble annotation was extended by mapping ENSEMBL gene ids without annotated gene names to entrez identifiers and to the homolog associated gene names using biomaRt[76]. Wherever existing, we extracted the gene name from the NCBI's All_Mammalia.gene_info (download from ftp://ftp.ncbi.nlm.nih.gov/gene/DATA/GENE_INFO/Mammalia/) table, capturing 1067 gene names. Otherwise, we used available homolog associated gene names yielding 1193 additional entries.

**Analysis of bulk RNA-sequencing data**. Reads were aligned to the genome using hisat2[77] and quantified using quasR[78]. We then performed gene set enrichment analysis with tmod[79] and Hallmark, Reactome and GO BP gene sets from MSigDB v7.0[80], ranking genes by the product of the sign of the log2 fold change and log10 adjusted *p*-value and converting hamster gene names to human using the biomaRt mouse-to-human mapping.

**Analysis of single-cell RNA-sequencing data**. Data analysis was done in R[81], using Seurat[82] and packages from tidyverse[83], and glmer[84]. All used code with annotation is available through Github at https://github.com/Berlin-Hamster-Single-Cell-Consortium.

Raw single-cell sequencing data were processed using CellRanger 3.1.0 (10× Genomics) with standard parameters, based on a combined MesAur1.0/SARS-CoV-2 (GenBank entry MN908947) reference. Raw feature barcode matrices from the CellRanger output were read into Seurat using the Read10X function and a Seurat object created using the CreateSeuratObject function. Cells with more than 7% mitochondrial reads, based on the percentage feature expression of the mitochondrial genes *Cox1*, *Cytb*, *Nd1*, *Nd2*, *Nd4*, *Nd5*, *Nd6* were excluded (reads from other mitochondrial genes were not detected in the data). Furthermore, cells with less than 1000 (lung) or 500 (blood) detected genes were also excluded from downstream analysis. Sample sets (all lung, or all blood, or blood/lung combined from the individual time points) were then integrated using the SCTransform workflow, as illustrated on the Seurat website[85]. Briefly, the Seurat object was split by the hamster that the data points originated from and separately transformed using SCTransform to normalise and scale the data. To prevent batch specific/animal specific effects from obscuring results, these split objects were integrated using the SelectIntegrationFeatures, PrepSCTIntegration, FindIntegrationAnchors, and IntegrateData functions in succession. PCA and UMAP dimensional reduction analyses respectively were performed on the integrated object, using 30 dimensions for the UMAP as the SCT workflow reportedly shows more robust results with higher dimensionality. Cells were subjected to Louvain clustering using the FindNeighbours and FindClusters (with a resolution parameter of 0.8 for lung samples and 0.5 for the blood samples) functions.

As there are currently no publicly available datasets derived from our model system that could be used for fully automated cell type assignment, we used a combination of marker expression and label transfer from available *Mus musculus* and human datasets. To annotate clusters in the lung scRNAseq data, we used Seurat's TransferData workflow[85] and two different reference datasets: Tabula Muris[86] and the Human Lung Cell Atlas[87]. Integration was performed using matching gene names between mouse and hamster, with gene names in the human data converted to mouse using biomaRt. We then used the predicted cell type of the majority of cells in each cluster as well as cell type marker genes from the literature and public databases to guide cluster annotation[88,89]. The following populations were confirmed: Alveolar macrophages (*Siglecf*$^{+}$, *Marco*$^{+}$)[90], interstitial macrophages (*C1qb*$^{+}$)[91], monocytic macrophages (*Ccr2*$^{+}$, *Ccr5*$^{+}$, *Arg1*$^{+}$)[92,93], *Treml4*$^{+}$-monocytes (*Treml4*$^{+}$)[94], neutrophils (*S100a8*$^{+}$, *Cxcr2*$^{+}$, *Camp*$^{+}$)[44,95], myeloid dendritic cells (mDC) (*Flt3*$^{+}$, *H2-Ab1*$^{hi}$, *Irf8*$^{lo}$, *Tcf4*$^{lo}$) and plasmacytoid dendritic cells (pDC) (*Flt3*$^{+}$, *H2-Ab1*$^{hi}$, *Irf8*$^{hi}$, *Tcf4*$^{hi}$)[86,96–98], T/NK/cells (*Cd3e*$^{+}$, *Cd4*$^{+}$ or *Cd8a*$^{+}$, *Gzma*$^{+}$, *Nkg7*$^{+}$)[86,95,99–101], B cells (*Cd79b*$^{+}$, *Ms4a1*$^{+}$)[44,102], alveolar epithelial cells type 1 (*Rtkn2*$^{+}$)[91], endothelial cells (*Pecam1*$^{+}$)[90], ciliated epithelial cells (*Foxj1*$^{+}$)[102], alveolar epithelial cells type 2 (*Lamp3*$^{+}$)[102], smooth muscle cells (*Tagln*$^{+}$, *Acta2*$^{+}$)[91,103], fibroblasts (*Dcn*$^{+}$)[91] as well as myofibroblasts (*Dcn*$^{+}$, *Tagln*$^{hi}$, *Acta2*$^{hi}$).

For the analysis of single-cell sequencing data for blood samples, we performed initial clustering and identified, cluster marker genes using the FindAllMarkers function. Clusters expressing high levels of erythrocyte marker genes *Snca*, *Fam46c*, and *Alas2* were identified as erythrocyte contamination[104–106]. Cells in these clusters, as well as a cluster of most likely dead cells, marked by the expression of mitochondrial genes, were removed and the data was re-integrated using the workflow described above. Cell type annotations were assigned to the identified cluster using the follow marker genes: Classical (inflammatory) monocytes (*Ccr2*$^{+}$, *Cx3cr1*$^{lo}$, *Adgre1*$^{+}$); non-classical (residential) monocytes (*Ccr2*$^{-}$, *Cx3cr1*$^{hi}$, *Adgre1*$^{+}$)[107–109]; mature neutrophils (*Cxcr2*$^{+}$, *S100a8*$^{+}$, *Camp*$^{lo}$, *Retn*$^{lo}$, *Ltf*$^{lo}$) and immature neutrophils (*Cxcr2*$^{+}$, *S100a8*$^{+}$, *Camp*$^{hi}$, *Retn*$^{hi}$, *Ltf*$^{hi}$)[44,95,110,111]; myeloid dendritic cells (*Flt3*$^{+}$, *H2-Ab1*$^{hi}$, *Irf8*$^{lo}$, *Tcf4*$^{lo}$) and plasmacytoid dendritic cells (*Flt3*$^{+}$, *H2-Ab1*$^{hi}$, *Irf8*$^{hi}$, *Tcf4*$^{hi}$)[86,96–98]; T cells (*Cd3e*$^{+}$, *Cd4*$^{+}$ or *Cd8a*$^{+}$) and activated T cells (*Cd3e*$^{+}$, *Cd4*$^{+}$ and/or *Cd8a*$^{+}$, *Gzma*$^{+}$)[86,95,99,101], natural killer (NK) cells (*Cd3e*$^{-}$, *Nkg7*$^{+}$)[95,100]; B cells (*Cd79a*$^{+}$, *Ms4a1*$^{+}$)[44,102,112] and platelets (*Gng11*$^{+}$, *Ppbp*$^{+}$)[22,113]. While cluster 17 showed no expression of *Ccr2*, the levels of *Adgre1* and *Cd14* were considerable and it was considered as comprising classical monocytes for the purposes of this study[114].

Previously published scRNAseq data of bronchoalveolar lavages originating from COVID-19 patients data from Liao et al.[25] was processed using the same (Seurat) workflow in R. We kept cells with less than 10% mitochondrial reads, less than 50,000 UMIs and less than 6000 genes and used IntegrateData to combine different samples. We then again used the Human Lung Cell Atlas reference and TransferData to annotate clusters.

Differential cell density was calculated as previously described[115] by plotting the log2 ratio of two separate 2D kernel density estimators interpolated on the UMAP coordinates of each cell.

Gene ontology and KEGG pathway analysis was performed using the STRING database at string-db.org[116].

**Reporting summary**. Further information on research design is available in the Nature Research Reporting Summary linked to this article.

## Data availability

Raw and processed data is available at the NCBI gene expression omnibus, entry "GSE162208". The mass spectrometry proteomics data have been deposited to the ProteomeXchange Consortium via the PRIDE partner repository[117] with the dataset identifier "PXD025164". Publicly available datasets that were used in this manuscript can be found at "GSE145926"[25], combined with on sample "GSM3660650"[26], as well as "doi: 10.6084/m9.figshare.12436517 [https://figshare.com/articles/dataset/COVID-19_severity_correlates_with_airway_epithelium-immune_cell_interactions_identified_by_single-cell_analysis/12436517]"[27]. Source data are provided with this paper.

## Code availability

The code used for data analysis is available at github.com, https://github.com/Berlin-Hamster-Single-Cell-Consortium and via https://doi.org/10.5281/zenodo.4983546[118] the code is citable. Further Supplementary data is available at http://www.mdc-berlin.de/singlecell-SARSCoV2.

Received: 15 January 2021; Accepted: 13 July 2021;
Published online: 11 August 2021

## References

1. Guan, W. J. et al. Clinical characteristics of coronavirus disease 2019 in China. *N. Engl. J. Med* **382**, 1708–1720 (2020).
2. Osterrieder, N. et al. Age-dependent progression of SARS-CoV-2 infection in Syrian hamsters. *Viruses* **12**, 779 (2020).
3. Imai, M. et al. Syrian hamsters as a small animal model for SARS-CoV-2 infection and countermeasure development. *Proc. Natl Acad. Sci. USA* **117**, 16587–16595 (2020).
4. Bertzbach, L. D. et al. SARS-CoV-2 infection of Chinese hamsters (Cricetulus griseus) reproduces COVID-19 pneumonia in a well-established small animal model. *Transbound Emerg. Dis.* **68**, 1075–1079 (2020).
5. Trimpert, J. et al. The Roborovski dwarf hamster is a highly susceptible model for a rapid and fatal course of SARS-CoV-2 Infection. *Cell Rep.* **33**, 108488 (2020).
6. Sia, S. F. et al. Pathogenesis and transmission of SARS-CoV-2 in golden hamsters. *Nature* **583**, 834–838 (2020).
7. Kreye, J. et al. A therapeutic non-self-reactive SARS-CoV-2 antibody protects from lung pathology in a COVID-19 hamster model. *Cell* **183**, 1058–1069 (2020). e1019.
8. Lee, A. C. et al. Oral SARS-CoV-2 Inoculation establishes subclinical respiratory infection with virus shedding in golden Syrian hamsters. *Cell Rep. Med* **1**, 100121 (2020).
9. Gruber, A. D. et al. Standardization of reporting criteria for lung pathology in SARS-CoV-2-infected hamsters: what matters? *Am. J. Respir. Cell Mol. Biol.* **63**, 856–859 (2020).
10. Roberts, A. et al. Severe acute respiratory syndrome coronavirus infection of golden Syrian hamsters. *J. Virol.* **79**, 503–511 (2005).
11. Gong, S. R. & Bao, L. L. The battle against SARS and MERS coronaviruses: Reservoirs and Animal Models. *Anim. Model Exp. Med.* **1**, 125–133 (2018).
12. Gretebeck, L. M. & Subbarao, K. Animal models for SARS and MERS coronaviruses. *Curr. Opin. Virol.* **13**, 123–129 (2015).
13. Subbarao, K. & Roberts, A. Is there an ideal animal model for SARS? *Trends Microbiol* **14**, 299–303 (2006).
14. Tostanoski, L. H. et al. Ad26 vaccine protects against SARS-CoV-2 severe clinical disease in hamsters. *Nat. Med* **26**, 1694–1700 (2020).
15. Jiang, R. D. et al. Pathogenesis of SARS-CoV-2 in transgenic mice expressing human angiotensin-converting enzyme 2. *Cell* **182**, 50–58 (2020). e58.
16. Winkler, E. S. et al. SARS-CoV-2 infection of human ACE2-transgenic mice causes severe lung inflammation and impaired function. *Nat. Immunol.* **21**, 1327–1335 (2020).
17. Lagunas-Rangel, F. A. Neutrophil-to-lymphocyte ratio and lymphocyte-to-C-reactive protein ratio in patients with severe coronavirus disease 2019 (COVID-19): a meta-analysis. *J. Med Virol.* **92**, 1733–1734 (2020).
18. Liu, J. et al. Longitudinal characteristics of lymphocyte responses and cytokine profiles in the peripheral blood of SARS-CoV-2 infected patients. *EBioMedicine* **55**, 102763 (2020).
19. Messner, C. B. et al. Ultra-high-throughput clinical proteomics reveals classifiers of COVID-19 infection. *Cell Syst.* **11**, 11–24 (2020). e14.
20. Demichev, V. et al. A time-resolved proteomic and prognostic map of COVID-19. *Cell systems*, https://doi.org/10.1016/j.cels.2021.05.005 (2021).
21. Zeng, H. L. et al. Proteomic characteristics of bronchoalveolar lavage fluid in critical COVID-19 patients. *FEBS J.* https://doi.org/10.1111/febs.15609 (2020).
22. Schoggins, J. W. Interferon-stimulated genes: what do they all do?.*Annu Rev. Virol.* **6**, 567–584 (2019).
23. Hou, Y. J. et al. SARS-CoV-2 reverse genetics reveals a variable infection gradient in the respiratory tract. *Cell* **182**, 429–446.e414 (2020).
24. Olajuyin, A. M., Zhang, X. & Ji, H. L. Alveolar type 2 progenitor cells for lung injury repair. *Cell Death Disco.* **5**, 63 (2019).
25. Liao, M. et al. Single-cell landscape of bronchoalveolar immune cells in patients with COVID-19. *Nat. Med* **26**, 842–844 (2020).
26. Morse, C. et al. Proliferating SPP1/MERTK-expressing macrophages in idiopathic pulmonary fibrosis. *Eur. Respir. J.* **54**, 1802441 (2019).
27. Chua, R. L. et al. COVID-19 severity correlates with airway epithelium-immune cell interactions identified by single-cell analysis. *Nat. Biotechnol.* **38**, 970–979 (2020).
28. Cantuti-Castelvetri, L. et al. Neuropilin-1 facilitates SARS-CoV-2 cell entry and infectivity. *Science* **370**, 856–860 (2020).
29. Daly, J. L. et al. Neuropilin-1 is a host factor for SARS-CoV-2 infection. *Science* **370**, 861–865 (2020).
30. Davies, J. et al. Neuropilin1 as a new potential SARSCoV2 infection mediator implicated in the neurologic features and central nervous system involvement of COVID19. *Mol. Med. Rep.* **22**, 4221–4226 (2020).
31. Liu T., Zhang L., Joo D. & Sun S. C. NF-kappaB signaling in inflammation. *Signal Transduct Target Ther* **2**, 17023 (2017).
32. Schneider, W. M., Chevillotte, M. D. & Rice, C. M. Interferon-stimulated genes: a complex web of host defenses. *Annu Rev. Immunol.* **32**, 513–545 (2014).
33. Michalick, L. et al. Plasma mediators in patients with severe COVID-19 cause lung endothelial barrier failure. *Eur. Respir. J.* **57**, 2002384 (2020).
34. Ackermann, M. et al. Pulmonary vascular endothelialitis, thrombosis, and angiogenesis in Covid-19. *N. Engl. J. Med* **383**, 120–128 (2020).
35. Ford, J. et al. CCL7 is a negative regulator of cutaneous inflammation following leishmania major infection. *Front. Immunol.* **9**, 3063 (2018).
36. Blaszczyk, J. et al. Complete crystal structure of monocyte chemotactic protein-2, a CC chemokine that interacts with multiple receptors. *Biochemistry* **39**, 14075–14081 (2000).
37. Schnoor, M., Alcaide, P., Voisin, M. B. & van Buul, J. D. Crossing the vascular wall: common and unique mechanisms exploited by different leukocyte subsets during extravasation. *Mediators Inflamm.* **2015**, 946509 (2015).
38. Johansen, M. D. et al. Animal and translational models of SARS-CoV-2 infection and COVID-19. *Mucosal Immunol.* **13**, 877–891 (2020).
39. Khoury, D. S. et al. Measuring immunity to SARS-CoV-2 infection: comparing assays and animal models. *Nat. Rev. Immunol.* **20**, 727–738 (2020).
40. 10x Genomics. Can I process neutrophils (or other granulocytes) using 10x Single Cell applications?) (2020).
41. Dietert, K. et al. Spectrum of pathogen- and model-specific histopathologies in mouse models of acute pneumonia. *PLoS ONE* **12**, e0188251 (2017).
42. Fu, J. et al. The clinical implication of dynamic neutrophil to lymphocyte ratio and D-dimer in COVID-19: a retrospective study in Suzhou China. *Thromb. Res* **192**, 3–8 (2020).
43. Middleton, E. A. et al. Neutrophil extracellular traps contribute to immunothrombosis in COVID-19 acute respiratory distress syndrome. *Blood* **136**, 1169–1179 (2020).
44. Schulte-Schrepping, J. et al. Severe COVID-19 is marked by a dysregulated myeloid cell compartment. *Cell* **182**, 1419–1440.e1423 (2020).
45. Hönzke, K. et al. Human lungs show limited permissiveness for SARS-CoV-2 due to scarce ACE2 levels but strong virus-induced immune activation in alveolar macrophages. *SSRN* https://ssrn.com/abstract=3687020 (2020).
46. Speranza, E. et al. Single-cell RNA sequencing reveals SARS-CoV-2 infection dynamics in lungs of African green monkeys. *Science Translational Medicine* **13**, eabe8146, https://doi.org/10.1126/scitranslmed.abe8146 (2021).
47. Van Strijp, J. A., Van Kessel, K. P., van der Tol, M. E. & Verhoef, J. Complement-mediated phagocytosis of herpes simplex virus by granulocytes. Binding or ingestion. *J. Clin. Invest* **84**, 107–112 (1989).
48. Merad, M. & Martin, J. C. Pathological inflammation in patients with COVID-19: a key role for monocytes and macrophages. *Nat. Rev. Immunol.* **20**, 355–362 (2020).
49. V'Kovski, P., Kratzel, A., Steiner, S., Stalder, H., & Thiel, V. Coronavirus biology and replication: implications for SARS-CoV-2. *Nat. Rev. Microbiol.* **19**, 155–170 (2020).
50. Fiege, J. K. et al. Single cell resolution of SARS-CoV-2 tropism, antiviral responses, and susceptibility to therapies in primary human airway epithelium. *PLoS pathogens* **17**, e1009292, https://doi.org/10.1371/journal.ppat.1009292 (2021).

51. Wyler, E. et al. Transcriptomic profiling of SARS-CoV-2 infected human cell lines identifies HSP90 as target for COVID-19 therapy. *iScience* **24**, 102151, https://doi.org/10.1016/j.isci.2021.102151 (2021).
52. Escher, R., Breakey, N. & Lammle, B. Severe COVID-19 infection associated with endothelial activation. *Thromb. Res.* **190**, 62 (2020).
53. Marchetti, M. COVID-19-driven endothelial damage: complement, HIF-1, and ABL2 are potential pathways of damage and targets for cure. *Ann. Hematol.* **99**, 1701–1707 (2020).
54. Thompson, B. T., Chambers, R. C. & Liu, K. D. Acute respiratory distress syndrome. *N. Engl. J. Med.* **377**, 562–572 (2017).
55. To, K. F. & Lo, A. W. Exploring the pathogenesis of severe acute respiratory syndrome (SARS): the tissue distribution of the coronavirus (SARS-CoV) and its putative receptor, angiotensin-converting enzyme 2 (ACE2). *J. Pathol.* **203**, 740–743 (2004).
56. Janice Oh, H. L., Ken-En Gan, S., Bertoletti, A. & Tan, Y. J. Understanding the T cell immune response in SARS coronavirus infection. *Emerg. Microbes Infect.* **1**, e23 (2012).
57. Shin, H. S. et al. Immune responses to middle east respiratory syndrome coronavirus during the acute and convalescent phases of human infection. *Clin. Infect. Dis.* **68**, 984–992 (2019).
58. Varchetta, S. et al. Unique immunological profile in patients with COVID-19. *Cell Mol. Immunol.* **18**, 604–612 (2020).
59. Peng, Y. et al. Broad and strong memory CD4(+) and CD8(+) T cells induced by SARS-CoV-2 in UK convalescent individuals following COVID-19. *Nat. Immunol.* **21**, 1336–1345 (2020).
60. Gudbjartsson, D. F. et al. Humoral immune response to SARS-CoV-2 in iceland. *N. Engl. J. Med* **383**, 1724–1734 (2020).
61. Ni, L. et al. Detection of SARS-CoV-2-specific humoral and cellular immunity in COVID-19 convalescent individuals. *Immunity.* **52**, 971–977 (2020). e973.
62. Mammoto, A. & Mammoto, T. Vascular niche in lung alveolar development, homeostasis, and regeneration. *Front Bioeng. Biotechnol.* **7**, 318 (2019).
63. Niethamer, T. K. et al. Defining the role of pulmonary endothelial cell heterogeneity in the response to acute lung injury. *Elife* **9**, e53072 (2020).
64. Palumbo-Zerr, K. et al. Orphan nuclear receptor NR4A1 regulates transforming growth factor-beta signaling and fibrosis. *Nat. Med.* **21**, 150–158 (2015).
65. Lee, H. S. et al. Altered AKAP12 expression in portal fibroblasts and liver sinusoids mediates transition from hepatic fibrogenesis to fibrosis resolution. *Exp. Mol. Med.* **50**, 48 (2018).
66. Cao, Z. et al. Targeting of the pulmonary capillary vascular niche promotes lung alveolar repair and ameliorates fibrosis. *Nat. Med.* **22**, 154–162 (2016).
67. Wolfel, R. et al. Virological assessment of hospitalized patients with COVID-2019. *Nature* **581**, 465–469 (2020).
68. Corman, V. M. et al. Detection of 2019 novel coronavirus (2019-nCoV) by real-time RT-PCR. *Euro Surveill.* **25**, 2000045 (2020).
69. Muller, T. et al. Automated sample preparation with SP3 for low-input clinical proteomics. *Mol. Syst. Biol.* **16**, e9111 (2020).
70. Messner, C. B. et al. Ultra-fast proteomics with Scanning SWATH. *Nat. Biotechnol.* **39**, 846–854 (2021).
71. Demichev, V., Messner, C. B., Vernardis, S. I., Lilley, K. S. & Ralser, M. DIA-NN: neural networks and interference correction enable deep proteome coverage in high throughput. *Nat. Methods* **17**, 41–44 (2020).
72. Cox, J. et al. Accurate proteome-wide label-free quantification by delayed normalization and maximal peptide ratio extraction, termed MaxLFQ. *Mol. Cell Proteom.* **13**, 2513–2526 (2014).
73. Ritchie, M. E. et al. limma powers differential expression analyses for RNA-sequencing and microarray studies. *Nucleic Acids Res* **43**, e47 (2015).
74. Kolberg, L. & Raudvere, U. gprofiler2: Interface to the'g:Profiler' Toolset (2020).
75. Supek, F., Bosnjak, M., Skunca, N. & Smuc, T. REVIGO summarizes and visualizes long lists of gene ontology terms. *PLoS One* **6**, e21800 (2011).
76. Durinck, S., Spellman, P. T., Birney, E. & Huber, W. Mapping identifiers for the integration of genomic datasets with the R/Bioconductor package biomaRt. *Nat. Protoc.* **4**, 1184–1191 (2009).
77. Kim, D., Paggi, J. M., Park, C., Bennett, C. & Salzberg, S. L. Graph-based genome alignment and genotyping with HISAT2 and HISAT-genotype. *Nat. Biotechnol.* **37**, 907–915 (2019).
78. Gaidatzis, D., Lerch, A., Hahne, F. & Stadler, M. B. QuasR: quantification and annotation of short reads in R. *Bioinformatics* **31**, 1130–1132 (2015).
79. Zyla, J. et al. Gene set enrichment for reproducible science: comparison of CERNO and eight other algorithms. *Bioinformatics* **35**, 5146–5154 (2019).
80. Liberzon, A. et al. The molecular signatures database (MSigDB) hallmark gene set collection. *Cell Syst.* **1**, 417–425 (2015).
81. R Core Team. R: A language and environment for statistical computing.). R Foundation for Statistical Computing (2019).
82. Butler, A., Hoffman, P., Smibert, P., Papalexi, E. & Satija, R. Integrating single-cell transcriptomic data across different conditions, technologies, and species. *Nat. Biotechnol.* **36**, 411–420 (2018).
83. Wickham, H. et al. Welcome to the Tidyverse. *J. Open Source Softw.* **4**, 1686 (2019).
84. Bates, D., Mächler, M., Bolker, B. & Walker, S. Fitting linear mixed-effects models using lme4. *J. Stat. Softw.* https://www.jstatsoft.org/article/view/v067i01/ (2015).
85. Stuart, T. et al. Comprehensive Integration of Single-. *Cell Data. Cell* **177**, 1888–1902 (2019). e1821.
86. Tabula Muris Consortium. Single-cell transcriptomics of 20 mouse organs creates a Tabula Muris. *Nature* **562**, 367–372 (2018).
87. Travaglini, K. J. et al. A molecular cell atlas of the human lung from single-cell RNA sequencing. *Nature* **587**, 619–625 (2020).
88. Franzen, O., Gan, L. M. & Bjorkegren, J. L. M. PanglaoDB: a web server for exploration of mouse and human single-cell RNA sequencing data. *Database (Oxford)* **2019**, baz046 (2019).
89. Zhang, X. et al. CellMarker: a manually curated resource of cell markers in human and mouse. *Nucleic Acids Res* **47**, D721–D728 (2019).
90. Han, X. et al. Mapping the mouse cell atlas by microwell-Seq. *Cell* **172**, 1091–1107.e1017 (2018).
91. Angelidis, I. et al. An atlas of the aging lung mapped by single cell transcriptomics and deep tissue proteomics. *Nat. Commun.* **10**, 963 (2019).
92. Lechner, A. J. et al. Recruited monocytes and type 2 immunity promote lung regeneration following pneumonectomy. *Cell Stem Cell* **21**, 120–134 (2017). e127.
93. Shaheen, Z. R. et al. CCR5 is a required signaling receptor for macrophage expression of inflammatory genes in response to viral double-stranded RNA. *Am. J. Physiol. Regul. Integr. Comp. Physiol.* **316**, R525–R534 (2019).
94. Briseno, C. G. et al. Distinct transcriptional programs control cross-priming in classical and monocyte-derived dendritic cells. *Cell Rep.* **15**, 2462–2474 (2016).
95. Zhao, Y. et al. Single-cell transcriptomic landscape of nucleated cells in umbilical cord blood. *Gigascience* **8**, giz047 (2019).
96. Dutertre, C. A. et al. Single-Cell Analysis of Human Mononuclear Phagocytes Reveals Subset-Defining Markers and Identifies Circulating Inflammatory Dendritic Cells. *Immunity* **51**, 573–589. e578 (2019).
97. Monaghan, K. L., Zheng, W., Hu, G. & Wan, E. C. K. Monocytes and monocyte-derived antigen-presenting cells have distinct gene signatures in experimental model of multiple sclerosis. *Front. Immunol.* **10**, 2779 (2019).
98. Rodrigues, P. F. et al. Distinct progenitor lineages contribute to the heterogeneity of plasmacytoid dendritic cells. *Nat. Immunol.* **19**, 711–722 (2018).
99. Raredon, M. S. B. et al. Single-cell connectomic analysis of adult mammalian lungs. *Sci. Adv.* **5**, eaaw3851 (2019).
100. Smith, S. L. et al. Diversity of peripheral blood human NK cells identified by single-cell RNA sequencing. *Blood Adv.* **4**, 1388–1406 (2020).
101. Zhu, P. et al. The cytotoxic T lymphocyte protease granzyme A cleaves and inactivates poly(adenosine 5′-diphosphate-ribose) polymerase-1. *Blood* **114**, 1205–1216 (2009).
102. Cohen, M. et al. Lung single-cell signaling interaction map reveals basophil role in macrophage imprinting. *Cell* **175**, 1031–1044.e1018 (2018).
103. Tawfik, O. et al. Transgelin, a novel marker of smooth muscle differentiation, effectively distinguishes endometrial stromal tumors from uterine smooth muscle tumors. *Int J. Gynecol. Obstet. Reprod. Med. Res.* **1**, 26–31 (2014).
104. Barbour, R. et al. Red blood cells are the major source of alpha-synuclein in blood. *Neurodegener. Dis.* **5**, 55–59 (2008).
105. Chiabrando, D., Mercurio, S. & Tolosano, E. Heme and erythropoieis: more than a structural role. *Haematologica* **99**, 973–983 (2014).
106. Durussel, J. et al. Blood transcriptional signature of recombinant human erythropoietin administration and implications for antidoping strategies. *Physiol. Genomics* **48**, 202–209 (2016).
107. Burgess, M., Wicks, K., Gardasevic, M. & Mace, K. A. Cx3CR1 expression identifies distinct macrophage populations that contribute differentially to inflammation and repair. *Immunohorizons* **3**, 262–273 (2019).
108. Cochain, C. et al. Single-cell RNA-Seq reveals the transcriptional landscape and heterogeneity of aortic macrophages in murine atherosclerosis. *Circ. Res* **122**, 1661–1674 (2018).
109. Ronning, K. E., Karlen, S. J., Miller, E. B. & Burns, M. E. Molecular profiling of resident and infiltrating mononuclear phagocytes during rapid adult retinal degeneration using single-cell RNA sequencing. *Sci. Rep.* **9**, 4858 (2019).
110. Kim, M. H. et al. A late-lineage murine neutrophil precursor population exhibits dynamic changes during demand-adapted granulopoiesis. *Sci. Rep.* **7**, 39804 (2017).
111. Xie, X. et al. Single-cell transcriptome profiling reveals neutrophil heterogeneity in homeostasis and infection. *Nat. Immunol.* **21**, 1119–1133 (2020).
112. Zuccolo, J. et al. Expression of MS4A and TMEM176 genes in human B lymphocytes. *Front. Immunol.* **4**, 195 (2013).
113. El-Gedaily, A., Schoedon, G., Schneemann, M. & Schaffner, A. Constitutive and regulated expression of platelet basic protein in human monocytes. *J. Leukoc. Biol.* **75**, 495–503 (2004).
114. Sampath, P., Moideen, K., Ranganathan, U. D. & Bethunaickan, R. Monocyte subsets: phenotypes and function in tuberculosis infection. *Front. Immunol.* **9**, 1726 (2018).

115. Praktiknjo, S. D. et al. Tracing tumorigenesis in a solid tumor model at single-cell resolution. *Nat. Commun.* **11**, 991 (2020).
116. Szklarczyk, D. et al. The STRING database in 2021: customizable protein-protein networks, and functional characterization of user-uploaded gene/measurement sets. *Nucleic Acids Res.* **49**, D605–D612 (2021).
117. Perez-Riverol, Y. et al. The PRIDE database and related tools and resources in 2019: improving support for quantification data. *Nucleic Acids Res.* **47**, D442–D450 (2019).
118. Wyler, E., Pennitz, P. & Postmus, D. Berlin-hamster-single-cell-consortium/single-cell-sequencing-of-COVID-19-pathogenesis-in-golden-hamsters: scRNAseq of COVID19 pathogenesis in golden Hamsters.). https://doi.org/10.5281/zenodo.4983546 (2021).

## Acknowledgements

The authors sincerely thank Drs. Jasmin Lienau and Alexis Vogelzang for excellent manuscript and figure editing. Computation has been performed on the HPC for Research cluster of the Berlin Institute of Health. The authors thank Angela Linke, Michaela Scholz, and Simon Dökel for excellent technical assistance with histopathology and ISH, and Jeannine Wilde, Madlen Sohn, and Tatiana Borodina (MDC Scientific Genomics Platforms) for sequencing. This research was funded by a Berlin Institute of Health (BIH) grant to G.N., a German Federal Ministry of Education and Research, Germany (BMBF) grant to M.W., grant number CAPSyS (01ZX1604B), and by a German Research Foundation (DFG) grant to J.T. and A.D.G., grant number SFB-TR84 Z01b. G.N., S.-M.W. and M.W. are supported by the BMBF and by the Agence nationale de la recherche (ANR) in the framework of MAPVAP (16GW0247). A.D.G. is supported by BMBF (NUM-COVID 19, Organo-Strat 01KX2021) and Einstein Foundation 3R (EZ-2020-597 FU). N.S. is supported by DFG (grant number SFB-TR84 B01, C09 and Z02) and BMBF (e:Med CAPSyS grants 01ZX1304B and 01ZX1604B). C.G. is supported by BMBF (NUM-COVID 19, Organo-Strat 01KX2021) and BIH. M.R. is supported by the Francis Crick Institute, which receives its core funding from Cancer Research UK (FC001134), the UK Medical Research Council (FC001134), and proteomic work in this manuscript has been conducted as part of the National Research Node 'Mass spectrometry in Systems Medicine (MSCoresys) BMBF, under grant agreement 031L0220. M.W. is supported by the DFG (SFB-TR84 C06 and C09, SFB1449 B02), by the BMBF in the framework of e:Med CAPSyS (01ZX1604B), PROVID (01KI20160A), e:Med SYMPATH (01ZX1906A), NUM-NAPKON (01KX2021) and by the BIH (CM-COVID). Supplementary Fig. 1a was generated with BioRender.com.

## Author contributions

Conceptualization, G.N., E.W., J.T. and M.W.; methodology, G.N., E.W., P.P., D.P., D.V., J.K., F.P., K.D., M.M., V.F., B.O., S.A., T.H., M.R., A.D.G. and J.T.; software/data analysis, G.N., E.W., P.P., D.P., F.P., K.D., M.M., V.F., B.O., S-M.W., S.A., T.H., M.R. and J.T.; investigation, G.N., E.W., P.P., D.P., D.V., J.K., F.P., K.D., M.M., V.F., B.O., S-M.W., S.A., T.H., C.D., L.E.S., J.T. and M.W.; resources, M.M., C.D., N.S., M.R., D.B., A.D.G., C.G., M.L., J.T. and M.W.; data curation, E.W.; writing—original draft preparation, G.N., E.W., J.T. and M.W..; writing—review and editing, G.N., E.W., P.P., D.P., J.K., F.P., K.D., M.M, V.F., B.O., S-M.W., C.D., L.E.S., N.S., M.R., D.B., A.D.G, C.G., M.L., J.T. and M.W.; supervision, G.N., E.W., J.T., C.G., M.L., and M.W.; project administration, G.N.; funding acquisition, G.N., J.T. and M.W. All authors have read and agreed to the published version of the manuscript."

## Funding

Open Access funding enabled and organized by Projekt DEAL.

## Competing interests

G.N. received funding for research from Biotest AG. E.W., P.P., D.P., D.V., J.K., F.P., K. D., M.M., V.F., B.O., S.-M.W., S.A., T.H., B.S., C.D., L.E.S., N.S., M.R., D.B., A.D.G., C.G., M.L. and J.T declare no conflict of interest. M.W. received funding for research from Actelion, Bayer Health Care, Biotest AG, Boehringer Ingelheim, Noxxon, Pantherna, Quark Pharma, Vaxxilon, and for advisory from Actelion, Aptarion, Astra Zeneca, Bayer Health Care, Berlin Chemie, Biotest, Boehringer Ingelheim, Chiesi, Glaxo Smith Kline, Novartis, Noxxon, Pantherna, Teva and Vaxxilon. The funders had no role in the design of the study, in the collection, analyses, or interpretation of data, in the writing of the manuscript, or in the decision to publish the results.

## Additional information

**Supplementary information** The online version contains supplementary material available at https://doi.org/10.1038/s41467-021-25030-7.

**Correspondence** and requests for materials should be addressed to G.N., E.W., J.T. or M.W.

**Peer review information** *Nature Communications* thanks Ujjwal Neogi and the other, anonymous, reviewer(s) for their contribution to the peer review of this work.

**Reprints and permission information** is available at http://www.nature.com/reprints

**Publisher's note** Springer Nature remains neutral with regard to jurisdictional claims in published maps and institutional affiliations.

### 2.3.2 COVID-19 Lebendimpfstoff induziert mukosale Immunität (Eigene Arbeit 5)

Veröffentlicht als: Forschungsartikel mit geteilter Erstautorenschaft*. Dieser Artikel ist ebenfalls Teil der unveröffentlichten Dissertation von J. M. Adler.

Der nachfolgende Text entspricht dem originalsprachlichen Abstrakt der Arbeit "*Live-attenuated vaccine sCPD9 elicits superior mucosal and systemic immunity to SARS-CoV-2 variants in hamsters*." (Nat Microbiol. 2023 Apr 3. doi: 10.1038/s41564-023-01352-8)[87] der Autoren **Geraldine Nouailles***, Julia M Adler*, Peter Pennitz, Stefan Peidli, Luiz Gustavo Teixeira Alves, Morris Baumgardt, Judith Bushe, Anne Voss, Alina Langenhagen, Christine Langner, Ricardo Martin Vidal, Fabian Pott, Julia Kazmierski, Aileen Ebenig, Mona V Lange, Michael D Mühlebach, Cengiz Goekeri, Szandor Simmons, Na Xing, Azza Abdelgawad, Susanne Herwig, Günter Cichon, Daniela Niemeyer, Christian Drosten, Christine Goffinet, Markus Landthaler, Nils Blüthgen, Haibo Wu, Martin Witzenrath, Achim D Gruber, Samantha D Praktiknjo, Nikolaus Osterrieder, Emanuel Wyler, Dusan Kunec, Jakob Trimpert.

> „Vaccines play a critical role in combating the COVID-19 pandemic. Future control of the pandemic requires improved vaccines with high efficacy against newly emerging SARS-CoV-2 variants and the ability to reduce virus transmission. Here we compare immune responses and preclinical efficacy of the mRNA vaccine BNT162b2, the adenovirus-vectored spike vaccine Ad2-spike and the live-attenuated virus vaccine candidate sCPD9 in Syrian hamsters, using both homogeneous and heterologous vaccination regimens. Comparative vaccine efficacy was assessed by employing readouts from virus titrations to single-cell RNA sequencing. Our results show that sCPD9 vaccination elicited the most robust immunity, including rapid viral clearance, reduced tissue damage, fast differentiation of pre-plasmablasts, strong systemic and mucosal humoral responses, and rapid recall of memory T cells from lung tissue after challenge with heterologous SARS-CoV-2. Overall, our results demonstrate that live-attenuated vaccines offer advantages over currently available COVID-19 vaccines."

nature microbiology

Article

https://doi.org/10.1038/s41564-023-01352-8

# Live-attenuated vaccine sCPD9 elicits superior mucosal and systemic immunity to SARS-CoV-2 variants in hamsters

Received: 30 June 2022

Accepted: 1 March 2023

Published online: 03 April 2023

Check for updates

Geraldine Nouailles[1,18], Julia M. Adler[1,2,18], Peter Pennitz[1], Stefan Peidli[3], Luiz Gustavo Teixeira Alves[4], Morris Baumgardt[1], Judith Bushe[5], Anne Voss[5], Alina Langenhagen[5], Christine Langner[2], Ricardo Martin Vidal[2], Fabian Pott[6,7], Julia Kazmierski[6,7], Aileen Ebenig[8], Mona V. Lange[8], Michael D. Mühlebach[8,9], Cengiz Goekeri[1,10], Szandor Simmons[11], Na Xing[2], Azza Abdelgawad[2], Susanne Herwig[12], Günter Cichon[12], Daniela Niemeyer[6,13], Christian Drosten[6,13], Christine Goffinet[6,7], Markus Landthaler[14], Nils Blüthgen[3], Haibo Wu[15], Martin Witzenrath[1], Achim D. Gruber[5], Samantha D. Praktiknjo[16], Nikolaus Osterrieder[2,17], Emanuel Wyler[4,19], Dusan Kunec[2,19] & Jakob Trimpert[2,19] ✉

Vaccines play a critical role in combating the COVID-19 pandemic. Future control of the pandemic requires improved vaccines with high efficacy against newly emerging SARS-CoV-2 variants and the ability to reduce virus transmission. Here we compare immune responses and preclinical efficacy of the mRNA vaccine BNT162b2, the adenovirus-vectored spike vaccine Ad2-spike and the live-attenuated virus vaccine candidate sCPD9 in Syrian hamsters, using both homogeneous and heterologous vaccination regimens. Comparative vaccine efficacy was assessed by employing readouts from virus titrations to single-cell RNA sequencing. Our results show that sCPD9 vaccination elicited the most robust immunity, including rapid viral clearance, reduced tissue damage, fast differentiation of pre-plasmablasts, strong systemic and mucosal humoral responses, and rapid recall of memory T cells from lung tissue after challenge with heterologous SARS-CoV-2. Overall, our results demonstrate that live-attenuated vaccines offer advantages over currently available COVID-19 vaccines.

As of 2023, 13 COVID-19 vaccines have met the standards for emergency use listing (EUL) by the WHO[1]. Authorized vaccines include inactivated virus and subunit vaccines, adenoviral-vectored spike and nucleoside-modified mRNA vaccines[2]. While available vaccines provide long-lasting protection from severe illness, waning of immunity is evident, particularly following the emergence and spread of omicron variants[3,4].

Optimal COVID-19 vaccines protect from severe disease, span a broad spectrum of virus variants and prevent or limit SARS-CoV-2 transmission. Live-attenuated vaccines (LAV), which have been successfully used against virus infections such as measles, mumps and rubella (MMR)[5], offer advantages over other types of vaccines. They do not require adjuvants[6] and can be administered locally, for example intranasally, as in the case of influenza LAVs[7]. Composed

A full list of affiliations appears at the end of the paper. ✉e-mail: trimpert.jakob@fu-berlin.de

of replication-competent viruses, intranasal LAVs mimic the natural course of infection and antigen production, which distinguishes them from locally administered, replication-incompetent vector- or antigen-based vaccines[8]. In contrast to empirically generated vaccines used in the past, modern LAV design utilizes molecular tools to limit virus replication and virulence while maintaining immunogenicity and antigenic integrity[9]. One recent strategy employed in the rational design of LAVs is codon pair deoptimization (CPD), which is suitable for both DNA[10] and RNA viruses[11], including SARS-CoV-2[12].

Current COVID-19 vaccines are administered intramuscularly and efficiently induce systemic immunity, including high titre of neutralizing antibodies, central and effector memory T cells[13], nasal-resident $CD8^+$ T cells[14], germinal centre B cells[15] and long-lived plasma cells[16]. However, this route is less effective in inducing durable mucosal IgA and IgG responses[17,18] and pulmonary tissue-resident memory cell responses[19]. Mucosal antibodies at the site of virus entry play crucial roles in limiting infectivity and transmission[20]. Accordingly, tissue-resident memory cells undergo faster recall responses due to local positioning and allow earlier cognate antigen recognition[21]. Hence, vaccines administered via respiratory routes are expected to provide robust local mucosal immunity against targeted pathogens[22]. Here we compare different vaccines and vaccine regimens, evaluating systemic and mucosal immunity conferred by each vaccine.

## Results

**In a heterologous SARS-CoV-2 Delta challenge setting, we evaluated efficacy and mode of action of the commercial mRNA vaccine** BNT162b2 and two vaccine candidates, Ad2-Spike, an adenoviral vector carrying the spike glycoprotein of SARS-CoV-2[23] and a live-attenuated SARS-CoV-2 named sCPD9[24,25]. To assess efficacy, Syrian hamsters were **vaccinated with a single dose (prime-only regimen) and challenged** with SARS-CoV-2 Delta variant 21 d post vaccination. Another group of hamsters received two vaccine doses 21 d apart (prime-boost regimen) and were challenge-infected 14 d after boosting (Fig. 1a). All vaccinations were well tolerated, as evidenced by steady weight gains post vaccination (Extended Data Fig. 1a).

### Vaccination alleviates clinical symptoms and reduces virus load

**All vaccination strategies protected hamsters from SARS-CoV-2 infection-induced body weight loss (Fig. 1b). Following a single vaccination, none of the vaccines completely prevented infection by SARS-CoV-2 Delta as evidenced by the presence of viral RNA in respiratory tracts (Fig. 1c,d). Only sCPD9 vaccine effectively reduced replicating virus to undetectable levels 2 d post challenge (dpc)** (Fig. 1e). Prime-boost vaccination improved overall vaccine efficacy against SARS-CoV-2 (Fig. 1f,g). Following prime-boost vaccination, viral RNA was significantly reduced, yet still detectable in all groups in oropharyngeal swabs and lungs. Vaccination schemes using sCPD9 were superior in reducing viral RNA (Fig. 1f,g). Similarly, levels of replication-competent virus in lungs were significantly reduced in vaccinated animals at 2 dpc. Importantly, only sCPD9 booster vaccination reduced replicating virus levels below the detection threshold, regardless of heterologous (mRNA) or homologous (sCPD9) priming (Fig. 1h). Results were confirmed by sequencing of bulk RNA from lungs (Extended Data Fig. 1b).

### LAV is superior in preventing inflammatory lung damage

To determine infection-induced lung damage, challenged hamsters were examined by histopathology. After single vaccination, sCPD9 was most efficient in preventing inflammation and pneumonia, as evidenced by lesser consolidated lung areas (Fig. 1m) and lower scores for lung inflammation, bronchitis and oedema (Fig. 1i,j and Extended Data Fig. 1c–f). Notably, animals that received other vaccination schedules displayed more prominent bronchial hyperplasia (Extended Data Fig. 2). A similar trend was observed for prime-boost regimens; however, particularly the mRNA vaccine displayed an improved histological outcome resulting from homologous boost (Fig. 1k,l and Extended Data Fig. 1g–j). Overall, homologous sCPD9 prime-boost vaccination provided superior lung protection from inflammation (Figs. 1m and 2a, and Extended Data Fig. 2). Lung transcriptome analysis also showed a broad downregulation of infection- and inflammation-related genes in vaccinated hamsters, with the greatest effects seen in homologous and heterologous sCDP9 vaccinations (Supplementary Fig. 1).

To correlate levels of inflammation with cellular responses, we performed single-cell RNA sequencing (scRNA-seq) of lung samples (Fig. 2b and Supplementary Fig. 2a). Results showed that pulmonary recruitment of monocytic macrophages was significantly reduced in sCPD9 + sCPD9-vaccinated animals at 2 dpc (Fig. 2c and Supplementary Fig. 2b). Similar, although less pronounced effects, were observed in animals that received sCPD9 prime-only vaccination (Fig. 2d and Supplementary Fig. 2c). Additionally, interferon-stimulated genes induced by SARS-CoV-2 infection[26] were broadly downregulated in vaccinated compared with unvaccinated animals, with monocytic macrophages, *Treml4*$^+$ monocytes and endothelial cells appearing particularly responsive (Supplementary Fig. 3). Inflammatory mediators such as *Cxcl10* or *Tnfsf10* showed a more uniform response pattern across cell types compared with interferon-stimulated genes (Fig. 2e and Supplementary Fig. 4a). Since macrophage subtypes showed different gene expression patterns between vaccination groups, we examined the distribution of viral RNA within lungs by in situ hybridization (Fig. 2f and Supplementary Fig. 4b). In unvaccinated animals, viral RNA was detected throughout the lungs, while mRNA+mRNA vaccination reduced its occurrence to single patches. In sCPD9 + sCPD9 animals, viral RNA was barely detectable (Supplementary Fig. 4b). Notably, in mRNA+mRNA animals, most of the detectable viral RNA was present in macrophages (Fig. 2f).

### LAV elicits the most potent humoral immunity against SARS-CoV-2

To determine humoral responses, we quantified the ability of hamster sera collected before challenge (0 dpc) and at 2 and 5 dpc of prime (Fig. 3a–d) and prime-boost (Fig. 3e–h) vaccinated hamsters to neutralize SARS-CoV-2 variants. The capacity of sera from sCPD9 vaccinees to neutralize ancestral SARS-CoV-2 variant B.1 significantly exceeded that of all other groups (Fig. 3a). Similarly, sCPD9 sera provided superior neutralization of variants of concern B.1.351 (Beta), B.1.617.2 (Delta) and B.1.1.529 (Omicron, BA.1) (Fig. 3b,c). For Omicron BA.1, neutralization capacity was considerably reduced in all groups; however, neutralization by sCPD9 sera was significant (Fig. 3d). Generally, challenge infection increased neutralizing antibodies over time in all groups by 5 dpc (Fig. 3a–d).

Hamsters boosted with sCPD9 or the mRNA vaccine produced measurably more neutralizing antibodies than those receiving prime-only vaccination. Overall, booster vaccination increased serum neutralization capacity across different variants (Fig. 3e–h). Among the tested variants, Omicron BA.1 displayed the greatest ability to escape neutralization. Only prime-boost vaccination with sCPD9 provided hamsters with a significant ability to neutralize Omicron BA.1 (Fig. 3h).

Prime-boost sCDP9 and mRNA+sCDP9-vaccinated hamsters mounted significant IgG antibody responses against spike, ORF3a and nucleocapsid protein (N), whereas IgG from prime-boost mRNA and Ad2-vaccinated hamsters only reacted with spike protein (Fig. 3i). Although antibodies directed against N and ORF3a are unlikely to contribute to virus neutralization, abundance of these antibodies illustrates the broader immunological response elicited by LAV vaccination. Higher virus neutralization titre in animals that underwent prime-boost vaccination (compare Fig. 3a–d with e–h) as well as increased IgG anti-spike reactivity following a challenge infection

https://doi.org/10.1038/s41564-023-01352-8

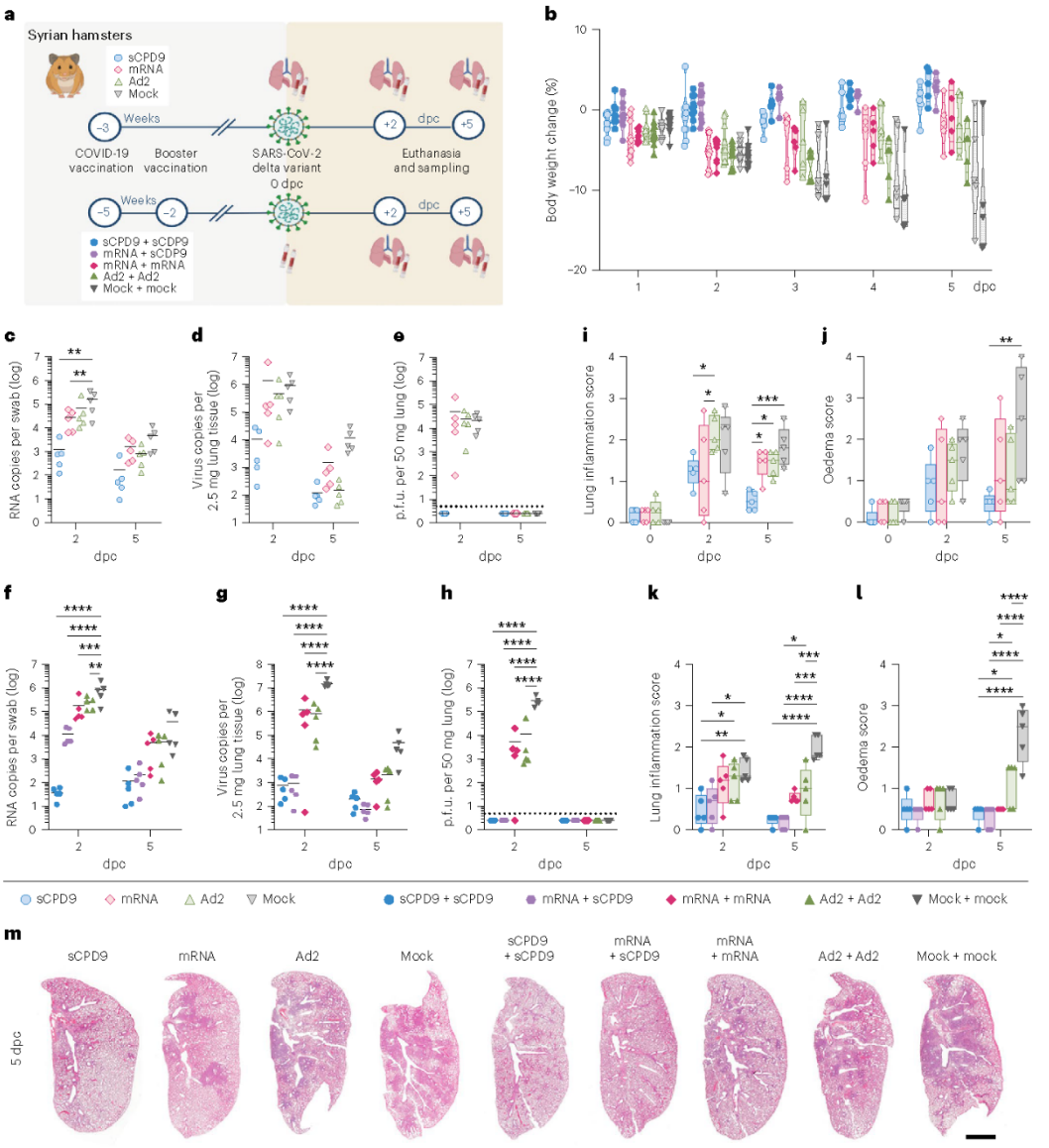


**Fig. 1 | Disease severity following SARS-CoV-2 infection in vaccinated and non-vaccinated hamsters. a**, Experimental scheme. Syrian hamsters were vaccinated as indicated and challenged with SARS-CoV-2 ($1 \times 10^5$ p.f.u. SARS-CoV-2 Delta). Prime and prime-boost experiments were performed independently. **b**, Body weights (in %) after virus challenge were measured until analysis timepoint and displayed according to vaccination group. Violin plot (truncated) with quartiles and median. **c**–**l**, Results of prime-vaccinated and challenged animals (**c**–**e**,**i**,**j**) and results of prime-boost-vaccinated and challenged animals (**f**–**h**,**k**,**l**): number of genomic RNA (gRNA) copies detected in oropharyngeal swabs (**c**,**f**) and homogenized lung tissue (**d**,**g**). **e**,**h**, Quantification of replication-competent virus as p.f.u. per 50 mg homogenized lung tissue. Dotted line marks the limit of detection (DL = 5 p.f.u.). Titre below the detection limits set to DL/2 = 2.5 p.f.u. **i**,**k**, Lung inflammation was scored including severity of pneumonia, alveolar epithelial necrosis and endothelialitis. **j**,**l**, Lung oedema score accounting for perivascular and alveolar oedema. **m**, H&E-stained left lung sections illustrate different severities of pneumonia including peribronchial cuffs and consolidated areas between different vaccine schedules and non-vaccinated animals at 5 dpc. Scale bar, 3 mm. In **c**–**e** and **f**–**h** scatter dot plots: lines indicate means, symbols represent individual hamsters. In **i**,**j**,**k**,**l**: centre lines represent medians, boxes the 25th to 75th percentiles, and whiskers the minimum to maximum values; symbols represent individual hamsters. In **c**–**l**, two-way analysis of variance (ANOVA) and Tukey's multiple comparisons test are shown. $n = 5$ animals per group. $^*P < 0.05$, $^{**}P < 0.01$, $^{***}P < 0.001$ and $^{****}P < 0.0001$. Fig. 1a was created with BioRender.com.

https://doi.org/10.1038/s41564-023-01352-8

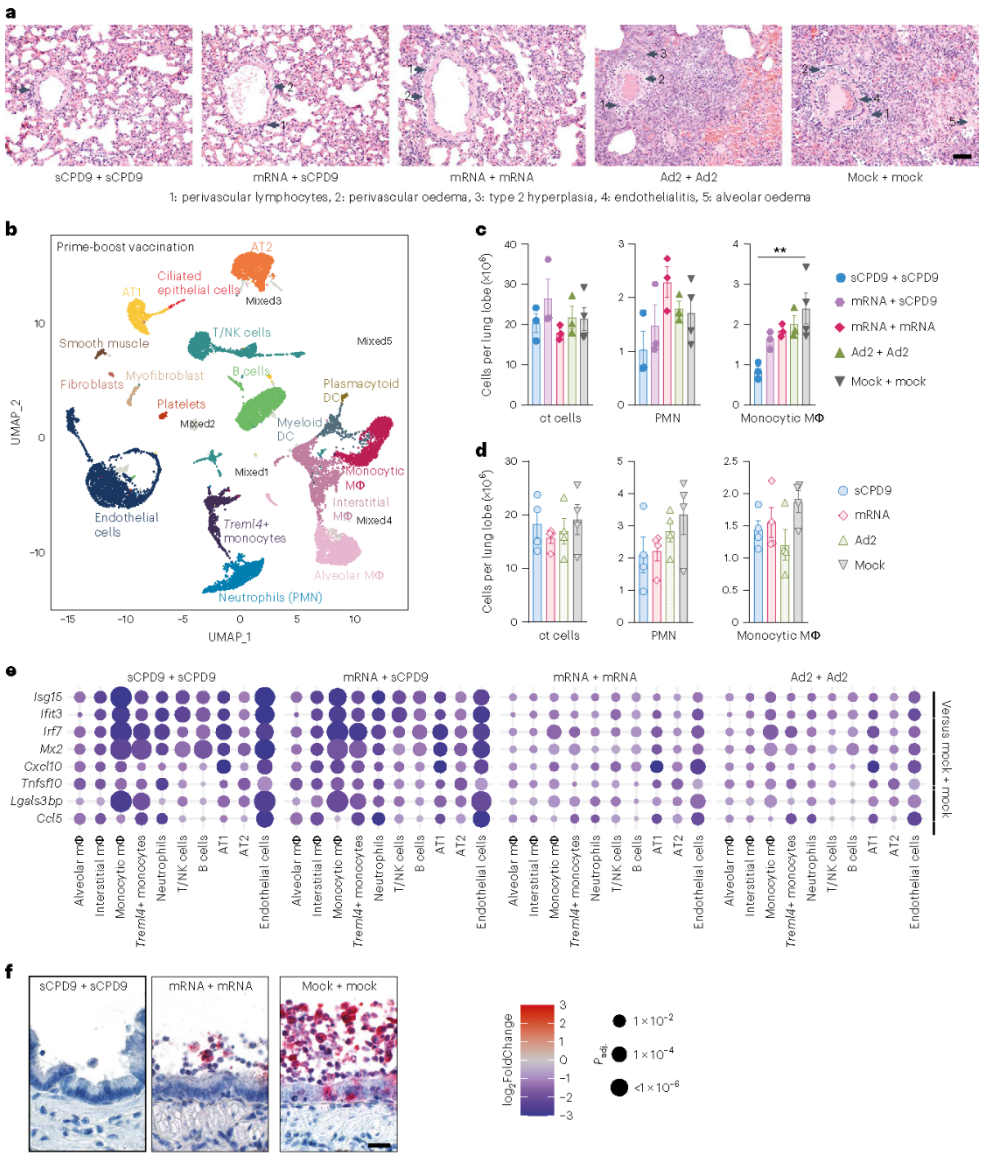


**Fig. 2 | Pneumonia and pro-inflammatory transcriptional response are strongly reduced in vaccinated animals. a**, H&E-stained lung sections at 5 dpc from the prime-boost vaccination experiment identified perivascular lymphocytes (1), perivascular oedema (2), metaplastic epithelial remodelling (3), endothelialitis (4) and alveolar oedema (5) as labeled by numbered arrows, groups as indicated. Scale bar, 90 µm. **b**, Two-dimensional projections of single-cell transcriptomes using uniform manifold approximation projection (UMAP) of lung cells (prime-boost experiment). Cells are coloured by cell type as annotated on the basis of known marker genes. **c**,**d**, Manual cell count of isolated lung cells per lung lobe (ct cells), calculated numbers of indicated cell types (PMN, monocytic macrophages) based on scRNA-seq-determined cell frequencies for the prime-boost experiment (**c**) and prime experiment (**d**). Bar plots with mean ± s.e.m., symbols represent individual hamsters ($n_{sCPD9} = 4$, $n_{mRNA} = 4$, $n_{Ad2} = 4$, $n_{mock} = 4$, $n_{sCPD9+sCPD9} = 3$, $n_{mRNA+sCPD9} = 3$, $n_{mRNA+mRNA} = 3$, $n_{Ad2+Ad2} = 3$, $n_{mock+mock} = 4$), ordinary one-way ANOVA and Tukey's multiple comparisons test, $^{**}P < 0.01$. **e**, Dot plots showing fold changes of gene expression in indicated cell types of the four prime-boost vaccination strategies compared to mock-mock-vaccinated animals. Selected interferon-stimulated genes and pro-inflammatory cytokines are visualized as follows: coloration and point size indicate $\log_2$-transformed fold changes (FC) and *P* values, respectively, in vaccinated compared to mock-mock-vaccinated animals. Adjusted *P* values ($P_{adj}$) were calculated by DESeq2 using Benjamini–Hochberg corrections of two-sided Wald test *P* values. Genes are ordered by unsupervised clustering. **f**, Localization of viral RNA by in situ hybridization in a longitudinal section of a bronchus at 2 dpc. Red signals, viral RNA; blue, hemalum counterstain. Scale bar, 30 µm.

https://doi.org/10.1038/s41564-023-01352-8

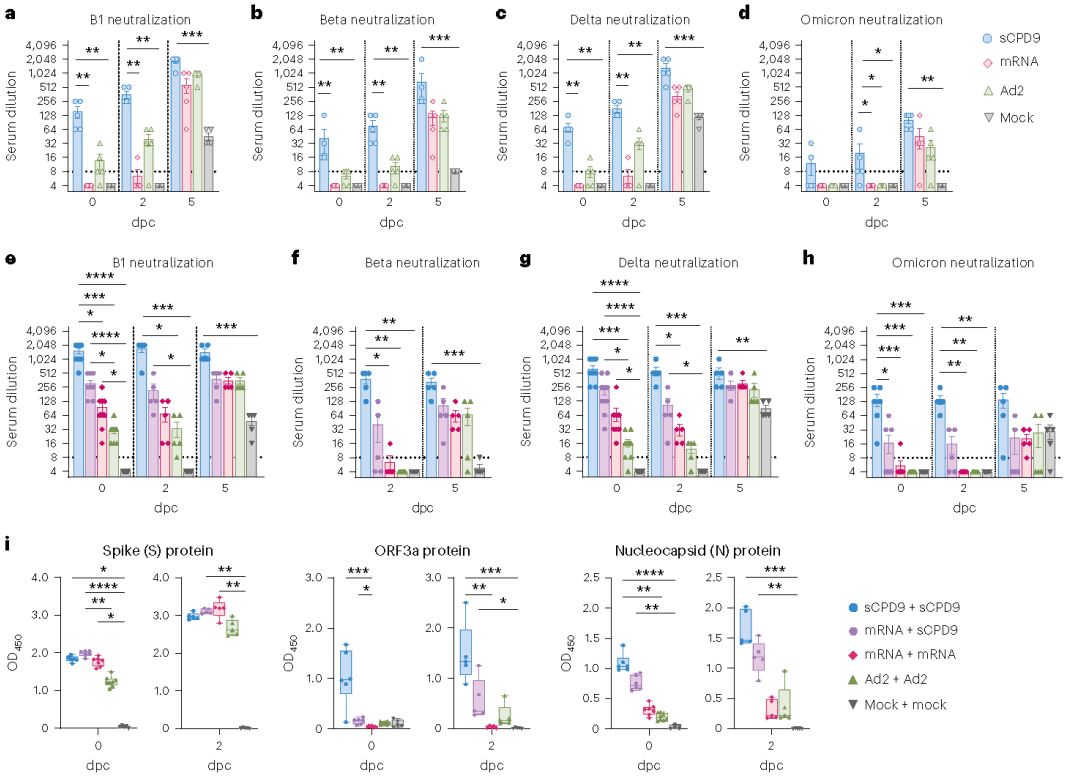


**Fig. 3 | Antibody and blood cellular immune response to vaccination and challenge. a**–**h**, Serum neutralization titres of hamsters that received prime (**a**–**d**) and prime-boost (**e**–**h**) vaccination before (0 dpc) and at 2 or 5 dpc with SARS-CoV-2. Neutralization capacity was tested against variant B1 (**a**,**e**), Beta (**b**,**f**), Delta (**c**,**g**) and Omicron BA.1 (**d**,**h**). The lower limit of detection was at dilution 1:8 (dotted line) and the upper limit at 1:2,048. Bar plots with mean ± s.e.m., $n = 5$ per condition; in **e**–**h**, $n = 10$ at baseline (0 dpc), except in **e** and **g** where $n_{sCPD9+sCPD9\,(0dpc)} = 9$ and in **h** where $n_{sCPD9+sCPD9\,(0dpc)} = 6$, $n_{mRNA+sCPD9\,(0dpc)} = 9$, $n_{mRNA+mRNA\,(0dpc)} = 8$, $n_{Ad2+Ad2(0dpc)} = 8$ and $n_{mock+mock\,(0dpc)} = 7$ due to limited serum quantities. **i**, SARS-specific IgG levels against spike, ORF3a and nucleocapsid protein in sera from prime-boost-vaccinated hamsters on days 0 and 2 after challenge. Results are shown as optical density (OD) determined at 450 nm. Centre line, median; box, 25th to 75th percentiles; whiskers, minimum to maximum; symbols indicate individual values, $n_{sCPD9+sCPD9\,(day\,0)} = 6$, $n_{mRNA+sCPD9\,(day\,0)} = 6$, $n_{mRNA+mRNA\,(day\,0)} = 7$, $n_{Ad2+Ad2\,(day\,0)} = 8$, $n_{mock+mock\,(day\,0)} = 5$, $n_{sCPD9+sCPD9\,(day\,2)} = 5$, $n_{mRNA+sCPD9\,(day\,2)} = 5$, $n_{mRNA+mRNA\,(day\,2)} = 5$, $n_{Ad2+Ad2\,(day\,2)} = 5$ and $n_{mock+mock\,(day\,2)} = 5$ animals. For **a**–**i**, Kruskal–Wallis and Dunn's multiple comparisons tests were performed; $^{*}P < 0.05$, $^{**}P < 0.01$, $^{***}P < 0.001$ and $^{****}P < 0.0001$.

of these animals (Supplementary Fig. 4c) suggest a benefit of booster vaccinations.

### LAV favours adaptive cellular immune responses in blood

Next, we evaluated blood single-cell immune responses to prime-boost vaccination (Extended Data Fig. 3a). Blood cell counting identified significantly higher cell densities in sCPD9- and Ad2-vaccinated prime-boost groups (Fig. 4a). Both relative and absolute cell numbers revealed substantial differences between vaccination strategies (Fig. 4b and Extended Data Fig. 3b–d). Frequencies of mature and immature neutrophils (imPMN), which are increased particularly in severe COVID-19[27] and in SARS-CoV-2-infected Syrian hamsters[26], were lowest for sCPD9 + sCPD9-vaccinated animals (Fig. 4b). In contrast, B, T and plasma cells followed the opposite trend and displayed highest abundancies following the sCPD9 + sCPD9 regime (Fig. 4b and Extended Data Fig. 3b). Concordant with our observations in lungs, genes related to infection and inflammation were broadly downregulated in myeloid cells of vaccinated animals (Fig. 4c and Supplementary Fig. 5).

To investigate activation of vaccine-induced immune memory, we first examined single-cell transcriptomes of circulating B cells, with a focus on B and plasma cells of prime-boost-vaccinated hamsters. Subclustering yielded 8 populations (Supplementary Fig. 6a), which were assigned to cellular states on the basis of known marker genes[28,29]. Of note, in the absence of surface marker information, these assignments probably remain incomplete. In our analysis, we therefore focused on differences in gene expression patterns and investigate whether a putative 'memory recall gene expression signature' would display differences. We first determined cluster 8 to probably represent plasmablasts/plasma cells due to the presence of, for example, *Prdm1* (which encodes Blimp-1) or *Irf4*. Cluster 3 featured intermediate *Prdm1* levels, as well as *Tnfrsf17* and *Tnfrsf13b*. Cluster 6 in comparison showed higher levels of *Pax5*, *Cd19*, *Cd27*, *Bach2* or *Aicda* and lower levels of *Prdm1*, *Xbp1* or *Spib* (Supplementary Fig. 6b). On the basis of these

https://doi.org/10.1038/s41564-023-01352-8

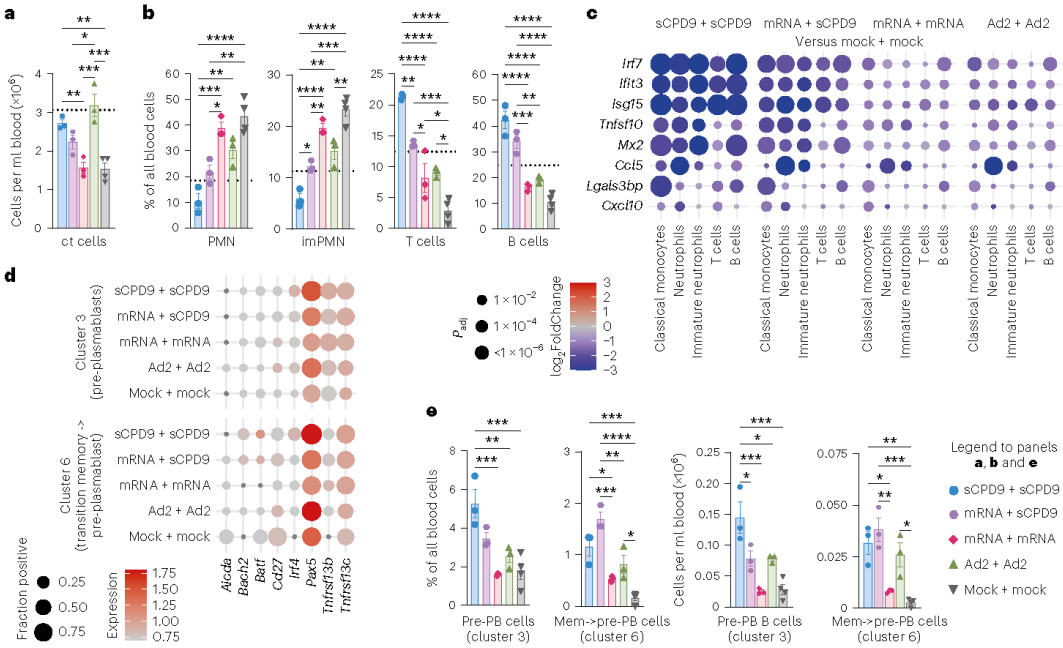


**Fig. 4 | Cellular immune response to vaccination and challenge in blood. a–e**, Analysis of cellular composition and gene expression by scRNA-seq at 2 dpc in blood of prime-boost-vaccinated hamsters. **a**, Manual count of cells per ml blood. **b**, Frequencies of indicated cell types among blood cells. Dotted lines mark the mean levels found in naïve hamsters ($n = 3$, naïve hamster data derived and reprocessed from ref. 26). Bar plots with mean ± s.e.m., $n = 3$. One-way ANOVA and Tukey's multiple comparisons test were conducted. **c**, Dot plots showing fold changes of gene expression in indicated cell types of the four prime-boost vaccination strategies compared to mock-mock-vaccinated animals. Selected interferon-stimulated genes and pro-inflammatory cytokines are visualized as follows: coloration and point size indicate $\log_2$-transformed FC and $P$ values, respectively, in vaccinated compared to mock-mock-vaccinated animals. $P_{adj}$ were calculated by DEseq2 using Benjamini–Hochberg corrections of two-sided Wald test $P$ values. Genes are ordered by unsupervised clustering. **d**, Dot plots showing expression of selected B-cell development marker genes in the blood B-cell subclusters shown in Supplementary Fig. 9a. The size of the dot represents the fraction of cells in which at least one unique molecular identifier (UMI) of the respective gene was detected, while the colour is proportional to the average expression in those cells. **e**, Frequencies and numbers of pre-plasmablast (pre-PB) identified in B-cell cluster 3 and memory to pre-plasmablast transitioning cells (mem->pre-PB) identified in B-cell cluster 6. Bar plots with mean ± s.e.m., $n = 3$. One-way ANOVA and Tukey's multiple comparisons tests were performed; *$P < 0.05$, **$P < 0.01$, ***$P < 0.001$, ****$P < 0.0001$.

patterns, we assumed that these two clusters would contain (pre-) plasmablasts and would therefore be most interesting for investigating memory recall. Probing a set of genes involved in B-cell regulation, we found upregulation of *Irf4*, *Pax5* and *Tnfrsf13b/c* in cluster 3, while in cluster 6, *Bach2*, *Irf4*, *Pax5* and *Tnfrsf13b/c* were upregulated and *Aicda*, *Batf* and *Cd27* were downregulated (Fig. 4d and Supplementary Fig. 6c). This potential early 'memory recall gene expression signature' was strongest upon homologous or heterologous prime-boost vaccination with sCPD9, which induced the highest antibody titre (Fig. 3e–h). In line with this, clusters 3 and 6 cells were significantly more abundant in sCPD9 + sCPD9-vaccinated hamsters (Fig. 4e).

## LAV enhances T-cell proliferation in response to SARS-CoV-2 challenge

To investigate occurrence of T-cell memory recall, we proceeded with subclustering T and natural killer (NK) cells. To this end, we assayed $CD4^+$, $CD8^+$ and proliferating T cells in blood (Fig. 5a,b, and Supplementary Figs. 7 and 8). Analyses of gene expression indicative of proliferation (*Mki67*, *Top2a*), naïve or central memory status (*Sell*, *Ccr7*, *Lef1*, *Il7r*) and activation of T cells (*Cd69*, *Cd44*, *Klrg1*, *Icos*, *Cd40lg*) revealed that most blood T cells displayed either naïve or central memory phenotypes (cluster 0–4, Supplementary Fig. 7b–e). At 2 dpc, type 1-immunity effector genes (*Tbx21*, *Gzma*, *Gzmb*, *Faslg*, *Ifn*) were only expressed by blood NK cells (cluster 5, Supplementary Fig. 8). The proliferating T-cell population consisted of activated T cells expressing memory markers, such as *Il7r* (cluster 6, Supplementary Fig. 8). Proliferating T cells, albeit generally small in numbers, were significantly increased after heterologous vaccination (Fig. 5b). In line with this, the fraction of cells and expression level of proliferation-associated genes were highest when sCPD9 was included in the vaccination regimen (Fig. 5c). To determine T-cell antigen specificity, we vaccinated hamsters with either sCDP9 or mRNA and stimulated their splenocytes 14 d later with recombinant SARS-CoV-2 S or N protein. Interferon gamma (IFN-γ) enzyme-linked immunosorbent spot (ELISpot) served as readout. Spike protein stimulation induced IFN-γ-secreting cells for both vaccines, whereas upon stimulation with N protein, only splenocytes from sCPD9 vaccines secreted significantly more IFN-γ over mock, revealing superior and broader T-cell immunity upon LAV vaccination (Fig. 5d).

Next, we examined whether different prime-boost vaccination strategies differed in the ability to re-activate tissue-resident memory T cells (Trm) in lungs[30]. To characterize pulmonary T-cell subsets, we subclustered the initial T- and NK-cell clusters into 10 subclusters

https://doi.org/10.1038/s41564-023-01352-8

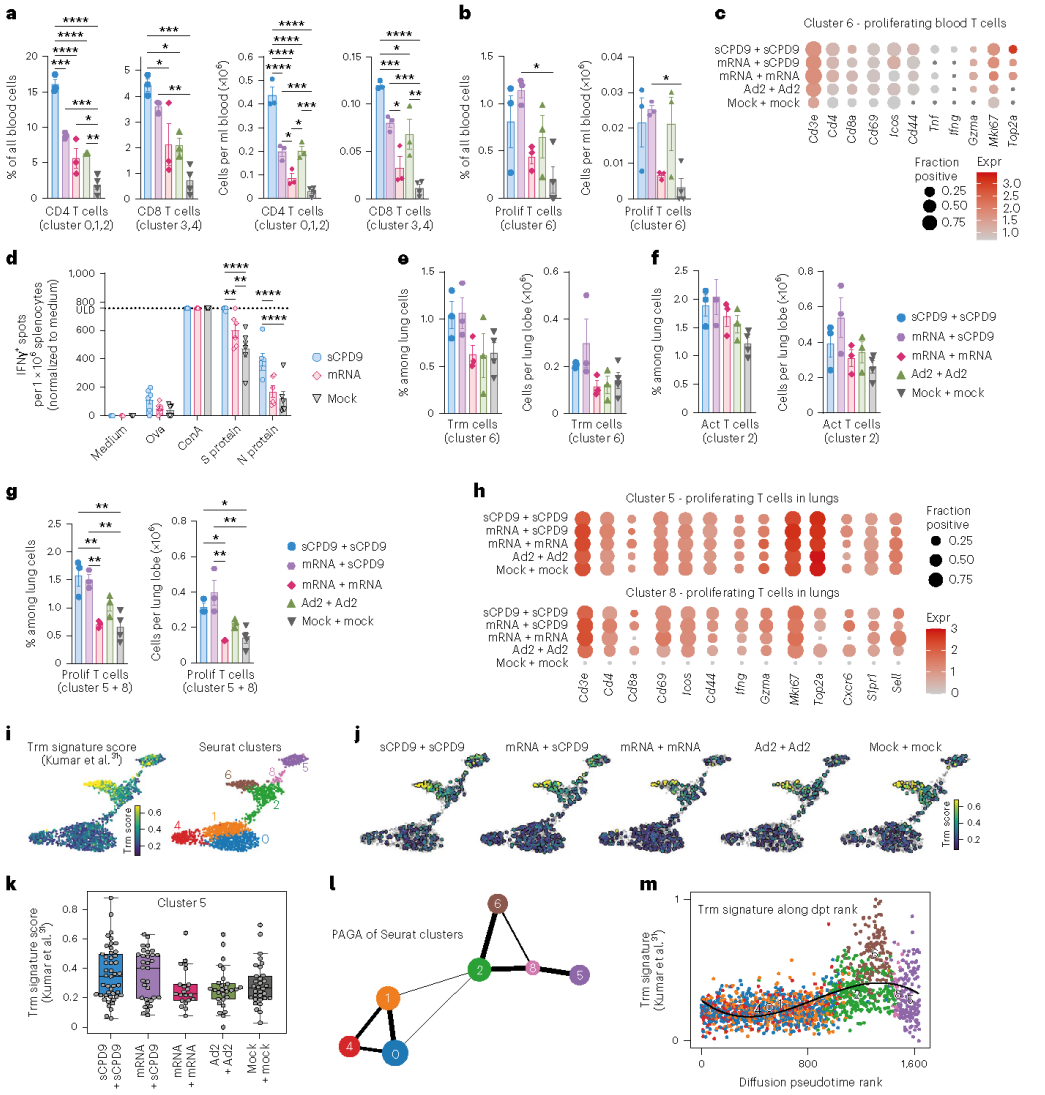


**Fig. 5 | T-cell responses to vaccination and challenge. a**–**k**, T-cell subsets by scRNA-seq (2 dpc) of prime-boost-vaccinated hamsters. Frequencies and numbers of (**a**) CD4 (cluster 0,1,2) and CD8 (cluster 3,4) T cells, and (**b**) proliferating T cells (cluster 6) in blood. Bar graph with mean ± s.e.m., $n = 3$ for all groups, except $n_{mock+mock} = 4$. Ordinary one-way ANOVA and Tukey's multiple comparisons test. **c**, Dot plots showing expression of selected genes in blood cluster 6 (T and NK subcluster analysis in Supplementary Fig. 7a). Dot size represents fraction of cells with UMI > 1, colour indicates expression. **d**, IFN-γ ELISpot analysis 14 d post prime vaccination. Bar graph with mean ± s.e.m., $n = 6$, displaying spot counts normalized to medium stimulation for each animal, individually. Dotted line, upper limit of detection (ULD). Two-way ANOVA and Tukey's multiple comparisons test. **e**–**g**, Frequencies and numbers of (**e**) tissue-resident memory T cells (Trm, cluster 6), (**f**) activated T cells (Act T, cluster 2) and (**g**) proliferating T cells (prolif T cells, cluster 5 + 8) in lungs. Ordinary one-way ANOVA and Tukey's multiple comparisons test. Bar graph with mean ± s.e.m., $n = 3$ for all groups, except $n_{mock+mock} = 4$. In **a**,**b**,**d**–**g**: *$P < 0.05$, **$P < 0.01$, ***$P < 0.001$, ****$P < 0.0001$. **h**, Dot plots showing expression of selected genes in lungs, clusters 5 and 8 (T and NK subcluster analysis in Supplementary Fig. 9a). Dot size represents fraction of cells with UMI > 1, colour indicates expression. **i**,**j**, Trm gene set (refs. 28,31) signature score in cells from selected T-cell subclusters over all groups (**i**) and for individual groups (**j**), colour indicates signature score for Trm gene set. **k**, Trm signature score in cells of cluster 5. Centre, median; box, 25th to 75th percentiles; and whiskers, minimum to maximum values. Circles indicate individual analysed cells in cluster 5 pooled from $n = 3$ for all groups, except $n_{mock+mock} = 4$ animals. **l**, PAGA. Nodes represent clusters, edges represent extent of cluster connection, node size corresponds to cluster cell number and line thickness is proportional to connectivity. **m**, Trm signature (refs. 28,31) score as a function of diffusion pseudotime rank, with black line showing a polynomial fit of degree three.

(Supplementary Fig. 9a). On the basis of *Nkg7*, *Cd3e*, *Cd4* and *Cd8a* gene expression, we assigned clusters 3, 7 and 9 as NK cells, cluster 4 as $CD8^+$ T cells, clusters 0, 1, 2 and 6 as $CD4^+$ T cells, and clusters 8 and 5 as proliferating T cells (*Mki67*, *Top2a*) (Supplementary Fig. 9b,c). Among $CD4^+$ T-cell clusters, cells in cluster 2 displayed a mixed phenotype of effector, activation and memory gene markers (Supplementary Figs. 9b–e and 10a,b), and cells in clusters 0 and 1 were of naïve or central memory type (*Sell*, *Ccr7*, *Lef1*, *Il7r*, *Tcf7*, *S1pr1*) (Supplementary Fig. 10a). In cluster 6, we did not find genes associated with naïve or central memory-associated signatures (Supplementary Fig. 10a) but combined and strong expression of T-cell-homing and tissue retention genes (*Cxcr6*, *Rgs1*, *Prdm1*, *Znf683*, *Itga1* and *Itgae*), a signature indicative of Trm status (Supplementary Figs. 10b,c and 11). Trm cells (cluster 6) displayed higher gene expression level and cell fraction expressing *Cxcr6*, a prominent tissue homing receptor, in sCPD9-vaccinated groups, while lymph node retention receptor *S1pr1* was least detected (Supplementary Fig. 12a). Across activated T cells (cluster 2), gene expression of activation and effector genes was independent of previous vaccination (Supplementary Fig. 12a). At 2 dpc, Trm cells, activated and proliferating T-cell populations were small and represented less than 2% of all lung cells. Trm cells and activated T cells trended towards higher frequencies and numbers in challenged sCPD9 vaccinees, yet only proliferating T cells displayed significantly higher values (Fig. 5e–g). Notably, contrary to proliferating T cells in blood, their lung counterparts expressed higher levels of *Ifng* and *Gzma* (Fig. 5h).

Next, we scored the Seurat clusters for a published human Trm gene set[31] and observed a subset of cells in cluster 5 (proliferating T cells) with a high Trm signature score (Fig. 5i). At 2 dpc, the Trm signature score in proliferating T cells (cluster 5) was remarkably higher in sCPD9 vaccinees (Fig. 5j,k). In cluster 8 (proliferating T cells), overall cell numbers were too low to generate interpretable scores, and no cells were identified from unvaccinated animals (Supplementary Fig. 12b). Using a partition-based graph abstraction (PAGA) approach[32], we identified particularly strong connectivity between clusters 2, 8 and 5, and clusters 2 and 6, as well as a possible connection between clusters 6 and 8 (Fig. 5l). Ordering cells according to global expression similarity by diffusion pseudotime[33] and plotting this rank against the Trm signature further corroborates a path between clusters 2 and 6, and clusters 8 and 5, which is accompanied by variable Trm-like gene expression (Fig. 5m and Supplementary Fig. 12c,d). Overall, these findings suggest that a subset of proliferating T cells is Trm recall-derived and activated in response to SARS-CoV-2 challenge infection in sCPD9-boosted hamsters.

### LAV induces superior mucosal immunity

In addition to potent T-cell memory and humoral immunity, induction of protective mucosal immunity is a distinguishing property of LAVs administered at sites of virus entry[34]. To correlate induction of mucosal immunity with vaccine regimens, we measured SARS-CoV-2 spike-specific IgA levels and neutralization capacity of nasal washes. We found that prime-only sCPD9-vaccinated animals harboured considerably larger quantities of IgA in nasal washes before and after challenge (Fig. 6a). Challenge infection further boosted levels of SARS-CoV-2 spike-specific IgA antibodies in sCPD9-vaccinated animals and induced detectable quantities in mRNA- and Ad2-vaccinated animals. Microneutralization assays against SARS-CoV-2 (variant B.1) with nasal washes obtained from prime-boosted animals confirmed IgA measurements. sCPD9 vaccinees exhibited markedly higher neutralization capacities at 2 and 5 dpc (Fig. 6b). Accordingly, we identified IgA-positive lymphocytes in the nasal mucosa of vaccinated animals (Fig. 6c). Histopathological scoring indicated that sCPD9-vaccinated animals displayed fewer affected tissue areas, less damage and reduced immune cells recruitment (Fig. 6d,e and Extended Data Fig. 4a). sCDP9 vaccination significantly reduced viral RNA in nasal washes compared with mock at 2 dpc (Fig. 6f), correlating with reduced signal in immunohistochemistry staining for viral N protein (Fig. 6d). To further evaluate putatively beneficial effects of mucosal immunity, we resorted to scRNA-seq of nasal tissue cells. First, we annotated cell types on the basis of previously published marker genes (Extended Data Fig. 4b[35]). Particularly in neuronal cells, differential gene expression analysis showed that interferon-stimulated genes (*Isg15*, *Oasl2* or *Rsad2*) were less expressed in sCPD9 vaccinees (Fig. 6g and Supplementary Fig. 13). Notably, bystander responses of neuronal cells in the olfactory epithelium are connected to loss of smell after SARS-CoV-2 infection[36]. Moreover, we find evidence that LAV vaccination prevents SARS-CoV-2 transmission. Following challenge infection, LAV-vaccinated animals shed significantly lower virus quantities compared with mRNA-vaccinated individuals. In this setup, LAV vaccination was able to prevent SARS-CoV-2 transmission while mRNA vaccination was not (Extended Data Fig. 5). Taken together, we provide evidence that the sCPD9 LAV provides superior protection against SARS-CoV-2 in both the lower and upper airways, making it a promising candidate for further investigation in clinical trials.

## Discussion

Current COVID-19 vaccines are highly effective in preventing severe disease; however, infection with newly emerging variants is not prevented and virus loads can be high in vaccinated individuals[37]. To control virus transmission and limit symptomatic infection, mucosal immunity at the site of virus entry is thought to be of paramount importance[38–40].

We here present a cross-platform vaccine comparison that includes a LAV, which we find elicits superior protection from SARS-CoV-2 infection especially at mucosal sites of virus entry. This agrees with previous preclinical COVID-19 vaccine studies using intranasal administration of LAV, protein-based or virus-vectored spike vaccines[24] and efficient induction of mucosal immunity[41–44]. Our observations on improved immunity induced by heterologous prime-boost vaccination are in line with recent studies that combine systemic priming followed by an intranasal boost with adenovirus vector or mRNA vaccines[19,45]. Importantly, virus-neutralizing anti-SARS-CoV-2 IgA at the nasal mucosa of vaccinated animals are much higher in sCPD9-vaccinated animals. It is well known that mucosal IgA exerts various functions, such as blocking virus entry, preventing intracellular fusion of virus and endosomal membranes as well as inhibiting release of viruses from host cells[46]. Overall protection from virus replication, tissue damage and lung inflammation were significantly better in sCPD9-vaccinated animals. At the same time, antigen recognition was considerably broader in animals that had received sCPD9, and these benefits are probably a result of important hallmark features of LAV. These include administration via the natural route of infection, presentation of the full antigenic repertoire of the virus and replication mimicking the target pathogen. Moreover, active replication of LAVs may cause prolonged and increased presentation of viral antigens compared with non-replicating vaccines—a factor that could contribute to the better efficacy observed here. In a small-scale experiment, LAV vaccination was able to abrogate onward transmission of SARS-CoV-2, while mRNA vaccination had only minor effects on transmission. The scRNA-seq analysis of samples from blood, lungs and nasal mucosa of vaccinated and SARS-CoV-2 challenge-infected hamsters revealed that across all important parameters, effects were strongest for sCPD9 vaccination in a prime-only setting. Similarly, in a prime-boost setting, double sCPD9 vaccination was superior to mRNA-sCPD9 vaccination, followed by double mRNA vaccination and double adenovirus vaccination. sCPD9-vaccinated animals had substantially reduced induction of pro-inflammatory gene expression programmes—a main feature of COVID-19 pathogenesis[47]. This was specifically true for cells of the innate immune system, such as monocytes and macrophages, which typically have strong pro-inflammatory transcriptional responses upon SARS-CoV-2 uptake[26]. If translatable to humans, this could mean a much

https://doi.org/10.1038/s41564-023-01352-8

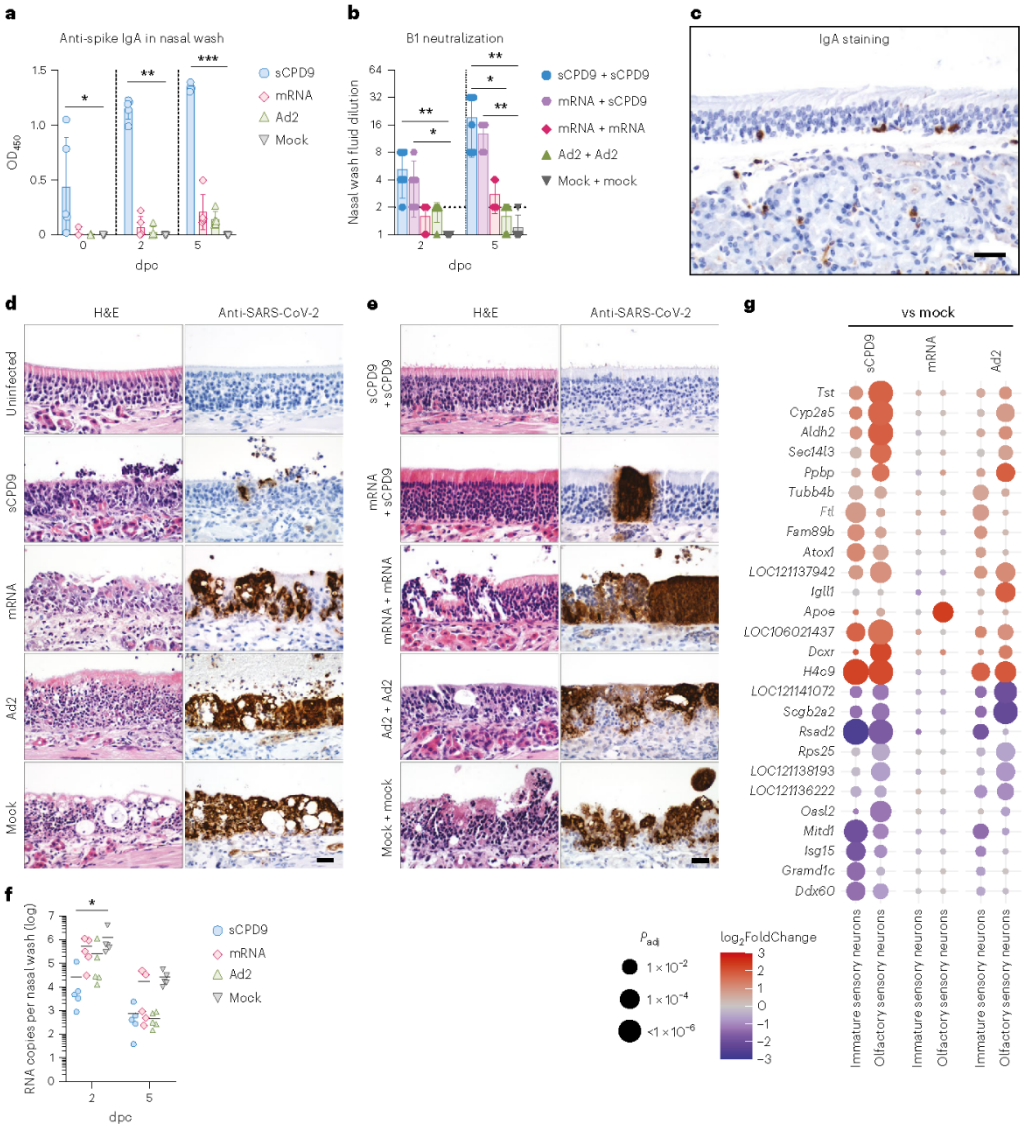


**Fig. 6 | Protective effects on the mucosa and development of local immunity after vaccination. a**, ELISA detecting anti-spike IgA levels in nasal washes of prime-vaccinated hamsters at indicated timepoints post challenge (dpc). Results display $OD_{450}$. **b**, Neutralizing capacity against B.1 of nasal wash fluids from prime-boost-vaccinated hamster at indicated timepoints. Bar plots show mean ± s.d. Kruskal-Wallis and Dunn's multiple comparisons test per timepoint: $^{*}P < 0.05$, $^{**}P < 0.01$, $^{***}P < 0.001$, $^{****}P < 0.0001$. Symbols indicate individual hamsters, $n = 5$ animals per group. **c**, Immunohistochemical staining of IgA in the olfactory epithelium and submucosal glands at 2 dpc. Scale bar, 60 µm. **d**, Longitudinal histopathological sections of olfactory epithelium, with H&E staining (left) and SARS-CoV-2 N protein immunohistochemistry (right) of the prime-only experiment at 2 dpc, with an additional section of an uninfected tissue. **e**, As in **d** but for the prime-boost vaccination experiment. Scale bar, 20 µm. In **c**–**e**, images are representative of $n = 5$ hamsters per indicated group. Prime and prime-boost experiments were performed independently. **f**, Virus RNA loads detected in nasal washes of prime-vaccinated hamsters at 2 and 5 dpc. In scatter dot plots, lines indicate means, symbols represent individual hamsters. $n = 5$. Two-way ANOVA and Tukey's multiple comparisons test; $^{*}P < 0.05$. **g**, Dot plots showing fold changes of gene expression in indicated cell types of the three prime vaccination strategies compared to mock-vaccinated animals. Selected interferon-stimulated genes and pro-inflammatory cytokines are visualized as follows: coloration and point size indicate $\log_2$-transformed FC and $P$ values, respectively, in vaccinated compared to mock-vaccinated animals. $P_{adj}$ were calculated by DEseq2 using Benjamini–Hochberg corrections of two-sided Wald test $P$ values. Genes are ordered by unsupervised clustering.

higher chance for a mild or asymptomatic course of disease even in the case of infection with heterologous SARS-CoV-2 variants.

Additionally, we detected several gene expression signatures related to activation of adaptive immune memory. The enhanced development towards pre-plasmablasts derived from memory B cells and enhanced T-cell proliferation in the blood of challenged animals by scRNA-seq point towards rapid activation of memory cells[48]. We also detected significantly increased numbers of proliferating T cells in lungs of hamsters that received sCPD9. A subset of these proliferating T cells shared a Trm-specific signature and showed connectivity to the identified Trm cluster. One possible explanation for this observation is that SARS-CoV-2-specific tissue-resident memory T-cell seeding is enhanced following sCPD9 vaccination, which may enable faster local recall responses, characterized by enhanced proliferating T cells in corresponding vaccine groups. LAVs mimic natural infection, which is known to induce SARS-CoV-2-specific $CD4^+$ Th1 cells secreting IFN-γ[49]. We detected IFN-γ upregulation in proliferating pulmonary T cells, indicating that SARS-CoV-2 challenge triggered a Th1 effector cell type response, and IFN-γ ELISpot analysis revealed multi-antigen reactivity in splenocytes of LAV-vaccinated hamsters. While mucosal IgA induction remains most important in limiting infection and thus transmission, airway memory $CD4^+$ T cells contribute to protection against other coronaviruses[50] and potentially enhance the antigenic repertoire recognized in a mucosal SARS-CoV-2 vaccine. Similarly, earlier studies using ovalbumin antigens and a combination of different vaccination routes indicated that not just IgA but also general Th1-mediated immunity is enhanced upon mucosal delivery[50].

Our single-cell RNA-sequencing analysis has several limitations. This technique, as employed here, cannot fully capture processes such as reactivation of memory cells due to lack of surface markers and cell type-specific enrichment. Due to incomplete annotation of the Syrian hamster genome, we were not able to identify IgA-positive cells. Data quality of nasal mucosa cells was comparatively low due to the difficult dissociation of the tissue, which limited our observations at the site of initial infection. The data we present on the effect of vaccination on challenge virus transmission are preliminary and require larger-scale studies, use of more recent SARS-CoV-2 variants and mechanistic analyses for validation. While our data show superiority and therefore promise for further development and refinement of LAVs, there is a caveat for extrapolating the results of preclinical animal trials to the situation in humans. Clearly, clinical studies regarding safety and efficacy of live-attenuated vaccines are mandated to realistically assess the potential of these vaccines to combat the yet ongoing pandemic.

One issue with LAVs is their potential susceptibility to previously established immunity[51], which would restrict vaccine virus replication and potentially limit their use as booster after initial immunization by vaccination or natural infection. We show here that sCPD9 does effectively boost immune responses and greatly improves protection when applied three weeks after initial vaccination. Importantly, sCPD9 enhances humoral immune responses, especially against known immune escape variants such as Beta and Omicron BA.1, while also improving the virological outcome of a heterologous challenge infection when applied as a booster three weeks after initial vaccination. This indicates a wide scope for the use of LAVs in populations that exhibit a high degree of baseline immunity induced by previous vaccination or infection.

Due to its high safety profile, sCPD9 was recently downgraded from biosafety level (BSL) 3 to BSL 2 by the relevant German state authority[52]. This is a key step towards clinical application of a SARS-CoV-2 LAV as it will facilitate production of a clinical grade vaccine and greatly ease clinical trials in humans.

## Methods

### Ethics statement

In vitro and animal work were conducted under appropriate biosafety conditions in a BSL-3 facility at the Institut für Virologie, Freie Universität Berlin, Germany. All animal experiments were performed in compliance with relevant institutional, national and international guidelines for the care and humane use of animals and approved by the competent state authority, Landesamt für Gesundheit und Soziales, Berlin, Germany (permit number 0086/20).

### Cells

Vero E6 (obtained from ATCC, CRL-1586), Vero E6-TMPRSS2 (obtained from the National Institute for Biological Standards and Control (NIBSC), 100978) and Calu-3 (obtained from ATCC, HTB-55) cells were cultured in minimal essential medium (MEM) containing 10% fetal bovine serum, 100 IU $ml^{-1}$ penicillin G and 100 µg $ml^{-1}$ streptomycin at 37 °C and 5% $CO_2$. In addition, the cell culture medium for Vero E6-TMPRSS2 cells contained 1,000 µg $ml^{-1}$ geneticin (G418) to ensure selection for cells expressing the genes for neomycin resistance and TMPRSS2.

### Viruses

The modified live-attenuated SARS-CoV-2 mutant sCPD9 and SARS-CoV-2 variants B.1 (BetaCoV/Munich/ChVir984/2020; B.1, EPI_ISL_406862), Beta (B.1.351; hCoV-19/Netherlands/NoordHolland_20159/2021) and Delta (B.1.617.2; SARS-CoV-2, Human, 2021, Germany ex India, 20A/452R (B.1.617)) were propagated on Vero E6-TMPRSS2 cells. Omicron BA.1 (B.1.1.529.1; hCoV-19/Germany/BE-ChVir26335/2021, EPI_ISL_7019047) was propagated on CaLu-3 cells. All virus stocks were whole genome sequenced before infection experiments to confirm genetic integrity in the majority of the population, specifically at the furin cleavage site. Before experimental infection, virus stocks were stored at −80 °C.

### Animal husbandry

Nine- to 11-week-old Syrian hamsters (*Mesocricetus auratus*; breed RjHan:AURA) were purchased from Janvier Labs and were housed in groups of 2 to 3 animals in individually ventilated cages. The hamsters had free access to food and water. They were allowed to get used to the housing conditions for 7 d before vaccination. For both experiments, the cage temperatures were maintained at a constant range of 22 to 24 °C with a relative humidity between 40 and 55%.

### Vaccination and infection experiments

For infection experiments, Syrian hamsters were randomly assigned to groups, with 50–60% of the animals in each group being female. In the first experiment, 15 hamsters were mock-vaccinated or vaccinated with live-attenuated sCPD9 virus, Ad2-spike or mRNA. Vaccination with sCPD9 was applied by intranasal instillation under anaesthesia ($1 \times 10^5$ focus-forming units (f.f.u.), 60 µl)[53]. Ad2-spike ($5 \times 10^8$ infectious units, 200 µl) and mRNA vaccine (5 µg mRNA, 100 µl) were applied intramuscularly. Mock-vaccinated hamsters were vaccinated by intranasal instillation with sterile cell culture supernatant obtained from uninfected Vero E6-TMPRSS2 cells. At 21 d after vaccination, hamsters were challenge-infected with SARS-CoV-2 Delta variant ($1 \times 10^5$ plaque-forming units (p.f.u.), 60 µl) by intranasal instillation under anaesthesia. In the second experiment, 10 hamsters were either mock-vaccinated or vaccinated with one of the three vaccines (see above) followed by a booster vaccination 21 d later. At 14 d after booster vaccination, the hamsters were challenged as described above.

### Transmission experiments

To determine onward transmission of challenge virus in vaccinated individuals, we vaccinated 3 animals per group in a prime-boost regimen. To this end, hamsters received either $1 \times 10^4$ f.f.u. sCPD9delFCS in 60 µl MEM intranasally, 5 µg BNT162b2 mRNA in 100 µl normal saline (0.9% NaCl in sterile water) intramuscularly or 60 µl plain MEM intranasally (mock). Vaccination was boosted using the same vaccines for each respective group 21 d after initial vaccination.

Vaccinated hamsters were challenge-infected with $1 \times 10^5$ p.f.u. SARS-CoV-2 variant B.1 as described above. At 24 h after infection, infected vaccinated hamsters were brought into contact with naïve animals and co-habitated to monitor transmission for 6 consecutive days. Daily oral swabs were obtained from each animal to monitor virus shedding and transmission.

### Vaccine preparations

sCPD9 was grown on Vero E6-TMRSS2 cells and titrated on Vero E6 cells as described previously; final titres were adjusted to $2 \times 10^6$ f.f.u. $ml^{-1}$ in MEM. Recombinant Ad2-spike was generated, produced on 293T cells and purified as previously described[23]. BNT162b2 was obtained as a commercial product (Comirnaty) and handled exactly as recommended by the manufacturer, except that the final concentration of mRNA was adjusted to 50 µg $ml^{-1}$ (100 µg $ml^{-1}$ is the recommended concentration for use in humans) by adding injection-grade saline (0.9% NaCl in sterile water) immediately before use.

To increase genetic stability of the sCPD9 construct, the furin cleavage site (FCS) of the spike protein was deleted to create sCPD-9delFCS. This FCS-deleted vaccine virus was only used for the transmission study of this paper (Extended Data Fig. 5). Importantly, all vaccines used in this study contain the same SARS-CoV-2 spike antigen derived from the ancestral B.1 (Wuhan) sequence.

### Vaccination

sCPD9 was administered intranasally under general anaesthesia (0.15 mg $kg^{-1}$ medetomidine, 2.0 mg $kg^{-1}$ midazolam and 2.5 mg $kg^{-1}$ butorphanol) at a dose of $1 \times 10^5$ f.f.u. per animal in a total volume of 60 µl MEM. For transmission experiments (Extended Data Fig. 5), $1 \times 10^4$ f.f.u. sCPD9delFCS was applied in the same way. Ad2-spike was injected intramuscularly at $5 \times 10^8$ infectious units in 200 µl injection buffer (3 mM KCl, 1 mM $MgCl_2$, 10% glycerol in PBS). BNT162b2 was injected intramuscularly at a dose of 5 µg mRNA per animal in 100 µl physiological saline (0.9% NaCl in sterile water).

### Nasal washes

Nasal washes were obtained from each hamster in this study. To this end, the skull of each animal was split slightly paramedian, such that the nasal septum remained intact on one side of the nose. Subsequently, a 200 µl pipette tip was carefully slid underneath the nasal septum and 150 µl wash fluid (PBS with 30 µg $ml^{-1}$ ofloxacin and 10 µg $ml^{-1}$ voriconazole) was applied. The wash was collected through the nostril and the washing procedure was repeated twice; approximately 100 µl of sample was recovered after the third wash.

Nasal washes obtained from the prime-only vaccination trial were subjected to enzyme-linked immunosorbent assay (ELISA) analysis of SARS-CoV-2 spike-specific IgA antibodies. Nasal washes obtained from the prime-boost vaccination trial were used for microneutralization assay to assess their capacity to neutralize the SARS-CoV-2 ancestral variant B1.

### Plaque assay

For quantification of replication-competent virus, 50 mg of lung tissue were used. Serial 10-fold dilutions were prepared after homogenizing the organ samples in a bead mill (Analytic Jena). The dilutions were plated on Vero E6 cells grown in 24-well plates and incubated for 2.5 h at 37 °C. Subsequently, cells were overlaid with MEM containing 1.5% carboxymethylcellulose sodium (Sigma Aldrich) and fixed with 4% formaldehyde solution 72 h after infection. To count the plaque-forming units, plates were stained with 0.75% methylene blue.

### Histopathology, immunohistochemistry and in situ hybridization

Lungs were processed as previously described[53]. After careful removal of the left lung lobe, tissue was fixed in PBS-buffered 4% formaldehyde solution (pH 7.0) for 48 h. For conchae preparation, parts of the left skull half were fixed accordingly. Afterwards, lungs or conchae were gently removed from the nasal cavity and embedded in paraffin, cut at 2 µm thickness and stained with hematoxylin and eosin (H&E). In situ hybridization on lungs was performed as previously described[54] using the ViewRNA ISH Tissue Assay kit (Invitrogen by Thermo Fisher) according to the manufacturer's instructions, with minor adjustments. For SARS-CoV-2 RNA localization, probes detecting N gene sequences (NCBI database NC_045512.2, nucleotides 28,274–29,533, assay ID: VPNKRHM) were used. Sequence-specific binding was controlled by using a probe for detection of pneumolysin. Immunohistochemistry on conchae was performed as described earlier[55] (details in Supplementary Methods).

Blinded microscopic analysis was performed by a board-certified veterinary pathologist (J.B.).

### SARS-specific Ig measurement by ELISA from serum and nasal washes

An in-house ELISA was performed to investigate SARS-specific IgG levels in serum and SARS-specific IgA levels in nasal washes after vaccination (details in Supplementary Methods).

### Neutralization assays from nasal washes

To assess the capacity of nasal washes obtained from the prime-boost vaccination trial to neutralize authentic SARS-CoV-2 (B.1), nasal washes were diluted 1:1 in 2× MEM containing 50 µg $ml^{-1}$ enrofloxacin and 10 µg $ml^{-1}$ voriconazole. Subsequent serial dilutions were performed in MEM containing 25 mg $ml^{-1}$ enrofloxacin, 5 µg $ml^{-1}$ voriconazole and 1% FBS. SARS-CoV-2 (50 p.f.u.) were added to the nasal wash dilutions and dilutions from 1:2 to 1:256 were plated on near-confluent Vero E6 cells seeded in 96-well cell culture plates. At 3 d after inoculation, cells were fixed and stained with methylene blue. To identify virus-neutralizing dilutions, the integrity of the cell monolayer was assessed by comparison with control wells that contained either no nasal wash or no virus. The last dilution with no evidence of virus-induced cytopathic effect was considered the neutralizing titre for the respective sample.

### Serum neutralization assay

Serum samples were tested for their ability to neutralize different SARS-CoV-2 variants. Day 0 samples of the prime-boost trial could not be tested for neutralizing antibodies against B.1.351 (Beta) due to lack of material. Sera were inactivated at 56 °C for 30 min. Two-fold serial dilutions (1:8 to 1:1,024) were plated on 96-well plates and 200 p.f.u. SARS-CoV-2 were pipetted into each well. After an incubation time of 1 h at 37 °C, the dilutions were transferred to 96-well plates containing sub-confluent Vero E6 cells and incubated for 72 h at 37 °C (B.1, Beta, Delta) or for 96 h at 37 °C (Omicron). The plates were fixed with 4% formaldehyde solution and stained with 0.75% methylene blue. Wells that showed no cytopathic effect were considered neutralized.

### IFN-γ ELISpot analysis

Hamster IFN-γ ELISpot analysis was performed as described previously[56]. In brief, the hamster IFN-γ ELISpot$^{BASIC}$ kit (MABTECH) was used to detect IFN-γ secretion by $5 \times 10^5$ isolated splenocytes, each in co-culture with different stimuli. Medium-treated splenocytes served as negative control and recombinant ovalbumin (10 mg $ml^{-1}$) was used as negative protein control stimulus. General stimulation of T cells was achieved using 5 µg $ml^{-1}$ concanavalin A (ConA, Sigma Aldrich). Recombinant SARS-CoV-2 (2019-nCoV) spike protein (S1 + S2 ECD, His tag; 10 mg $ml^{-1}$; Sino Biological Europe) or 10 mg $ml^{-1}$ recombinant SARS-CoV-2 (2019-nCoV) nucleocapsid protein (N) (Sino Biological Europe) were used to re-stimulate SARS-CoV-2-specific T cells. Spots were counted using an Eli.Scan ELISpot scanner (AE.L.VIS) and the analysis software ELI.Analyse v5.0 (AE.L.VIS).

### RNA extraction and qPCR

To quantify genomic copies in oropharyngeal swabs and 25 mg homogenized lung tissue, RNA was extracted using innuPREP Virus DNA/RNA kit (Analytic Jena) according to the manufacturer's instructions. qPCR was performed using the NEB Luna Universal Probe One-Step RT–qPCR kit (New England Biolabs) with cycling conditions of 10 min at 55 °C for reverse transcription, 3 min at 94 °C for activation of the enzyme, and 40 cycles of 15 s at 94 °C and 30 s at 58 °C on a qTower G3 cycler (Analytic Jena) in sealed qPCR 96-well plates. Primers and probes were used as previously reported[57]. Oligonucleotides (Sequence (5′-3′)):

E_Sarbeco_F: ACAGGTACGTTAATAGTTAATAGCGT;
E_Sarbeco_R: ATATTGCAGCAGTACGCACACA;
E_Sarbeco_P1: FAM-ACACTAGCCATCCTTACTGCGCTTCG-BBQ.

### *Mesocricetus auratus* genome annotation

For quantification of gene expression, we used the MesAur 2.0 genome assembly and annotation available via the NCBI genome database (https://www.ncbi.nlm.nih.gov/genome/11998?genome_assembly_id=1585474). The GFF file was converted to GTF using gffread 0.12.7[58]. Where no overlaps were produced, 3′-UTRs in the annotation were extended by 1,000 bp as described previously[59]. Further polishing steps for the GTF file are described on the GitHub page accompanying this paper (https://github.com/Berlin-Hamster-Single-Cell-Consortium/Live-attenuated-vaccine-strategy-confers-superior-mucosal-and-systemic-immunity-to-SARS-CoV-2). The final gtf file used for the analysis is available through GEO (https://www.ncbi.nlm.nih.gov/geo/query/acc.cgi?acc=GSE200596).

### Bulk RNA extraction

To perform RNA bulk sequencing, RNA was isolated from lung tissue using Trizol reagent according to the manufacturer's instructions (Ambion, Life Technologies). Briefly, 1 ml Trizol was added to the homogenized organ sample and vortexed thoroughly. After an incubation time of 20 min, 200 µl of chloroform were added. The samples were vortexed again and incubated for 10 min at room temperature. Subsequently, tubes were centrifuged at 12,000 × *g* for 15 min at 4 °C and 500 µl of the aqueous phase were transferred into a new tube containing 10 µg GlycoBlue. Isopropanol (500 µl) was added, followed by vortexing, incubating and centrifuging the samples as described above. Thereafter, isopropanol was removed and 1 ml of ethanol (75%) was applied. The tubes were inverted shortly and centrifuged at 8,000 × *g* for 10 min. After freeing the pellet from ethanol, RNA was resuspended in 30 µl of RNase-free water and stored at −80 °C.

### Cell isolation from blood and lungs

White blood cells were isolated from EDTA-blood as previously described; steps included red blood cell lysis and cell filtration before counting. Lung cells (caudal lobe) were isolated as previously described[26,60]; steps included enzymatic digestion, mechanical dissociation and filtration before counting in trypan blue. Buffers contained 2 µg ml$^{-1}$ actinomycin D to prevent de novo transcription during the procedures.

### Cell isolation from nasal cavities

To obtain single-cell suspensions from the nasal mucosa of SARS-CoV-2-challenged hamsters, the skull of each animal was split slightly paramedian so that the nasal septum remained intact on the left side of the nose. The right side of the nose was carefully removed from the cranium and stored in ice-cold 1× PBS with 1% BSA and 2 µg ml$^{-1}$ actinomycin D until further use. Nose parts were transferred into 5 ml Corning Dispase solution supplemented with 750 U ml$^{-1}$ Collagenase CLS II and 1 mg ml$^{-1}$ DNase, and incubated at 37 °C for 15 min. For preparation of cells from the nasal mucosa, the conchae were carefully removed from the nasal cavity and re-incubated in digestion medium for 20 min at 37 °C. Conchae tissue was dissociated by pipetting and pressing through a 70 µm filter with a plunger. Ice-cold PBS with 1% BSA and 2 µg ml$^{-1}$ actinomycin D was added to stop the enzymatic digestion. The cell suspension was centrifuged at 400 × *g* at 4 °C for 15 min and the supernatant discarded. The pelleted nasal cells were resuspended in 5 ml red blood cell lysis buffer and incubated at room temperature for 2 min. Lysis reaction was stopped with 1× PBS with 0.04% BSA and cells centrifuged at 400 × *g* at 4 °C for 10 min. Pelleted cells were resuspended in 1× PBS with 0.04% BSA and 40 µm-filtered. Live cells were counted in trypan blue and viability rates determined using a counting chamber. Cell concentration for scRNA-seq was adjusted by dilution.

### Single-cell RNA sequencing

Isolated cells from blood, lungs and nasal cavities of Syrian hamsters were subjected to scRNA-seq using the 10× Genomics Chromium Single Cell 3′ Gene Expression system with feature barcoding technology for cell multiplexing (details in Supplementary Methods).

### Analysis of single-cell RNA sequencing data

Sequencing reads were initially processed using bcl2fastq 2.20.0 and the multi command of the Cell Ranger 6.0.2 software. For the cellplex demultiplexing, the assignment thresholds were partially adjusted (for details, see the GitHub page at https://github.com/Berlin-Hamster-Single-Cell-Consortium/Live-attenuated-vaccine-strategy-confers-superior-mucosal-and-systemic-immunity-to-SARS-CoV-2). Further processing was done in R 4.0.4 Seurat R 4.0.6 package[61], as well as R packages ggplot2 3.3.5, dplyr 1.0.7, DESeq2 1.30.1, lme4 1.1–27.1 and dependencies, and in Python 3.9.13 as well as Python packages scanpy 1.9.1, scvelo 0.2.4 and dependencies. In the next step, cells were filtered by a loose quality threshold (minimum of 250 detected genes per cell) and clustered. Cell types were then annotated per cluster and filtered using cell type-specific thresholds (cells below the median or in the lowest quartile within a cell type were removed). The remaining cells were processed using the SCT/integrate workflow[62] and cell types again annotated on the resulting Seurat object. All code for downstream analysis is available on GitHub at https://github.com/Berlin-Hamster-Single-Cell-Consortium/Live-attenuated-vaccine-strategy-confers-superior-mucosal-and-systemic-immunity-to-SARS-CoV-2.

### Statistics and reproducibility

Details on statistical analysis of sequencing data including pre-processing steps are described in the individual Methods section. Analyses of virological, histopathological, ELISA, cell frequencies and cell number statistics were performed with GraphPad Prism 9. Statistical details are provided in respective figure legends. No statistical method was used to predetermine sample size. Data distribution was assumed to be normal but this was not formally tested. No data were excluded from the analyses. All experiments involving live animals were randomized, other experiments were not randomized. The investigators were blinded to allocation of hamsters during animal experiments and primary outcome assessment (clinical development, virus titrations, qPCR, ELISpot, serology and histopathology). Investigators were not blinded to allocation in other experiments and analyses.

### Reporting summary

Further information on research design is available in the Nature Portfolio Reporting Summary linked to this article.

## Data availability

Raw sequencing data are available on GEO (https://www.ncbi.nlm.nih.gov/geo/query/acc.cgi?acc=GSE200596), along with bulk RNA-seq read count tables, and h5 matrices and Seurat objects for the scRNA-seq data. Source data are provided with this paper.

## Code availability

Code is available on GitHub at https://github.com/Berlin-Hamster-Single-Cell-Consortium/Live-attenuated-vaccine-strategy-confers-superior-mucosal-and-systemic-immunity-to-SARS-CoV-2.

## References


1. *COVID-19 Vaccines with WHO Emergency Use Listing* (WHO, 2022).
2. *COVID-19 Vaccine Tracker and Landscape* (WHO, 2022).
3. *COVID-19 Vaccine Surveillance Report Week 24* (UK Health Security Agency, 2022); https://assets.publishing.service.gov.uk/government/uploads/system/uploads/attachment_data/file/1072064/Vaccine-surveillance-report-week-17.pdf
4. Xia, H. et al. Neutralization and durability of 2 or 3 doses of the BNT162b2 vaccine against Omicron SARS-CoV-2. *Cell Host Microbe* **30**, 485–488.e3 (2022).
5. Di Pietrantonj, C., Rivetti, A., Marchione, P., Debalini, M. G. & Demicheli, V. Vaccines for measles, mumps, rubella, and varicella in children. *Cochrane Database Syst. Rev.* **4**, CD004407 (2020).
6. Lin, Y. J. et al. Oil-in-water emulsion adjuvants for pediatric influenza vaccines: a systematic review and meta-analysis. *Nat. Commun.* **11**, 315 (2020).
7. Recommendations on the use of live, attenuated influenza vaccine (FluMist®): supplemental statement on seasonal influenza vaccine for 2011-2012. *Can. Commun. Dis. Rep.* **37**, 1–77 (2011).
8. Hassan, A. O. et al. An intranasal vaccine durably protects against SARS-CoV-2 variants in mice. *Cell Rep.* **36**, 109452 (2021).
9. Lauring, A. S., Jones, J. O. & Andino, R. Rationalizing the development of live attenuated virus vaccines. *Nat. Biotechnol.* **28**, 573–579 (2010).
10. Eschke, K., Trimpert, J., Osterrieder, N. & Kunec, D. Attenuation of a very virulent Marek's disease herpesvirus (MDV) by codon pair bias deoptimization. *PLoS Pathog.* **14**, e1006857 (2018).
11. Coleman, J. R. et al. Virus attenuation by genome-scale changes in codon pair bias. *Science* **320**, 1784–1787 (2008).
12. Wang, Y. et al. Scalable live-attenuated SARS-CoV-2 vaccine candidate demonstrates preclinical safety and efficacy. *Proc. Natl Acad. Sci. USA* https://doi.org/10.1073/pnas.2102775118 (2021).
13. Oberhardt, V. et al. Rapid and stable mobilization of CD8(+) T cells by SARS-CoV-2 mRNA vaccine. *Nature* **597**, 268–273 (2021).
14. Ssemaganda, A. et al. Expansion of cytotoxic tissue-resident $CD8^+$ T cells and $CCR6^+CD161^+$ $CD4^+$ T cells in the nasal mucosa following mRNA COVID-19 vaccination. *Nat. Commun.* **13**, 3357 (2022).
15. Turner, J. S. et al. SARS-CoV-2 mRNA vaccines induce persistent human germinal centre responses. *Nature* **596**, 109–113 (2021).
16. Laczko, D. et al. A single immunization with nucleoside-modified mRNA vaccines elicits strong cellular and humoral immune responses against SARS-CoV-2 in mice. *Immunity* **53**, 724–732.e7 (2020).
17. Ren, C. et al. Respiratory mucosal immunity: kinetics of secretory immunoglobulin A in sputum and throat swabs from COVID-19 patients and vaccine recipients. *Front. Microbiol.* **13**, 782421 (2022).
18. Sheikh-Mohamed, S. et al. Systemic and mucosal IgA responses are variably induced in response to SARS-CoV-2 mRNA vaccination and are associated with protection against subsequent infection. *Mucosal Immunol.* https://doi.org/10.1038/s41385-022-00511-0 (2022).
19. Künzli, M. et al. Route of self-amplifying mRNA vaccination modulates the establishment of pulmonary resident memory CD8 and CD4 T cells. *Sci. Immunol.* **7**, eadd3075 (2022).
20. Brandtzaeg, P. Secretory immunity with special reference to the oral cavity. *J. Oral Microbiol.* https://doi.org/10.3402/jom.v5i0.20401 (2013).
21. Beura, L. K. et al. $CD4^+$ resident memory T cells dominate immunosurveillance and orchestrate local recall responses. *J. Exp. Med.* **216**, 1214–1229 (2019).
22. Focosi, D., Maggi, F. & Casadevall, A. Mucosal vaccines, sterilizing immunity, and the future of SARS-CoV-2 virulence. *Viruses* https://doi.org/10.3390/v14020187 (2022).
23. Trimpert, J. et al. Deciphering the role of humoral and cellular immune responses in different COVID-19 vaccines—a comparison of vaccine candidate genes in Roborovski dwarf hamsters. *Viruses* https://doi.org/10.3390/v13112290 (2021).
24. Trimpert, J. et al. Live attenuated virus vaccine protects against SARS-CoV-2 variants of concern B.1.1.7 (Alpha) and B.1.351 (Beta). *Sci. Adv.* **7**, eabk0172 (2021).
25. Trimpert, J. et al. Development of safe and highly protective live-attenuated SARS-CoV-2 vaccine candidates by genome recoding. *Cell Rep.* **36**, 109493 (2021).
26. Nouailles, G. et al. Temporal omics analysis in Syrian hamsters unravel cellular effector responses to moderate COVID-19. *Nat. Commun.* **12**, 4869 (2021).
27. Carissimo, G. et al. Whole blood immunophenotyping uncovers immature neutrophil-to-VD2 T-cell ratio as an early marker for severe COVID-19. *Nat. Commun.* **11**, 5243 (2020).
28. Kassambara, A. et al. RNA-sequencing data-driven dissection of human plasma cell differentiation reveals new potential transcription regulators. *Leukemia* **35**, 1451–1462 (2021).
29. Morgan, D. & Tergaonkar, V. Unraveling B cell trajectories at single cell resolution. *Trends Immunol.* **43**, 210–229 (2022).
30. Zhao, J. et al. Airway memory $CD4^+$ T cells mediate protective immunity against emerging respiratory coronaviruses. *Immunity* **44**, 1379–1391 (2016).
31. Kumar, B. V. et al. Human tissue-resident memory T cells are defined by core transcriptional and functional signatures in lymphoid and mucosal sites. *Cell Rep.* **20**, 2921–2934 (2017).
32. Wolf, F. A. et al. PAGA: graph abstraction reconciles clustering with trajectory inference through a topology preserving map of single cells. *Genome Biol.* **20**, 59 (2019).
33. Haghverdi, L., Buttner, M., Wolf, F. A., Buettner, F. & Theis, F. J. Diffusion pseudotime robustly reconstructs lineage branching. *Nat. Methods* **13**, 845–848 (2016).
34. Lycke, N. Recent progress in mucosal vaccine development: potential and limitations. *Nat. Rev. Immunol.* **12**, 592–605 (2012).
35. Durante, M. A. et al. Single-cell analysis of olfactory neurogenesis and differentiation in adult humans. *Nat. Neurosci.* **23**, 323–326 (2020).
36. Zazhytska, M. et al. Non-cell-autonomous disruption of nuclear architecture as a potential cause of COVID-19-induced anosmia. *Cell* **185**, 1052–1064.e12 (2022).
37. Blom, K. et al. Immune responses after omicron infection in triple-vaccinated health-care workers with and without previous SARS-CoV-2 infection. *Lancet Infect. Dis.* https://doi.org/10.1016/S1473-3099(22)00362-0 (2022).
38. Mao, T. et al. Unadjuvanted intranasal spike vaccine elicits protective mucosal immunity against sarbecoviruses. Science **378**, eabo2523 (2022).
39. Russell, M. W., Moldoveanu, Z., Ogra, P. L. & Mestecky, J. Mucosal immunity in COVID-19: a neglected but critical aspect of SARS-CoV-2 infection. *Front. Immunol.* **11**, 611337 (2020).
40. Mettelman, R. C., Allen, E. K. & Thomas, P. G. Mucosal immune responses to infection and vaccination in the respiratory tract. *Immunity* **55**, 749–780 (2022).
41. Afkhami, S. et al. Respiratory mucosal delivery of next-generation COVID-19 vaccine provides robust protection against both ancestral and variant strains of SARS-CoV-2. *Cell* **185**, 896–915.e19 (2022).

42. Bricker, T. L. et al. A single intranasal or intramuscular immunization with chimpanzee adenovirus-vectored SARS-CoV-2 vaccine protects against pneumonia in hamsters. *Cell Rep.* **36**, 109400 (2021).
43. Hassan, A. O. et al. A single-dose intranasal ChAd vaccine protects upper and lower respiratory tracts against SARS-CoV-2. *Cell* **183**, 169–184.e13 (2020).
44. Langel, S. N. et al. Adenovirus type 5 SARS-CoV-2 vaccines delivered orally or intranasally reduced disease severity and transmission in a hamster model. *Sci. Transl. Med.* https://doi.org/10.1126/scitranslmed.abn6868 (2022).
45. Vesin, B. et al. An intranasal lentiviral booster reinforces the waning mRNA vaccine-induced SARS-CoV-2 immunity that it targets to lung mucosa. *Mol. Ther.* https://doi.org/10.1016/j.ymthe.2022.04.016 (2022).
46. Krammer, F. The human antibody response to influenza A virus infection and vaccination. *Nat. Rev. Immunol.* **19**, 383–397 (2019).
47. Lamers, M. M. & Haagmans, B. L. SARS-CoV-2 pathogenesis. *Nat. Rev. Microbiol.* **20**, 270–284 (2022).
48. Lauvau, G. & Soudja, S. M. Mechanisms of memory T cell activation and effective immunity. *Adv. Exp. Med. Biol.* **850**, 73–80 (2015).
49. Braun, J. et al. SARS-CoV-2-reactive T cells in healthy donors and patients with COVID-19. *Nature* **587**, 270–274 (2020).
50. Fiorino, F., Pettini, E., Pozzi, G., Medaglini, D. & Ciabattini, A. Prime-boost strategies in mucosal immunization affect local IgA production and the type of Th response. *Front. Immunol.* **4**, 128 (2013).
51. Mok, D. Z. L. & Chan, K. R. The effects of pre-existing antibodies on live-attenuated viral vaccines. *Viruses* https://doi.org/10.3390/v12050520 (2020).
52. Kunec, D., Osterrieder, N. & Trimpert, J. Synthetically recoded virus sCPD9 - a tool to accelerate SARS-CoV-2 research under biosafety level 2 conditions. *Comput. Struct. Biotechnol. J.* **20**, 4376–4380 (2022).
53. Osterrieder, N. et al. Age-dependent progression of SARS-CoV-2 infection in Syrian hamsters. *Viruses* https://doi.org/10.3390/v12070779 (2020).
54. Bertzbach, L. D. et al. SARS-CoV-2 infection of Chinese hamsters (*Cricetulus griseus*) reproduces COVID-19 pneumonia in a well-established small animal model. *Transbound. Emerg. Dis.* **68**, 1075–1079 (2021).
55. Merz, S. E., Klopfleisch, R., Breithaupt, A. & Gruber, A. D. Aging and senescence in canine testes. *Vet. Pathol.* **56**, 715–724 (2019).
56. Ebenig, A. et al. Vaccine-associated enhanced respiratory pathology in COVID-19 hamsters after $T_H2$-biased immunization. *Cell Rep.* **40**, 111214 (2022).
57. Corman, V. M. et al. Detection of 2019 novel coronavirus (2019-nCoV) by real-time RT-PCR. *Euro Surveill.* https://doi.org/10.2807/1560-7917.ES.2020.25.3.2000045 (2020).
58. Pertea, G. & Pertea, M. GFF Utilities: GffRead and GffCompare. *F1000Research* https://doi.org/10.12688/f1000research.23297.2 (2020).
59. Andreotti, S. et al. De novo whole genome assembly of the Roborovski dwarf hamster (*Phodopus roborovskii*) genome, an animal model for severe/critical COVID-19. Preprint at *bioRxiv* https://doi.org/10.1101/2021.10.02.462569 (2021).
60. Pennitz, P. et al. Protocol to dissociate healthy and infected murine- and hamster-derived lung tissue for single-cell transcriptome analysis. *STAR Protoc.* **4**, 101957 (2022).
61. Hao, Y. et al. Integrated analysis of multimodal single-cell data. *Cell* **184**, 3573–3587.e29 (2021).
62. Stuart, T. et al. Comprehensive integration of single-cell data. *Cell* **177**, 1888–1902.e21 (2019).


## Acknowledgements

We thank V. M. Corman of Charité for help in study design and prolific discussions on results and conclusions; S. Reiche (Friedrich-Loeffler-Institut, Greifswald, Germany) for providing anti-SARS-CoV-2 nucleocapsid antibody; C. Thöne-Reineke for support in animal welfare and husbandry; and the European Virus Archive, D. Bourquain (Robert-Koch-Institut, Berlin, Germany) and C. Reusken (National Institute for Public Health and the Environment, Bilthoven, Netherlands) for providing SARS-CoV-2 variants used in this study. Vero E6-TMPRSS2 cells were provided by the NIBSC Research Reagent Repository, UK, with thanks to M. Takeda. Funding was provided by: the European Union's Horizon 2020 Research and Innovation Programme - EVA-GLOBAL grant 871029; Deutsche Forschungsgemeinschaft grant OS 143/16-1 (N.O.); Deutsche Forschungsgemeinschaft grant SFB TR84, sub-project Z01b (J.T., A.D.G.); Deutsche Forschungsgemeinschaft grant SFB TR84, sub-project C06 and C09 (M.W.); Deutsche Forschungsgemeinschaft grant SFB 1449–431232613, sub-project B02 (M.W., G.N.); Bundesministerium für Bildung und Forschung - MAPVAP grant 16GW0247 (G.N., M.W.); Bundesministerium für Bildung und Forschung - Organo-Strat grant 01KX2021 (A.D.G.); Bundesministerium für Bildung und Forschung - e:Med CAPSyS grant 01ZX1604B (M.W.); Bundesministerium für Bildung und Forschung - e:Med SYMPATH grant 01ZX1906A (M.W.); Bundesministerium für Gesundheit – CHARIS 6a grant (M.D.M.); Einstein Foundation 3R grant EZ-2020-597 FU (A.D.G.); Helmholtz Association's Initiative and Networking Fund - COVIPA grant KA1-Co-02 (G.T.A., M.L., E.W.); and a Charité 3R grant (P.P., C.G.). The funders had no role in study design, data collection and analysis, decision to publish or preparation of the manuscript.

## Author contributions

D.K. and J.T. conceptualized the project. G.N., J.M.A., P.P., S.P., G.T.A., M.B., J.B., A.V., A.L., F.P., J.K., C. Goekeri, D.N., H.W., S.D.P., E.W., D.K. and J.T. developed the methodology. G.N., J.M.A., P.P., S.P., G.T.A., J.B., A.V., A.L., A.E., M.V.L., M.D.M., S.S., N.X., C.L., R.M.V., A.A., S.H., H.W., A.D.G., S.D.P., E.W., D.K. and J.T. conducted the investigations. G.N., J.M.A., P.P., S.P., G.T.A., J.B., A.V., A.L., S.D.P., E.W., D.K. and J.T. performed visualization. G.N., G.C., A.D.G., C. Goffinet, M.W., D.N., C.D. and J.T. acquired resources. N.O. and J.T. acquired funding. J.T. administered the project. G.N., G.C., C.D., C. Goffinet, M.L., N.B., M.W., A.D.G., S.D.P., N.O., D.K., E.W. and J.T. supervised the project. G.N., J.M.A., E.W., D.K. and J.T. wrote the original draft. All authors reviewed and edited the manuscript.

## Funding

Open access funding provided by Freie Universität Berlin.

## Competing interests

Related to this work, Freie Universität Berlin has filed a patent application (FU227EP - 22193939.0- 1111, Freie Universität Berlin, Germany) for the use of sCPD9 as vaccine in humans. In this application, J.T., N.O. and D.K. are named as inventors of sCPD9. Freie Universität Berlin is collaborating with RocketVax Inc. for further development of sCPD9 and receives funding for research. Independent of this work, G.N. has received project funding from Biotest AG; and M.W. received funding for research from Bayer Health Care, Biotest, Pantherna and Vaxxilon, and for lectures and advisorship from Alexion, Aptarion, Astra Zeneca, Bayer Health Care, Berlin Chemie, Biotest, Boehringer Ingelheim, Chiesi, Glaxo Smith Kline, Insmed, Novartis, Teva and Vaxxilon. The other authors declare no competing interests.

## Additional information

**Extended data** is available for this paper at https://doi.org/10.1038/s41564-023-01352-8.

**Supplementary information** The online version contains supplementary material available at https://doi.org/10.1038/s41564-023-01352-8.

**Correspondence and requests for materials** should be addressed to Jakob Trimpert.

**Peer review information** *Nature Microbiology* thanks Duane Wesemann and the other, anonymous, reviewer(s) for their contribution to the peer review of this work.



[1]Department of Infectious Diseases, Respiratory Medicine and Critical Care, Charité – Universitätsmedizin Berlin, corporate member of Freie Universität Berlin and Humboldt-Universität zu Berlin, Berlin, Germany. [2]Institut für Virologie, Freie Universität Berlin, Berlin, Germany. [3]Institute of Pathology Charité - Universitätsmedizin Berlin, corporate member of Freie Universität Berlin and Humboldt-Universität zu Berlin, and Institute for Biology, IRI Life Sciences, Humboldt-Universität zu Berlin, Berlin, Germany. [4]Berlin Institute for Medical Systems Biology (BIMSB), Max Delbrück Center for Molecular Medicine in the Helmholtz Association (MDC), Berlin, Germany. [5]Institut für Tierpathologie, Freie Universität Berlin, Berlin, Germany. [6]Institute of Virology, Charité - Universitätsmedizin Berlin, corporate member of Freie Universität Berlin and Humboldt-Universität zu Berlin, Berlin, Germany. [7]Berlin Institute of Health (BIH), Berlin, Germany. [8]Product Testing of IVMPs, Division of Veterinary Medicines, Paul-Ehrlich-Institut, Langen, Germany. [9]German Center for Infection Research (DZIF), partner site Gießen-Marburg-Langen, Giessen, Germany. [10]Faculty of Medicine, Cyprus International University, Nicosia, Cyprus. [11]Institute of Physiology, Charité - Universitätsmedizin Berlin, corporate member of Freie Universität Berlin and Humboldt-Universität zu Berlin, Berlin, Germany. [12]Department of Gynecology, Charité - Universitätsmedizin Berlin, corporate member of Freie Universität Berlin and Humboldt-Universität zu Berlin, Berlin, Germany. [13]German Center for Infection Research (DZIF), partner site Charité, Berlin, Germany. [14]Berlin Institute for Medical Systems Biology (BIMSB) Max Delbrück Center for Molecular Medicine in the Helmholtz Association (MDC), and Institute for Biology, Humboldt-Universität zu Berlin, Berlin, Germany. [15]School of Life Sciences, Chongqing University, Chongqing, China. [16]Berlin Institute of Health at Charité, Universitätsmedizin Berlin, Berlin, Germany. [17]Department of Infectious Diseases and Public Health, Jockey Club College of Veterinary Medicine and Life Sciences, City University of Hong Kong, Kowloon, Hong Kong, China. [18]These authors contributed equally: Geraldine Nouailles, Julia M. Adler. [19]These authors jointly supervised this work: Emanuel Wyler, Dusan Kunec, Jakob Trimpert. ✉e-mail: trimpert.jakob@fu-berlin.de

https://doi.org/10.1038/s41564-023-01352-8

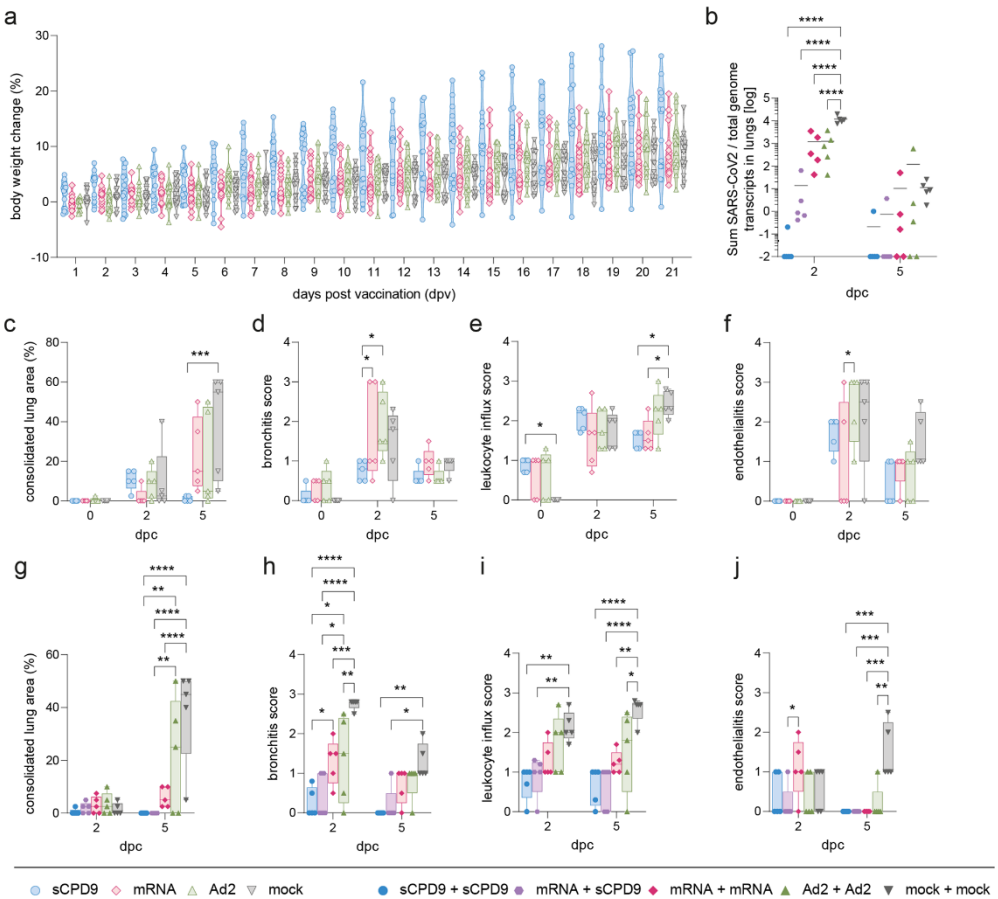


**Extended Data Fig. 1 | Body weight development post vaccination.** (**a**) Body weight development in percent of prime vaccinated hamsters were measured for 21 days until virus challenge time point and displayed according to vaccination group. Violine plot (truncated) with quartiles and median. (**b**) Prime-boost experiment: Relative expression of SARS-CoV-2 total canonical junction-spanning viral mRNA transcripts, compared to the total genomic transcripts, generated after bulk RNA sequencing analysis from homogenized lung tissue. Values are shown in log10 scale for both time-points analyzed. Scatter dot plot with mean. Two-way ANOVA (analysis of variance) and Tukey's multiple comparison test. (**c** – **j**) Semi-quantitative scoring of histopathological findings of Syrian hamsters included in prime (**c** – **f**) and prime-boost setting (**g** – **j**): (**c**, **g**) Consolidated lung area found in the left lung lobe is displayed in percentage. (**d**, **h**) Bronchitis score accounts for severity of bronchial epithelial necrosis and bronchitis. (**e**, **i**) To consider local cellular immune response, pulmonary infiltration of neutrophils, lymphocytes and macrophages was assessed in the leukocyte influx score. (**f**, **j**) The extent of endothelialitis in the left lung lobe is indicated in the endothelialitis score. (**c** – **j**) Results are shown as centre (median), box ($25^{th}$ to $75^{th}$ percentile) and whiskers (Min to Max.) plots. Two-way ANOVA and Tukey's multiple comparison test. $*p < 0.05$, $**p < 0.01$, $***p < 0.001$, and $****p < 0.0001$. (**b** – **j**) n = 5 individual hamsters for all groups. Prime and prime-boost experiment were conducted independently.

https://doi.org/10.1038/s41564-023-01352-8

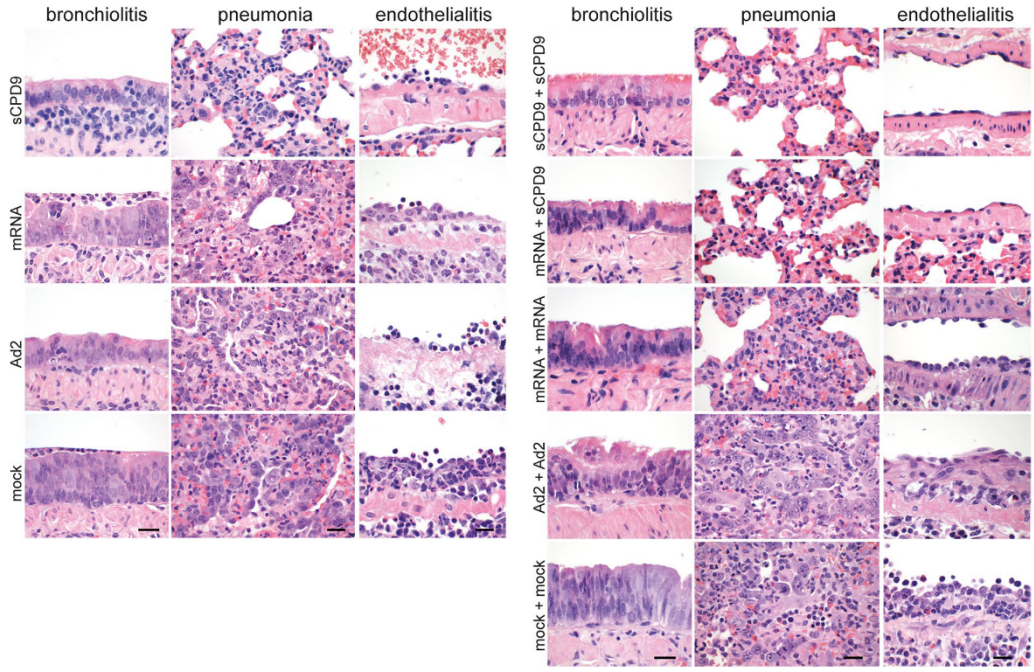


**Extended Data Fig. 2 | Lung histopathology.** Representative histopathology of haematoxylin and eosin-stained lung sections from prime-only and prime-boost vaccination experiments at 5 dpc. Images are representative of n = 5 hamsters per indicated group. Prime and prime-boost experiments were performed independently. For both experiments, columns show, from left to right, bronchitis, pneumonia affecting the respiratory alveoli and blood vessels with endothelialitis. In the prime-only approach, and in contrast to all other groups that developed necrosupperative and hyperplastic bronchitis, only sCPD9 vaccinated hamsters had negligible bronchitis in the presence of BALT-like subepithelial infiltration with lymphocytes and plasma cells. In the lungs, alveoli of sCPD9 vaccinated animals presented with much less consolidated respiratory parenchyma, with less infiltrating macrophages and neutrophils. Only Ad2 and mock- vaccinated animals developed marked alveolar metaplastic remodeling, indicating regeneration after necrosis of alveolar epithelia. Endothelialitis was milder in all vaccinated groups compared to mock-vaccinated animals. In the prime-boost experiments, hyperplastic bronchitis was mildest in sCPD9+sCPD9 and mRNA+sCPD9 vaccinated hamsters. Consolidation of respiratory parenchyma and alveolitis were least severe in both sCPD9 boostered groups. Metaplastic epithelial remodeling was particularly pronounced in Ad2-Ad2 vaccinated animals. Endothelialitis was strongly reduced to similar degrees in all boostered groups. Scale bars = 20 µm for each column.

https://doi.org/10.1038/s41564-023-01352-8

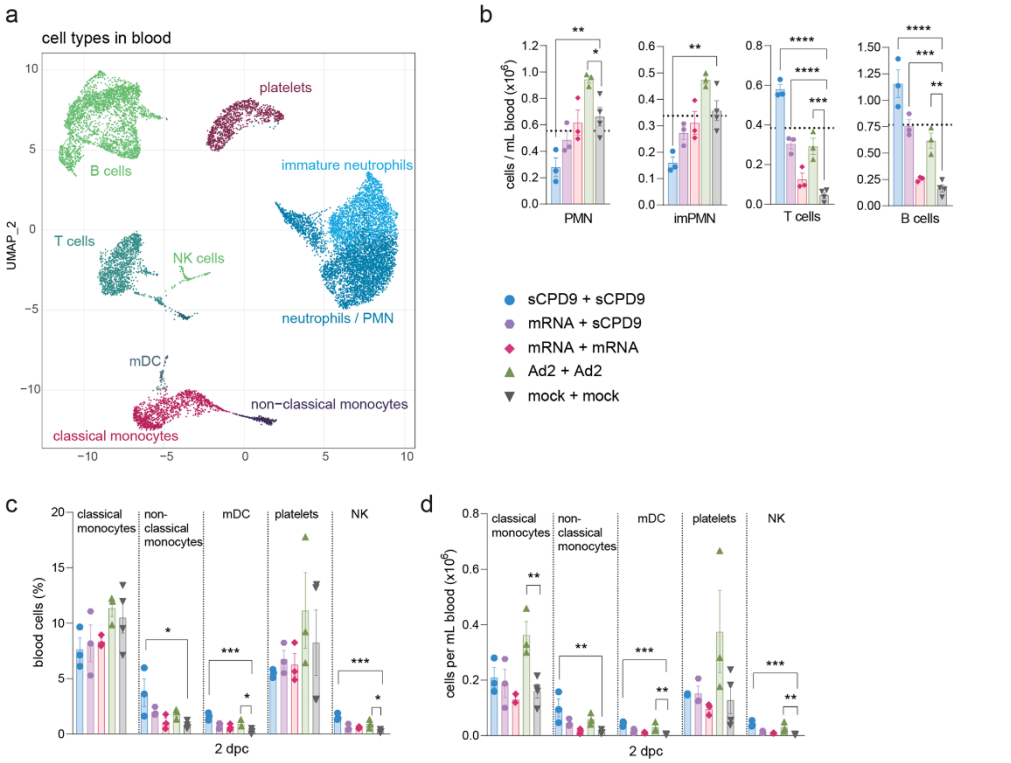


**Extended Data Fig. 3 | Immune cell responses in blood.** (**a**) Two-dimensional projections of single-cell transcriptomes using UMAP of blood cells from prime-boost experiment. Cells are colored by cell types as annotated based on known marker genes. (**b**, **d**) Numbers of cellular components per ml blood for the prime-boost experiment. (**c**) Percentage of blood cellular components for the prime-boost experiment. (**b** – **d**) One-way ANOVA and Dunnett's multiple comparisons test against mock-mock group per cell type are shown. Mean ± SEM, symbols represent individual hamster. $n_{sCPD9-sCPD9} = 3$, $n_{mRNA+sCPD9} = 3$, $n_{mRNA+mRNA} = 3$, $n_{Ad2-Ad2} = 3$, $n_{mock+mock} = 4$ individual hamsters as symbols. $*p < 0.05$, $**p < 0.01$, and $***p < 0.001$.

https://doi.org/10.1038/s41564-023-01352-8

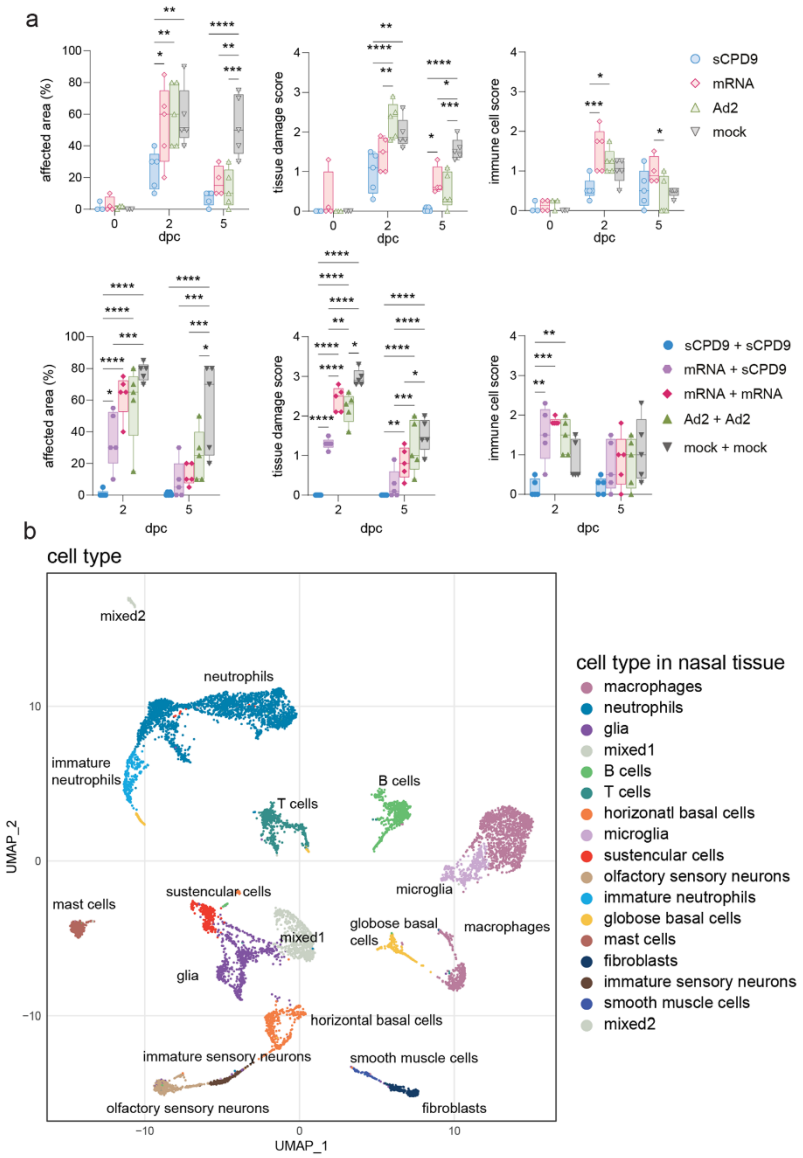


**Extended Data Fig. 4 | Mucosal immune responses.** (**a**) Semi-quantitative scorings of histopathological findings in hamsters that received prime vaccination (top row) or prime-boost vaccination (bottom row). The area affected by mucosal damage due to SARS-CoV-2 infection is shown in percentage. The tissue damage score accounts for epithelial exfoliation, necrosis, apoptosis, cellular debris and cilium loss. Presence of neutrophils and lymphocyte in the nasal conchae is assessed by the immune cell score. Centre (median), Box (25th to 75th percentile) and whiskers (Min to Max). Two-way ANOVA and Tukey's multiple comparison test were performed for statistical evaluation. N = 5 individual hamster per group. $*p < 0.05$, $**p < 0.01$, $***p < 0.001$, $****p < 0.0001$. (**b**) Two-dimensional projections of single-cell transcriptomes using UMAP of nasal tissue cells from prime experiment. Coloration indicates cell types as annotated based on known marker genes.

https://doi.org/10.1038/s41564-023-01352-8

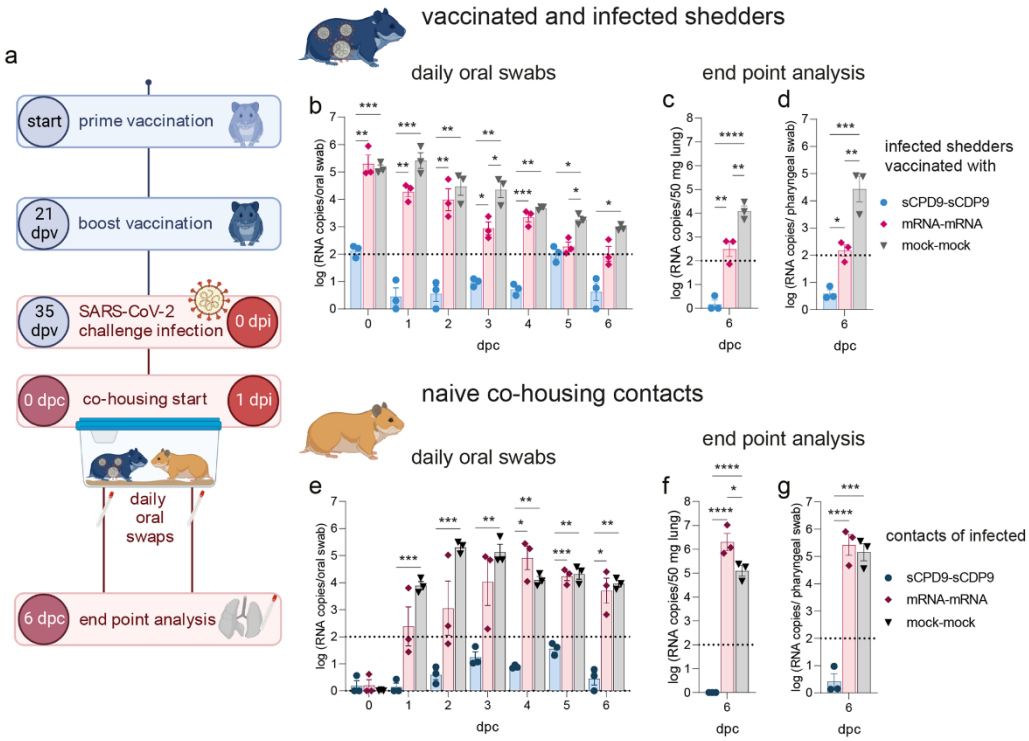


**Extended Data Fig. 5 | Onward transmission analysis.** (**a**) Design of a proof-of-principle onward transmission experiment. Hamsters were vaccinated with a furin cleavage site deleted sCPD9 LAV or the BNT162b2 mRNA vaccine in a prime-boost schedule. Challenge infection was performed with SARS-CoV-2 variant B.1, vaccinated and challenged animals were co-habitated with naïve contacts starting 24 hours post challenge for 6 consecutive days. (**b**) SARS-CoV-2 RNA load in daily oral swabs taken from vaccinated shedders throughout the period of co-housing. N = 3 per group, mean ± SEM. Two-way ANOVA, Tukey's multiple comparisons test. (**c**) SARS-CoV-2 RNA load in lungs and (**d**) pharyngeal swabs at termination of vaccinated shedder animals. N = 3, mean ± SEM, One-way ANOVA, Tukey's multiple comparisons test. (**e**) SARS-CoV-2 RNA load in daily oral swabs taken from naïve contact animals throughout the period of co-housing. N = 3, mean ± SEM. Two-way ANOVA, Tukey's multiple comparisons test. (**f**) SARS-CoV-2 RNA load in lungs and (**G**) pharyngeal swabs at termination of naïve contact animals. N = 3, mean ± SEM, One-way ANOVA, Tukey's multiple comparisons test. $*p < 0.05$, $**p < 0.01$, $***p < 0.001$, $****p < 0.0001$. Panel a was created with BioRender.com.

# 3 Diskussion und Ausblick

Die Immunologie begründet sich als Infektionsimmunologie mit den Arbeiten von Jenner, Koch und Pasteur im 18. und 19. Jahrhundert. Mit dem Ziel, tödliche Krankheitsverläufe zu verhindern und Krankheitsmechanismen zu entschlüsseln, entwickelten sie die ersten Impfstoffe und identifizierten Keime als Ursache von Krankheiten[89]. Die Entdeckung der Phagozytose durch Metchnikoff und die Beschreibung der Antikörper durch Behring und Ehrlich ebneten den Weg für die Entdeckung weiterer Immunzellen[90,91]. Entgegen den Hoffnungen der ersten Infektionsimmunologen sind die Pocken bis heute die einzige offiziell ausgerottete Infektionskrankheit[92].

Das Verständnis der Immunität hat sich seit den ersten Impfversuchen von Edward Jenner vor fast 230 Jahren stark verändert. Die Grundprinzipien der Wirkung der Immunität sind verstanden, aber bis heute werden neue Immunzellen entdeckt und ihre Bedeutung bei der Bekämpfung von Pathomechanismen oder Autoimmunität entschlüsselt[93,94]. Zu den neueren Konzepten der Immunologie gehört zum einen, dass Immunantworten auf Krankheitserreger nicht per se positiv zu bewerten sind, sondern im Übermaß oder nicht zielgerichtet auch sogenannte Immunpathologien auslösen können. Zum anderen weiß man heute, dass Gewebe nicht nur Organ-typische Funktionen ausüben, sondern auch aktiv an der Erregererkennung und Immunantwort beteiligt sind[50,71,95].

In den vorliegenden sowie weiteren Forschungsarbeiten konnten wir durch die Etablierung und Evaluierung neuer Tier- und Infektionsmodelle für *Mycobacterium tuberculosis*, *Streptococcus pneumoniae* und SARS-CoV-2 in Mäusen und Hamstern relevante pathologische und protektive Immunmechanismen nachweisen und interventionelle Therapiestrategien wie präventive Impfstrategien charakterisieren.

### Immunpathologien bei Tuberkulose, CAP und COVID-19

Die Weltgesundheitsversammlung verabschiedete 2014 die „*post-2015 End TB Strategy*" der WHO mit dem Ziel, bis 2030 die TB-Inzidenz um 80% und die Rate der TB-Todesfälle um 90% zu senken[96]. Ein wissenschaftlicher Ansatz, sich diesem Ziel zu nähern, ist die Aufklärung der Frage, welche infizierten Personen, ausgehend von einer latenten TB, eine aktive TB entwickeln. Die rechtzeitige Identifikation und medikamentöse Behandlung dieser sogenannten „Progressoren" könnte die Transmissionsrate und somit die Inzidenz und die daraus resultierenden Todesfälle deutlich senken.

Immun- und Pathomechanismen, die eine aktive TB und Progression begünstigen, wurden von uns und anderen in Patienten- und Populationskohorten sowie Tiermodellen untersucht. Hierbei zeigte sich, dass Typ-I-IFN, Neutrophilenantwort und die Granulomnatur eine Rolle spielen. 2010 wurde erstmalig beschrieben, dass Patienten mit einer aktiven TB eine distinkte Transkriptom-Signatur im Blut aufweisen. Anhand von 86 Genen ließ sich die aktive TB von anderen inflammatorischen und Infektionskrankheiten unterscheiden. Für die Grundlagenforschung war hierbei insbesondere die Beobachtung relevant, dass es sich um eine IFN-γ, vor allem aber auch eine Typ-I-IFN getriebene Gensignatur von Neutrophilen handelte[97]. Typ-I-IFN und Neutrophile waren keine Immunkomponenten, die bis dato mit intrazellulären Mykobakterien assoziiert waren. Diese Entdeckung motivierte uns und andere, die Rolle von Typ-I-IFN und Neutrophilen für die Pathogenese der TB genauer zu untersuchen. In mit *Mycobacterium leprae*-infizierten Patienten und *in vitro* Modellen zeigte sich, dass die Typ-I-IFN Antwort nachteilig ist, da sie über Interleukin (IL)-10 Induktion die effektive anti-mykobakterielle Typ-

II-IFN Antwort (IFN-γ) unterbindet[98]. Mayer-Barber et al. beschrieben für *Mycobacterium tuberculosis* Infektionen in Mäusen und Patienten ein Immunnetzwerk, welches aus Typ-I-IFN, IL-1, und Prostaglandin E2 ($PGE_2$) besteht. Auch hier aggraviert Typ-I-IFN den Krankheitsverlauf, wohingegen IL-1 und IL-1-induziertes $PGE_2$ protektiv wirken. IL-1 und $PGE_2$ inhibieren ihrerseits die Typ-I-IFN Produktion[99]. Wir konnten anhand von Typ-I-IFN-Rezeptor (IFNAR1)-defizienten Mäusen bestätigen, dass Typ-I-IFN Signalisierung zu letalen TB Verläufen führt. Darüber hinaus haben wir gezeigt, dass die Ursache in einer ausgeprägten Neutrophilenrekrutierung lag, und konnten diese mittels Neutrophilendepletion reversieren[100]. In einer weiteren Studie konnten wir zeigen, dass die pathologische Neutrophilenantwort in der murinen TB durch Epithelzellen vermittelt wird, die nach Aktivierung das Neutrophilen-rekrutierende C-X-C motif Chemokin 5 (CXCL5) produzieren[50]. Darüber hinaus zeigte sich, dass eine Überaktivierung der Neutrophilen durch eine Deletion einer regulatorischen mikro-Ribonukleinsäure (miR), der miR-223, zu letalen Verläufen führt[69]. Diese Studien legen nahe, dass sowohl Typ-I-IFN, die primär mit viralen Erkrankungen, als auch insbesondere Neutrophile, die primär mit extrazellulären Pathogenen assoziiert sind, maßgeblich an TB Pathologien beteiligt sind und deuten ursächlich auf eine fehlgeleite Immunität hin[101].

Die Bedeutung von Neutrophilen und Typ-I-IFN bei aktiver TB war etabliert, jedoch blieb unklar, welche Faktoren die Progression von latenter TB zu aktiver TB begünstigen. Eine weitere großangelegte multizentrische TB-Studie konnte 2016 eine 16-Gen-Signatur identifizieren, die statistisch die Progression von Patienten mit latenter TB zu aktiver TB vorhersagen konnte[102]. Diese Studie beschrieb die gefundenen Gene jedoch ausschließlich als Biomarker, ohne Translation ihrer Bedeutung für Immunpathologie und -antwort. Im Zuge einer Progression zur aktiven TB kommt es zur Reaktivierung der Mykobakterien und Strukturänderungen der Granulome. Deswegen sind Tiermodelle, die Granulome bilden, wie sie im Menschen beobachtet werden, essentiell, um die Progression, aber auch Reversion dieser Prozesse zu studieren. Klassische Labormausstämme wie Balb/c und C57BL/6 bilden nur granulomartige Strukturen nach Infektion aus[55]. Daher haben wir humane Stammzellen der fetalen Leber in NOD *scid* gamma (NSG)-defiziente Mäuse transferiert, um sogenannte humanisierte Mäuse (Humanes Immunsystem (HIS)-NSG Mäuse) zu generieren[103]. Die HIS-NSG Mäuse zeigten nach *Mycobacterium tuberculosis* Infektion nekrotische Granulome und waren geeignet, die Effektivität einer Chemotherapie bei voll ausgebildeten Granulomen zu evaluieren[104]. HIS-NSG Mäuse haben jedoch den Nachteil, dass man auf humane Spenderorgane, wie fetale Lebern angewiesen ist und der Generierungsprozess technisch und zeitlich aufwendig ist. Nachdem Studien gezeigt hatten, dass *diversity outbred* Mäuse ebenfalls ein breites Spektrum an Granulomen abbilden können, setzte sich dieses einfachere Modell durch[105,106]. Ribonukleinsäuren (RNA)-Sequenzierungsdaten aus verschiedenen TB-Modellen, wie dem *diversity outbred* Mausmodell und nichtmenschlichen Primaten, wurden mit Daten von TB-Patienten integriert, um spezies-übergreifende Mechanismen zu identifizieren, die TB-progrediente oder TB-kontrollierende Krankheitsmechanismen bedingen. Viele der zuvor genannten Gene der 16-Gen-Signatur wurden auch in den Tiermodellen gefunden[107].

Die mathematische Integration von Tiermodelldaten mit Patienten-Daten ist auch ein Ansatz, den wir in unserer Forschung verfolgen. Wir verwenden jedoch Einzelzellsequenzierungsdaten, da der Informationsgehalt hier wesentlich feingranularer ist und auf einzelne Zellpopulationen heruntergebrochen werden kann[82]. So können wir einerseits abschätzen, welche Tiermodelle für welche Forschungsfragen geeignet sind, um andererseits, welche Immunprozesse zwischen den Spezies konserviert sind.

CAP zeichnet sich durch eine erhöhte Morbidität mit einer beachtlichen Sterblichkeitsrate aus[108,109]. ARDS ist eine durch Immunpathologie gekennzeichnete Komplikation der schweren CAP, die bei ~3% der Streptokokken-CAP auftritt[110]. Zu Beginn der COVID-19 Pandemie lag die ARDS-Rate in Ermangelung etablierter Behandlungsschemata und Impfstoffe bei 33% aller hospitalisierten COVID-19 Patienten und damit deutlich höher als bei der Streptokokken-CAP[109,111]. Bei der zielgerichteten Behandlung von bakteriellen sowie viralen Pneumonien steht neben der Pathogenreduktion auch die Prävention eines ARDS und des damit verbundenen akuten Lungenversagens im Vordergrund.

Die Bedeutung der miR-223 und des Chemokins CXCL5 haben wir nicht nur im Kontext von TB, sondern auch im *Streptococcus pneumoniae* Infektionsmodell untersucht[71,112]. Auch hier zeigte sich, dass trotz des extrazellulären Pathogens und der Notwendigkeit von Neutrophilen zur Klärung der Bakterien[67], überschießende Neutrophilenantworten schwere Immunpathologien in vulnerablen Organen wie der Lunge auslösen können. Im Pneumokokken-Pneumonie Mausmodell konnten wir zeigen, dass insbesondere die Schädigung der alveolo-kapillaren Barriere für letale Verläufe verantwortlich ist. Bemerkenswert hierbei war, dass eine zeitige, nicht aber eine verzögerte Antibiotikagabe die Lungenbarriere schützte. Der Schutz war unabhängig von der Wirksamkeit der Antibiotika, da zu allen Zeitpunkten bakterielle Lasten effektiv reduziert wurden. Diese Daten wurden in weiteren Untersuchungen bestätigt, insbesondere die Stabilisierung der Integrität der Lungenbarriere, zum Beispiel mit dem Angiopoietin-1-Mimetikum Vasculotide. erwies sich als geeignete Strategie für adjuvante Antibiotikatherapien[113]. CXCL5-defiziente Mäuse zeigen neben der eingangs erwähnten verringerten Rekrutierung von Neutrophilen und damit einhergehenden Reduktion inflammatorischer Parameter, auch eine geschützte Lungenbarriere[112]. Wir konnten zeigen, dass CXCL5 direkt auf pulmonale Epithelzellen wirkt und ihre Durchlässigkeit erhöht, somit ist die Neutralisation von CXCL5 eine vielversprechende adjuvante Therapie, da sie zwei kritische Faktoren, die erhöhte Neutrophilen-getriebene Inflammation, aber auch die Destabilisierung der epithelialen Lungenbarriere gleichzeitig behandelt. Aber auch Strategien, die gezielt inflammatorische Prozesse hemmen, wie die Gabe von Komplementkomponente C5a (C5a)-Spiegelmeren, können letale Prozesse wie Lungen- und extrapulmonales Organversagen bei schweren bakteriellen Pneumonien unterbinden[114]. Entsprechend zeichnete sich Vilobelimab, ein anti-C5a Antikörper, auch in ventilierten COVID-19 Patienten als mortalitätsverringernd aus[115]. Inflammations-suppressive adjuvante Therapien wie Kortikosteroide bei schwerer CAP anzuwenden, liegt auf der Hand. Dennoch empfahl die „*American Thoracic Society and the Infectious Diseases Society of America*" 2019 Kortikosteroide nicht als adjuvante Therapie bei adulter CAP einzusetzen[22]. Die Studienlage war nicht eindeutig und insbesondere bei Influenzapatienten gab es Anzeichen, dass eine Kortikosteroidbehandlung den Krankheitsverlauf aggravieren könnte[116]. Die Ergebnisse der von 2015 – 2020 gelaufenen und 2023 veröffentlichten CAPE COD Studie legen jedoch nahe, dass Kortikosteroide die Sterblichkeit einer Untergruppe von CAP-Patienten (erhöhter Sauerstoffbedarf, Intensivpflichtigkeit, keine Influenzainfektion sowie kein septischer Schock), senken können[117]. Das Umdenken ist sicherlich auch auf die COVID-19 Pandemie und die seit der 2021-veröffentlichten RECOVERY Studie erfolgreich und vielfach eingesetzten Kortikosteroiden zurückzuführen[78]. Trotz des routinemäßigen Einsatzes von Kortikosteroiden waren die Mechanismen, die ihrer Schutzwirkung bei COVID-19 Patienten zugrunde liegen, unbekannt. Wir haben daher in COVID-19 Hamstermodellen die Wirkungsweisen von Kortikosteroiden und monoklonalen Antikörpern gegen SARS-CoV-2 untersucht. Wir konnten zeigen, dass ähnlich wie bei aktiver TB und schwerer CAP, eine Überaktivierung der Neutrophilen ursächlich für schwere bis letale Krankheitsverläufe war. Die Kortikosteroidtherapie adressierte gezielt inflammatorische Leukozytenpopulationen und dämpfte insbesondere eine Subpopulation überaktivierter Neutrophile. Monoklonale Antikörpertherapie reduzierte die virale Last, konnte aber nur in Kombination mit

Dexamethason schwere Krankheitsverläufe verhindern[118]. Dies entspricht unseren Beobachtungen im Mausmodell der schweren CAP, wo eine zu spät antibiotisch-behandelte Pneumokokken-Pneumonie trotz Reduktion der Bakterienlast einen letalen Verlauf nimmt[70].

Im Rahmen unserer COVID-19 Studien haben wir auch die erfolgreiche Immunantwort der Syrischen Hamster mittels Einzelzellsequenzierung charakterisiert. Hierbei zeigte sich, dass eine ausgewogene Typ 1 Immunität inklusive rekrutierter NK Zellen, CD4 Th1 und zytotoxischen CD8 T-Zellen sowie neutralisierender Antikörper die Virusantwort kontrolliert und reversible Lungenpathologien auslöst. Die Neutrophilenantwort fiel im Vergleich zu den Roborovski Hamstern, welche sich durch schwere letale COVID-19 Verläufe auszeichnen, geringer aus[86,88]. Der beste Schutz vor Infektionskrankheiten bleibt jedoch die Prävention der Infektion.

### Mukosale Immunität durch Impfung

Impfungen erzielen im besten Fall eine Infektionsprävention, mindestens erreichen sie jedoch asymptomatische bis mildere Verläufe der Infektionskrankheit. Die ersten Versuche der Impfstoffentwicklung basierten auf der Beobachtung, dass Genesene sich nicht erneut ansteckten. Heute weiß man, dass ein erfolgreicher Impfstoff sowohl Pathogen-Antigene als auch Stimulanzien der angeborenen Immunantwort enthalten muss. Ist der Impfstoff nicht endogen immunstimulierend, so müssen Adjuvantien zugesetzt werden. Das Adjuvant stimuliert die Aktivierung der PRR und stellt sicher, dass das applizierte Antigen als fremd erkannt wird und somit immunogen wirkt. Die Aktivierung der adaptiven Immunzellen und Ausbildung von Gedächtnis-T und -B-Zellen findet in den lymphatischen Organen statt[89].
Zugelassene COVID-19-Impfstoffe sind sehr erfolgreich, schwere Krankheitsverläufe abzumildern, in dem sie neutralisierende Serumantikörper, Plasmazellen und Gedächtnis-T-Zellen induzieren, die im Fall einer Infektion eine schnellere und stärkere gezielte Immunantwort auslösen[119,120]. Aktuelle COVID-19-Vakzine nutzen hierbei unterschiedliche Vakzin-Plattformen und Adjuvant-Formulierungen. Adenovirus-Vektor-basierte sowie die neuartigen Boten-RNA (engl. messenger-(m)RNA) Impfstoffe werden intramuskulär verabreicht und induzieren somit primär systemische Immunantworten. Diese systemische Immunität verhindert jedoch keine initiale Infektion der oberen Atemwege, was sich an der weiteren Übertragung des SARS-CoV-2 Virus durch Geimpfte erkennen lässt. So zeigten Studien, die auf den nationalen Datenbanken des israelischen Gesundheitswesens basierten, dass die Transmissionsraten durch die Pfizer/BioNTech BNT162b2 Impfung moderat reduziert, aber nicht verhindert werden[121,122]. Ziel der Impfstoffweiterentwicklung ist es zum einen, Transmissionsraten zu senken und zum anderen möglichst breite Immunität zu erzeugen, die nicht nur aktuelle, sondern auch zukünftige Virus-Varianten abdeckt. Insbesondere die Induktion von neutralisierenden IgA Antikörpern verhindert die initiale Infektion der lokalen Gewebezellen und die Replikation der Viren in den oberen Atemwegen[123].

In unserer Impfstudie verwendeten wir einen lebend-attenuierten Impfstoffkandidaten, der transnasal appliziert wird, um diese Ziele zu erreichen. Unsere Kollegen aus dem Institut für Virologie, Fachbereich Veterinärmedizin der FU Berlin haben hierfür mittels Codon-Paar-Deoptimierung[124] ein lebend-attenuiertes SARS-CoV-2 generiert[125]. Der Impfstoff-Kandidat sCPD9 wurde mittlerweile durch Entfernung der Furin-Spaltstelle so modifiziert, dass er nicht mehr übertragbar ist[126]. Wir konnten zeigen, dass der Impfstoff-Kandidat sCPD9 mukosale Immunität in Form von re-aktivierbaren geweberesidenten Gedächtnis-T-Zellen sowie neutralisierende IgA Antikörper induziert. Darüber

hinaus schützte sCPD9 auch gegen neuartige Virusvarianten, inklusive Omicron[87]. Die Induktion einer mukosalen Immunität ist hier vor allem auf die transnasale Applikation zurückzuführen, die die natürliche Infektionsroute widerspiegelt[127]. Auch andere Vakzinplattformen induzieren mukosale Immunität, wenn sie nasal appliziert werden, wie eine Reihe neuerer Studien zeigen. Ein intranasal verabreichter Impfstoff-Kandidat, der auf einem SARS-CoV-2 Spike Trimer Protein in Kombination mit einem neuartigen Adjuvant (LP-GMP), welches TLR2 und Sting stimuliert, basiert, induzierte ebenfalls erfolgreich mukosale Immunität in Form von Spike-spezifischen IgA und gewebe-residenten Gedächtnis-T-Zellen in K18-hACE2 transgenen Mäusen und schützte vor Infektion mit dem parentalen Delta SARS-CoV-2 Stamm[128]. Eine einfache intranasale Immunisierung mit einem trivalenten COVID-19-Impfstoff basierend auf einer Adenovirus-Plattform, welche Antigene der 3 SARS-CoV-2 Proteine Spike, Nukleokapsid, und RNA-abhängige RNA Polymerase (engl. *RNA-dependent RNA polymerase* (RdRp)) exprimiert, induzierte mukosale Immunität, schützte vor dem parentalen SARS-CoV-2 Stamm, sowie gegen die Varianten Alpha und Beta[129]. Sogar die adjuvantien-freie intranasale Applikation des Spike Proteins als Auffrischungsimpfung (engl. *Boost*) einer vorangegangenen intramuskulären Pfizer/BioNTech BNT162b2in Impfung induzierte mukosale Immunität in Form von IgA und gewebe-residenten Gedächtnis-T- und B-Zellen. Diese Strategie reduzierte, im Gegensatz zum klassischem intramuskulären *Boost*, auch die Transmissionsraten der Versuchstiere[130]. Ad5-nCoV ist ein aerosolisierter mukosaler Impfstoff, der für Hochrisikogruppen in Indien und China zugelassen ist. Eine kürzlich veröffentliche Studie bestätigte die Sicherheit und Immunogenität von Ad5-nCoV anhand von 10.059 Probanden in der Sicherheitsstudie und 416 Probanden in der Immunogenitätsstudie. Probanden, die mit aerosolisiertem Ad5-nCoV im Gegensatz zu inaktiviertem Impfstoff geboostert wurden, hatten signifikant erhöhte neutralisierende Antikörper gegen die Omicron Varianten BA.4/5[131].

Die Erkenntnis der Bedeutung der Induktion einer mukosalen Immunität durch Impfstoffe[127] ist eine wichtige Entwicklung, ein weiterhin bestehender Nachteil der gängigen COVID-19-Impfstoffe bleibt jedoch die Fokussierung auf das Virushüllen Glykoprotein Spike. Das SARS-CoV-2 Spike Protein bindet an den Wirtszellen-Rezeptor ACE2 und vermittelt die Virus-Zell-Fusion sowie die Fusion von Zellmembranen und ist essentiell für die Infektiosität und Vermehrung von SARS-CoV-2. Nicht nur COVID-19-Impfstoffe, sondern auch die natürliche Immunität generiert neutralisierende Antikörper gegen Spike[132-134]. Die Entstehung von Escape-Varianten mit Fluchtmutationen im Spike Gen legt nahe, die antigene Wirkung der zukünftigen Impfstoffe breiter anzulegen[135]. Eine Möglichkeit, diese Problematik zu adressieren, ist die Verwendung von lebend-attenuierten Impfstoffen, die, wie wir in unserer Studie zeigen konnten, ein breiteres Antigenspektrum abdecken[87]. Eine Alternative ist die Supplementierung lizensierter Vakzin-Plattformen mit zusätzlichen Antigenen, die sowohl zelluläre T-Zellimmunität und ein breiteres Spektrum an neutralisierenden Antikörpern stimulieren. Der auf mRNA-Plattform basierende Impfstoffkandidat BNT162b4 soll gezielt T- Zellen stimulieren und beinhaltet hierfür Antigene des Nukleokapsids, der Membran und der ORF1ab-Proteine, jedoch keine Spike Antigene[136]. Der zuvor erwähnte intransal verabreichte trivalente COVID-19-Impfstoff beinhaltet Antigene der Proteine Spike, Nukleokapsid und RdRp[129]. Beide multi-antigenen Impfstoffe vermittelten ebenfalls Schutz gegen die nicht-parentale SARS-CoV-2 Variante [129,136].

Abschließend lässt sich feststellen, dass die erfolgreiche Entwicklung von Impfstoffen wie auch von Medikamenten gegen Immunpathologien profunde Kenntnisse der protektiven und pathologischen Immunität, aber auch der Erregerbiologie voraussetzt. Die Infektionsimmunologie ist eine wichtige Schnittstelle zwischen Grundlagenforschung und translationaler Forschung. Aktuelle Entwicklungen in Richtung Multi-Omics Analysen bieten die Möglichkeit, komplexe Sachverhalte und parallel

ablaufende Prozesse synchronisiert zu betrachten und auszuwerten. Insbesondere die Integration und Auswertung von Cross-Spezies Datensätzen bietet die Chance, allgemeingültige immunologische Korrelate für Schutz sowie Pathologie zu identifizieren und dieses Wissen in neue, im Tiermodell untersuchbare und im Patienten wirksamen Medikamente zu translatieren[82].

# 4 Zusammenfassung

Diese Arbeit untersucht die Entstehung von Immunpathologien, die schweren pathogen-induzierten Pneumonien zugrunde liegen, und zeigt mögliche Behandlungs- und Präventionsstrategien anhand eigens etablierter und angewandter Tiermodelle auf. Dazu wurden modernste Untersuchungsmethoden wie die Einzelzellsequenzierung eingesetzt und neuartige Tiermodelle wie humanisierte Mäuse und CAP Modelle für die Evaluierung adjuvanter Therapien sowie COVID-19-Hamstermodelle entwickelt.

Wir zeigen, dass in den drei untersuchten Infektionskrankheiten TB, CAP und COVID-19 eine fehlgeleitete Neutrophilenantwort schwerwiegende Lungenschäden und Krankheitsverläufe verursachen kann. Gleichzeitig demonstrieren wir den Erfolg einer gezielten therapeutischen Adressierung dieser inflammatorischen Immunzellen. In der TB sind vor allem Neutrophilenantworten, die durch Typ-I-IFN stimuliert werden, für eine Reaktivierung von dormanten Mykobakterien in Granulomen und somit für den Übergang von latenten zu akuten infektiösen Krankheitsbildern verantwortlich. Auch schwere akute TB-Verläufe zeichnen sich durch überschießende Neutrophilenantworten aus, die unter anderem durch die lokale Aktivierung des Epithels und die Ausschüttung des Chemokins CXCL5 verursacht werden. In der CAP und bei COVID-19 treten bei schweren Verläufen überschießende Neutrophilenantworten auf, die Schäden an der alveolo-kapillären Barriere verursachen und somit akutes Lungenversagen provozieren können. Moderate COVID-19 Verläufe zeichnen sich dagegen durch eine mäßige und reversible Rekrutierung von Neutrophilen aus. Neben Therapien, die die Pathogenlast reduzieren - wie Antibiotika bei Pneumokokken-CAP sowie Virostatika und anti-virale Antikörper bei COVID-19 - sind vor allem adjuvante Therapien wirksam, die die Inflammation reduzieren. Wir konnten nachweisen, dass die Anwendung von Kortikosteroiden in COVID-19 die inflammatorischen Reaktionen von Neutrophilen limitiert und somit letale Krankheitsverläufe unterbindet. Kortikosteroide hatten zwar in unseren Analysen den stärksten Einfluss auf Neutrophile, jedoch beeinflussen sie auch ein breites Spektrum an Immun- und Gewebezellen. Eine ideale adjuvante Therapie würde einen bekannten und zielgerichteten Wirkmechanismus haben. Hier hat sich *Vasculotide* als wirksames Adjuvans erwiesen. Es aktiviert den Tie-2 Rezeptor und stabilisiert gezielt die endotheliale Lungenbarriere. Ein weiterer vielversprechender Kandidat ist CXCL5. CXCL5 wird von aktivierten Epithelzellen lokal produziert, um inflammatorische Neutrophile zu rekrutieren und die Lungenbarriere direkt zu destabilisieren. Die Therapie würde also lokal wirken und sowohl die Zahl der Entzündungszellen begrenzen als auch der Destabilisierung der Lungenbarriere entgegenwirken.
Die effektivste Strategie zur Bekämpfung von Infektionskrankheiten bleibt jedoch die Prävention. Wir konnten nachweisen, dass eine Impfstrategie mit intranasaler Applikation eines Lebendimpfstoffs besonders erfolgreich ist. Dies liegt daran, dass sie durch das erweiterte Antigenspektrum auch vor nicht-parentalen Virusvarianten schützt und die Infektions- und Transmissionsrate drastisch senkt, indem sie die mukosale Immunität induziert.

# 5 Literaturangaben


1. World Health Organization. Global Health Estimates 2020: Deaths by Cause, Age, Sex, by Country and by Region, 2000-2019. World Health Organization, Geneva, 2020.
2. World Health Organization. Tuberculosis. World Health Organization, Geneva, 2023. https://www.who.int/news-room/fact-sheets/detail/tuberculosis (accessed 22.05.2023 ).
3. World Health Organization. WHO Coronavirus (COVID-19) Dashboard. World Health Organization, Geneva, 2023. https://covid19.who.int/ (accessed 30.10.2023 ).
4. World Health Organization. Pneumonia in children. World Health Organization, Geneva, 2022. https://www.who.int/news-room/fact-sheets/detail/pneumonia (accessed 22.05.2023 ).
5. World Health Organization. Global tuberculosis report 2022, World Health Organization, Geneva, 2022.
6. Barry CE, 3rd, Boshoff HI, Dartois V, et al. The spectrum of latent tuberculosis: rethinking the biology and intervention strategies. *Nat Rev Microbiol* 2009; **7**(12): 845-55.
7. Lu LL, Chung AW, Rosebrock TR, et al. A Functional Role for Antibodies in Tuberculosis. *Cell* 2016; **167**(2): 433-43 e14.
8. McCaffrey EF, Donato M, Keren L, et al. The immunoregulatory landscape of human tuberculosis granulomas. *Nat Immunol* 2022; **23**(2): 318-29.
9. McCaffrey EF, Donato M, Keren L, et al. Author Correction: The immunoregulatory landscape of human tuberculosis granulomas. *Nat Immunol* 2022; **23**(5): 814.
10. World Health Organization. WHO consolidated guidelines on tuberculosis. Module 3: diagnosis - rapid diagnostics for tuberculosis detection, 2021 update. World Health Organization, Geneva, 2021.
11. World Health Organization. WHO operational handbook on tuberculosis Module 4: Treatment – drug-susceptible tuberculosis treatment. World Health Organization, Geneva, 2022.
12. Suarez I, Funger SM, Kroger S, Rademacher J, Fatkenheuer G, Rybniker J. The Diagnosis and Treatment of Tuberculosis. *Dtsch Arztebl Int* 2019; **116**(43): 729-35.
13. GBD 2019 Diseases and Injuries Collaborators.. Global burden of 369 diseases and injuries in 204 countries and territories, 1990-2019: a systematic analysis for the Global Burden of Disease Study 2019. *Lancet* 2020; **396**(10258): 1204-22.
14. Department of Error. *Lancet* 2020; **396**(10262): 1562.
15. GBD 2019 LRI Collaborators. Age-sex differences in the global burden of lower respiratory infections and risk factors, 1990-2019: results from the Global Burden of Disease Study 2019. *Lancet Infect Dis* 2022; **22**(11): 1626-47.
16. Shoar S, Musher DM. Etiology of community-acquired pneumonia in adults: a systematic review. *Pneumonia (Nathan)* 2020; **12**: 11.
17. Cilloniz C, Ewig S, Polverino E, et al. Microbial aetiology of community-acquired pneumonia and its relation to severity. *Thorax* 2011; **66**(4): 340-6.
18. Prina E, Ranzani OT, Torres A. Community-acquired pneumonia. *Lancet* 2015; **386**(9998): 1097-108.
19. Centers for Disease Control and Prevention. Pneumonia Can Be Prevented—Vaccines Can Help. Center for Disease Control and Prevention, 2022. https://www.cdc.gov/pneumonia/prevention.html (accessed 22.05.2023).
20. Martin-Loeches I, Torres A, Nagavci B, et al. ERS/ESICM/ESCMID/ALAT guidelines for the management of severe community-acquired pneumonia. *Intensive Care Med* 2023: 1-18.
21. Martin-Loeches I, Torres A, Nagavci B, et al. Correction: ERS/ESICM/ESCMID/ALAT guidelines for the management of severe community-acquired pneumonia. *Intensive Care Med* 2023; Jun;49(6):615-632.
22. Metlay JP, Waterer GW, Long AC, et al. Diagnosis and Treatment of Adults with Community-acquired Pneumonia. An Official Clinical Practice Guideline of the American Thoracic Society and Infectious Diseases Society of America. *Am J Respir Crit Care Med* 2019; **200**(7): e45-e67.
23. World Health Organization. Coronavirus disease (COVID-19) pandemic. World Health Organization, Geneva, 2023. https://www.who.int/europe/emergencies/situations/covid-19 (accessed 22.5.2023).
24. Stadnytskyi V, Bax CE, Bax A, Anfinrud P. The airborne lifetime of small speech droplets and their potential importance in SARS-CoV-2 transmission. *Proc Natl Acad Sci U S A* 2020; **117**(22): 11875-7.
25. Galmiche S, Cortier T, Charmet T, et al. SARS-CoV-2 incubation period across variants of concern, individual factors, and circumstances of infection in France: a case series analysis from the ComCor study. *Lancet Microbe* 2023; Jun;4(6):e409-e417
26. Meyer NJ, Gattinoni L, Calfee CS. Acute respiratory distress syndrome. *Lancet* 2021; **398**(10300): 622-37.
27. World Health Organization. Clinical management of COVID-19: living guideline, 13 January 2023. World Health Organization, Geneva, 2023.
28. Kluge S, Janssens U, Welte T, et al. S3-Leitlinie - Empfehlungen zur Therapie von Patienten mit COVID-19, Version März 2023, 2023.
29. Li C, Jiang J, Kim K, et al. Nasal Structural and Aerodynamic Features That May Benefit Normal Olfactory Sensitivity. *Chem Senses* 2018; **43**(4): 229-37.
30. Pedan H, Janosova V, Hajtman A, Calkovsky V. Non-Reflex Defense Mechanisms of Upper Airway Mucosa: Possible Clinical Application. *Physiol Res* 2020; **69**(Suppl 1): S55-S67.
31. Button B, Cai LH, Ehre C, et al. A periciliary brush promotes the lung health by separating the mucus layer from airway epithelia. *Science* 2012; **337**(6097): 937-41.
32. Fahy JV, Dickey BF. Airway mucus function and dysfunction. *N Engl J Med* 2010; **363**(23): 2233-47.
33. Brune K, Frank J, Schwingshackl A, Finigan J, Sidhaye VK. Pulmonary epithelial barrier function: some new players and mechanisms. *Am J Physiol Lung Cell Mol Physiol* 2015; **308**(8): L731-45.
34. Hewitt RJ, Lloyd CM. Regulation of immune responses by the airway epithelial cell landscape. *Nat Rev Immunol* 2021; **21**(6): 347-62.
35. Delclaux C, Azoulay E. Inflammatory response to infectious pulmonary injury. *Eur Respir J Suppl* 2003; **42**: 10s-4s.
36. Pilette C, Ouadrhiri Y, Godding V, Vaerman JP, Sibille Y. Lung mucosal immunity: immunoglobulin-A revisited. *Eur Respir J* 2001; **18**(3): 571-88.
37. Effah CY, Drokow EK, Agboyibor C, et al. Neutrophil-Dependent Immunity During Pulmonary Infections and Inflammations. *Front Immunol* 2021; **12**: 689866.
38. Chaput C, Sander LE, Suttorp N, Opitz B. NOD-Like Receptors in Lung Diseases. *Front Immunol* 2013; **4**: 393.
39. Mosser DM, Edwards JP. Exploring the full spectrum of macrophage activation. *Nat Rev Immunol* 2008; **8**(12): 958-69.
40. Gasteiger G, Fan X, Dikiy S, Lee SY, Rudensky AY. Tissue residency of innate lymphoid cells in lymphoid and nonlymphoid organs. *Science* 2015; **350**(6263): 981-5.
41. Lambrecht BN, Prins JB, Hoogsteden HC. Lung dendritic cells and host immunity to infection. *Eur Respir J* 2001; **18**(4): 692-704.
42. Bousso P. T-cell activation by dendritic cells in the lymph node: lessons from the movies. *Nat Rev Immunol* 2008; **8**(9): 675-84.
43. Kaech SM, Wherry EJ, Ahmed R. Effector and memory T-cell differentiation: implications for vaccine development. *Nat Rev Immunol* 2002; **2**(4): 251-62.
44. Chen K, Kolls JK. T cell-mediated host immune defenses in the lung. *Annu Rev Immunol* 2013; **31**: 605-33.
45. Moore BB, Moore TA, Toews GB. Role of T- and B-lymphocytes in pulmonary host defences. *Eur Respir J* 2001; **18**(5): 846-56.
46. World Health Organization. Meeting report of the WHO expert consultation on the definition of extensively drug-resistant tuberculosis, 27-29 October 2020. World Health Organization, Geneva, 2021.
47. Cooper AM, Dalton DK, Stewart TA, Griffin JP, Russell DG, Orme IM. Disseminated tuberculosis in interferon gamma gene-disrupted mice. *J Exp Med* 1993; **178**(6): 2243-7.
48. Flynn JL, Chan J, Triebold KJ, Dalton DK, Stewart TA, Bloom BR. An essential role for interferon gamma in resistance to Mycobacterium tuberculosis infection. *J Exp Med* 1993; **178**(6): 2249-54.

49. Dorhoi A, Yeremeev V, Nouailles G, et al. Type I IFN signaling triggers immunopathology in tuberculosis-susceptible mice by modulating lung phagocyte dynamics. *Eur J Immunol* 2014; **44**(8): 2380-93.
50. Nouailles G, Dorhoi A, Koch M, et al. CXCL5-secreting pulmonary epithelial cells drive destructive neutrophilic inflammation in tuberculosis. *J Clin Invest* 2014; **124**(3): 1268-82.
51. Reece ST, Loddenkemper C, Askew DJ, et al. Serine protease activity contributes to control of Mycobacterium tuberculosis in hypoxic lung granulomas in mice. *J Clin Invest* 2010; **120**(9): 3365-76.
52. Esaulova E, Das S, Singh DK, et al. The immune landscape in tuberculosis reveals populations linked to disease and latency. *Cell Host Microbe* 2021; **29**(2): 165-78 e8.
53. Scott NR, Swanson RV, Al-Hammadi N, et al. S100A8/A9 regulates CD11b expression and neutrophil recruitment during chronic tuberculosis. *J Clin Invest* 2020; **130**(6): 3098-112.
54. Cadena AM, Fortune SM, Flynn JL. Heterogeneity in tuberculosis. *Nat Rev Immunol* 2017; **17**(11): 691-702.
55. Gupta UD, Katoch VM. Animal models of tuberculosis. *Tuberculosis (Edinb)* 2005; **85**(5-6): 277-93.
56. Slight SR, Rangel-Moreno J, Gopal R, et al. CXCR5(+) T helper cells mediate protective immunity against tuberculosis. *J Clin Invest* 2013; **123**(2): 712-26.
57. Arrey F, Lowe D, Kuhlmann S, et al. Humanized Mouse Model Mimicking Pathology of Human Tuberculosis for in vivo Evaluation of Drug Regimens. *Front Immunol* 2019; **10**.
58. Lynch JP, 3rd, Zhanel GG. Streptococcus pneumoniae: does antimicrobial resistance matter? *Semin Respir Crit Care Med* 2009; **30**(2): 210-38.
59. World Health Organization. WHO publishes list of bacteria for which new antibiotics are urgently needed. World Health Organization, Geneva, 2017. https://www.who.int/news/item/27-02-2017-who-publishes-list-of-bacteria-for-which-new-antibiotics-are-urgently-needed (accessed 22.05.2023)
60. Feldman C, Anderson R. The Role of Streptococcus pneumoniae in Community-Acquired Pneumonia. *Semin Respir Crit Care Med* 2020; **41**(4): 455-69.
61. Tleyjeh IM, Tlaygeh HM, Hejal R, Montori VM, Baddour LM. The impact of penicillin resistance on short-term mortality in hospitalized adults with pneumococcal pneumonia: a systematic review and meta-analysis. *Clin Infect Dis* 2006; **42**(6): 788-97.
62. Lujan M, Gallego M, Rello J. Optimal therapy for severe pneumococcal community-acquired pneumonia. *Intensive Care Med* 2006; **32**(7): 971-80.
63. Lujan M, Gallego M, Fontanals D, Mariscal D, Rello J. Prospective observational study of bacteremic pneumococcal pneumonia: Effect of discordant therapy on mortality. *Crit Care Med* 2004; **32**(3): 625-31.
64. Roson B, Carratala J, Fernandez-Sabe N, Tubau F, Manresa F, Gudiol F. Causes and factors associated with early failure in hospitalized patients with community-acquired pneumonia. *Arch Intern Med* 2004; **164**(5): 502-8.
65. Ramos-Sevillano E, Ercoli G, Brown JS. Mechanisms of Naturally Acquired Immunity to Streptococcus pneumoniae. *Front Immunol* 2019; **10**: 358.
66. Garvy BA, Harmsen AG. The importance of neutrophils in resistance to pneumococcal pneumonia in adult and neonatal mice. *Inflammation* 1996; **20**(5): 499-512.
67. Herbold W, Maus R, Hahn I, et al. Importance of CXC chemokine receptor 2 in alveolar neutrophil and exudate macrophage recruitment in response to pneumococcal lung infection. *Infect Immun* 2010; **78**(6): 2620-30.
68. Sun K, Salmon SL, Lotz SA, Metzger DW. Interleukin-12 promotes gamma interferon-dependent neutrophil recruitment in the lung and improves protection against respiratory Streptococcus pneumoniae infection. *Infect Immun* 2007; **75**(3): 1196-202.
69. Dorhoi A, Iannaccone M, Farinacci M, et al. MicroRNA-223 controls susceptibility to tuberculosis by regulating lung neutrophil recruitment. *J Clin Invest* 2013; **123**(11): 4836-48.
70. Berger S, Goekeri C, Gupta SK, et al. Delay in antibiotic therapy results in fatal disease outcome in murine pneumococcal pneumonia. *Crit Care* 2018; **22**(1): 287.
71. Goekeri C, Pennitz P, Groenewald W, et al. MicroRNA-223 Dampens Pulmonary Inflammation during Pneumococcal Pneumonia. *Cells* 2023; **12**(6).
72. Winkler ES, Bailey AL, Kafai NM, et al. Publisher Correction: SARS-CoV-2 infection of human ACE2-transgenic mice causes severe lung inflammation and impaired function. *Nat Immunol* 2020; **21**(11): 1470.
73. Winkler ES, Bailey AL, Kafai NM, et al. SARS-CoV-2 infection of human ACE2-transgenic mice causes severe lung inflammation and impaired function. *Nat Immunol* 2020; **21**(11): 1327-35.
74. Lakdawala SS, Menachery VD. The search for a COVID-19 animal model. *Science* 2020; **368**(6494): 942-3.
75. Clark A, Jit M, Warren-Gash C, et al. Global, regional, and national estimates of the population at increased risk of severe COVID-19 due to underlying health conditions in 2020: a modelling study. *Lancet Glob Health* 2020; **8**(8): e1003-e17.
76. Bastard P, Rosen LB, Zhang Q, et al. Autoantibodies against type I IFNs in patients with life-threatening COVID-19. *Science* 2020; **370**(6515).
77. Combes AJ, Courau T, Kuhn NF, et al. Global absence and targeting of protective immune states in severe COVID-19. *Nature* 2021; **591**(7848): 124-30.
78. Group RC, Horby P, Lim WS, et al. Dexamethasone in Hospitalized Patients with Covid-19. *N Engl J Med* 2021; **384**(8): 693-704.
79. Sinha S, Rosin NL, Arora R, et al. Dexamethasone modulates immature neutrophils and interferon programming in severe COVID-19. *Nat Med* 2022; **28**(1): 201-11.
80. Tang Y, Liu J, Zhang D, Xu Z, Ji J, Wen C. Cytokine Storm in COVID-19: The Current Evidence and Treatment Strategies. *Front Immunol* 2020; **11**: 1708.
81. Yang Y, Shen C, Li J, et al. Plasma IP-10 and MCP-3 levels are highly associated with disease severity and predict the progression of COVID-19. *J Allergy Clin Immunol* 2020; **146**(1): 119-27 e4.
82. Pennitz P, Kirsten H, Friedrich VD, et al. A pulmonologist's guide to perform and analyse cross-species single lung cell transcriptomics. *Eur Respir Rev* 2022; **31**(165).
83. Gruber AD, Firsching TC, Trimpert J, Dietert K. Hamster models of COVID-19 pneumonia reviewed: How human can they be? *Vet Pathol* 2022; **59**(4): 528-45.
84. Gruber AD, Osterrieder N, Bertzbach LD, et al. Standardization of Reporting Criteria for Lung Pathology in SARS-CoV-2-infected Hamsters: What Matters? *Am J Respir Cell Mol Biol* 2020; **63**(6): 856-9.
85. Osterrieder N, Bertzbach LD, Dietert K, et al. Age-Dependent Progression of SARS-CoV-2 Infection in Syrian Hamsters. *Viruses* 2020; **12**(7).
86. Nouailles G, Wyler E, Pennitz P, et al. Temporal omics analysis in Syrian hamsters unravel cellular effector responses to moderate COVID-19. *Nat Commun* 2021; **12**(1): 4869.
87. Nouailles G, Adler JM, Pennitz P, et al. Live-attenuated vaccine sCPD9 elicits superior mucosal and systemic immunity to SARS-CoV-2 variants in hamsters. *Nat Microbiol* 2023; **8**(5): 860-74.
88. Wyler E, Adler JM, Eschke K, et al. Key benefits of dexamethasone and antibody treatment in COVID-19 hamster models revealed by single-cell transcriptomics. *Mol Ther* 2022; **30**(5): 1952-65.
89. Iwasaki A, Omer SB. Why and How Vaccines Work. *Cell* 2020; **183**(2): 290-5.
90. Gordon S. Phagocytosis: The Legacy of Metchnikoff. *Cell* 2016; **166**(5): 1065-8.
91. Llewelyn MB, Hawkins RE, Russell SJ. Discovery of antibodies. *BMJ* 1992; **305**(6864): 1269-72.
92. World Health Organization. Global Commission for the Certification of Smallpox Eradication. The global eradication of smallpox : final report of the Global Commission for the Certification of Smallpox Eradication, Geneva, December 1979. World Health Organization, Geneva, 1980.
93. Vivier E, Artis D, Colonna M, et al. Innate Lymphoid Cells: 10 Years On. *Cell* 2018; **174**(5): 1054-66.
94. Plasschaert LW, Zilionis R, Choo-Wing R, et al. A single-cell atlas of the airway epithelium reveals the CFTR-rich pulmonary ionocyte. *Nature* 2018; **560**(7718): 377-81.
95. Disteldorf EM, Krebs CF, Paust HJ, et al. CXCL5 drives neutrophil recruitment in TH17-mediated GN. *J Am Soc Nephrol* 2015; **26**(1): 55-66.

96. Uplekar M, Weil D, Lonnroth K, et al. WHO's new end TB strategy. *Lancet* 2015; **385**(9979): 1799-801.
97. Berry MP, Graham CM, McNab FW, et al. An interferon-inducible neutrophil-driven blood transcriptional signature in human tuberculosis. *Nature* 2010; **466**(7309): 973-7.
98. Teles RM, Graeber TG, Krutzik SR, et al. Type I interferon suppresses type II interferon-triggered human anti-mycobacterial responses. *Science* 2013; **339**(6126): 1448-53.
99. Mayer-Barber KD, Andrade BB, Oland SD, et al. Host-directed therapy of tuberculosis based on interleukin-1 and type I interferon crosstalk. *Nature* 2014; **511**(7507): 99-103.
100. Dorhoi A, Yeremeev V, Nouailles G, et al. Type I IFN signaling triggers immunopathology in tuberculosis-susceptible mice by modulating lung phagocyte dynamics. *Eur J Immunol* 2014; **44**(8): 2380-93.
101. Dorhoi A, Iannaccone M, Maertzdorf J, Nouailles G, Weiner J, 3rd, Kaufmann SH. Reverse translation in tuberculosis: neutrophils provide clues for understanding development of active disease. *Front Immunol* 2014; **5**: 36.
102. Zak DE, Penn-Nicholson A, Scriba TJ, et al. A blood RNA signature for tuberculosis disease risk: a prospective cohort study. *Lancet* 2016; **387**(10035): 2312-22.
103. Shultz LD, Ishikawa F, Greiner DL. Humanized mice in translational biomedical research. *Nat Rev Immunol* 2007; **7**(2): 118-30.
104. Arrey F, Lowe D, Kuhlmann S, et al. Humanized Mouse Model Mimicking Pathology of Human Tuberculosis for in vivo Evaluation of Drug Regimens. *Front Immunol* 2019; **10**: 89.
105. Niazi MK, Dhulekar N, Schmidt D, et al. Lung necrosis and neutrophils reflect common pathways of susceptibility to Mycobacterium tuberculosis in genetically diverse, immune-competent mice. *Dis Model Mech* 2015; **8**(9): 1141-53.
106. Harrison DE, Astle CM, Niazi MKK, Major S, Beamer GL. Genetically diverse mice are novel and valuable models of age-associated susceptibility to Mycobacterium tuberculosis. *Immun Ageing* 2014; **11**(1): 24.
107. Ahmed M, Thirunavukkarasu S, Rosa BA, et al. Immune correlates of tuberculosis disease and risk translate across species. *Sci Transl Med* 2020; **12**(528).
108. Liapikou A, Ferrer M, Polverino E, et al. Severe community-acquired pneumonia: validation of the Infectious Diseases Society of America/American Thoracic Society guidelines to predict an intensive care unit admission. *Clin Infect Dis* 2009; **48**(4): 377-85.
109. Ceccato A, Torres A, Cilloniz C, et al. Invasive Disease vs Urinary Antigen-Confirmed Pneumococcal Community-Acquired Pneumonia. *Chest* 2017; **151**(6): 1311-9.
110. Bellani G, Laffey JG, Pham T, et al. Epidemiology, Patterns of Care, and Mortality for Patients With Acute Respiratory Distress Syndrome in Intensive Care Units in 50 Countries. *JAMA* 2016; **315**(8): 788-800.
111. Tzotzos SJ, Fischer B, Fischer H, Zeitlinger M. Incidence of ARDS and outcomes in hospitalized patients with COVID-19: a global literature survey. *Crit Care* 2020; **24**(1): 516.
112. Berger S, Wienhold SM, Goekeri C, et al. CXCL5-dependent neutrophil recruitment harms lung barrier function in acute lung injury. *Eur Respir J* 2018; **52**(suppl 62): PA4295.
113. Lask A, Gutbier B, Kershaw O, et al. Adjunctive therapy with the Tie2 agonist Vasculotide reduces pulmonary permeability in Streptococcus pneumoniae infected and mechanically ventilated mice. *Sci Rep* 2022; **12**(1): 15531.
114. Muller-Redetzky H, Kellermann U, Wienhold SM, et al. Neutralizing Complement C5a Protects Mice with Pneumococcal Pulmonary Sepsis. *Anesthesiology* 2020; **132**(4): 795-807.
115. Vlaar APJ, Witzenrath M, van Paassen P, et al. Anti-C5a antibody (vilobelimab) therapy for critically ill, invasively mechanically ventilated patients with COVID-19 (PANAMO): a multicentre, double-blind, randomised, placebo-controlled, phase 3 trial. *Lancet Respir Med* 2022; **10**(12): 1137-46.
116. Rodrigo C, Leonardi-Bee J, Nguyen-Van-Tam J, Lim WS. Corticosteroids as adjunctive therapy in the treatment of influenza. *Cochrane Database Syst Rev* 2016; **3**: CD010406.
117. Dequin PF, Meziani F, Quenot JP, et al. Hydrocortisone in Severe Community-Acquired Pneumonia. *N Engl J Med* 2023; **388**(21): 1931-41.
118. Wyler E, Adler JM, Eschke K, et al. Key benefits of dexamethasone and antibody treatment in COVID-19 hamster models revealed by single-cell transcriptomics. *Mol Ther* 2022; **30**(5): 1952-65.
119. Oberhardt V, Luxenburger H, Kemming J, et al. Rapid and stable mobilization of CD8(+) T cells by SARS-CoV-2 mRNA vaccine. *Nature* 2021; **597**(7875): 268-73.
120. Laczko D, Hogan MJ, Toulmin SA, et al. A Single Immunization with Nucleoside-Modified mRNA Vaccines Elicits Strong Cellular and Humoral Immune Responses against SARS-CoV-2 in Mice. *Immunity* 2020; **53**(4): 724-32 e7.
121. Prunas O, Warren JL, Crawford FW, et al. Vaccination with BNT162b2 reduces transmission of SARS-CoV-2 to household contacts in Israel. *Science* 2022; **375**(6585): 1151-4.
122. Hayek S, Shaham G, Ben-Shlomo Y, et al. Indirect protection of children from SARS-CoV-2 infection through parental vaccination. *Science* 2022; **375**(6585): 1155-9.
123. Krammer F. The human antibody response to influenza A virus infection and vaccination. *Nat Rev Immunol* 2019; **19**(6): 383-97.
124. Coleman JR, Papamichail D, Skiena S, Futcher B, Wimmer E, Mueller S. Virus attenuation by genome-scale changes in codon pair bias. *Science* 2008; **320**(5884): 1784-7.
125. Trimpert J, Dietert K, Firsching TC, et al. Development of safe and highly protective live-attenuated SARS-CoV-2 vaccine candidates by genome recoding. *Cell Rep* 2021; **36**(5): 109493.
126. Adler JM, Martin Vidal R, Voss A, et al. A non-transmissible live attenuated SARS-CoV-2 vaccine. *Mol Ther* 2023.
127. Topol EJ, Iwasaki A. Operation Nasal Vaccine-Lightning speed to counter COVID-19. *Sci Immunol* 2022; **7**(74): eadd9947.
128. Diallo BK, Ni Chasaide C, Wong TY, et al. Intranasal COVID-19 vaccine induces respiratory memory T cells and protects K18-hACE mice against SARS-CoV-2 infection. *NPJ Vaccines* 2023; **8**(1): 68.
129. Afkhami S, D'Agostino MR, Zhang A, et al. Respiratory mucosal delivery of next-generation COVID-19 vaccine provides robust protection against both ancestral and variant strains of SARS-CoV-2. *Cell* 2022; **185**(5): 896-915 e19.
130. Mao T, Israelow B, Pena-Hernandez MA, et al. Unadjuvanted intranasal spike vaccine elicits protective mucosal immunity against sarbecoviruses. *Science* 2022; **378**(6622): eabo2523.
131. Li JX, Hou LH, Gou JB, et al. Safety, immunogenicity and protection of heterologous boost with an aerosolised Ad5-nCoV after two-dose inactivated COVID-19 vaccines in adults: a multicentre, open-label phase 3 trial. *Lancet Infect Dis* 2023.
132. Piccoli L, Park YJ, Tortorici MA, et al. Mapping Neutralizing and Immunodominant Sites on the SARS-CoV-2 Spike Receptor-Binding Domain by Structure-Guided High-Resolution Serology. *Cell* 2020; **183**(4): 1024-42 e21.
133. Liu L, Wang P, Nair MS, et al. Potent neutralizing antibodies against multiple epitopes on SARS-CoV-2 spike. *Nature* 2020; **584**(7821): 450-6.
134. Dai L, Gao GF. Viral targets for vaccines against COVID-19. *Nat Rev Immunol* 2021; **21**(2): 73-82.
135. Willett BJ, Grove J, MacLean OA, et al. SARS-CoV-2 Omicron is an immune escape variant with an altered cell entry pathway. *Nat Microbiol* 2022; **7**(8): 1161-79.
136. Arieta CM, Xie YJ, Rothenberg DA, et al. The T-cell-directed vaccine BNT162b4 encoding conserved non-spike antigens protects animals from severe SARS-CoV-2 infection. *Cell* 2023; **186**(11): 2392-409 e21.

# Danksagung

An dieser Stelle möchte ich mich ganz herzlich bedanken. Die Fertigstellung meiner Habilitationsschrift war ein Meilenstein in meiner akademischen Laufbahn und wäre ohne die Unterstützung und Ermutigung vieler Menschen nicht möglich gewesen.

An erster Stelle möchte ich meinen Mentor*innen Prof. Roland Lauster, Prof. Martin Witzenrath, Prof. Anca Dorhoi, Dr. Markus Koch und Prof. Stefan HE Kaufmann meinen tiefsten Dank aussprechen. Eure wertvollen Ratschläge, Euer unermüdliches Engagement und Euer Fachwissen haben meine Forschung maßgeblich geprägt und meine wissenschaftliche Entwicklung gefördert. Für Eure Begleitung und Unterstützung bin ich zutiefst dankbar.

Mein Dank gilt auch meinen liebsten Kolleg*innen, am MPIIB Stefanie Kuhlmann und Dr. Tracey Day, an der Charité Dr. Sandra-Maria Wienhold, Dr. Birgitt Gutbier, Dr. Jasmin Lienau und Ulrike Behrendt, an der FU Berlin Dr. Jakob Trimpert und am MDC Dr. Emanuel Wyler. Eure intellektuellen Anregungen, inspirierenden Diskussionen und konstruktiven Kritiken haben meine Arbeit maßgeblich beeinflusst. Eure Unterstützung und Euer Humor haben mir durch lange Nächte geholfen und nicht nur mein Forscherleben bereichert.

Mein besonderer Dank gilt auch meinen ehemaligen Doktorand*innen Dr. Frida Takubetang Array, Dr. Sarah Berger, Dr. Cengiz Gökeri sowie Julia Adler, die während meiner Habilitation mit mir zusammengearbeitet haben. Eure Neugier, Euer Eifer und Eure wertvollen Beiträge haben meinen Horizont erweitert und eine wunderbare Zusammenarbeit ermöglicht. Eure Fragen und Diskussionen haben mich inspiriert, mein Wissen weiterzugeben und die Freude am Lehren zu entdecken. Ich bin stolz darauf, Euch auf Eurer wissenschaftlichen Reise begleitet zu haben.

Abschließend möchte ich mich bei meinen Freunden und meiner Familie bedanken. Eure Freundschaft und Liebe ist das Schönste in meinem Leben.

Euch allen noch einmal von ganzem Herzen vielen Dank für Euren Beitrag und für all die schönen Jahre und Momente und auf die vielen, die noch kommen werden.

# Erklärung

§ 4 Abs. 3 (k) der HabOMed der Charité

Hiermit erkläre ich, dass

- weder früher noch gleichzeitig ein Habilitationsverfahren durchgeführt oder angemeldet wurde,
- die vorgelegte Habilitationsschrift ohne fremde Hilfe verfasst, die beschriebenen Ergebnisse selbst gewonnen sowie die verwendeten Hilfsmittel, die Zusammenarbeit mit anderen Wissenschaftlern/Wissenschaftlerinnen und mit technischen Hilfskräften sowie die verwendete Literatur vollständig in der Habilitationsschrift angegeben wurden,
- mir die geltende Habilitationsordnung bekannt ist.

Ich erkläre ferner, dass mir die Satzung der Charité – Universitätsmedizin Berlin zur Sicherung Guter Wissenschaftlicher Praxis bekannt ist und ich mich zur Einhaltung dieser Satzung verpflichte.

Berlin, den 11.01.24 .....

Datum Geraldine Nouailles-Kursar